
THE UNIVERSITY *of* EDINBURGH

# Biomimetic Cochlea Filters: from Modelling, Design to Analogue VLSI Implementation

*Shiwei Wang*


A thesis submitted for the degree of Doctor of Philosophy.
**The University of Edinburgh**.
August 2014

# Abstract

This thesis presents a novel biomimetic cochlea filter which closely resembles the biological cochlea behaviour. The filter is highly feasible for analogue very-large-scale integration (VLSI) circuits, which leads to a micro-watt-power and millimetre-sized hardware implementation. By virtue of such features, the presented filter contributes to a solid foundation for future biologically-inspired audio signal processors.

Unlike existing works, the presented filter is developed by taking direct inspirations from the physiologically measured results of the biological cochlea. Since the biological cochlea has prominently different characteristics of frequency response from low to high frequencies, the biomimetic cochlea filter is built by cascading three sub-filters accordingly: a $2^{\mathrm{nd}}$-order band-pass filter for the constant gentle low-frequency response, a $2^{\mathrm{nd}}$-order tunable low-pass filter for the variable and selective centre frequency response and a $5^{\mathrm{th}}$-order elliptic filter for the ultra-steep roll-off at stop-band. As a proof of concept, a biomimetic cochlea filter bank is built to process audio signals, which demonstrates the highly discriminative spectral decomposition and high-resolution time-frequency analysis capabilities similar to the biological cochlea.

The filter has simple representation in the Laplace domain which leads to a convenient analogue circuit realisation. A floating-active-inductor circuit cell is developed to build the corresponding RLC ladder for each of the three sub-filters. The circuits are designed based on complementary metal-oxide-semiconductor (CMOS) transistors for VLSI implementation. Non-ideal factors of CMOS transistors including parasitics, noise and mismatches are extensively analysed and consciously considered in the circuit design. An analogue VLSI chip is successfully fabricated using 0.35 $\mu$m CMOS process. The chip measurements demonstrate that the centre frequency response of the filter has about 20 dB wide gain tuning range and a high quality factor reaching maximally over 19. The filter has a 20 dB/decade constant gentle low-frequency tail and an over 300 dB/decade sharp stop-band roll-off slope. The measured results agree with the filter model expectations and are comparable with the biological cochlea characteristics. Each filter channel consumes as low as 59.5$\sim$90 $\mu$W power and occupies only 0.9 $mm^2$ area. Besides, the biomimetic cochlea filter chip is characterised from a wide range of angles and the experimental results cover not only the auditory filter specifications but also the integrated circuit design considerations.

Furthermore, following the progressive development of the acoustic resonator based on micro-electro-mechanical systems (MEMS) technology, a MEMS-CMOS implementation of the proposed filter becomes possible in the future. A key challenge for such implementation is the low sensing capacitance of the MEMS resonator which suffers significantly from sensitivity degradation due to the parasitic capacitance. A novel MEMS capacitive interface circuit chip is additionally developed to solve this issue. As shown in the chip results, the interface circuit is able to cancel the parasitic capacitance and increase the sensitivity of capacitive sensors by 35 dB without consuming any extra power. Besides, the chopper-stabilisation technique is employed which effectively reduces the circuit flicker noise and offsets. Due to these features, the interface circuit chip is capable of converting a 7.5 fF capacitance change of a 1-Volt-biased 0.5 pF capacitive sensor pair into a 0.745 V signal-conditioned output while consuming only 165.2 $\mu$W power.

***This work is dedicated to the memory of my dear grandmother.***

# Lay Summary

This thesis presents a novel method to build electronic filters that emulate the behaviour of the cochlea. Elaboration is made on how the filter is modelled, designed and implemented in integrated electronic chips. The experimental results from the fabricated chip prove that the proposed filter is able to resemble a wide range of physiologically measured response characteristics of the cochlea and shows much better biological fidelity than the existing designs.

The importance of this work includes three aspects. Firstly, the biological fidelity of the filter response will potentially contribute to better prosthetic devices that are used to treat the hearing loss problem induced by cochlea damage. Secondly, by closely emulating the cochlea which is a powerful and power-efficient sound processing organ engineered by the nature, the proposed filter leads to promising possibilities to improve the performance of man-made sound processors. Thirdly, based on the proposed filter, a faithful electronic model of the biological auditory system can be built to better investigate and understand how hearing mechanism works.

# Declaration of originality

I hereby declare that this thesis was composed and originated entirely by myself in the School of Engineering at The University of Edinburgh except where explicitly stated otherwise in the text, and that this work has not been submitted for any other degree or professional qualifications.

Shiwei Wang

# Acknowledgements

I would like to acknowledge the Engineering and Physical Sciences Research Council (EPSRC) for funding this project under the grant to the University of Edinburgh (EP/G063710/1). Also, I would like to thank the China Scholarship Council (CSC) and the University of Edinburgh for jointly sponsoring my PhD study.

There are many individuals who have kindly helped me during the past four years. Dr. Alister Hamilton, my supervisor, has continuously supported me throughout my PhD. I appreciate his trust and the freedom he gave me to explore my own research interest, without which this research outcome could never be possible. Dr. Thomas Jacob Koickal, who was like my mentor, has helped me a lot with his experience. I became used to discussing with him whenever I had a new research idea; he was always able to give me constructive feedbacks and make me clearly aware of where the key points are.

I would like to thank everyone else in the EPSRC project, Prof. Rebecca Cheung, Prof. Leslie S. Smith, Dr. Enrico Mastropaolo, Dr. Michael Newton, Dr. Rhonira Latif, Dr. Andrew Abel and Eldad Grady. This is such a multi-disciplinary research project and I did enjoy the idea-sharing with people from very different backgrounds. My thanks also go to Tao Chen for taking the chip micrographs in this thesis, Dr. Katherine Cameron for her support in the Cadence IC design software and everyone who has worked with me in the Alrick building office room 2.3 for all the helpful technical discussions and the interesting non-technical conversations.

I am grateful for all the friends I met in the University of Edinburgh. Especially, a thank goes to Xiaonan Wang, my girlfriend, for accompanying me through the toughest period of my PhD and helping me to shape myself into a better man. Also, I would like to thank Dr. Cheng-Kai Lu, my senior, for giving me so many career advices and frequently inviting me to his feasts of Taiwanese cuisine.

Finally, I would like to express my special gratitude to my parents for their unconditional love and support as always. Their encouragement and anticipation are the main source of my motivation to pursue excellence.

# Contents

# List of figures

# List of tables

# Acronyms and abbreviations

| | |
|---|---|
| AMS | AustriaMicroSystems |
| APFC | All-Pole Filter Cascade |
| APGF | All-Pole Gamma-tone Filter |
| ASR | Automatic Speech Recognition |
| ATC | Automatic Tuning Control |
| AQC | Automatic Q Control |
| BM | Basilar Membrane |
| BPF | Band-pass Filter |
| CASA | Computational Auditory Scene Analysis |
| CF | Centre Frequency |
| CHS | Chopper-Stabilisation |
| CI | Cochlea Implant |
| CMFB | Commom-Mode Feedback |
| CMOS | Complementary Metal-Oxide-Semiconductor |
| DAQ | Data Acquisition |
| dBFS | Decibels Relative to Full Scale |
| ELF | Elliptic Low-pass Filter |
| ERB | Equivalent Rectangular Bandwidth |
| FAI | Floating Active Inductor |
| FDDA | Fully Differential Difference Amplifier |
| FDOTA | Fully Differential Operational Transconductance Amplifier |
| GBW | Gain-Bandwidth Product |
| HQ | High-Q |
| IHC | Inner Hair Cell |
| LPF | Low-pass Filter |
| LQ | Low-Q |
| MEMS | Eicro-Electro-Mechanical System |
| MOS | Metal-Oxide-Semiconductor |
| MQ | Medium-Q |

| | |
|---|---|
| NI | National Instruments |
| OHC | Outer Hair Cell |
| OpAmp | Operational Amplifier |
| OTA | Operational Transconductance Amplifier |
| PC | Parasitic-Cancellation |
| PCB | Printed Circuit Board |
| PGDR | Peak Gain Dynamic Range |
| PSD | Power Spectral Density |
| Q factor | Quality Factor |
| $Q_{10}$ factor | 10 dB Quality Factor |
| RC | Resistor-Capacitor |
| RCS | Resistor-Capacitor-Super-Capacitor |
| RLC | Resistor-Inductor-Capacitor |
| RM | Reissner's Membrane |
| SC | Switched-Capacitor |
| SFDR | Spurious-Free Dynamic Range |
| SINAD | Signal-to-Noise and Distortion Ratio |
| SNR | Signal-to-Noise Ratio |
| SOTA | Single-End Operational Transconductance Amplifier |
| THD | Total Harmonic Distortion |
| TM | Tectorial Membrane |
| VLSI | Very-Large-Scale Integration |

# Chapter 1
# Introduction

## 1.1 Motivation

The cochlea is the core organ for sound preprocessing in the mammalian auditory systems. It decomposes the sound inputs into multiple channels of frequency segments before encoding them into neural impulses [2–5]. In engineering perspective, the cochlea operates analogously to a bank of band-pass filters with centre frequencies spanning over the audible frequency range [6]. According to the findings in physiologically experiments [1, 7–11], the cochlea frequency response has extraordinary band-pass characteristics. As shown in Fig. 1.1, the cochlea response around the centre frequency (CF) demonstrates a wide range of tuning depending on the input intensity. The peak gain and selectivity increase when the input intensity is low and decrease when the input intensity is high. By contrast, the response at low frequencies is constant and independent of the input intensities. Moreover, while the rising curve at low frequencies has a fairly gentle slope, the roll-off slope towards stop-band is very steep and reaches a maximum over 300 dB/decade. These frequency response characteristics are crucial for the cochlea signal processing capabilities. For example, the ultra-steep roll-off is the basis for the discriminative spectral decomposition and the wide range CF tuning enables the cochlea to dynamically adapt to input intensities and thus compresses the wide-range sound input into the narrow-range neural impulse rate. Additionally, the CF tuning is simultaneously controlled by the central auditory system in the brain, which contributes to the periphery-level selective attention ability of mammal [12].

During the past two decades, a number of engineering problems have been addressed by designing biologically-inspired auditory systems that incorporate the cochlea mechanism. For example, the cochlea implant (CI), which is a prosthetic device that resembles the cochlea functionality, has been applied for treatment of hearing loss due to cochlea impairments [13, 14]; the cochlea-type filter banks have been employed in computational auditory scene analysis (CASA) systems for a variety of auditory processing tasks such as automatic speech recognition (ASR) and sound localisation [15]; besides, the realisation of cochlea models in silicon

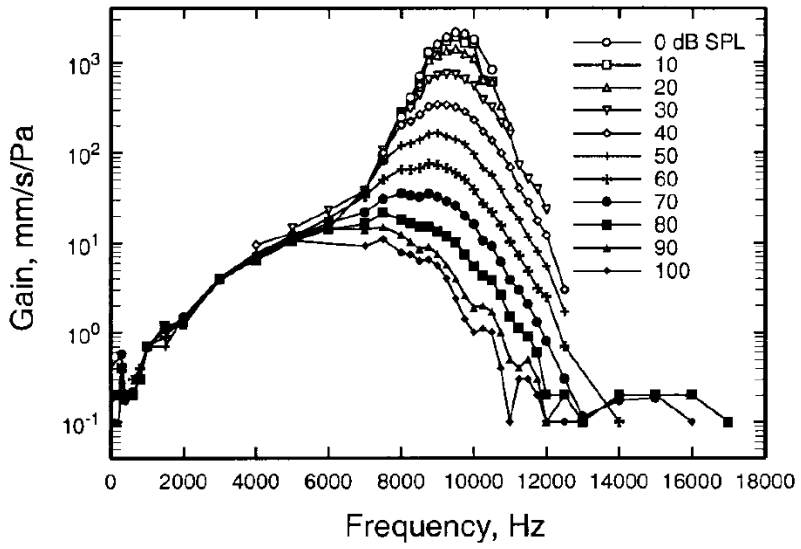


**Figure 1.1:** *Measured frequency response at the 3.5-mm site of chinchilla cochlea. The legends refer to the sound pressure level (SPL) of inputs. (Image is taken from [1].)*

chips (silicon cochlea) has established new platforms for hearing research and provided inspirations for future artificial intelligent hearing systems [16–20]. However, the behaviour of these cochlea-type systems remains considerably inconsistent with the aforementioned biological cochlea characteristics. The existing CIs generally employ rudimentary band-pass filters for spectral decomposition which are hardly adequate to provide the same hearing experience as a real cochlea [21]. The typical filter banks used in CASA systems are based on the gamma-tone filter whose frequency response is symmetric with respect to CF and is highly dissimilar to the biological cochlea frequency response [22]. The silicon cochlea systems focus on replication of the anatomical organisation and hydrodynamic principles of the biological cochlea which, as will be shown in Chapter 2, has not guaranteed the response fidelity, since the elementary components in silicon are hardly comparable to the biological counterparts on the basis of existing technologies.

Under this background, a novel biomimetic cochlea filter which faithfully resembles the biological cochlea frequency response is proposed and investigated in this thesis. Since the frequency response characteristics are crucial for the cochlea signal processing functions, the proposed filter will prospectively bring performance improvements to the existing cochlea-type auditory systems. Moreover, the frequency response is directly related with a variety of cochlea properties such as the phase response and group delay in addition to those aforementioned frequency response characteristics. Therefore, by replicating the frequency response, the proposed filter

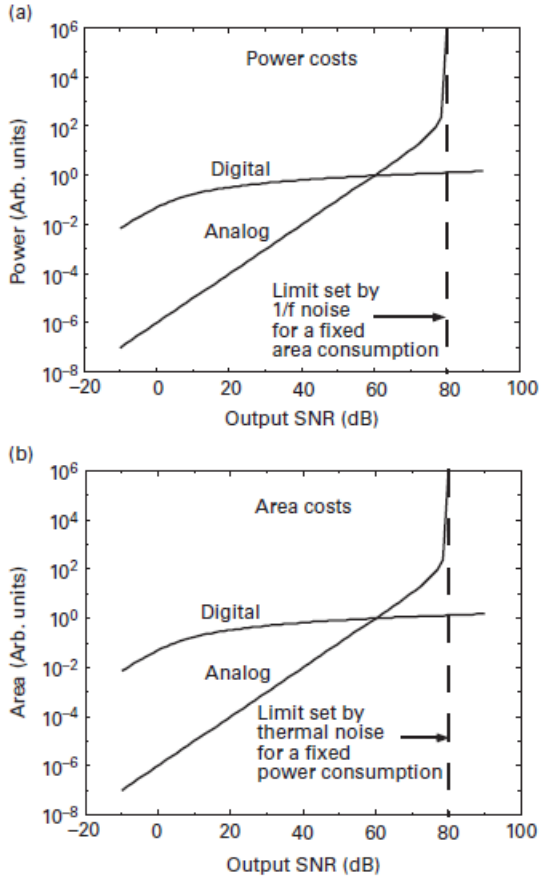


**Figure 1.2:** *Comparison between analogue and digital VLSI implementations regarding power consumption and occupied area. (Image is take from [23].)*

will resemble the biological cochlea behaviour in a wide range of aspects.

Additionally, the feasibility for low-power and compact-size hardware implementation is another critical issue to be addressed in the filter design. In functionality perspective, a large number of channels can be integrated in a filter bank if the power and size of each filter channel are minimised, which increases the resolution of frequency analysis and provides a massively parallel architecture for collective processing. In the application perspective, low-power and small-size hardware implementation is stringently required in hearing prosthetic devices and is also favoured if the filter is to be widely applicable for portable systems. Therefore, the filter implementation in analogue very-large-scale integration (VLSI) hardware is emphasised in this thesis. As revealed in Fig. 1.2, the analogue VLSI implementation leads to less power consumption and smaller chip area compared with the digital counterpart unless extremely high output signal-to-noise ratio (SNR) is required [23, 24]. In fact, the analogue VLSI approach has

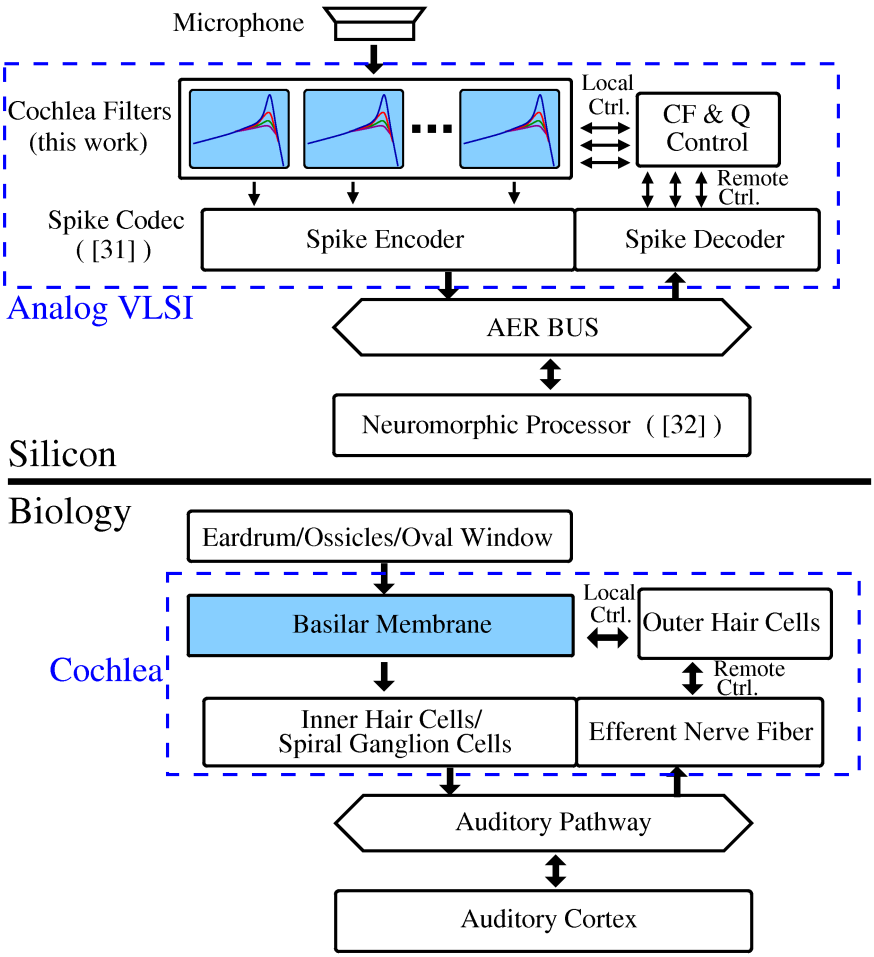


**Figure 1.3:** *The position of this work in a future biologically-inspired auditory system. The system-level diagram of the biological auditory system is also illustrated for comparison.*

been favoured for implementation of silicon cochlea systems [16–20], and is becoming popular for CIs [25–27] and speech recognition hardware [28–30].

With the features of biologically faithful response and feasibility for low-power and compact-size analogue VLSI implementation, the biomimetic cochlea filter proposed in this thesis has the potential to become an attractive option for future cochlea-type auditory processing front-ends. In particular, the contribution from this work will be compatibly integrated with the existing research outcomes of the Analogue and Mixed Signal VLSI group of the University of Edinburgh about spike-based neuromorphic processing techniques [31, 32], which will prospectively lead to a complete eardrum-to-cortex biologically-inspired hearing system as shown in Fig. 1.3

## 1.2 Objectives

The core objective of this work is to develop a biomimetic cochlea filter which closely resembles the biological cochlea response and is feasible for low-power and compact-size analogue VLSI implementation. Specifically, the filter will meet the following criteria:

- The filter response around CF is highly tunable: the peak gain should have at least 20 dB wide range of variation [1, 8–11]; the CF selectivity, which is reflected by the filter quality factor, should also increase when the peak gain increases, and the maximum 10 dB quality factor ($Q_{10}$) is expected to reach at least 3 to be substantially comparable to the biological cochlea [1, 8–11]; the CF should also shift accordingly with the variation of peak gain and selectivity in a similar way as the biological cochlea does [1, 8–11].
- The frequency response curve in low frequencies should demonstrate a gentle rising slope, which also has to keep constant while the CF response varies [1, 8–11].
- The roll-off slope towards stop-band has to be ultra steep, matching the over 300 dB/decade biological figure [1, 8–11]. From an overall perspective, the filter has a highly asymmetric shape of frequency response: a gentle low-frequency tail and an ultra-steep stop-band roll-off.
- Since the biological cochlea has minimum-phase property [33], the filter should be a minimum-phase filter so that its phase response and group delay are also biologically faithful.
- The filter is easy to realise using analogue VLSI circuits. A sufficient condition to meet this criterion is that the filter has a simple form of representation in the Laplace-domain.
- As mentioned above, the CF tuning of the filter includes three aspects: the peak gain, the selectivity and the CF shift. Due to the imprecise nature of analogue VLSI circuits, the variable circuit parameters that are involved in the tuning should be as few as possible in order to reduce tuning inaccuracy and instability risk. Ideally, those three aspects of CF tuning should be achievable by adjusting only one circuit parameter.
- To meet the power consumption and area requirements, the filter complexity should be minimised. A low-order filter is definitely preferred.
- The filter operation is robust against the non-ideal factors of analogue VLSI circuits such as parasitics, noise, and transistor mismatches.

## 1.3 Thesis Overview

The thesis is organised as follows:

- A background review is carried out in Chapter 2, which focuses on two aspects: the important physiological findings about the biological cochlea and the representative cochlea filter models that have been developed in the past.

- In Chapter 3, a mathematical model of the biomimetic cochlea filter is established. The model behaviour is compared with the biological cochlea from many angles such as the magnitude frequency response, phase response, group delay and impulse response. A cochlea filter bank is implemented in the MATLAB Simulink software based on the mathematical model. The cochlea filter bank is used to process audio signals and generate cochleagrams for a proof of concept.

- In Chapter 4, the method to realise the biomimetic cochlea filter using analogue VLSI circuits is elaborated. The effects of the circuit non-ideal factors including the parasitics, noise and transistor mismatches are extensively analysed and consciously considered in the filter design. Finally, the biomimetic cochlea filter is implemented in an analogue VLSI chip which is fabricated using AustriaMicroSystems (AMS) 0.35 $\mu$m standard CMOS process.

- Chapter 5 gives the detailed experimental results from the prototype chip. The biologically faithful response of the biomimetic cochlea filter is verified by the chip results. Apart from the aforementioned magnitude response, phase response, group delay and impulse response, the biomimetic cochlea filter chip is also comprehensively characterised regarding circuit design specifications such as noise, harmonic distortion and intermodulation distortion. Additionally, the chip is used to process acoustic signals.

- Chapter 6 investigates the possibility of an alternative approach which takes advantage of MEMS technology to implement the proposed biomimetic cochlea filter. A novel MEMS interface circuit is developed to address the key challenge for such an approach. The MEMS interface chip is implemented in a second analogue VLSI chip which is fabricated using the same AMS 0.35 $\mu$m standard CMOS process. The chip measurement results which verify the functionality and performance of the proposed MEMS interface circuit are shown and discussed.

- Chapter 7 concludes this thesis. Elaboration is made on how those objectives listed in Section 1.2 are achieved in this work. Also, the contribution of this work to knowledge is summarised. Eventually, an outlook is made on possible future work that is relevant to this thesis.

# Chapter 2
# Background Review

In this chapter, a background review is carried out focusing on two aspects: the biological cochlea and the existing cochlea filter models. Important physiological findings about the anatomy, mechanism and frequency response of the biological cochlea are introduced. The existing cochlea filter models are classified into two categories: the travelling-wave architectures and the parallel cochlea filter banks, both of which are reviewed roughly in chronological order. In the end, a comparison between the frequency response of the biological cochlea and the existing cochlea filter models is performed.

## 2.1 Physiological Findings about the Biological Cochlea

### 2.1.1 Anatomical Structure

The cochlea anatomy has been adequately understood thus far [2–5]. As shown in Fig. 2.1, the cochlea is located in the inner ear part of the auditory periphery, and it is interfaced with the middle ear osscicles through the oval window. The cochlea has a spiral shape and its cross-sectional view is illustrated in Fig. 2.2. There are three chambers in the cochlea: the scala vestibuli, the scala tympani, and the scala media. The three chambers are partitioned by two membranes, the Reissner's membrane (RM) and the basilar membrane (BM). Inside the scala media on top of the BM sits the organ of Corti, which is interfaced with the cochlea nerve fibres.

The detailed anatomy of the organ of Corti is illustrated in Fig. 2.3. There are two types of sensory hair cells in the organ of Corti, namely the inner hair cell (IHC) and the outer hair cell (OHC). In the human ear there are about 3500 IHCs which stand in a single row and 12000 OHCs which stand in three rows [34, 35]. As shown in Fig. 2.3, both the IHCs and the OHCs have stereocillas which stick out and touch another type of membrane structure called the tectorial membrane (TM). And both the IHCs and OHCs are innervated with the cochlea nerve fibres. There are two type of nerve fibres: the afferent nerve fibres which transmit neural

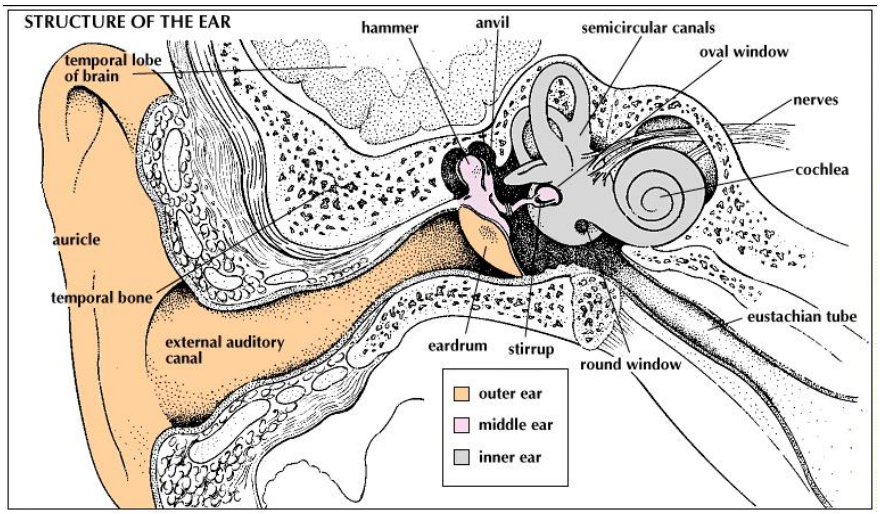


**Figure 2.1:** *Location of the cochlea in the human auditory periphery. (Image is take from http://oto2.wustl.edu/cochlea/intro1.htm.)*

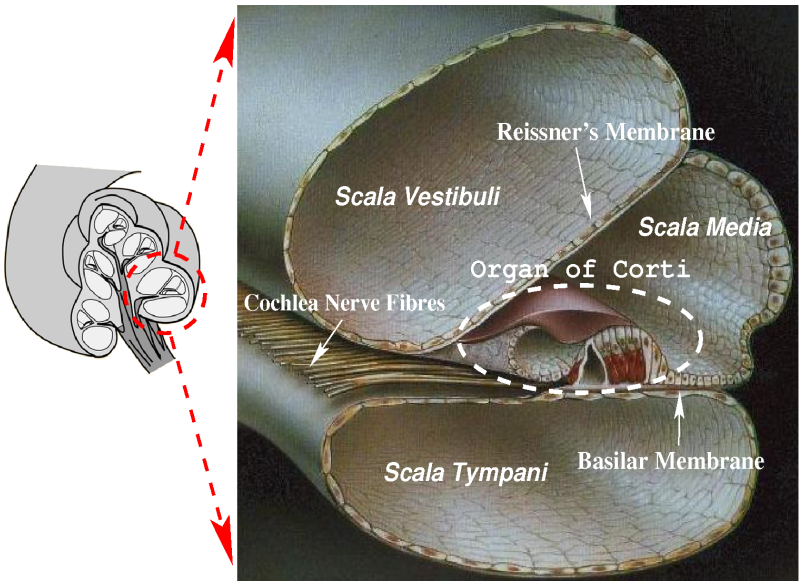


**Figure 2.2:** *Cross-sectional view of the cochlea. (Image is adapted from two figures respectively taken from http://hyperphysics.phy-astr.gsu.edu/hbase/sound/cochlea.html and http://www.ece.rice.edu/%7edhj/cochlea.html. Additional labels are added based on the descriptions of cochlea structure in [2–5].)*

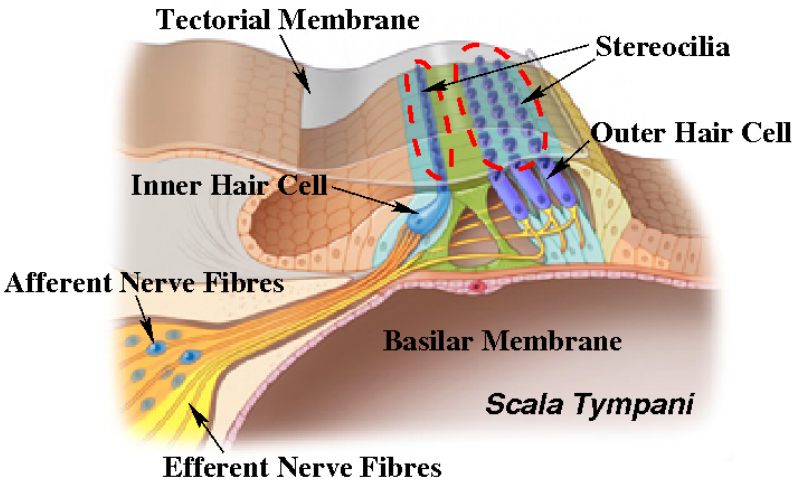


**Figure 2.3:** *Anatomy of organ of Corti. (Image is adapted from https://hearinglosscure.stanford.edu/infogallery. Additional labels are added based on the description of organ of Corti anatomy given in [2–5].)*

impulses to the brain and the efferent nerve fibres which receive the neural impulses from the brain [34, 35]. The IHCs predominantly receive innervations from the afferent nerve fibres while the OHCs predominantly receive innervations from the efferent nerve fibres [34, 35].

### 2.1.2 Sound Reception Mechanism

As shown in Fig. 2.1, the oval window of the cochlea is attached to a kind of middle ear osscicle called the stapes (or "stirrups" in Latin). A lever system is formed by the stapes and the other two types of ossicles, the malleus (or "hammer" in Latin) and the incus (or "anvil" in Latin) [4]. With this lever system, the mechanical force converted from the sound-induced eardrum movement is significantly boosted so that the pressure applied by the stapes on the oval window becomes intense enough to drive the high-impedance cochlea fluid [4]. Fig. 2.4 illustrates the uncoiled structure of the cochlea and the flow of the cochlea fluid. There are two types of cochlea fluid: the perilymph which fills the the scala vestibuli and the scala tympani, and the endolymph which fills the scala media [2–5]. As shown in Fig. 2.4, when the stapes press the oval window, the perilymph in the scala vestibuli is driven to flow towards the apical end of the cochlea. Since the scala vestibuli and the scala tympani are connected at the apical end of the cochlea, the fluid flows further back to the basal end through the scala tympani and eventually causes the round window of the cochlea to bulge out and release the force [2–5].

The travelling wave induced by the flow of the cochlea fluid activates the resonant movement of

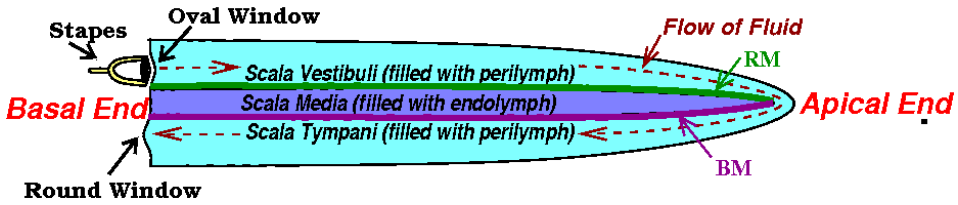


**Figure 2.4:** *Depiction of the flow of fluid in the uncoiled cochlea. (The image is drawn according to the description of the cochlea structure and mechanism given in [2–5].)*

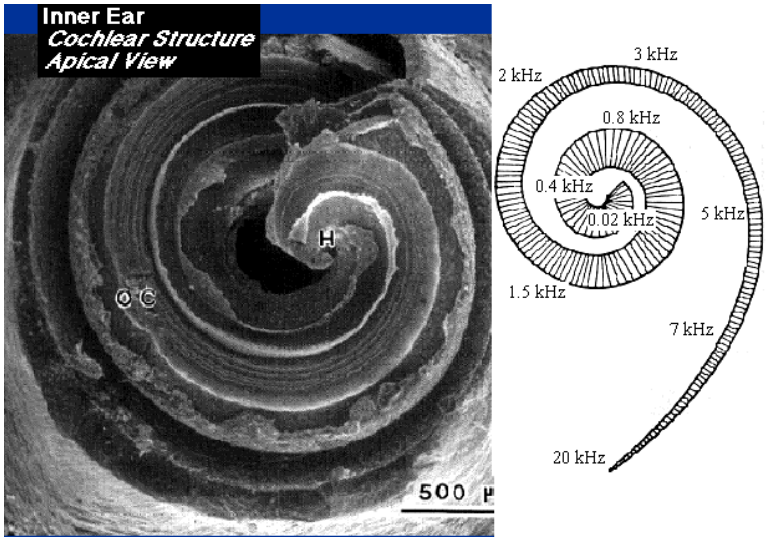


**Figure 2.5:** *Micrograph of the cochlea and the tonotopy of BM resonant frequencies. (Image is adapted from http://www.neurophys.wisc.edu/h&b/auditory/anatomy/a13.html.)*

the BM, which leads to the spectral decomposition mechanism of the cochlea [36]. The BM is stiff and narrow at the basal end; its compliance and width gradually increase from the basal to the apical end [2–5, 36]. Accordingly, the resonant frequency of the BM is highest at the basal end (20 kHz) and gradually decreases to the lowest at the apical end (20 Hz). The resonant frequencies at different locations on the BM are shown in Fig. 2.5. This spatial arrangement of separate frequencies in the cochlea is called tonotopy, which is preserved all the way through the auditory nerves and eventually projected in the auditory cortex [37, 38]. Discoveries have shown that the tonotopic feature of the cochlea is essential for the high-level sound perception in the brain [37, 38].

The BM movements are encoded into the neural impulses through a complex sensory process in the organ of Corti [2–5]. Fig. 2.6 presents two sketches from [2] which comprehensibly depict this process. As shown in Fig. 2.6(a), the vertical movement of the BM induces a shear force between the stereocilia of the hair cells and the overlying TM. The stereocilia is deflected

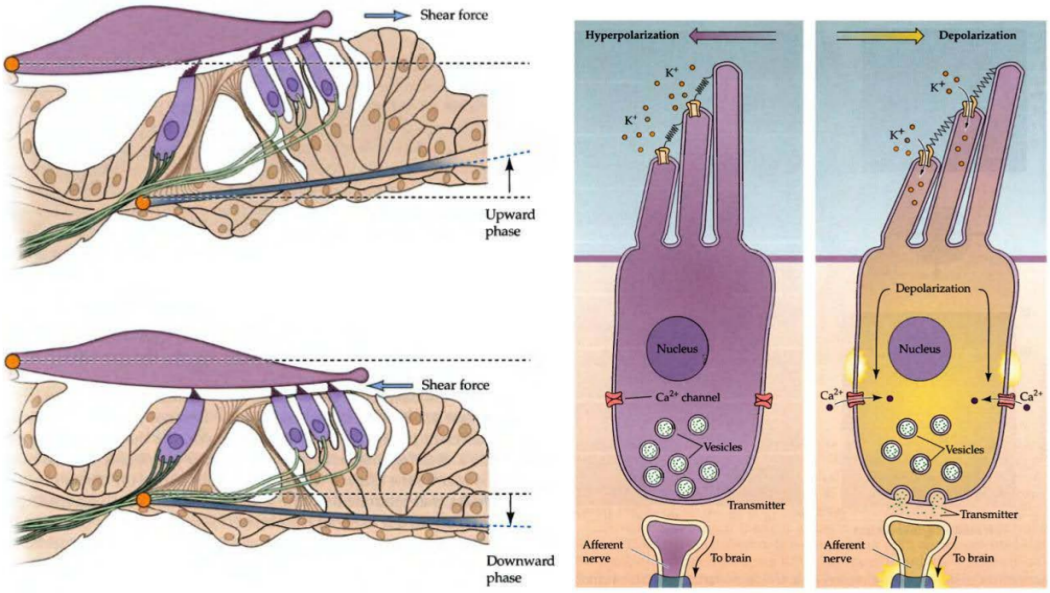


**(a)** Deflections of hair cell stereocilia induced by the BM movement

**(b)** Electrochemical activities and neural excitations within hair cells induced by the stereocilia deflection

**Figure 2.6:** *The sound sensory process in the organ of Corti. (Images are taken from [2].)*

by the shear force, which accordingly modulates the ion channels on the tip of the stereocilia. As shown in Fig. 2.6(b), the downward BM movement brings about the hyper-polarisation of the hair cells while the upward BM movement leads to the depolarisation of the hair cells [2]. Eventually, the electrochemical activities in the hair cells trigger the neural excitations which are subsequently transmitted to the nerve fibres [2].

Notably, the two types of hair cells have quite different functions in the sound sensory process. The IHC passively transduces the BM movement into the electrochemical activities and eventually into the neural impulses [2, 35]. By contrast, the OHC not only performs the passive sound transduction but also demonstrates highly active behaviour. The otoacoustic emission phenomenon observed by Kemp and Zurck around 1980s indicates that there exists certain negative-damping effect in the inner ear, which is significant enough to emit oscillatory wave back out of the ear and produce a detectable sound [39, 40]. The origin of this negative-damping effect was revealed when Brownell discovered the OHC electro-motility a couple of years later [41]. The evidence given in [41] demonstrates that the OHC is able to actively alter its shape in accordance with the hair cell hyper-polarisation and depolarisation. The OHC elongates when hyper-polarised and becomes contracted when depolarised so that the shape variation performs a positive feedback on the BM movement under both circumstances. As hy-

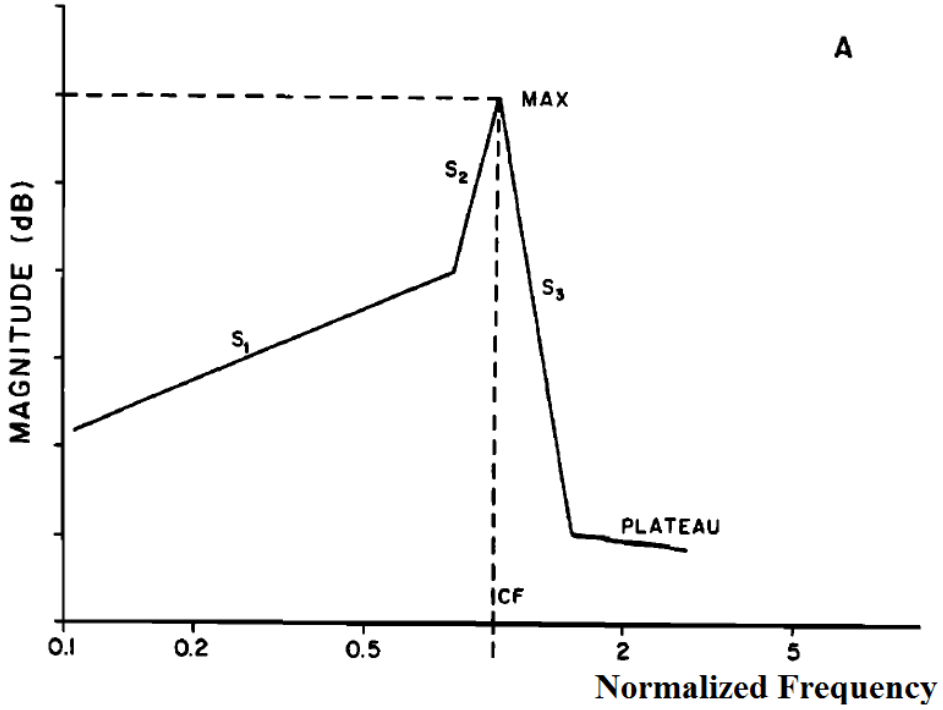


**Figure 2.7:** *Triple-stage division of the cochlea frequency response curve. (Image is taken from [7].)*

pothesised by Kim and Neely [35, 42], the active mechanism of OHC overcomes the viscosity-induced energy loss in the cochlea, which is essential for the enhancement of sound sensitivity with low-intensity inputs. Also, the OHC action is significantly suppressed when the input intensity is high so that the ear is protected from over-stimulation [43, 44]. Moreover, the OHC is dynamically mediated by the innervations from the efferent nerve fibres which carry information from the brain [45]. Therefore, the central auditory system is able to perform a top-down control on the cochlea response [5, 12, 46] and thus the selective attention is applicable at the auditory periphery level [12, 47].

### 2.1.3 Frequency Response

The accurate physiological measurement of the cochlea frequency response became possible around 1970s by virtue of the Mössbauer technique. Based on extensive measurement results, Rhode summarised in his 1978 paper that the magnitude curve of the cochlea frequency response can be generally divided into three stages [7]. As shown in Fig. 2.7, the low-frequency band curve $S_1$ gently slopes upwards with increasing frequency; the mid-frequency curve $S_2$ slopes upwards more steeply before reaching the prominent peak of gain at CF; the high-

frequency curve $S_3$ slopes downwards towards the stop-band with ultra-high steepness. This triple-stage division of the cochlea frequency response has been repeatedly verified by a number of subsequent measurement results including the one shown in Fig. 1.1 [1, 8–11, 48]. These measurement results also reveal the input-dependent variation of the CF response; when the input intensity decreases, the peak gain and Q factor increases and the CF shifts to a slightly higher frequency [1, 8–11, 48]. The comparative experiment between the live and dead cochleas in [10] proves that the variation of CF response is a result of the active OHC behaviour. Table. 2.1 summarises the detailed numerical results about the cochlea frequency response measured in these physiological experiments [1, 7–11, 48].

| Animal Type | $S_1$ (dB/dec) | Max. $S_2$ (dB/dec) | Max. $S_3$ (dB/dec) | $\omega_{LQ}$* (kHz) | Max. $\omega_{HQ}$* (kHz) | PGDR* (dB) | Max. $Q_{10}$* |
|---|---|---|---|---|---|---|---|
| Squirrel Monkey[7] | 22.9 | 233 | -472 | – | 7.7 | – | 6.93 |
| Guinea Pig[7] | 23.3 | 49.8 | -289 | – | 12.3 | – | 2.21 |
| Chinchilla[8] | 47.8 | 209 | -330 | 7 | 10 | 32.5 | 5.66 |
| Chinchilla[1] | 41.9 | 230 | -360 | 6 | 9.5 | ≈40 | 6.20 |
| Chinchilla[9] | 20 ∼23 | 180 | -380 | 4.5 | 6.6 | ≈30 | 5.48 |
| Mongolian Gerbils[10] | 20 | 274 | -373 | 10 | 14 | ≈40 | 6.93 |
| Mongolian Gerbils[11] | 54.7 | 98 | -236 | 7 | 11.2 | ≈20 | 3.21 |

*$\omega_{LQ}$ = centre frequency when peak gain and quality factor is lowest (high intensity input);

*$\omega_{HQ}$ = centre frequency when peak gain and quality factor is highest (low intensity input);

*PGDR = peak gain dynamic range;

*$Q_{10}$ = -10 dB quality factor = CF/-10 dB bandwidth.

**Table 2.1:** *Characteristic specifications of cochlea frequency response. The numeric values are calculated based on the magnitude curve of cochlea frequency response measured in the the physiological experiments [1, 7–11].*

## 2.2 A Historic Review of Cochlea Filter Models and Their Hardware Implementations

### 2.2.1 Cochlea Models Based on Travelling Wave Theory

The travelling wave theory of cochlea mechanics is established by Georg von Békésy, who became the first-ever man to observe the BM movement in his pioneering experimental cochlea research during 1920s [49]. Based on the observations, Békésy revealed that the BM vibrates in the form of travelling transverse wave, which can be analogously represented by a mechanical model shown in Fig. 2.8(a) [36]. The model employs a brass tube filled with water which

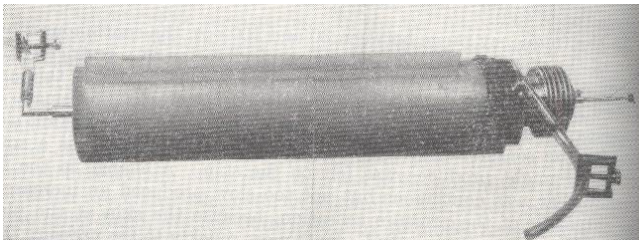

**(a)** Representation of cochlea by a brass tube.

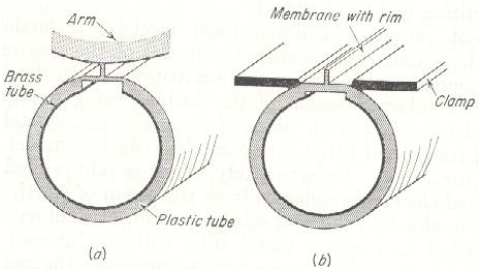


**(b)** Cross section of the model

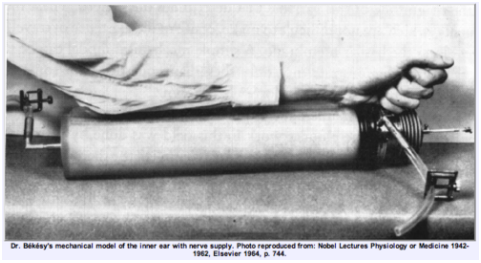


**(c)** Sensation of the travelling waves using the arm skin as equivalent sensory cells and nerve supplies

**Figure 2.8:** *Békésy's mechanical cochlea model. (Images are taken from [36].)*

represents the perilymph-filled scala tympani canal. One end of the tube is attached to a vibrating piston which functions as the stapes in the middle ear and drives the water in motion. A rubber membrane is fitted on one side of the brass tube which functions as the BM and vibrates in accordance with the travelling wave produced by the water motion. The dimensions of the rubber membrane is optimised to match the elastic properties such that the produced travelling wave resembles that in the cochlea. As shown in Fig. 2.8(c), Békésy used his arm skin as the sense organ for the travelling wave, since the skin shares several similar neural effects with the cochlea [36]. Apparently, Békésy's mechanical model was not built for any practical applications. However, using this model, Békésy successfully replicated many auditory phenomena that have been found in the real cochlea, which proves the travelling wave theory as the underlying basis for the the cochlea mechanics.

Inspired by Békésy's work, mathematical analyses of the travelling wave propagation in the cochlea were performed by Zwislocki [51] and Peterson [52] based on the hydrodynamic principles. The derived partial differential equations (PDE) as Eq. 2.1 reveal the relationship between the wave propagation and the cochlea mechanical properties including mass, viscosity and compliance, based on which the transmission-line cochlea model was established. As shown in Fig. 2.9, the transmission-line model can be represented by an equivalent RLC network by mapping the mass with inductance, viscosity with resistance and compliance with

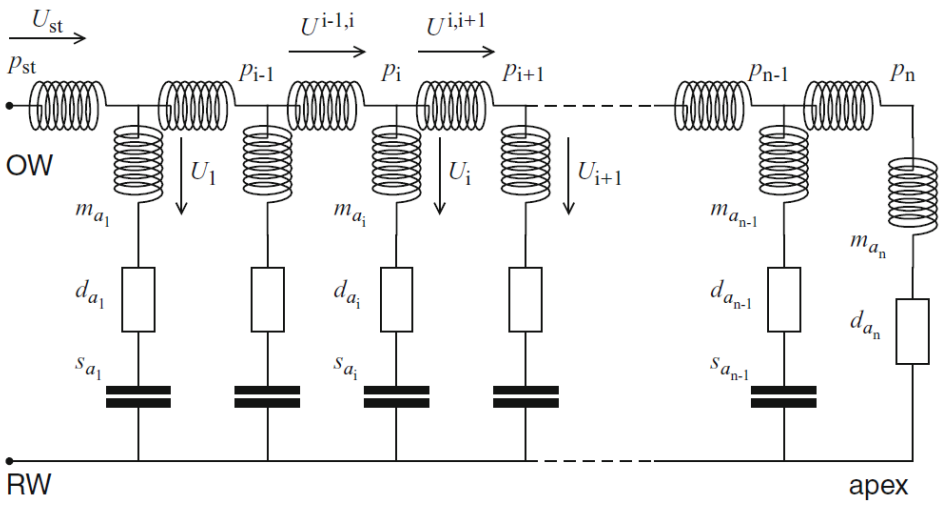


**Figure 2.9:** *Equivalent RLC network representation of the transmission-line cochlea model. The series and shunt inductances respectively correspond to the mass of the fluid in the scala tympani (perilymph) and the mass of the BM in addition to its loaded fluid in the scala media (endolymph). The resistances correspond to the BM damping which mainly results from the viscosities of the endolymph in the scala media. The capacitances correspond to the compliance of the BM which increases by over two orders of magnitude from the basal (OW & RW) to the apical (apex) end [36]. The lateral ($U^{i,i+1}$) and shunt ($U_i$) currents respectively correspond to the longitudinal volume velocities of the cochlea fluid and the transverse volume velocities of the BM. The voltages ($p_i$) correspond to the pressures on the BM. (Image is take from [50].)*

capacitance:

$$\begin{cases} \frac{\partial p(\omega,x)}{\partial x} = -\bar{Z}(x) \cdot U(\omega, x); \\ \frac{\partial U(\omega,x)}{\partial x} = -\frac{1}{Z(x)} \cdot p(\omega, x), \end{cases} \tag{2.1}$$

where $x$ represents the longitudinal location on the BM, $p$ is the pressure on BM which corresponds to the node voltages in the equivalent RLC circuit shown in Fig. 2.9, $U$ is the cochlea fluid volume velocity which corresponds to the currents in Fig. 2.9, $\bar{Z}$ is the lateral impedance of the cochlea which corresponds to the equivalent series inductance in Fig. 2.9 and $Z$ is the shunt impedance which corresponds to the shunt inductance, resistance and capacitance in Fig. 2.9. Detailed mapping between the cochlea mechanical properties and the equivalent circuit impedances is elaborated in Fig. 2.9.

The solution of Eq. 2.1 is highly complicated and thus the transmission-line model was not feasible for practical application until Zweig introduced the Wentzel-Kramers-Brillouin (WKB) approximated solution [53, 54], which assumes the cochlea mechanical properties do not vary rapidly with distance along the BM. This assumption is supported by Békésy's observation that the wave propagation on the BM is unidirectional without reflections [36]. By using the normalised variable $s_n$ Zweig decoupled Eq. 2.1 for $p$ and derived the following PDE:

$$\frac{\partial^2 p(s_n)}{\partial x^2} = k^2(s_n) \cdot p(s_n), \tag{2.2}$$

The normalised variable $s_n$ is defined as

$$s_n(x, \omega) \equiv j\frac{\omega}{\omega_c(x)}. \tag{2.3}$$

where $\omega_c(x)$ is the characteristic frequency of the corresponding BM position. Assuming characteristic frequencies on the BM are exponentially distributed, the following expression stands

$$\omega_c(x) = \omega_c(0) \cdot e^{-\frac{x}{l}}. \tag{2.4}$$

where $\omega_c(o)$ is the characteristic frequency at the stapes and $l$ is the characteristic length of the

BM. The variable $k$ in Eq. 2.2 in physics represents the wavenumber and is defined as:[1]

$$k(s_n) = \frac{l}{s} \cdot \sqrt{\frac{\bar{Z}(s_n)}{Z(s_n)}}. \tag{2.5}$$

$\bar{Z}(s_n)$ and $Z(s_n)$ can be represented by

$$\bar{Z}(s_n(\omega, x)) = j\omega\bar{L}(x), \tag{2.6}$$

$$Z(s_n(\omega, x)) = j\omega L(x) + R(x) + \frac{1}{j\omega C(x)}. \tag{2.7}$$

where $\bar{L}$, $L$, $R$ and $C$ respectively correspond to the equivalent series inductance, shunt inductance, resistance and capacitance shown in Fig. 2.9. Furthermore, based on the scale-invariant nature of BM response [55], the following expressions stand:

$$j\omega_c(x)\bar{L}(x) = j\omega_c(0)\bar{L}(0), \tag{2.8}$$

$$j\omega_c(x)L(x) = j\omega_c(0)L(0), \tag{2.9}$$

$$R(x) = R(0), \tag{2.10}$$

$$\frac{1}{j\omega_c(x)C(x)} = \frac{1}{j\omega_c(0)C(0)}. \tag{2.11}$$

Applying the first-order WKB approximation for Eq. 2.2 and considering only forward-travelling waves, the following solution is derived:

$$p(s_n) \approx p_0(\omega)k(s_n)^{-\frac{1}{2}} \exp\,[\int_{s_{n,0}}^{s_n} k(s'_n)\mathrm{d}s'_n], \tag{2.12}$$

where $p_0$ is independent of $x$ and is defined by the boundary conditions (position at the stapes). Combining the above equations, the cochlea transfer function represented using $s_n(x, \omega)$ can be derived as follows[2]

$$\begin{aligned} H(s_n) &\propto H_0(\omega) \cdot s_n k(s_n)^{\frac{3}{2}} \cdot \exp\,[-\int_{s_{n,0}}^{s_n} k(s'_n)\mathrm{d}s'_n] \\ &\propto H_0(\omega) \cdot \frac{s_n}{(s_n^2 + \delta s_n + 1)^{\frac{3}{4}}} \cdot \exp\,[-\int_{s_{n,0}}^{s_n} k(s'_n)\mathrm{d}s'_n], \end{aligned} \tag{2.13}$$

[1] In the original Zweig's works [53, 54], the wavelength $\lambda$ is used which is the reciprocal of $k$. The use of $k$ here is for purpose of coherence with following paragraphs.

[2] The cochlea transfer function is defined by dividing the BM velocity at the position $x$ (equivalently $\frac{\partial U}{\partial x}$) with the fluid velocity at the stapes.

where $H_0(\omega)$ is defined by the boundary conditions at the stapes, and $\delta$ is the damping constant of $Z$ defined as

$$\delta = R_0\sqrt{\frac{C_0}{L_0}} \tag{2.14}$$

The above equations derived by Zweig established the relationship between cochlea response and the equivalent circuit parameters in Fig. 2.9, so that the transmission-line model can be practically implemented in hardware. In particular, the transmission-line model has been successfully implemented in silicon based on Zweig's derivations such as the MEMS implementation introduced by Tanaka using an equivalent "fishbone" mechanical structure [56], and the analogue VLSI implementations introduced by Bor and Mandal using respectively the equivalent switched-capacitor circuits [57] and the on-chip passive inductors [58].

Lyon's work that maps Zweig's WKB-approximated solution to a filter cascade circuit architecture is another remarkable milestone in the development of travelling-wave-based cochlea model [16, 59–61]. Eq. 2.13 can be rewritten in the following form:

$$\begin{aligned} H(s_n) &\propto H_0(\omega)\cdot\frac{s_n}{(s_n^2+\delta s_n+1)^{\frac{3}{4}}}\cdot\exp\left[-\sum_{i=1}^{x/\Delta x}\int_{s_{n,(i-1)\Delta x}}^{s_{n,i\Delta x}} k(s_n')\mathrm{d}s_n'\right] \\ &= H_0(\omega)\cdot\frac{s_n}{(s_n^2+\delta s_n+1)^{\frac{3}{4}}}\cdot\prod_{i=1}^{x/\Delta x}\exp\left[-\int_{s_{n,(i-1)\Delta x}}^{s_{n,i\Delta x}} k(s_n')\mathrm{d}s_n'\right] \\ &= H_0(\omega)\cdot\frac{s_n}{(s_n^2+\delta s_n+1)^{\frac{3}{4}}}\cdot\prod_{i=1}^{x/\Delta x}\exp\left[-\int_{(i-1)\Delta x}^{i\Delta x} k_x(x')\mathrm{d}x'\right] \\ &= H_0(\omega)\cdot\frac{s_n}{(s_n^2+\delta s_n+1)^{\frac{3}{4}}}\cdot\prod_{i=1}^{x/\Delta x}\exp\left[-\bar{k_x}(i\Delta x)\cdot\Delta x\right], \end{aligned} \tag{2.15}$$

where $k_x$ is the wave-number in $x$ domain and is given by

$$k_x(x) = \left[\frac{\bar{Z}(x)}{Z(x)}\right]^{\frac{1}{2}}, \tag{2.16}$$

and $\bar{k_x}(i\Delta x)$ represents the average wave-number over the small section $\Delta x$ on the BM. In physics, Eq. 2.15 is interpreted as follows:

- the $H_0(\omega)$ term corresponds to the transfer function of the stapes and is independent of position;
- the polynomial term corresponds to the resonant response at the certain position of the

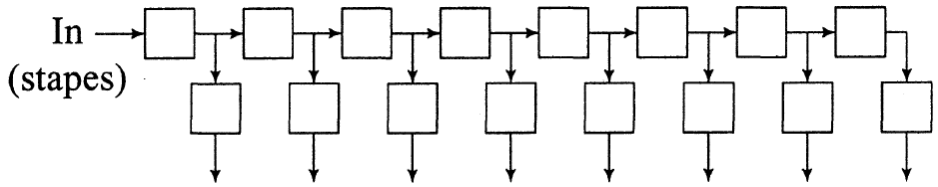


**Figure 2.10:** *Filter cascade cochlea model proposed by Lyon. The cascaded sections correspond to the product term and the sections at each taps of the cascade correspond to the polynomial term in Eq. 2.15. (Image is taken from [61].)*

basilar membrane;

- the product term corresponds to the cascaded transfer functions of numerous small sections (with length of $\Delta x$) on the BM: as assumed in the WKB approximation, the cochlea mechanical properties change slowly along the BM and thus each small section can be treated as a uniform media where Eq. 2.1 becomes ordinary differential equations (ODE). Consequently, the equivalent transfer function of each small section can be derived as

$$H_{\Delta x} = \exp\left[-\bar{k_x}(i\Delta x)\Delta x\right]. \tag{2.17}$$

Therefore Lyon mapped Eq. 2.15 into the filter cascade structure as shown Fig. 2.10.

Notably, the transmission-line models developed by Zwislocki, Peterson and Zweig are all based on the long-wave assumption that the wavelength of travelling wave is far longer than the cross-sectional dimensions of the cochlea scala [51–54]. The long-wave assumption enables the approximation of the 3-dimensional (3-D) cochlea hydrodynamics using the 1-dimensional (1-D) dynamic equations (Eq. 2.1) which consider only the wave propagation in $x$ direction (the longitudinal axis of BM). Nevertheless, although Lyon established the filter cascade structure by mapping the 1-D transmission-line model, he did not follow the long-wave approximation in deriving the filter transfer functions. Apparently as indicated by Eq. 2.16 the wave-number will be extremely large at resonance and thus as its reciprocal, the wave-length will be extremely small. In fact, Zweig also conceded the long-wave assumption is unrealistic in the region where the BM undergoes maximum excitation [53, 54]. Therefore, Lyon analysed the cochlea hydrodynamics using the 2-D transmission-line model which originated from Ranke's short-wave hypothesis [62] and was numerically accomplished by Siebert [63], Lesser [64] and Steele [65]. The following PDEs were derived from the Euler equation for the 2-D cochlea

hydrodynamics:

$$\nabla^2\phi(x,y,\omega) = \frac{\partial^2\phi(x,y,\omega)}{\partial x^2} + \frac{\partial^2\phi(x,y,\omega)}{\partial y^2} = 0, \tag{2.18}$$

$$U_x(x,y,\omega) = \frac{\partial\phi(x,y,\omega)}{\partial x} \quad and \quad U_y(x,y,\omega) = \frac{\partial\phi(x,y,\omega)}{\partial y}, \tag{2.19}$$

$$p(x,y,\omega) = -\rho(x,y)\cdot j\omega\phi(x,y,\omega). \tag{2.20}$$

where $\phi$ is the velocity potential, $\rho$ is the cochlea fluid density and $y$ is the ordinate in the axis perpendicular to the BM, and $Z$ is the BM impedance as defined above. The boundary condition at the BM ($y = 0$) is give by

$$p(x,0,\omega) = U_y(x,0,\omega)\cdot Z(x,\omega). \tag{2.21}$$

And the boundary condition at the rigid wall of the scala tympnai ($y = -h$) is given by

$$U_y(x,-h,\omega) = 0, \tag{2.22}$$

where $h$ is the height of the scala tympani. In analysing BM impedance, Lyon took into account the tension and bending effects in addition to mass, viscosity and compliance, which lead to a complex representation of $Z$ and the derived wave-number $k_x$ [60]. However, Lyon used different types of biquad filters (two-pole two-zero, two-pole-non-zero, etc.) instead to approximate the transfer functions given in Eq. 2.17 [16, 59, 61]. Besides, the polynomial term in Eq. 2.15 was also approximated using biquad filters, and the transmission-line cochlea model was thus built in the form of biquad-filter cascade. Based on the biquad-filter cascade structure, Lyon and Mead implemented the first silicon cochlea in analogue VLSI [16] which was one of the foundation stones for the emergence of the neuromorphic engineering subject [66]. During the past two decades, Lyon's filter cascade cochlea model has been followed and improved by numerous researchers in the neuromorphic engineering community [17, 20, 28, 67–75]; their successive contributions have substantially influenced modern auditory research and brought promising hints for future intelligent hearing systems [76–81].

Furthermore, based on Lyon's analysis on the 2-D cochlea hydrodynamics [60], Watts initiated another revolution and successfully implemented the 2-D cochlea model in analogue VLSI [83]. Watts used the resistive network to model the cochlea fluid, in which case the voltages and currents respectively represent the velocity potentials and fluid velocities in the

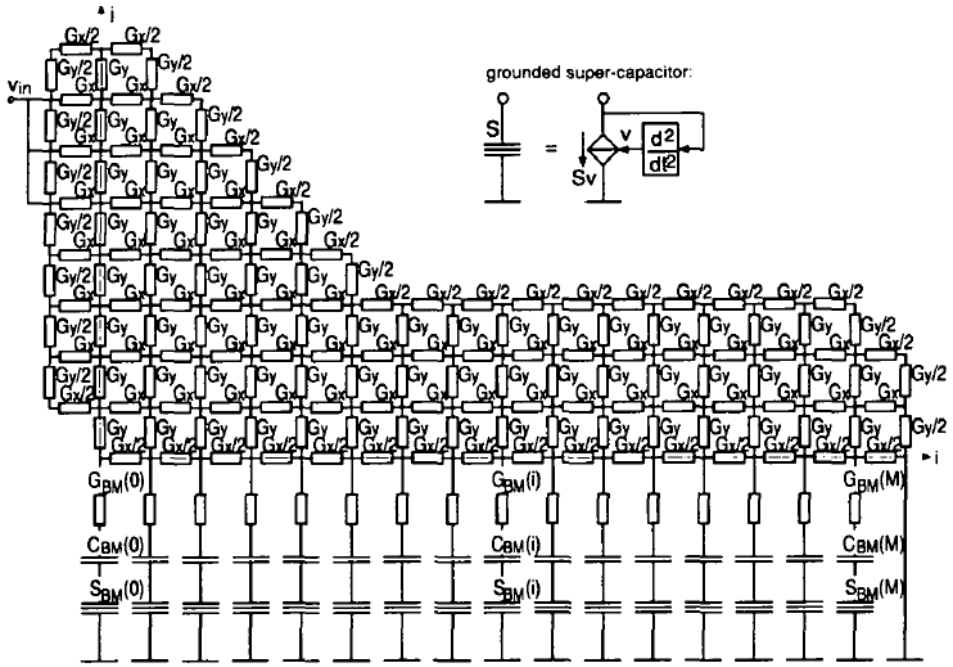


**Figure 2.11:** *Electrical equivalent of the 2-D cochlea model. (Image is taken from [82].)*

cochlea hydrodynamics. As for the BM, Watts neglected the tension and bending effects and introduced several transconductor-C circuit topologies to model the BM impedance which is defined by the following equation:

$$Z(\omega, x) = \frac{\phi(\omega, x)}{U(\omega, x)} = \frac{S(x)}{(j\omega)^2} + \frac{\beta(x)}{j\omega} + M(x), \tag{2.23}$$

where $S$, $\beta$ and $M$ are respectively the stiffness, damping and mass of the BM [83]. Fragnière subsequently followed Watts' work and interpreted the electrical equivalent of Eq. 2.23 as the combination of serially connected resistor (R), capacitor (C) and super-capacitor (S), where the super-capacitor has such electrical characteristic that the voltages across it is proportional to the double integral of the current [82]. Therefore, the 2-D cochlea model was represented as the electrical equivalent shown in Fig. 2.11. Compared with the model in Fig. 2.9, the impedance of all the electrical equivalents demonstrate one more order of integration. Watts explained in [83] that, as long as the Laplace equation of Eq. 2.19 is solved, the cochlea fluid can be modelled using the network of any impedance elements based on appropriate mappings between the variables in the cochlea hydrodynamics and the electrical circuits. However, since it is highly difficult to fabricate passive inductors with high inductance and high quality factor on VLSI chip, the topology of resistive network with RCS resonators shown in Fig. 2.11 is apparently more feasible for VLSI implementation compared with the RLC transmission-line represen-

tation shown in Fig. 2.9 and employed in [53, 54][3]. Following this topology, the 2-D silicon cochlea was subsequently improved by van Schaik employing the pseudo-voltage domain implementation [84], refined by Hamilton with the log-domain techniques and the enhancement of automatic quality factor control (AQC) [18], and extended by Wen with the addition of active coupling mechanism between BM resonators [19].

### 2.2.2 Parallel Cochlea Filter Bank

The origin of modelling the cochlea as a bank of parallel auditory filters dates back to Helmholtz's resonance theory in the 19th century. Helmholtz hypothesised that each bundle of nerves on a specific position of the BM acts as a resonator tuned to a different frequency corresponding to its length and tension, and the BM vibrates as a set of such place-coded independent resonators [85]. Although von Békésy revealed the travelling wave theory as the better interpretation for the BM vibratory pattern, the parallel cochlea filter bank model has been preferentially employed in the psychoacoustic field to study the sound perception in human ears. Fletcher introduced the critical band concept of hearing in 1940 based on the auditory masking experiment in which he used white noise to mask a sine wave signal whose frequency was same as the CF of the masking noise [6]. Fletcher observed that the detection threshold of the sine wave signal was independent of the masking noise bandwidth as long as the bandwidth was higher than certain critical value, and this critical value, which he named as the critical bandwidth, was dependent on the CF. To explain the experimental results, Fletcher made the following assumptions

- The cochlea behaves as a bank of band-pass filters;
- In detection of a signal in noise background, only the filter with CF close to the signal frequency is activated.
- Only the noise that passes through the filter contributes to masking the signal, and the detection threshold is determined by the amount of noise that pass through the filter.

During Fletcher's time, it was difficult to estimate the shape of the cochlea filters, and in fact, Fletcher used the unrealistic rectangular filters as a simplified representation. Extensive ef-

[3]The RLC transmission-line model implemented by Mandal [58] is an Radio-Frequency (RF) cochlea where high inductance and high quality factor are less required for the inductors.

forts to model the shape of the cochlea filters were made by Patterson [86], Glasberg [87] and Moore [88] who employed notched-noise for masking experiments. The $roex$ function was initially suggested to approximate the cochlea filter shape [86–88]. However, Patterson subsequently opted for the gamma-tone function due to its matching with the shape of the $roex$ function and the closer similarity with the cochlea impulse response [22, 89]. The expression for the gamma-tone function in time domain is given by

$$G_t(t) = \alpha t^{n-1} e^{-2\pi bt} cos(2\pi f_c t + \Phi), \tag{2.24}$$

where $\alpha$ is the amplitude constant, $n$ is the filter order, $b$ is the filter bandwidth, $f_c$ is the filter centre frequency and $\Phi$ is the initial phase. A revised expression for the relationship between cochlea filter bandwidth and CF was derived by Glasberg based on the data obtained from the notched-noise measurement [87]:

$$ERB(f_c) = 0.108 f_c + 24.7, \tag{2.25}$$

where ERB is the equivalent rectangular bandwidth [87]. By combining Eq. 2.24 and Eq. 2.25, a gamma-tone cochlea filter bank was built by Patterson [22], which thus far has been widely used as the front-end to produce cochleagrams in CASA systems [15]. The efficient digital implementations of the gamma-tone cochlea filter bank were proposed by Holdsworth [90], Cooke [91] and Slaney [92]. Notably, Slaney suggested the approximation of the fourth-order gamma-tone impulse response using a cascade of four second-order filters and introduced the all-pole gamma-tone filter (APGF) which discards the complex zeros in the gamma-tone transfer function [92]. As commented by Lyon [93], the APGF has at least three advantages compared with the original gamma-tone filter:

- while the original gamma-tone filter has a nearly symmetric shape of frequency response as conceded by Patterson [22], the APGF frequency response is relatively asymmetric which is more faithful to the biological cochlea;

- the APGF has simple pole-zero description in the Laplace-domain, which leads to convenient control of its frequency response through parameterisation;

- it is linked with the travelling-wave-based all-pole filter cascade (APFC) structure which was employed in the first silicon cochlea [16].

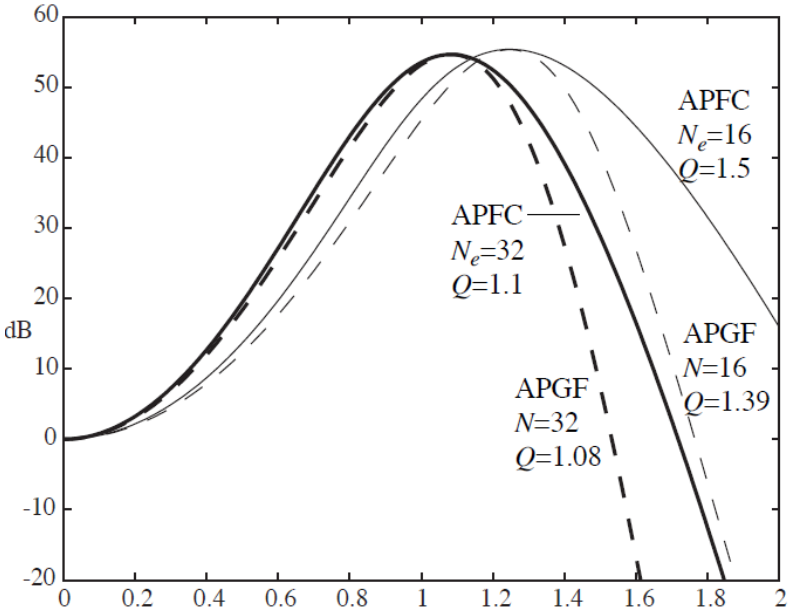


**Figure 2.12:** *Comparison between the frequency response of APGF and APFC. The dashed lines represent the APGF response and the solid lines represent the APFC response. Image is taken from [93]*

The relationship between the APGF, which is derived from the gamma-tone filter, and the APFC, which is derived from the travelling wave theory, are subsequently elaborated by Lyon [93]. The APGF can be regarded as a cascade of two-pole non-zero biquad filters, since its transfer function is given by:

$$H_{APGF}(s) = \frac{K}{[(s-p)(s-p^*)]^N}, \tag{2.26}$$

where $K$ is the constant representing the DC gain, $p$ and $p^*$ are a pair of conjugate poles, and $N$ represents the order of cascade [93]. The APFC refers to the filter cascade structure in which all the biquad filters used to approximate Eq. 2.17 are two-pole non-zero filters [93]. Therefore, both the APGF and the APFC are built with a cascade of two-pole non-zero biquad filters. However, the APGF differs from the APFC in the fact that the poles of its cascaded biquads are aligned, while the poles in the APFC are distributed in a gradient. As a result, the APGF demonstrates a sharper and more asymmetric frequency response than the APFC as shown in Fig. 2.12 [93].

The variants of the APGF include the differentiated all-pole gamma-tone filter (DAPGF) which has one zero at DC, and the one-zero gamma-tone filter (OZGF) which has one real zero [93, 94]. Notably, by virtue of the simple Laplace-domain representation, the APGF and its variants are highly feasible for analogue VLSI implementation, which is another advantage over the

original gamma-tone filter. For example, Katsiamis implemented an OZGF cochlea channel in analogue VLSI which, to the best of the author's knowledge, has the best fitting with the biological response among all the hardware implementations of cochlea filter thus far [95].

Besides, the parallel cochlea filter bank is also preferentially employed in the CI systems [13, 14]. As mentioned in Chapter 1, the filter used in the CIs are very basic [13, 14]. For example, the $2^{\mathrm{nd}}$-order band-pass filters are used by Germanovix [25] and Georgiou [26], and the $4^{\mathrm{th}}$-order band-pass filters are used by Sarpeshkar [27] in their analogue CI systems. However, it is notable that more complex filters which better resemble the biological cochlea have been suggested in recent years [96, 97]. This technology trend is motivated by the suggestion of Wilson[4] in 2005 that a closer mimicking of the signal processing in the biological cochlea should be emphasised in future CI processors [21].

## 2.3 Comparisons and Conclusions

In this chapter, many important physiological findings about the biological cochlea including its anatomy, mechanism and frequency response are introduced. Subsequently, a historic review is carried out about the existing representative cochlea filter models and their hardware implementations. Since the focus of this thesis is about the frequency response fidelity, a comparison between the frequency response of the biological cochlea and the existing cochlea filter implementations is detailed in Table. 2.2.

[4]Black S. Wilson is the inventor of the continuous interleaved sampling (CIS) strategy, which is the mainstream stimulation strategy for present CI products.

| | | | Application | $S_1$ (dB/dec) | Max. $S_2$ (dB/dec) | Max. $S_3$ (dB/dec) | Max. $\omega_{HQ}$ / $\omega_{LQ}$ | PGDR (dB) | Max. $Q_{10}$ |
|---|---|---|---|---|---|---|---|---|---|
| Biological Cochlea | | | - | $20^{[9]}$ $\sim 47.8^{[8]}$ | $49.8^{[7]}$ $\sim 274^{[10]}$ | $-472^{[7]}$ $\sim -236^{[11]}$ | $1.4^{[10]} \sim 1.6^{[11]}$ | $20^{[11]}$ $\sim 40^{[1,\,10]}$ | $2.21^{[7]}$ $\sim 6.93^{[7,\,10]}$ |
| Travelling-Wave Architectures | 1-D | [16] | General | ≈0 | 17.2 | 101.9 | - | - | 1.01 |
| | | [67] | General | - | 20 | -94.3 | - | - | 1.04 |
| | | [69] | General | - | 20 | -120 | - | - | 1.12 |
| | | [70]* | CI | 0 | 5 | -40 | - | - | 0.56 |
| | | [72] | General | - | 20 | -120 | - | - | 1.12 |
| | | [73]* | General | **19.9** | **76.4** | -181.2 | 2.46 | **46** | **2.53** |
| | | [17] | General | ≈0 | **67** | -175.5 | 1.4 | **34** | **2.32** |
| | | [74]* | CI | 0 | 18 | -60 | - | - | 0.84 |
| | | [75] | General | - | 14.6 | -20 | - | - | 0.34 |
| | | [20] | General | 0 | **57.3** | -34.1 | 0.57 | 7.5 | 0.77 |
| | 2-D | [83] | General | - | 30 | **-215.8** | - | - | 1.54 |
| | | [29] | ASR | **19.9** | **60.3** | -106 | 0.9 | **28** | 1.79 |
| | | [18] | General | ≈5 | 28.9 | -66.4 | 2.67 | 16 | 1.04 |
| | | [19] | General | ≈10 | 83 | -179.4 | 1 | **24** | **2.7** |
| Parallel Cochlea Filter Banks | Gamma-tone | Original[22]* | CASA | - | **85.8** | **235** | - | - | **2.96** |
| | | APGF[92]* | CASA | - | **106.9** | **-298.4** | - | - | **3.65** |
| | | OZGF[95] | General | **17** | **232.5** | **-299** | 1 | **70** | **5.74** |
| | Basic Filters | [26] | CI | - | 33.2 | -39.6 | - | - | 0.78 |
| | | [27] | CI | - | 30.6 | -42.9 | - | 17.1 | 0.81 |

*Simulated Results

**Table 2.2:** *Comparison of frequency response between the biological cochlea and existing cochlea filter models. The data which match or roughly match with biology have been highlighted.*

Apparently, although those cochlea models derived from the travelling wave theory are based on a relatively accurate replication of the biological cochlea hydrodynamics, their frequency responses are not adequately matched with biology. Generally speaking, the OZGF developed by Katsiamis [95] is the only biomimetic cochlea filter that demonstrates reasonably faithful frequency response, though its CF does not shift as the biological cochlea does. Unfortunately, the operation of Katsiamis' OZGF relies on a floating current source as the input [95], which means it is not yet an applicable hardware implementation at present, since it can not be interfaced with microphones or used to process real acoustic signals.

In conclusion, the review in this chapter reveals that the frequency response of the biological cochlea has not been adequately replicated in the existing cochlea filter models and their hardware implementations. This issue will be addressed in the following chapters of this thesis.

# Chapter 3
# A Cochlea Filter Model with Biologically Faithful Frequency Response

A mathematical cochlea filter is established in this chapter based on the physiological observations introduced in Chapter 2. The filter response is compared with the biological cochlea in many aspects including the frequency response, phase response, group delay and impulse response. In the end, the filter model is implemented in MATLAB Simulink for a variety of proof-of-concept demonstrations.

## 3.1 Principle and Methodology

The filter model is inspired by the triple-stage representation of the biological cochlea frequency response given by Rhode (Fig. 2.7). The triple-stage response can be achieved by cascading three sub-filters. The low-band stage $S_1$, as indicated in Table 2.1, has a slope of $20 \sim 50$ dB/dec which approximately corresponds to the slope steepness of a first or second order filter; the mid-band stage $S_2$ is variable and its maximum slope steepness corresponds to the resonance bump of a filter with as high as $3.6 \sim 19.8$ Q factor[1]; the high-band stage $S_3$ demonstrates a roll-off steepness of over 300 dB/dec which is equivalent to the roll-off slope of a fifteenth-order all-pole low-pass filter. Therefore, $S_1$ and $S_2$ can be emulated with a second-order band-pass filter with low Q factor (BPF) and a tunable second-order low-pass filter (LPF) with high Q factor. Besides, the challenge of high order filter requirement for the steep roll-off of $S_3$ can be addressed by employing the elliptic low-pass filter (ELF) which has the steepest stop-band transition among all filter types. Based on the filter specification design handbook [98], a fifth-order ELF can provide enough roll-off steepness to match the biological response. The architecture of the triple-stage cascaded cochlea filter is illustrated in Fig. 3.1.

[1]The derivation is elaborated in Appendix A.1.

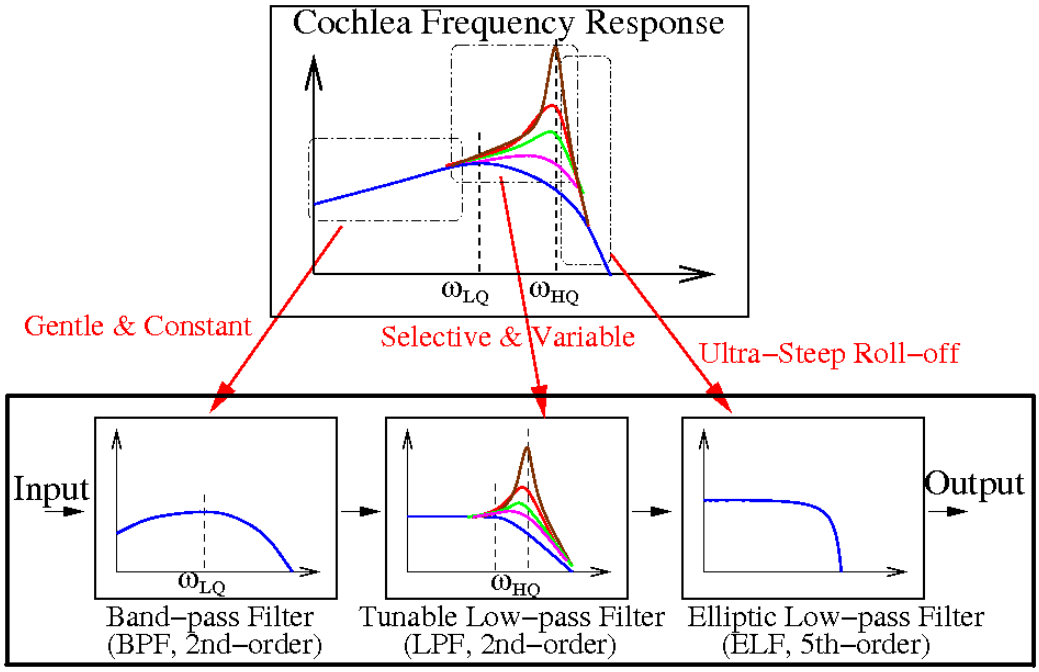


**Figure 3.1:** *Architecture of the cascaded cochlea filter: each of the sub-filters emulates one stage of the BM response.*

| Design Parameters | | Expected Filter Specifications | |
|---|---|---|---|
| Filter Order | 5 | Pass-band Ripple | 0.01 dB |
| Reflection coefficient | 5 % | Steepness Factor | 1.7013 |
| Modular Angle | 36° | Minimum Stop-band Attenuation | 40.81 dB |
| Power Loss Factor | $\infty$ | Roll-off Slope | 176.8 dB/dec |

**Table 3.1:** *Design parameters and expected specifications of the ELF.*

The transfer function of the BPF is given by

$$H_{BPF}(s) = A \cdot \frac{s + \frac{\omega_{BP}}{Q_{BP}}}{s^2 + \frac{\omega_{BP}}{Q_{BP}} s + \omega_{BP}^2}, \tag{3.1}$$

where $A$ represents the gain constant; $\omega_{BP}$ and $Q_{BP}$ respectively represent its undamped natural frequency and Q factor. The transfer function of the LPF is given by

$$H_{LPF}(s) = \frac{\omega_{LP}^2}{s^2 + \frac{\omega_{LP}}{Q_{LP}} s + \omega_{LP}^2}, \tag{3.2}$$

where $\omega_{LP}$ and $Q_{LP}$ respectively represent its undamped natural frequency and Q factor. The design parameters for the ELF are listed in Table. 3.1, so are the expected filter specifications.

By referring to the filter design table [98], the transfer function of the ELF is given by

$$H_{ELF}(s) = \frac{0.0699\omega_{ELF} \cdot (s^2 + 7.34\omega_{ELF}^2)(s^2 + 3.14\omega_{ELF}^2)}{(s + 0.962\omega_{ELF})(s^2 + 1.24\omega_{ELF} \cdot s + 1.17\omega_{ELF}^2)(s^2 + 0.344\omega_{ELF} \cdot s + 1.43\omega_{ELF}^2)} \tag{3.3}$$

where $\omega_{ELF}$ is the -3 dB cut-off frequency.

As shown in Fig. 3.1, the $\omega_{LQ}$ of the cochlea filter is determined by the CF of the BPF which is related with $Q_{BP}$ and $\omega_{BP}$ as follows

$$\omega_{LQ} = \omega_{BP} \cdot (\sqrt{\frac{2}{Q_{BP}^2} + 1} - \frac{1}{Q_{BP}^2})^{\frac{1}{2}}. \tag{3.4}$$

And the $\omega_{HQ}$ of the cochlea filter is determined by the CF of the LPF which is related with $Q_{LP}$ and $\omega_{LP}$ as follows

$$\omega_{HQ} = \omega_{LP} \cdot \sqrt{1 - \frac{1}{2Q_{LP}^2}}. \tag{3.5}$$

Besides, the cut-off frequency of the ELF should be always higher than $\omega_{HQ}$ and it is reasonable to set $\omega_{ELF} = \sqrt{2}\omega_{LQ}$.

The parameters of the BPF and ELF are constant and the parameters of the LPF, $Q_{LP}$ and $\omega_{LP}$, are made variable. The parameter values can be determined by mapping the filter specifications with the physiological results as follows:

- The DC gain of the cascaded filter is given by

$$H_{BPF}(0) \cdot H_{LPF}(0) \cdot H_{ELF}(0) = \frac{A}{Q_{BP}\omega_{BP}}, \tag{3.6}$$

  which should be in accordance with the -20 $\sim$ 0 dB physiological results [1, 7–11].

- The peak gain of the BPF is determined by

$$H_{BPF}(j\omega_{LQ}) = \frac{A}{\omega_{BP} \cdot (2\sqrt{\frac{2}{Q_{BP}^2} + 1} - \frac{1}{Q_{BP}^2} - 2)^{\frac{1}{2}}}, \tag{3.7}$$

  which contributes to the majority of the LQ peak gain. Physiological results indicate the LQ peak gain should be in the range of 20 $\sim$ 30 dB [1, 8–11]. Eq. 3.6 and Eq. 3.7 show that a high $Q_{BP}$ is necessary for the above-mentioned requirements. However, a high $Q_{BP}$ results in a sharp BPF peak, the roll-off of which will significantly reduce the HQ

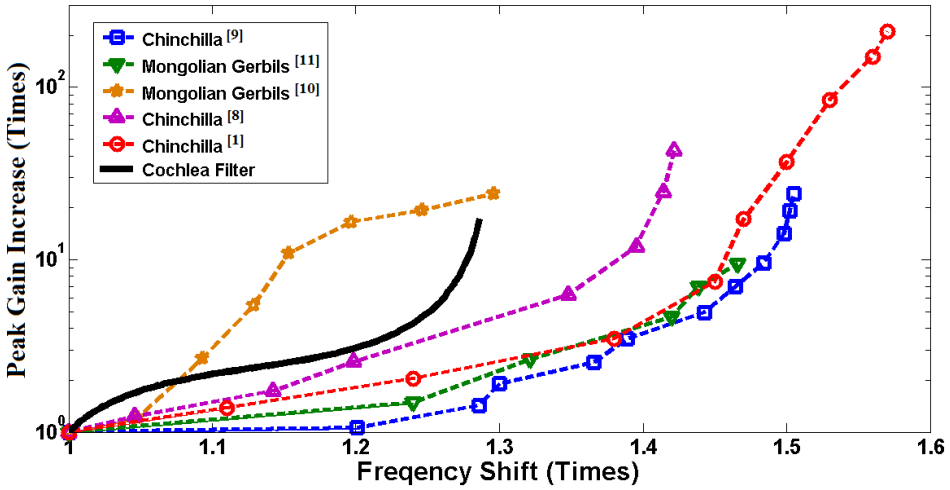


**Figure 3.2:** *Fitting of the relationship curves between the peak gain increase and the CF shift based on the data from physiological experiments and the cochlea filter transfer function (Eq. 3.11).*

peak gain. To make a compromise, the following settings are applied for the BPF:

$$\begin{cases} A = 2.2\omega_{BP} \\ Q_{BP} = 3, \end{cases} \tag{3.8}$$

so that Eq. 3.4 leads to

$$\omega_{LQ} = 0.997\omega_{BP} \approx \omega_{BP}. \tag{3.9}$$

- The lower bound for $\omega_{LP}$ is set equal to $\omega_{LQ}$ ($\omega_{BP}$) and the lower bound for $Q_{LP}$ is set as 1.5 so that the LPF provides an extra 1.5 times gain at $\omega_{LQ}$ in the LQ response.

With the above settings, the cochlea filter has a DC gain of -2.7 dB and an LQ peak gain of 20.1 dB which agree well with the physiological results.

To reduce the tuning complexity of the cochlea filter, an equation between $Q_{LP}$ and $\omega_{LP}$ is established as in Eq. 3.10 so that the filter function contains only one variable parameter.

$$Q_{LP} = \frac{0.9 \cdot \beta}{1.6 - \beta^2}, \tag{3.10}$$

where $\beta$ denotes the ratio between $\omega_{LP}$ and $\omega_{BP}$.

Therefore the transfer function of the entire cochlea filter is rewritten as

$$H_{tot}(s) = \frac{0.217\beta^2\omega_{BP}^4 \cdot (s + 0.333\omega_{BP})}{(s^2 + 0.333\omega_{BP} \cdot s + \omega_{BP}^2)[s^2 + 1.11\omega_{BP}(1.6 - \beta^2)s + \beta^2\omega_{BP}^2)]} \cdot \frac{(s^2 + 14.7\omega_{BP}^2)(s^2 + 6.28\omega_{BP}^2)}{(s + 1.36\omega_{BP})(s^2 + 1.75\omega_{BP} \cdot s + 2.34\omega_{BP}^2)(s^2 + 0.486\omega_{BP} \cdot s + 2.86\omega_{BP}^2)}, \tag{3.11}$$

where $\omega_{LP}$, $\omega_{ELF}$ and $A$ are rewritten as functions of $\omega_{BP}$, and $Q_{LP}$ is replaced by the expression in Eq. 3.10. $\omega_{BP}$ is constant and it determines the CF range of the cochlea filter, while $\beta$ is variable and determines the peak gain increase and the CF shift. To evaluate the fitting of Eq. 3.10 with physiological data, the derived relationship curve between the peak gain increase and the CF shift is plotted in Fig. 3.2 in comparison with the physiological curve. The maximum CF shift of the proposed cochlea filter is relatively smaller, but the curve generally follows a similar trend with the physiological results.

The normalised pole-zero plot of the cascaded cochlea filter is shown in Fig. 3.3. As none of its poles and zeros are located in the right-hand half of the s-plane, the cochlea filter agrees with the minimum-phase property of the biological cochlea response [33]. This property is crucial since it ensures that the phase response of the proposed cochlea filter will also match the physiological results as long as its magnitude frequency responses is biologically faithful. The matching of phase response is examined in the following section.

## 3.2 Response Characteristics of the Biomimetic Cochlea Filter

In this section, the frequency response, phase response, group delay and transient response characteristics of the biomimetic cochlea filter are examined.

### 3.2.1 Frequency Response

The magnitude frequency response is shown in Fig. 3.4. When $\beta$ equals unity, the peak gain and Q factor of the response is minimum, which is named in this thesis as low Q (LQ) response. The peak gain and Q factor reaches maximum when $\beta$ increases to 1.255, which is named in this thesis as high Q (HQ) response. In comparison with the physiological results, the LQ curve corresponds to the high intensity stimulus response, while the HQ curve corresponds to

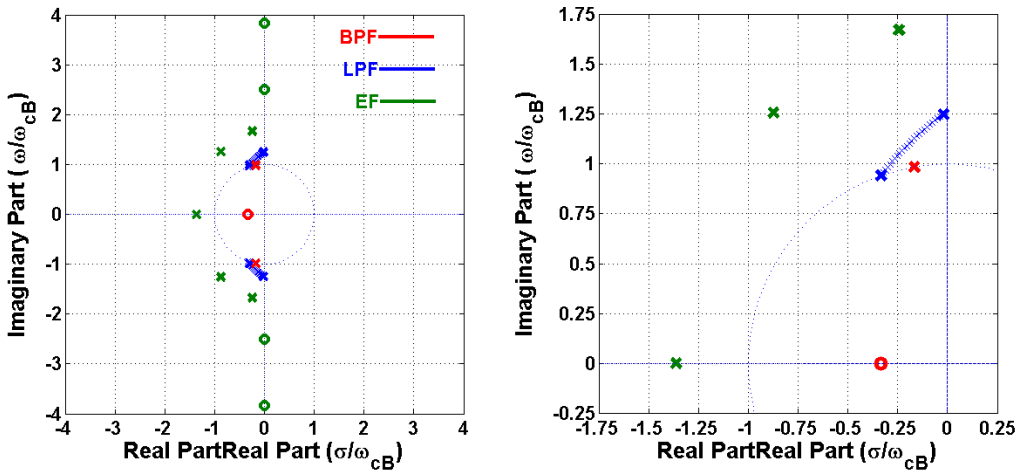


**Figure 3.3:** *Normalised pole-zero plot of the cochlea filter (left); pole-zero plot zoomed to left-up corner (right). The $\beta$ factor is adjusted from 1 to 1.255 which leads to the shift of LPF from the edge of the unity circle to approaching the imaginary axis.*

the low intensity stimulus response. Therefore, the results shown in Fig. 3.4 agree well with the physiologically measured curves in Fig. 1.1. The characteristic specifications are listed in Table. 3.2 to compare with those in Table. 2.1. Furthermore, a parallel cochlea filter bank can be built by setting different $\omega_{BP}$ ($\omega_{LQ}$). Fig. 3.5 shows the frequency response of a cochlea filter bank with CFs distributed in the one-third octave scale.

| $S_1$ (dB/dec) | Max. $S_2$ (dB/dec) | Max. $S_3$ (dB/dec) | $\omega_{LQ}$ (kHz) | Max. $\omega_{HQ}$ (kHz) | PGDR (dB) | Max. $Q_{10}$ |
|---|---|---|---|---|---|---|
| 22.7 | 176 | -320 | - | 1.255·$\omega_{LQ}$ | 25.1 | 5.07 |

**Table 3.2:** *Frequency response characteristics of the biomimetic cochlea filter.*

### 3.2.2 Phase Response

The phase response of the cochlea filter is shown in Fig. 3.6 together with the physiology results [7]. As shown in the figure, the tuning of LPF also makes significant impact on the phase response. To investigate the response variation, the filter phase lag is plotted with respect to the LQ response as shown in Fig. 3.7, together with the physiologically measured results [99]. Compared with the physiological results, the cochlea filter phase response has a number of similarities such as :

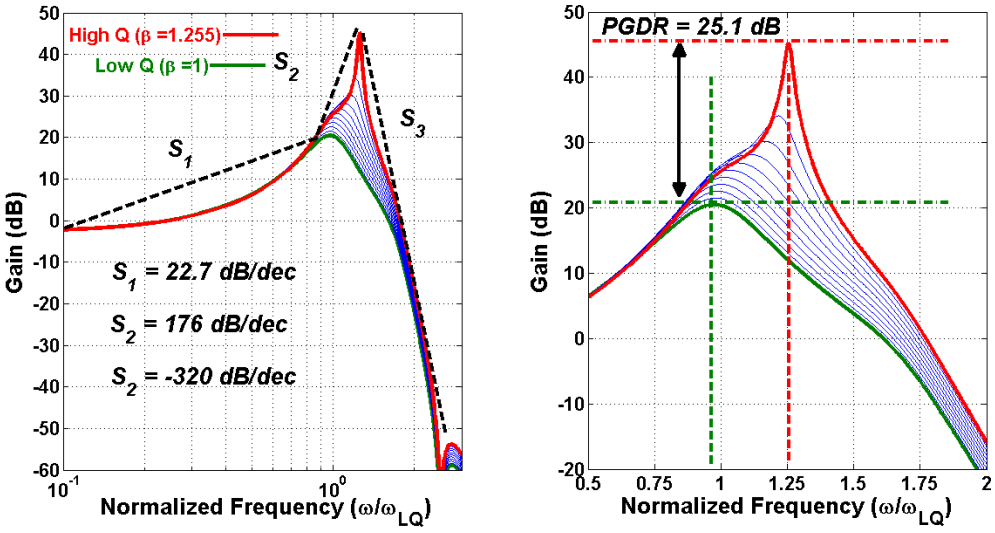


**Figure 3.4:** *Frequency response of the cochlea filter in linear (left) and log scale (right). The labelled values of response characteristics show good accordance with physiological results in Table. 2.1.*

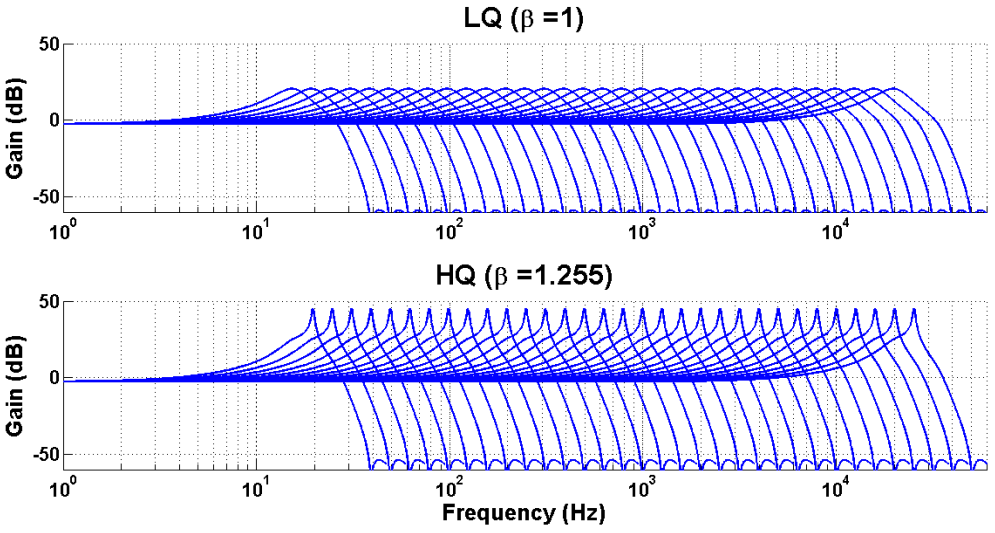


**Figure 3.5:** *Frequency response of a parallel bank of the cochlea filters in one-third octave scale.*

- In the pass-band, the phase lag increases when frequency moves from low to high. ( [1, 9–11, 48, 99–101] )
- In the pass-band, the slope of the phase-frequency curve becomes steeper when frequency moves from low to high. ( [1, 9–11, 48, 99, 101] )
- Phase lag reaches 0.4∼0.8 cycles at $\omega_{LQ}$ and 0.9∼2.8 cycles at $\omega_{HQ}$. ( [1, 9–11, 48, 99–101] )
- Compared with HQ response, the LQ response has more phase lag in frequencies lower than $\omega_{HQ}$, but has less in frequencies much higher than $\omega_{HQ}$. ( [9–11, 99, 100] )
- The HQ phase response has a much steeper slope in the vicinity of CF than the LQ response. ( [1, 9, 11, 100, 101] )

The detailed characteristics of the filter phase response together with a number of physiological results are summarised in Table. 3.3.

| Animal Type | $\omega_{LQ}$ | $\omega_{HQ}$ | Phase @$\omega_{LQ}$ (cycles) | Phase @$\omega_{LQ}$ (cycles) | Phase Lag re. LQ (cycles) | Max. LQ Group Delay ($2\pi/\omega_{LQ}$) | Max. HQ Group Delay ($2\pi/\omega_{LQ}$) |
|---|---|---|---|---|---|---|---|
| Chinchilla[8] | 7 | 10 | -0.75 | -2.5 | -0.44 ∼0.25 | 2.7 | 7 |
| Chinchilla[1] | 6 | 9.5 | -0.75 | -2.3 | -0.56 ∼0.13 | 1.5 | 6.86 |
| Chinchilla[9] | 4.5 | 6.6 | -0.5 | -2 | -0.6 ∼0.4 | 4.5 | 8.1 |
| Chinchilla[99] | 6 | 9.5 | 0 | -0.9 | -1 ∼0.6 | 1.2 | 9 |
| Mongolian Gerbils[10] | 10 | 14 | -0.69 | - 1.9 | -1.6 ∼0.19 | 1.34 | 5.28 |
| Mongolian Gerbils[11] | 7 | 11.2 | -0.7 | -1.6 | -0.2 ∼0.5 | 0.39 | 3.58 |
| Mongolian Gerbils[101] | 11 | 11.7 | -0.8 | -1.4 | – | 2.92 | 10.1 |
| Guinea Pigs[100] | 15 | 19.2 | -0.46 | -2.8 | -0.29 ∼0.09 | – | 12.2 |
| Cochlea Filter Model | – | $1.255\omega_{LQ}$ | -0.58 | -0.93 | -0.11 ∼0.3 | 2 | 12.1 |

**Table 3.3:** *Comparison of phase response characteristics between the biological cochlea and the proposed cochlea filter. The numeric values are calculated based on the BM phase response curve obtained from the physiological experiment [1, 8–11, 99–101].*

### 3.2.3 Group Delay

The normalised group delay of the cochlea filter is shown in Fig. 3.8. The maximum group delay is located at $\omega_{HQ}$ where the phase response curve has steepest slope. The HQ response has much higher maximum group delay compared with the LQ response. Similarly, the group delay

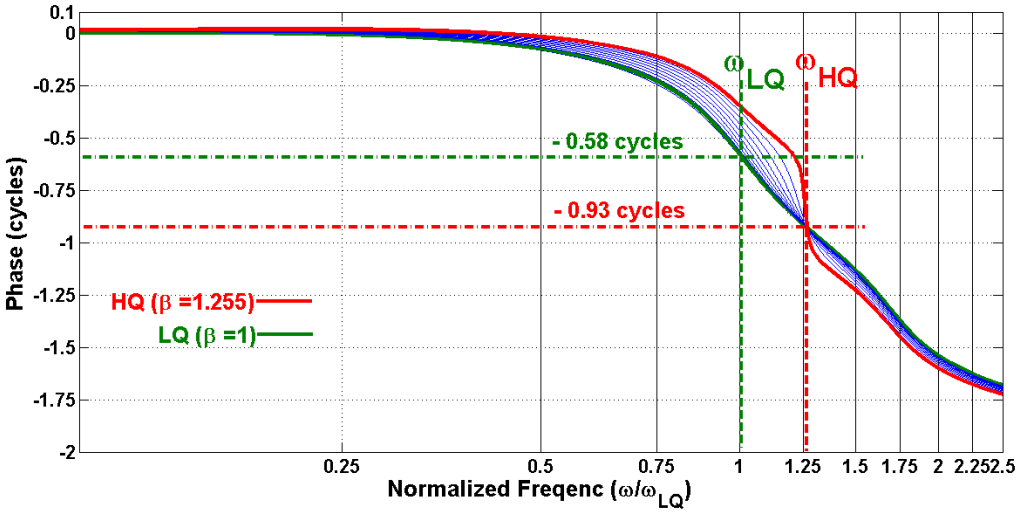


**(a)** Phase response of the cochlea filter model.

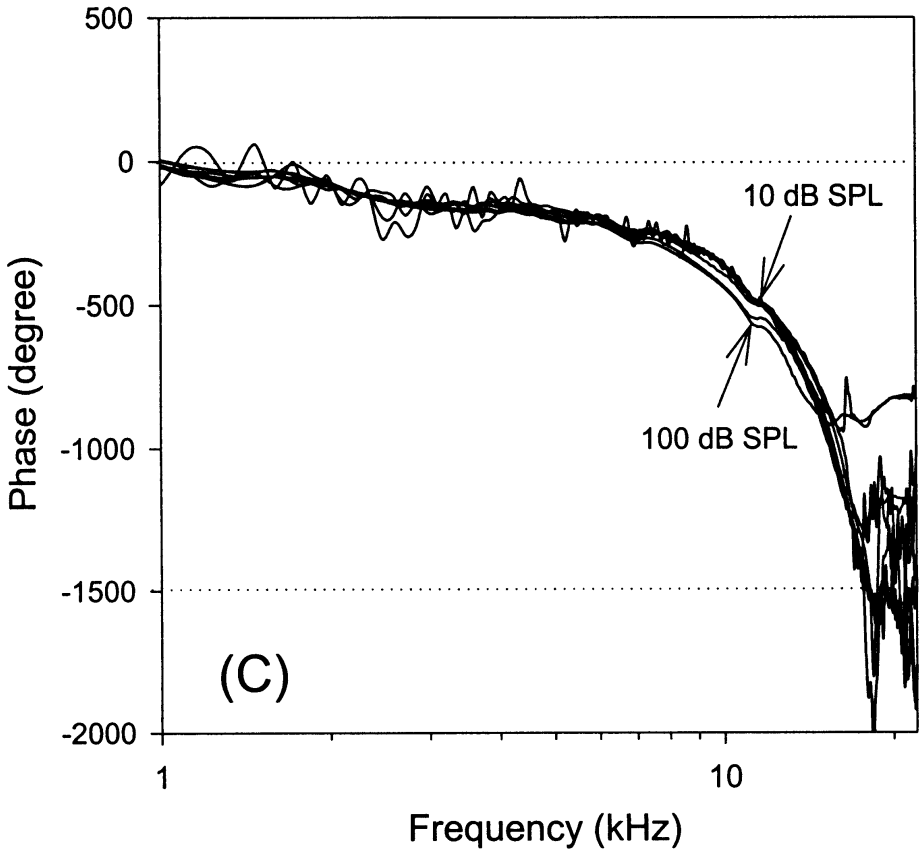


**(b)** Phase response in the 10 kHz region of Mongolian gerbils [10].

**Figure 3.6:** *Cochlea filter phase response in comparison with the physiological results. (Fig. 3.6(b) is take from [10].)*

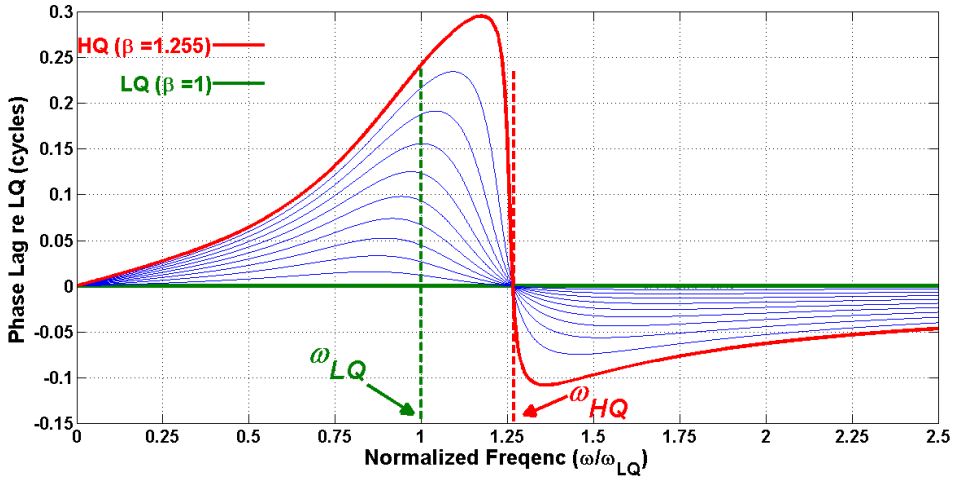


**(a)** Phase response respecting to the LQ response.

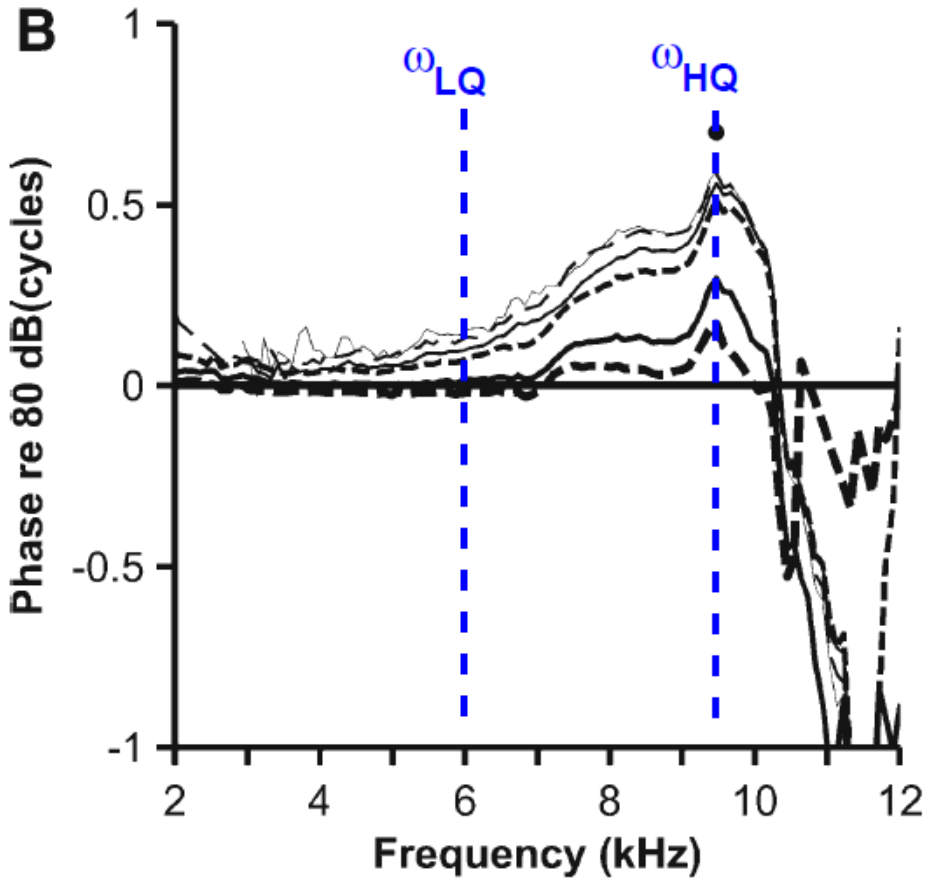


**(b)** Physiologically measured phase lag respecting to the high-intensity input response [99].

**Figure 3.7:** *Cochlea Filter Phase Lag respecting to the LQ response, in comparison with the physiological results. In the physiological measurement, the CF with high intensity (80 dB SPL) input stimuli is around 6kHz, and low intensity (20 dB SPL) CF is around 9.5 kHz. (Fig. 3.7(b) is adapted from [99].)*

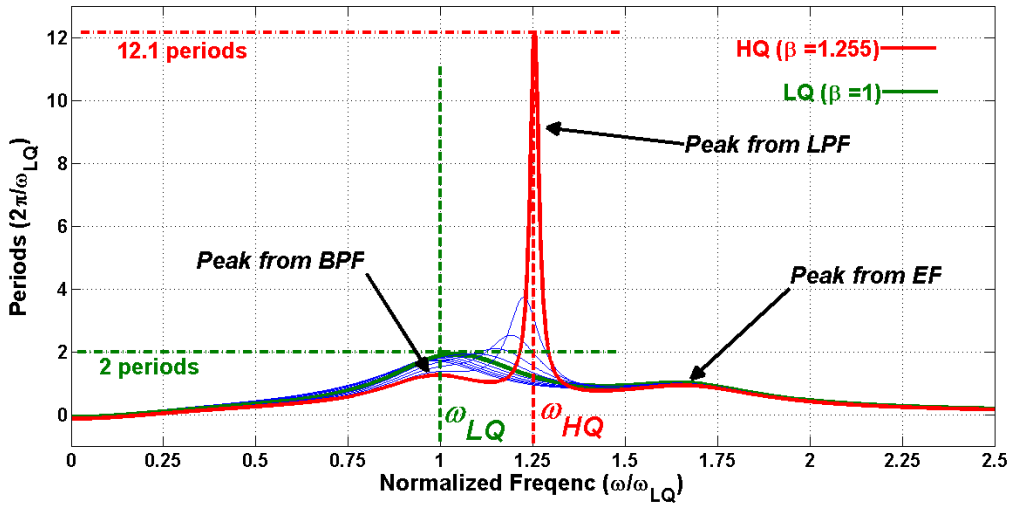


**Figure 3.8:** *Normalised group delay of the cochlea filter.*

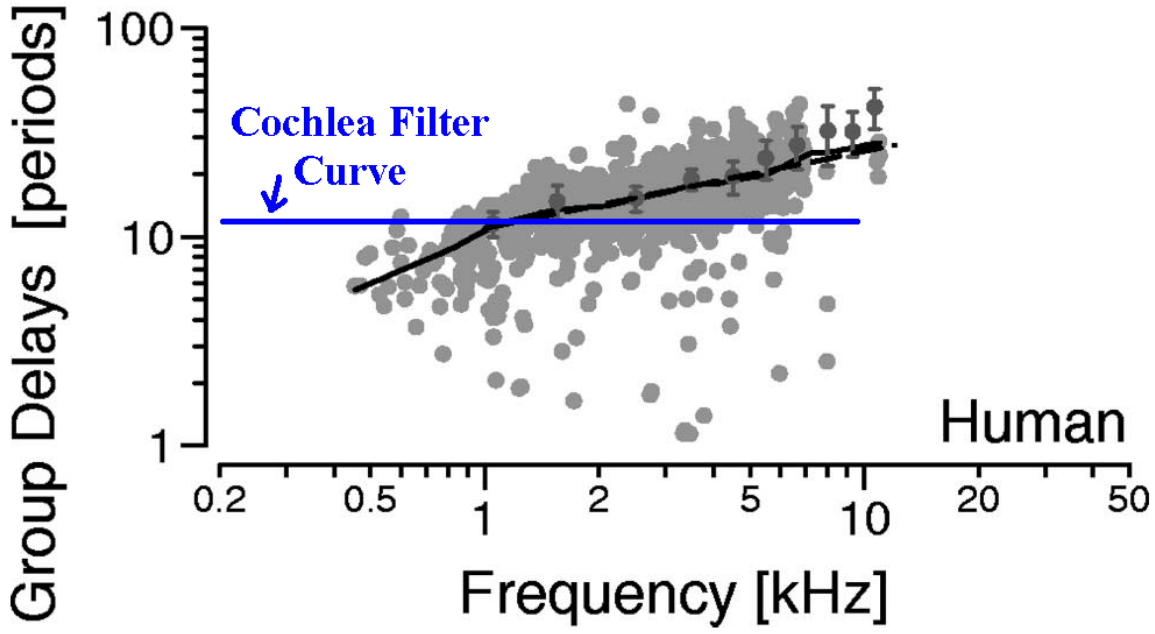


**Figure 3.9:** *Comparison of group delays between the proposed cochlea filter and the human cochlea. The maximum group delays are plotted agains CF. The grey dots are scatter-plot of measured data from the human cochlea which are given by Shera [102]; the dots with bars are data from Dreisbach [103]; the black solid line is the trend curve based on the human cochlea data; the blue solid line is the curve from the proposed cochlea filter. Since the SFOAE experiment is based on low-intensity stimulation, the group delays measured from the human cochlea correspond equivalently to the peak HQ group delay of the proposed cochlea filter. (Image is adapted from [102])*

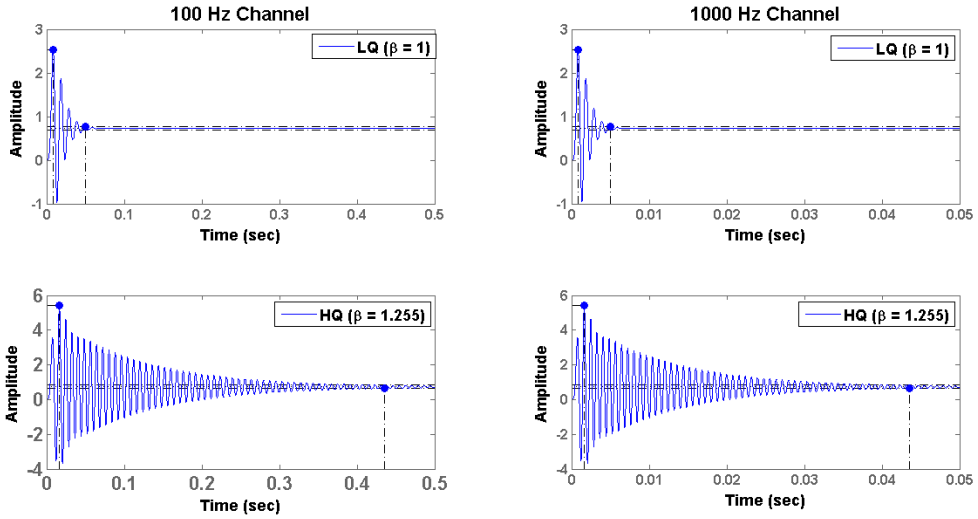


**Figure 3.10:** *Unit step responses of the cochlea filters in 100 Hz channel and 1000 Hz channel*

.

is also reciprocally related with bandwidth in the biological cochlea, with sharper tuning (HQ) corresponding to longer group delay at CF [102]. Furthermore, the physiological experiments based on stimulus-frequency-emission (SFOAE) group delay test predict that, for low-intensity input (HQ response), the human cochlea has roughly 10 periods group delay at 1 kHz area of the BM which increases to 20 periods at 10 kHz area [102]. The 12.1 periods HQ group delay shown in Fig. 3.8 approximately matches the physiological results. However, due to the exact scale-invariant property, the proposed cochlea filter has constant maximum group delay in unit of periods for different frequency channels. The group delay curve versus CF is shown in Fig. 3.9 which compares the results from the proposed cochlea filter with the SFOAE-based prediction of the human cochlea behaviour. As detailed in Table. 3.3, the HQ group delay of the proposed cochlea filter is slightly higher than those of the other animals, while the LQ group delay generally demonstrates reasonable matching with biology.

### 3.2.4 Transient Response

The unit step responses of the cochlea filters with $\omega_{BP} = 2\pi \cdot 100Hz$ and $\omega_{BP} = 2\pi \cdot 100Hz$ are plotted in Fig. 3.10. The comparison between the two channels shows that the step response of the cochlea filter is scale-invariant. The overshoot percentage of response is determined by the damping factor which is independent of CF. Therefore the peak amplitudes in the 100 Hz

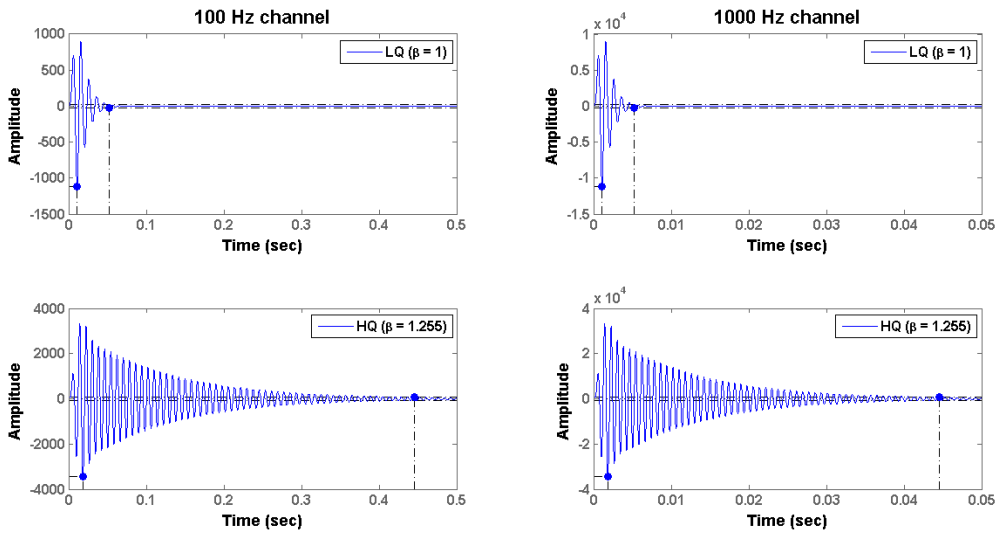


**Figure 3.11:** *Unit impulse responses of the cochlea filters in 100 Hz channel and 1000 Hz channel .*

and 1000 Hz channels are same. The peak amplitude and settling time are higher in the HQ response due to the decrease of damping (increase of $\beta$).

The unit impulse responses are plotted in Fig. 3.11. The peak amplitude is proportional to the CF as shown in Fig. 3.11, since the impulse response is the derivative of the scale-invariant step response.

The impulse response of the biological cochlea, as discovered by de Boer [104], has an asymmetric envelope: the rise time is shorter than the decay time. In physiology, the cochlea impulse response is approximated using the reverse correlation (revcor) functions which are derived based on the cochlea response to the 'click' signals [104–107]. Fig. 3.12(a) shows the impulse response waveform approximated by de Boer regarding the 1 kHz region of the cat's cochlea [104], which is similar with the impulse response of the proposed cochlea filter.

Another important characteristic of the cochlea impulse response that has been emphasised by the physiologists is the frequency modulation (or frequency glides) effect [105–107]. As shown in Fig. 3.13(a), the instantaneous frequency of the cochlea impulse response increases over time until it settles at a steady-state. In fact, de Boer has suggested to use this characteristic as a standard to evaluate cochlea models [107]. The frequency glides of the proposed cochlea filter are illustrated in Fig. 3.13(b). Notably, physiological experiments show that the frequency glides

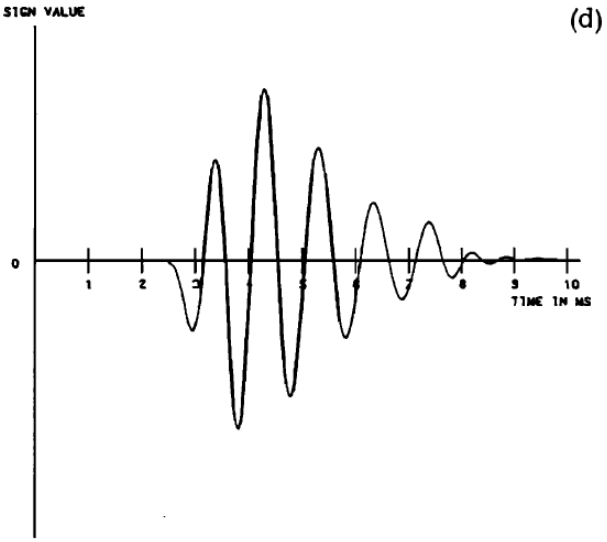


**(a)** Impulse response of 1 kHz region of cat's cochlea (input intensity: 60 dB SPL) [104]

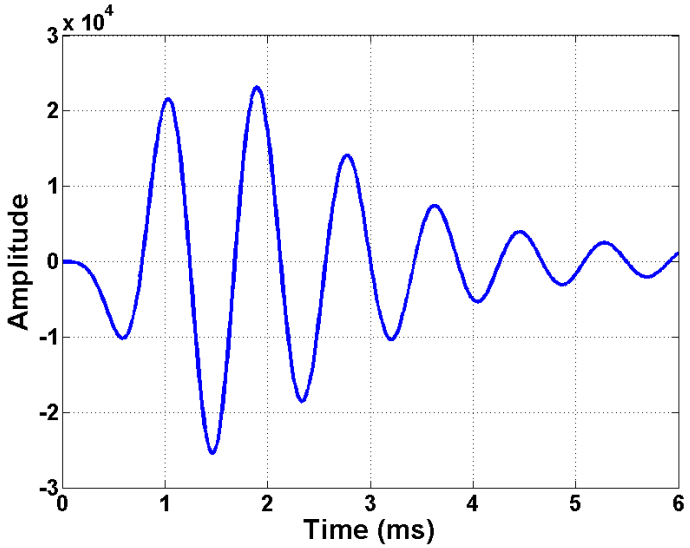


**(b)** Impulse response of the proposed cochlea filter ($\omega_{LQ}$=2$\pi$·1000 Hz, $\beta$=1.2)

**Figure 3.12:** *Comparison of impulse response between the biological cochlea and the proposed cochlea filter. (Fig. 3.12(a) is adapted from [104])*

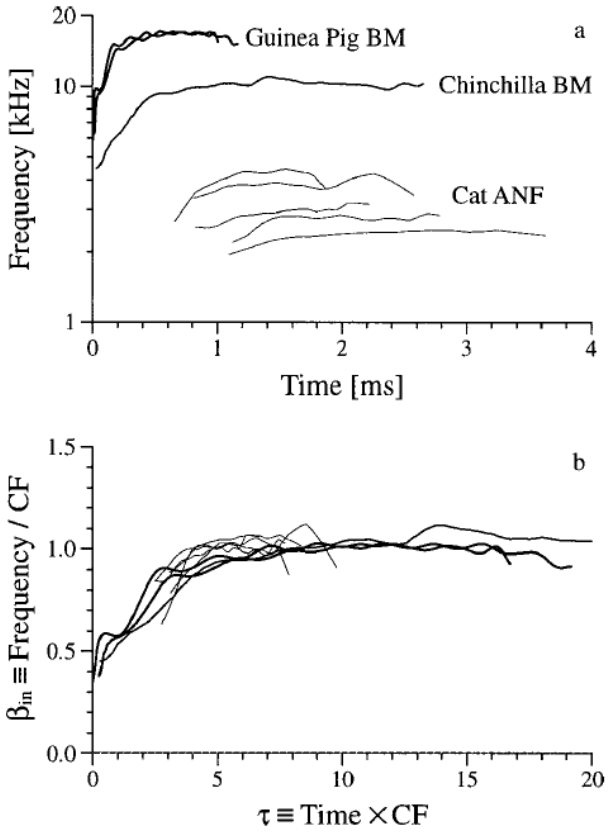


**(a)** Instantaneous frequency versus time in the impulse response of biological cochlea.

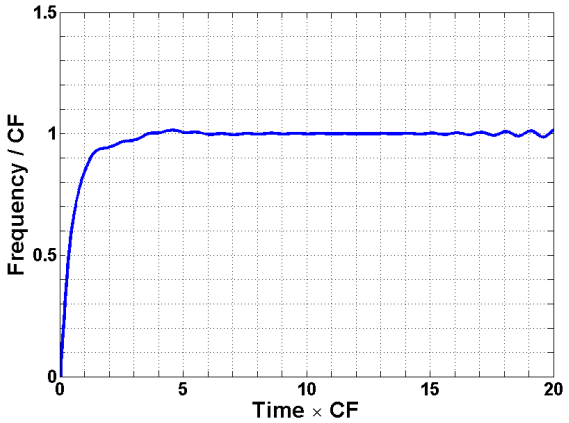


**(b)** Instantaneous frequency versus time in the impulse response of the proposed cochlea filter.

**Figure 3.13:** *Comparison of frequency glides between the biological cochlea and the proposed cochlea filter. (Fig. 3.13(a) is adapted from [105])*

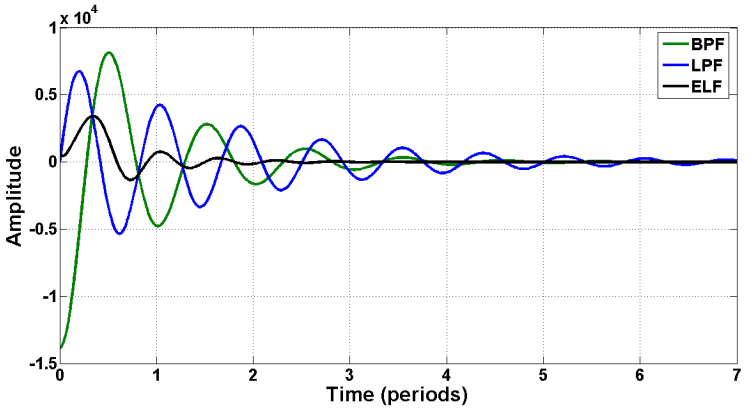


**Figure 3.14:** *Decomposed impulse responses from the three sub-filters.*

are independent of the stimulation intensity, which indicates it is not a result of the non-linear process of cochlea [105, 107]. Similarly, the frequency glides of the proposed cochlea filter are not based on any filter tuning mechanism. The origin of the frequency glides in the proposed cochlea filter is revealed in Fig. 3.14. Since the cochlea filter is a composite of three filters in cascade, its overall impulse response is the convolution of three individual responses. As shown in the decomposed response in Fig. 3.14, the BPF response has substantial influence on the convolved overall response at the early stage; however, both the BPF and the LPF settle much quicker than the LPF, and thus after 3 periods, the LPF response becomes fully dominant. Since the BPF has a lower natural frequency than the LPF, the instantaneous frequency of the overall impulse response appears to increase with time.

## 3.3 Simulink Implementation of the Cochlea Filter with Automatic Tuning Control

In this section, the cochlea filter is implemented in the MATLAB Simulink software for a proof of concept. The automatic tuning control (ATC) block is also integrated with the cochlea filter so that the filter is able to perform level-dependent signal processing.

### 3.3.1 Simulink Implementation of the Cochlea Filter

The Simulink model of the cochlea filter is established to further investigate its behaviour. Based on Eq. 3.1, the BPF model is designed as shown in Fig. 3.15. Based on Eq. 3.2, the LPF model is designed as shown in Fig. 3.16. Besides, the elliptic filter is available in the Simulink

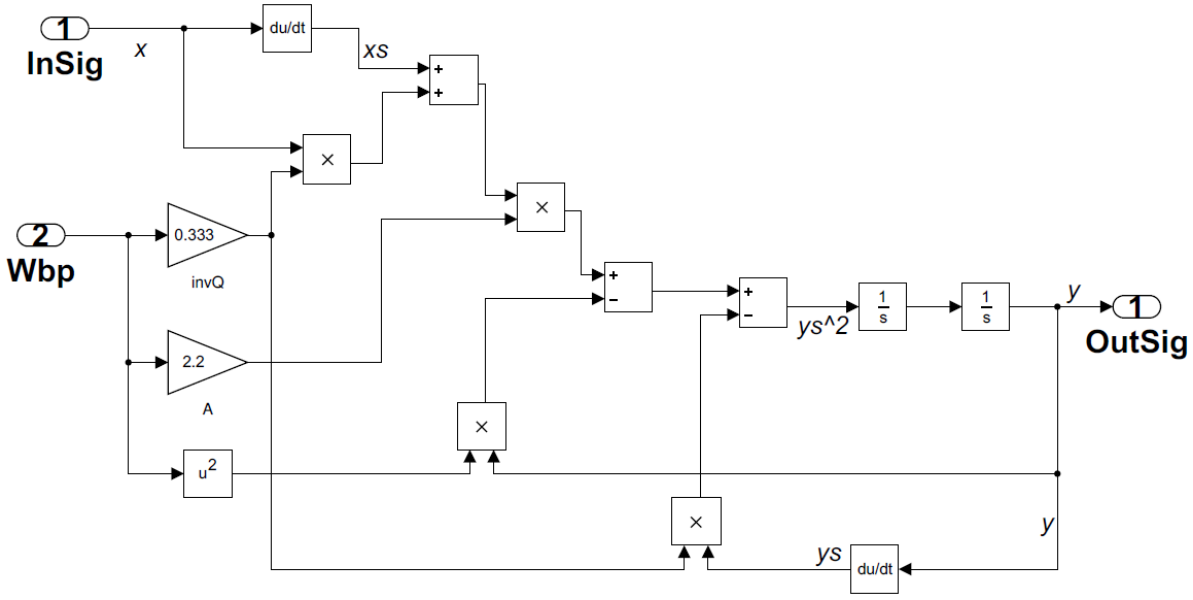


**Figure 3.15:** *Simulink implementation of the BPF.*

model library. Therefore, the Simulink model of the cochlea filter is built as shown in Fig. 3.17.

### 3.3.2 Automatic Tuning Control (ATC)

As mentioned above, the response of biological cochlea is level-dependent. In the proposed cochlea filter, $\beta$ is the tuning parameter which adjusts the CF and peak gain. To emulate the behaviour in biology, $\beta$ should be automatically adjusted in accordance with the intensity of input. Therefore the ATC block of the cochlea filter consists of an amplitude detector (AD) and an amplitude-$\beta$ mapper (ABM). The architecture of the cochlea filter with ATC is illustrated in Fig. 3.17. The AD detects the amplitude of the BPF output, and the ABM maps the amplitude into the corresponding $\beta$ value which is fed to the LPF. The signal amplitude is estimated based on the BPF output because the auditory masking effects observed in psycho-acoustical experiments suggest that in the biological cochlea the sensitivity adaptation at each position on the BM is performed according to the relevant in-band signal strength. Furthermore, the feed-forward structure is preferred for LPF tuning due to its significant delays which makes the feed-back structure suffer severely from latency problems.

The signal amplitude can be estimated by squaring followed with DC extraction (low-pass

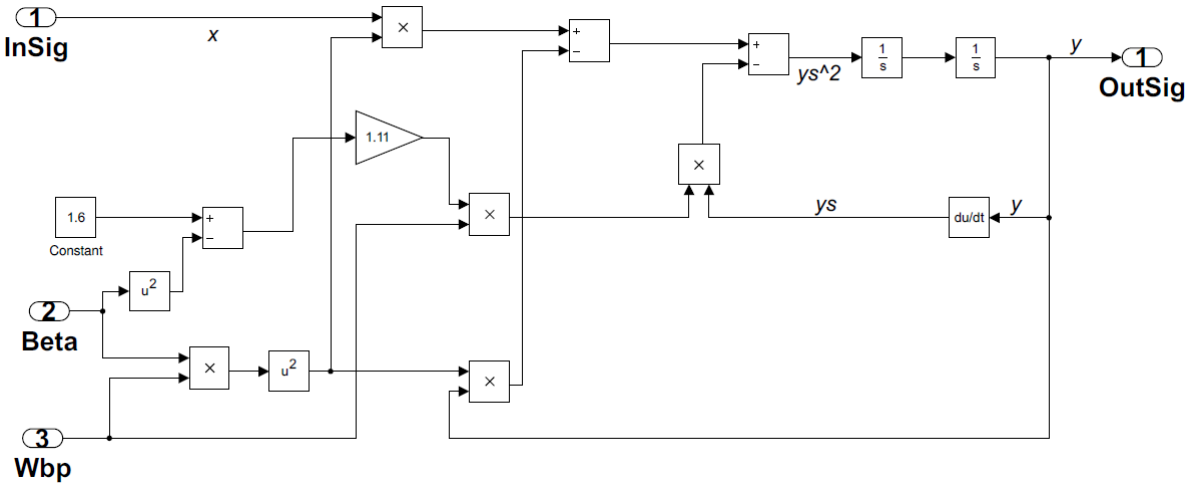


**Figure 3.16:** *Simulink implementation of the LPF.*

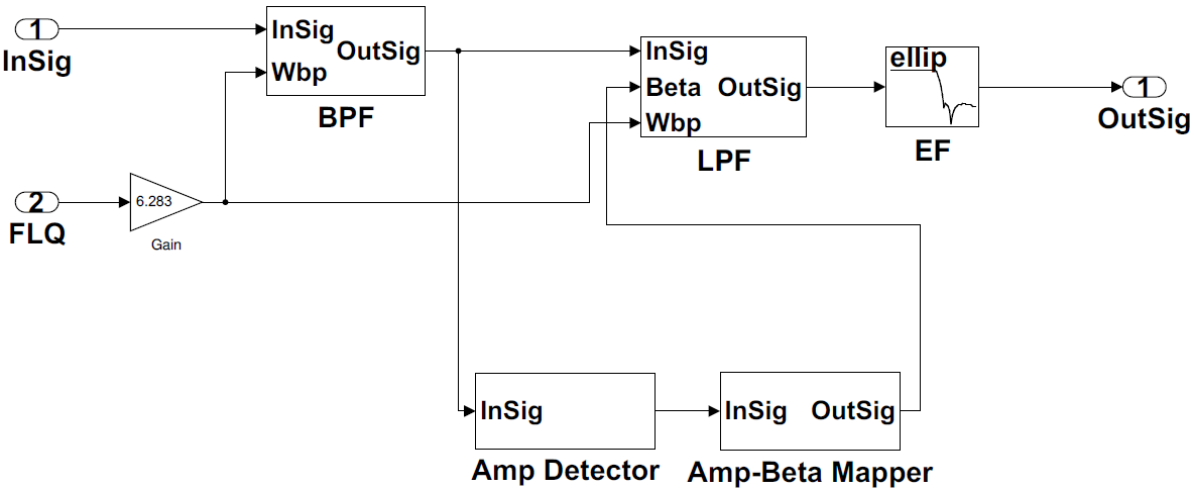


**Figure 3.17:** *Simulink implementation of the cochlea filter with ATC.*

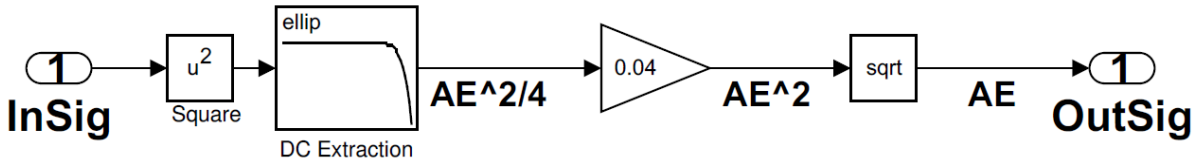


**Figure 3.18:** *Simulink implementation of the amplitude detector.*

filtering). Assume the signal is in the form of

$$x(t) = [A_E sin(\omega_E t + \phi_E)] sin(\omega_c t + \phi_c), \tag{3.12}$$

where $A_E sin(\omega_E t + \phi_E)$ represents the envelop signal and $sin(\omega_C t + \phi_C)$ is the carrier signal. The envelop frequency $\omega_E$ is much lower than the carrier frequency $\omega_C$. The amplitude to be extracted is the value of $A_E$. By squaring Eq. 3.12, the following is derived:

$$x(t)^2 = \frac{A_E^2}{4} - \frac{A_E cos(2\omega_E + 2\phi_E)}{4} - \frac{A_E cos(2\omega_C + 2\phi_C)}{4} + \frac{A_E^2 cos(2\omega_E + 2\phi_E) cos(2\omega_C + 2\phi_C)}{4}. \tag{3.13}$$

Therefore the $\frac{A_E^2}{4}$ term can be extracted by low-pass filtering. The simulink block of the AD is shown in Fig. 3.18.

The mapping function between signal amplitude and $\beta$ is derived by taking inspirations from the physiological data. In the cochlea filter, the $\beta$ factor is the ratio between $\omega_{LP}$ and $\omega_{BP}$ which is approximately equivalent with the ratio between $\omega_{HQ}$ and $\omega_{LQ}$. In other words, $\beta$ directly reflects the CF shift of the filter. The relationship curves between CF shift and the input intensity are plotted in Fig. 3.19 based on the results from the physiological measurement; the CF shift factor $\gamma$ is defined as follows

$$\gamma = \frac{\omega_{HQ} - \omega_{LQ}}{Max.(\omega_{HQ}) - \omega_{LQ}}. \tag{3.14}$$

As shown in Fig. 3.19, the following function gives a reasonable approximation of the relationship between $\gamma$ and the input intensity:

$$\gamma = log_{21}(21 - \frac{i}{5}), \tag{3.15}$$

where $i$ stands for the input intensity in decimal scale. In physiological results, the range of input is generally between 0$\sim$100 dB SPL. In the cochlea filter, the input range is assumed to

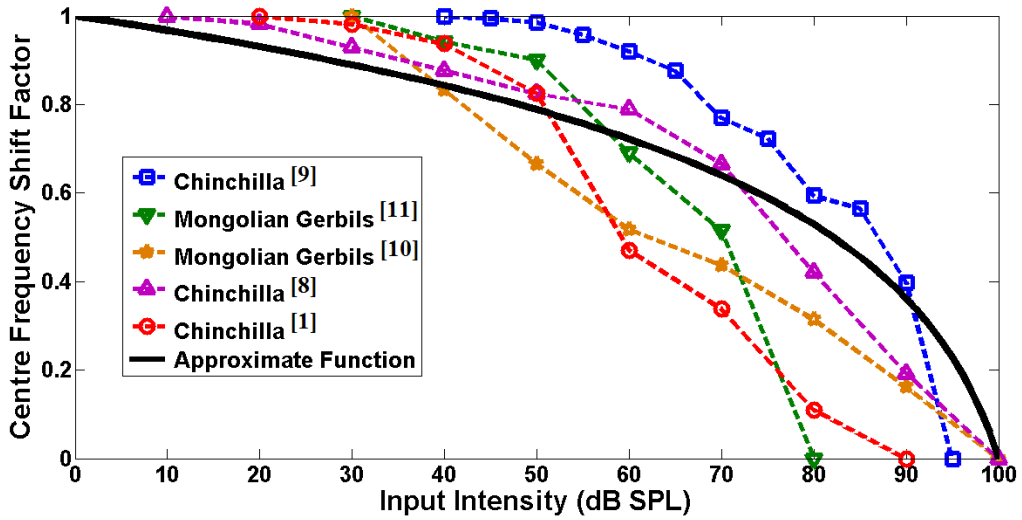


**Figure 3.19:** *Relationship curves between CF shift and input intensity based on the physiological data and the approximation of Eq. 3.15.*

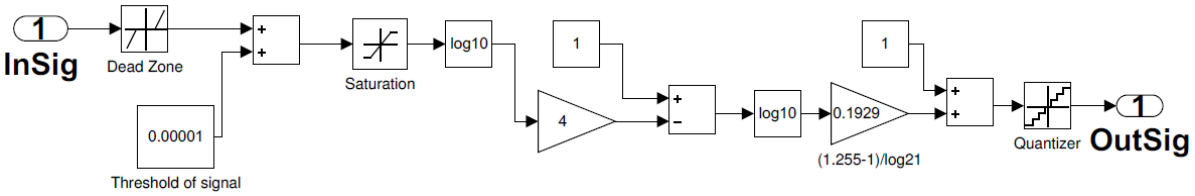


**Figure 3.20:** *Simulink implementation of the amplitude-$\beta$ mapper.*

be in the same order with amplitude level from $10^{-5}$ V to 1 V. Besides, as $\beta$ approximately equals $\frac{\omega_{HQ}}{\omega_{LQ}}$, the following equation stands:

$$\gamma = \frac{\beta - 1}{1.255 - 1} = log_{21}[21 - 4log(\frac{A_E}{10^{-5}})] = log_{21}(1 - 4logA_E). \tag{3.16}$$

Based on Eq. 3.16, the Simulink model of the ABM is built as shown in Fig. 3.20. Additionally, in order to make the $\beta$ value obtained from Eq. 3.16 rational, a dead-zone block and a saturation block are used prior to the corresponding arithmetic functions. Also, the quantiser with interval of 0.001 is used to stabilise the variation of $\beta$.

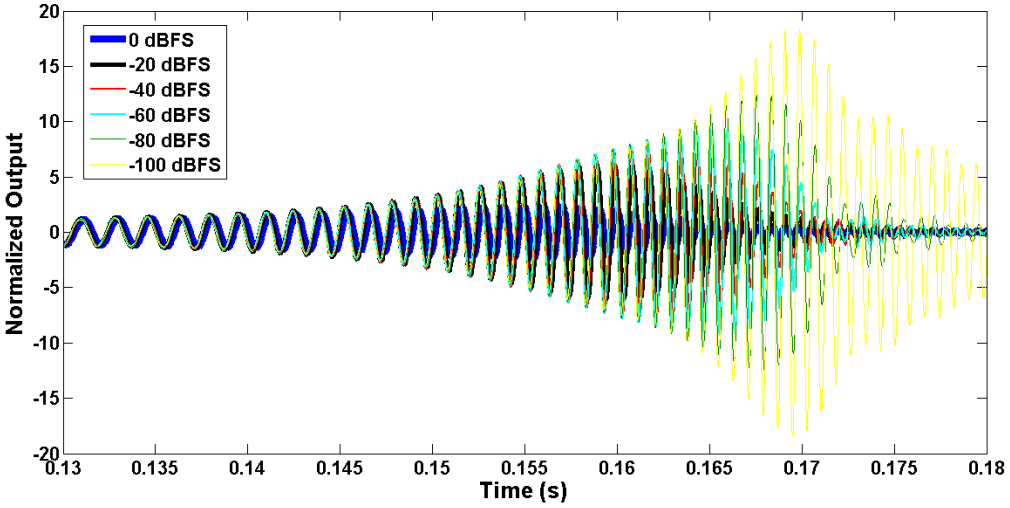


**Figure 3.21:** *Level-dependent behaviour of the cochlea filter with ATC in response to chirp signals. $\omega_{LQ}$ of the cochlea filter model is set as $2\pi \cdot 1000Hz$. The chirp signal sweeps logarithmically from 20 Hz to 20 kHz in 0.3 seconds.*

### 3.3.3 Simulation Results for the Cochlea Filter with Automatic Tuning Control

#### 3.3.3.1 Response from single channel

The $\omega_{LQ}$ of the cochlea filter model is set as $2\pi \cdot 1000$ Hz so that the filter operates with CF from 1000 Hz to 1255 Hz. A series of chirp signals logarithmically sweeping from 20 Hz to 3000 Hz is applied to the filter. The length of the chirp signal is 0.2 s and the amplitudes range from 0 dBFS (1 V) to -100 dBFS (10 $\mu$V) with -20 dBFS step. The response of the cochlea filter with ATC is plotted in Fig. 3.21. The output amplitude has been normalised by the input amplitude so that Fig. 3.21 shows a clear level-dependent adaptation of the peak gain and CF.

A male speech signal is used to test the filter. The time domain waveform, spectrum and spectrogram of the speech signal is shown in Fig. 3.22. The spectrogram shows that rich information is contained in the region of 2 kHz band, so $\omega_{LQ}$ is set as $2\pi \cdot 1000Hz$. The output of the filter is illustrated in Fig. 3.23. The output spectrum and cochleagram show that the 2 kHz region is emphasised. Besides, the high frequency signals are well attenuated, as shown in the spectrogram in Fig. 3.23(c).

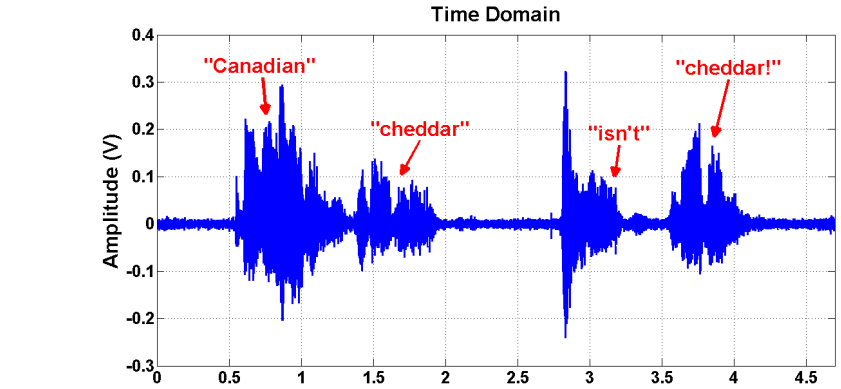


(a)

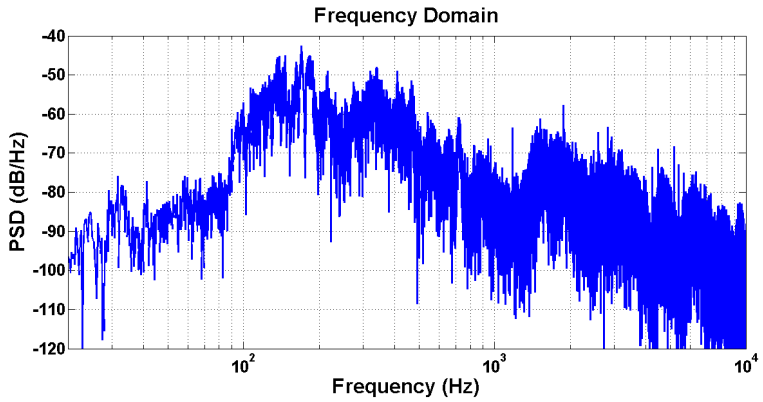


(b)

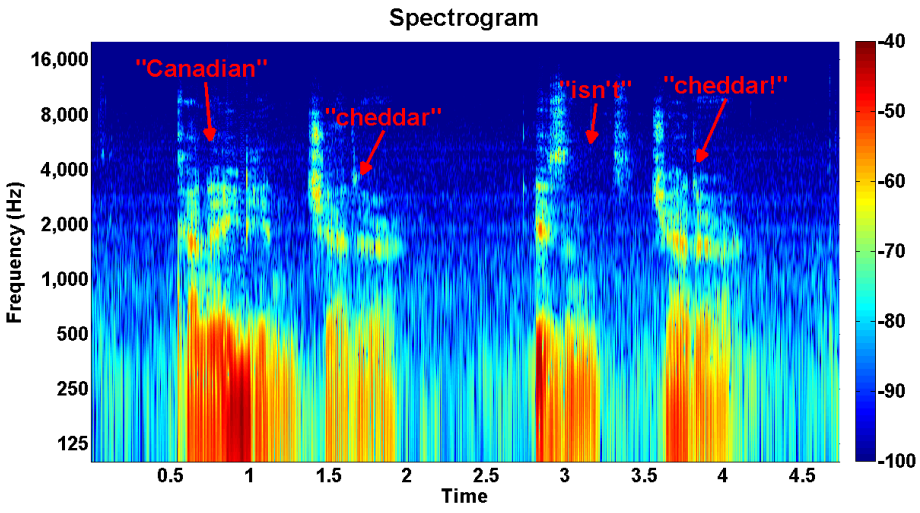


(c)

**Figure 3.22:** *The male speech signal "Canadian cheddar, isn't cheddar!" represented in time domain (a), frequency domain (b) and spectrogram (c). The spectrogram is generated using short-time fast Fourier transform (FFT) with following parameters: rectangular window with length of 256 length, %20 overlap and FFT length of 8096.*

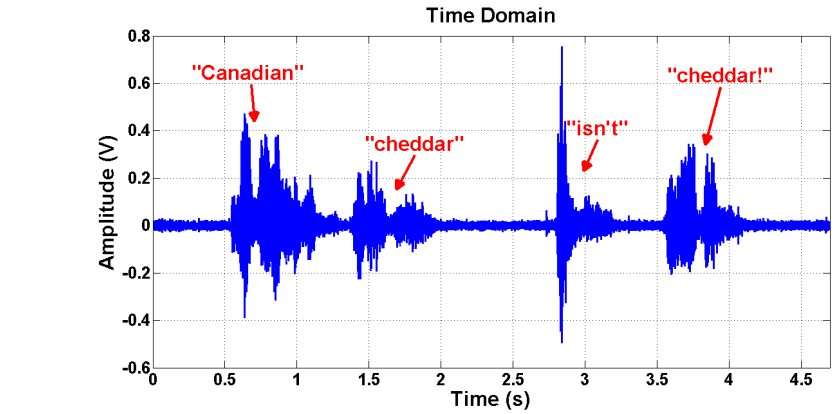


(a)

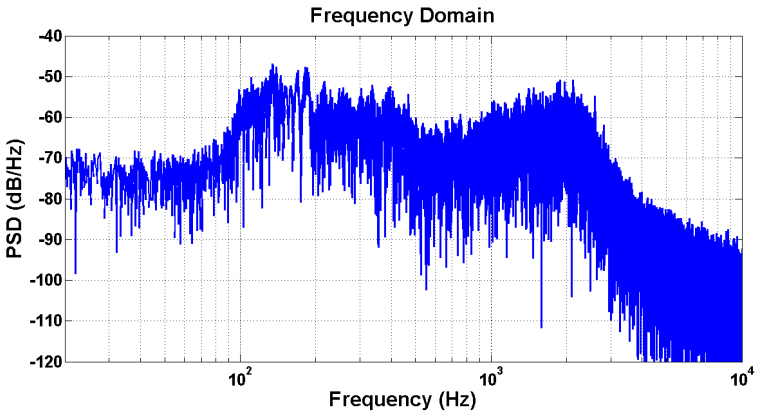


(b)

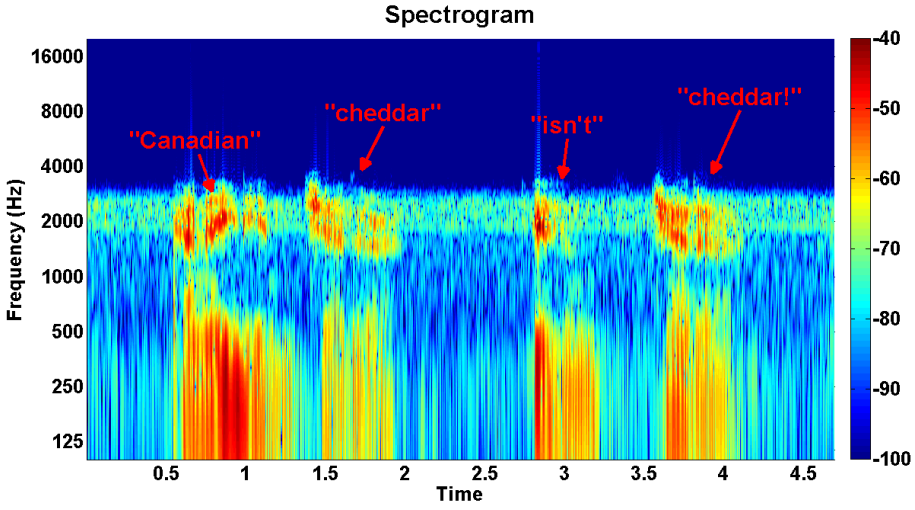


(c)

**Figure 3.23:** *The male speech signal "Canadian cheddar, isn't cheddar!" after processed by the 2 kHz cochlea filter: (a) time domain waveform; (b) frequency spectrum; (c) spectrogram.*


**Figure 3.24:** *Simulink model of the cochlea filter bank in one-third octave scale.*

#### 3.3.3.2 Response of the cochlea filter bank

A cochlea filter bank is built in the one-third octave scale, as shown in Fig. 3.24. The chirp signals, pulse signals and the male speech are applied to the filter bank. All signals are applied with separate intensities of 0 dBFS and -72 dBFS for comparison. The results are illustrated in Fig. 3.25, Fig. 3.26 and Fig. 3.27 where cochleagram-like images are generated based on the output amplitudes of the filter bank. The outputs have been full-wave rectified and normalised by the peak amplitude, so that the time-frequency map of the signals is clearly shown in the images.

The frequency selectivity of the cochlea filter bank is proved by the chirp signal results in Fig. 3.25, where both images show a prominent peak line spanning from the bottom-left to the top-right corner. The peak line width in Fig. 3.25(b) is narrower than that in Fig. 3.25(a), which indicates that the filter bandwidth becomes narrower when input signal is low. Besides, Fig. 3.25(b) shows a bigger colour drop from the peak line to the top-left region, which indicates that the filter peak gain increases when input signal is low. Therefore, as expected, the frequency selectivity of the filter bank is adaptively improved for the low-intensity input. Moreover, the ringing after peak lasts for a longer time period in Fig. 3.25(b). The observation of otoacoustic emission in biological cochlea indicates that such effect also exists in biology [39, 40, 108]. As introduced in Chapter. 2, the cochlea reflects energy back into the air and cause detectable

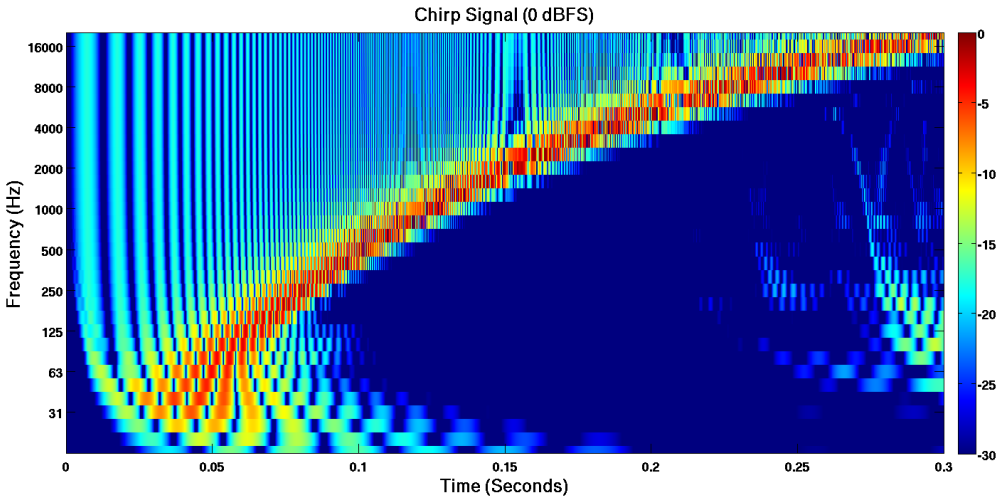


**(a)**

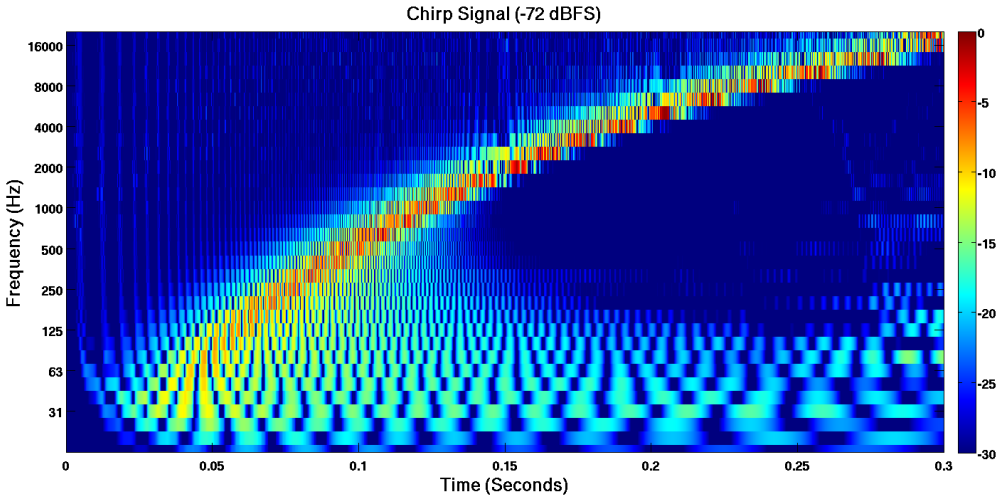


**(b)**

**Figure 3.25:** *The cochlea filter bank response to chirp signal which sweeps logarithmically from 20 Hz to 20 kHz in 0.3 seconds. The output signals from each channels are full-wave rectified and normalised by the maximum amplitude in the entire filter bank. Separate test are performed with 0 dBFS and -72 dBFS input intensities.*

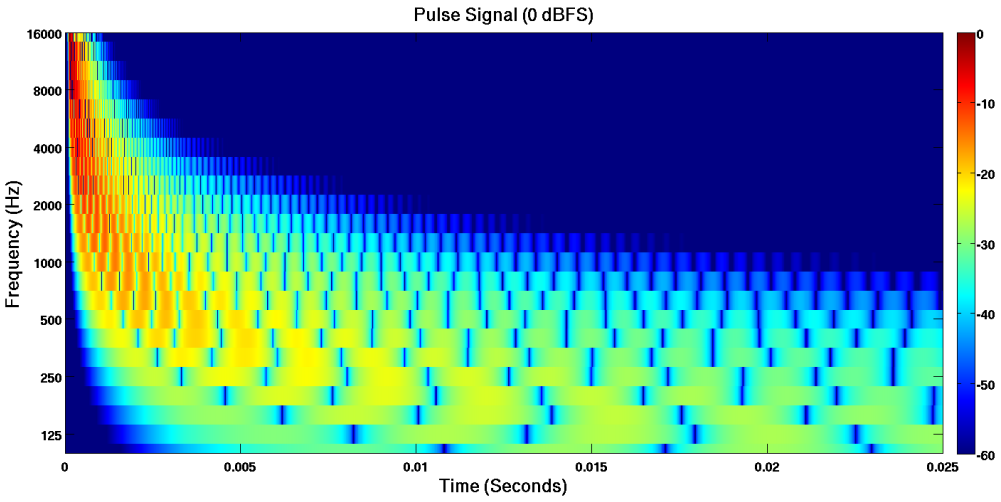


**(a)**

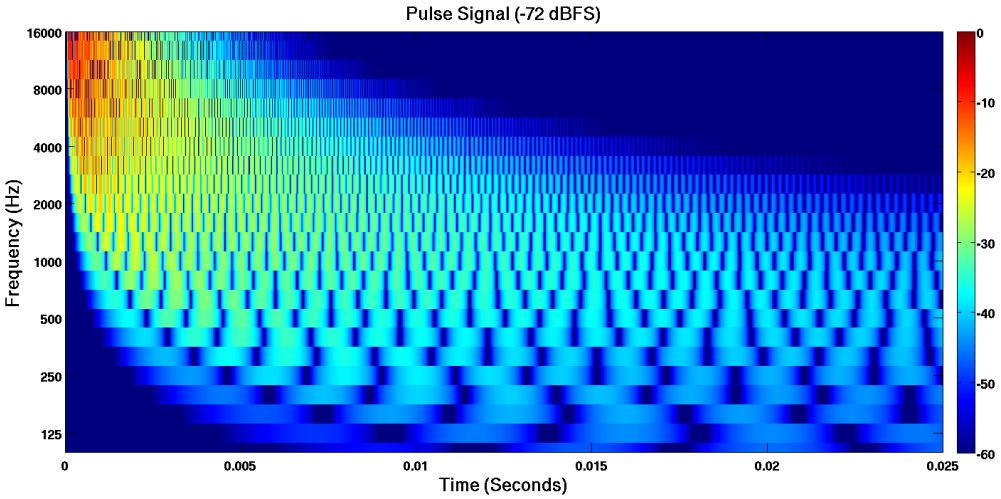


**(b)**

**Figure 3.26:** *The cochlea filter bank response to pulse signal which has a pulse width of 10 $\mu$ seconds. The output signals from each channels are full-wave rectified and normalised by the maximum amplitude in the entire filter bank. Separate test are performed with 0 dBFS and -72 dBFS input intensities.*

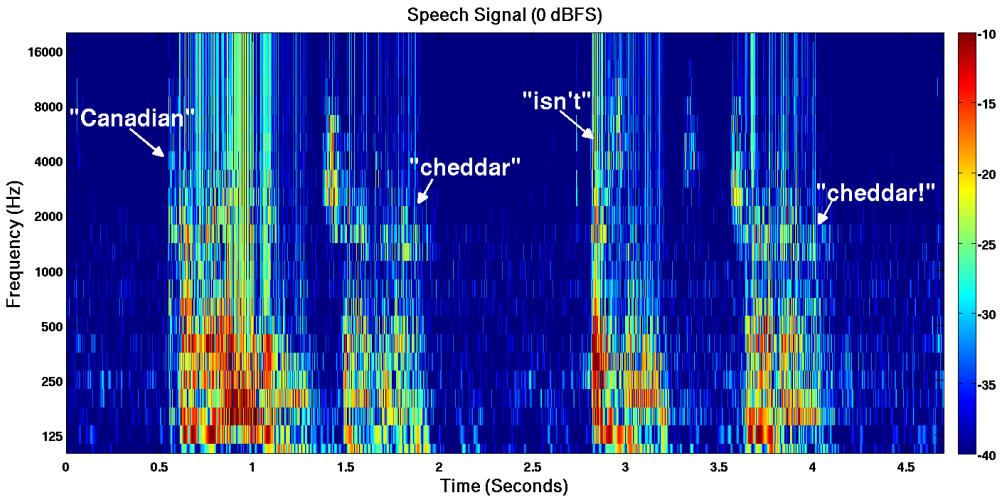


**(a)**

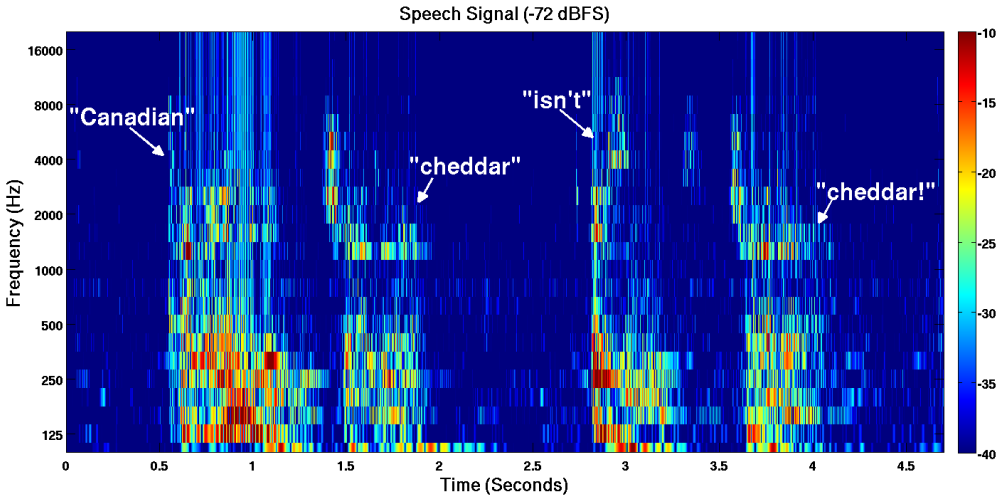


**(b)**

**Figure 3.27:** *The cochlea filter bank response to male speech signal "Canadian cheddar, isn't cheddar!". The output signals from each channels are full-wave rectified and normalised by the maximum amplitude in the entire filter bank. Separate test are performed with 0 dBFS and -72 dBFS input intensities.*

sounds after receiving near-threshold stimulus.

Also as expected, both the 0 dBFS and -72 dBFS pulse responses in Fig. 3.26 show that the high frequency channels have higher energy than the low frequency channels. Notably, the 0 dBFS results in Fig. 3.26(a) show a significant compression of response amplitude. As stated above, the impulse response amplitude of the cochlea filter is proportional to its CF, so the peak amplitude in the 16 kHz channel should be over 42 dB higher than the 500 Hz channel without automatic tuning control. Fig. 3.26(a) indicates this amplitude difference has been compressed to about 20 dB. The compression comes from the fact that in higher frequency channels, the amplitude detected at the output of the BPF is higher because of its wider pass-band so that higher level suppression is applied by the ATC. By contrast, the -72 dBFS results in Fig. 3.26(b) show a higher level of energy concentration because the input intensity is so low that the detected amplitudes from the BPFs are close to the threshold level in all channels. Since similar levels of tuning are applied among the channels, the response amplitude appears to be roughly proportional to the channel CF in Fig. 3.26(b).

The increase of onset delay from high to low frequency channels resembles the physiological findings that the onset latencies of IHC impulse response increase from the basal (high frequency) to the apical (low frequency) end of BM [48]. In biological cochlea, the response in the 200 Hz region has about 2 ms delay compared with the 10 kHz region [48]. The onset latency between the 250 Hz and the 16 kHz channel is about 2 ms in the 0 dBFS response and is about 3 ms in the -72 dBFS response, which agrees well with the physiological result.

The speech signal responses in Fig. 3.27 reflect nearly all of the speech features shown in the signal spectrogram (Fig. 3.22(c)). Similar with the pulse signal test, the response to 0 dBFS speech shows a higher level of amplitude compression than the -72 dBFS response. The colours in Fig. 3.27 appears highly discontinuous because it is based on the varying signal amplitude and the number of channel is limited. Therefore the envelope extraction and channel interpolation are applied so that smooth cochleagrams are obtained as shown in Fig. 3.28. Compared with the spectrogram in Fig. 3.22(c), the cochleagrams reflect more details in low frequency bands.

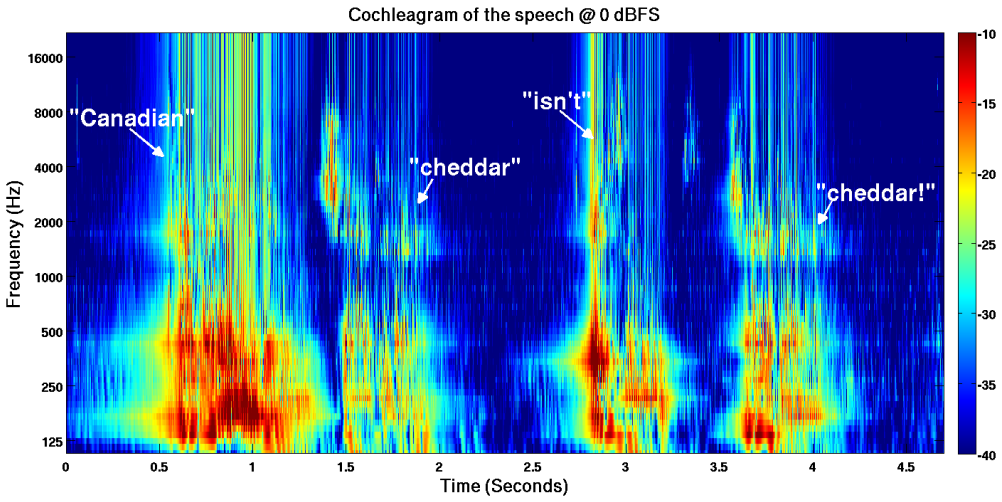


**(a)**

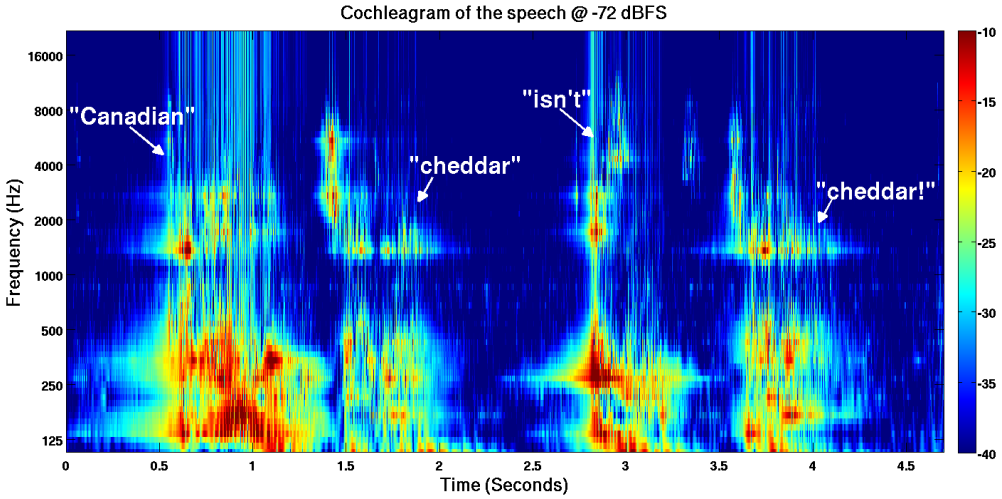


**(b)**

**Figure 3.28:** *Cochleagrams generated from Fig. 3.27 after channel interpolation and and envelope extraction. Two extra channels are interpolated between two original channels, the amplitudes of which are derived by taking geometric mean of the original channels. The envelope extraction is based on Hilbert transform. Details about the channel intermodulation and envelope extraction process can be found in Appendix A.2.*

## 3.4 Summary

This chapter presents the mathematical modelling of the proposed biomimetic cochlea filter. The model is established based on Rhode's three-stage representation of the cochlea frequency response. A cascade of three sub-filters is employed to replicate the cochlea frequency response: a second-order BPF corresponds to the gentle and constant low-frequency tail; a tunable second-order LPF corresponds to the selective and variable mid-band response; a fifth-order ELF corresponds to the ultra-steep roll-off at stop-band. Moreover, a relationship function between the peak gain increase and the CF shift is established to replicate the CF tuning characteristics of the biological cochlea. With these features, the proposed cochlea filter model demonstrates a frequency response curve which is highly faithful with that observed from the biological cochlea.

Furthermore, as proven in its pole-zero plot, the proposed cochlea filter is a minimum-phase filter, as is the biological cochlea. Therefore, the proposed cochlea filter also matches the biological cochlea in phase response and group delay. Besides, the filter impulse response is compared with biological cochlea, which shows reasonable similarity in the asymmetric response envelope and the frequency glides effect.

The proposed filter model is implemented in the MATLAB Simulink software for simulation. An ATC block is integrated with the filter and the level-dependent behaviour of the filter is verified in the simulations results. A cochlea filter bank is built and used to process a variety of acoustic signals including the chirp, pulse and speech signals for a proof of concept. In the end, its capability of generating a cochleagram is demonstrated.

# Chapter 4
# Design and Implementation of the Cochlea Filter in Analogue VLSI

Following the filter model proposed in Chapter 3, the method to realise the filter using analogue VLSI circuit is elaborated in this chapter.

## 4.1 Circuit Design

### 4.1.1 Introduction

The techniques for implementation of low order filters in analogue VLSI have been well developed. The mainstream implementation methods include active RC, MOSFET-C, switched-capacitor (SC), and Gm-C filters. These techniques can be classified into two categories: the Op-Amp-based and the Op-Amp-less types. The Op-Amp-based types include the active RC, MOSFET-C and SC techniques, which use resistors (or equivalent resistors) and capacitors in the Op-Amp-based feed-back loop to achieve integral or differential functions. The passive on-chip resistor is used in the active RC filters, the on-resistance of the MOSFET transistors is used in the MOSFET-C filters, and the equivalent switching resistance is used in the SC filters. By contrast, the Gm-C filter is based on the combinations of transconductors and capacitors, which belongs to the Op-Amp-less category. The Op-Amp is not required in the Gm-C filters, since the transconductor not only has the function of resistor-equivalent I-V conversion, but also can be used to build feed-back structures like the Op-Amp. Consequently, the Gm-C filters are highly suitable for implementation of low-power high-order filters. In comparison, the Op-Amp-based filters require equivalent number of Op-Amps as the filter order. The cochlea filter proposed in this thesis is ninth-order which means nine Op-Amps are needed for each channel. Since a large number of Op-Amps will lead to high power dissipation, the Gm-C technique is selected to implement the proposed cochlea filter.

In general, there are two approaches to map the complex ninth-order cochlea filter function (Eq. 3.11) into circuit schematics. The first approach is inspired from mathematics. As shown

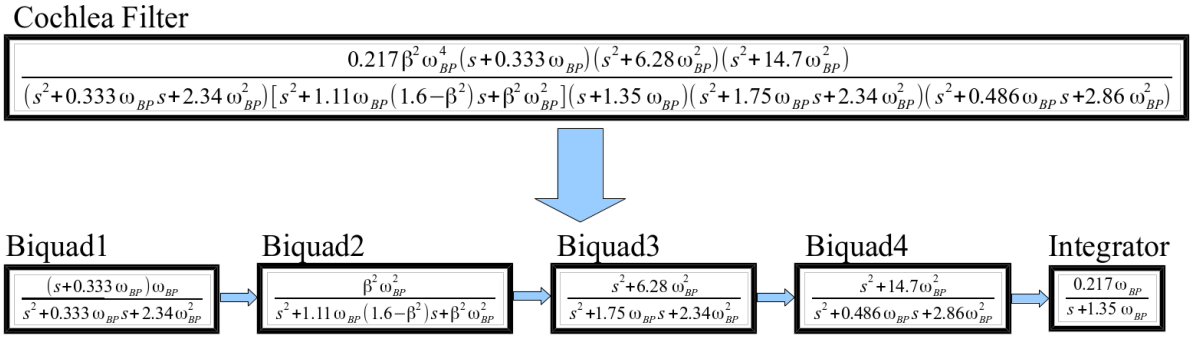


**(a)** Math-inspired implementation of the cochlea filter

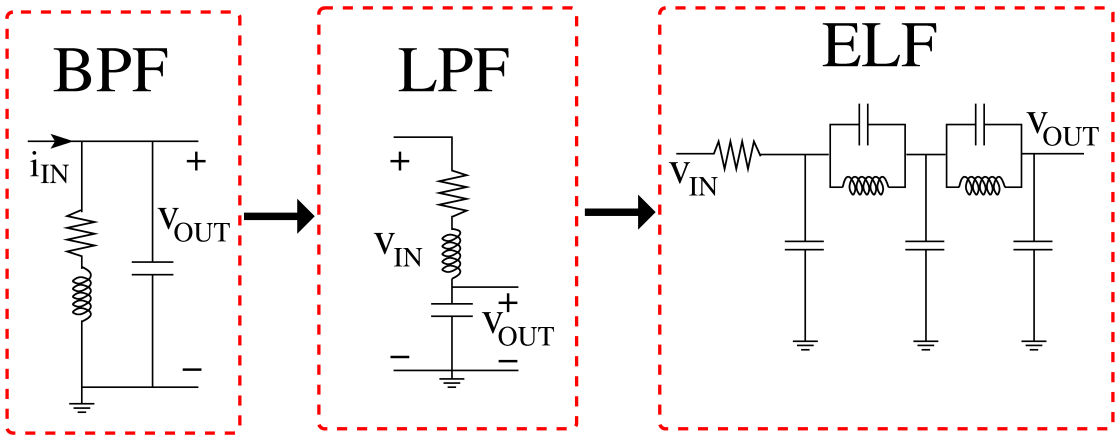


**(b)** Physics-inspired implementation of the cochlea filter

.

**Figure 4.1:** *Two approaches to implement the cochlea filter.*

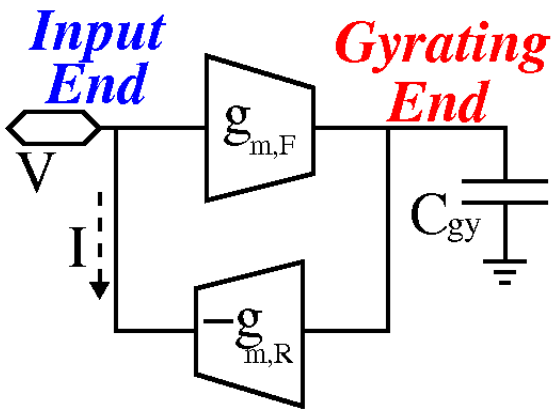


**Figure 4.2:** *Gyrator-C topology for an active inductor.*

in Fig. 4.1(a), the ninth-order filter function can be decomposed into 4 bi-quadratic (biquad) transfer functions in addition to an integral function. Therefore, the cochlea filter can be built as a cascade of 4 biquad filters and an integrator, which are feasibly realisable using Gm-C circuits [109]. The second approach is inspired from physics. As shown in Fig. 4.1(b), all of the three sub-filters can be represented using equivalent RLC ladders [98], where the Gm-C circuit can be used to implement the active inductors [110]. In this thesis, the second approach is chosen; as will be introduced in the following text, the identical active inductors can be reused in all the RLC ladders, which significantly reduces the circuit design complexity.

### 4.1.2 Floating Active Inductor (FAI) Design

Development of the active inductor is one of the key challenges in the RLC ladder-based cochlea filter circuit design. The active inductors have to be operating in floating mode as required by the ELF. Besides, the quality factor should be easily adjustable as required by the tuning features of the LPF. The classical method to build CMOS active inductors is based on the gyrator-C technique [110]. As shown in Fig. 4.2, the gyrator is built with a pair of transconductors between the input end and the gyrating end. The transconductor from the input end to the gyrating end is called the forward transconductor, while the transconductor from the gyrating end to the input end is called the reverse transconductor [110]. A capacitor is loaded at the gyrating port, and therefore the impedance at the input port becomes inductive. The equivalent impedance at the input port is given by:

$$Z(s) = \frac{V}{I} = \frac{V}{-V \cdot g_{m,F} \cdot \frac{1}{C_{gy}s} \cdot (-g_{m,R})} = \frac{C_{gy} \cdot s}{g_{m,F} \cdot g_{m,R}}, \tag{4.1}$$

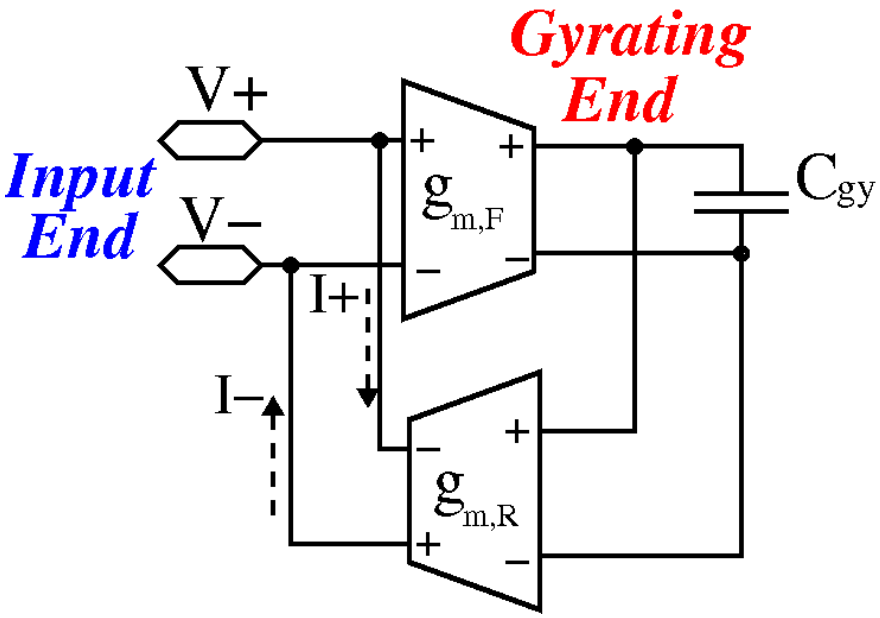


**Figure 4.3:** *Fully differential gyrator-C topology for a floating active inductor*

where $g_{m,F}$ and $g_{m,R}$ are respectively the forward and reverse transconductances, and $C_{gy}$ represents the loading capacitor. Eq. 4.1 shows that the equivalent impedance of the gyrator-C circuit is inductive. A floating active inductor can be constructed by using fully differential transconductors, as shown in Fig. 4.3. The equivalent impedance is given by

$$\begin{aligned} Z(s) &= \frac{V_+ - V_-}{I_+} = \frac{V_+ - V_-}{I_-} = \frac{V_+ - V_-}{\frac{1}{2}(I_+ - I_-)} \\ &= \frac{2(V_+ - V_-)}{\frac{1}{2}[(V_+ - V_-) \cdot g_{m,F}] \cdot \frac{1}{C_{gy}s} \cdot g_{m,R}} \\ &= \frac{4C_{gy} \cdot s}{g_{m,F} \cdot g_{m,R}}, \end{aligned} \tag{4.2}$$

Fig. 4.2 and Fig. 4.3 assume that there is infinite high resistance at the gyrating end. However, the actual VLSI circuits always have parasitics, and the parasitic resistance at the gyrating end will reduce the quality factor of the active inductor. To deal with this issue, a compensation transconductor which provides negative resistance is added at the gyrating end as shown in Fig. 4.4. In this case the equivalent resistance at the gyrating end becomes

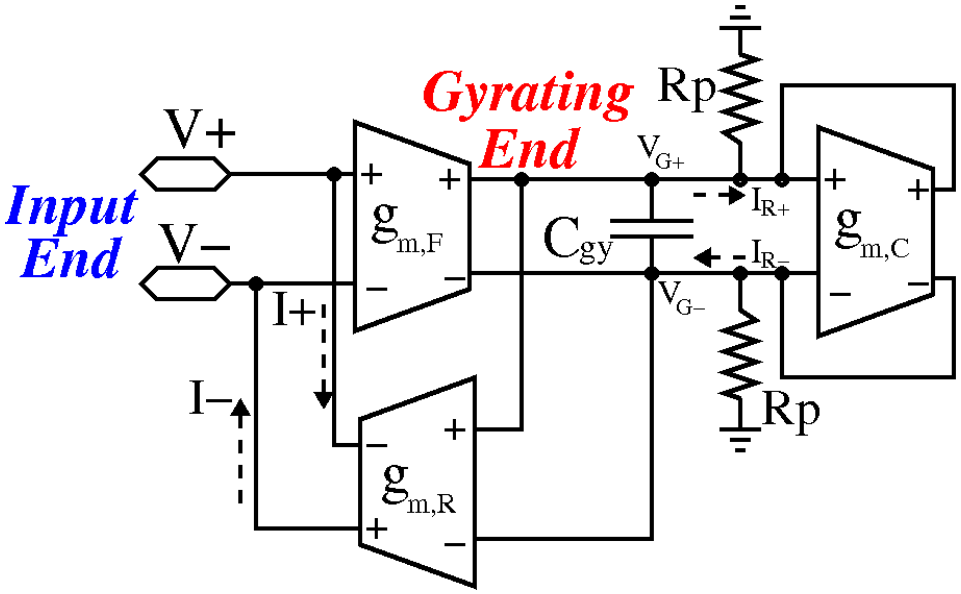


**Figure 4.4:** *A floating active inductor with parasitic compensation.*

$$\begin{aligned} R_G &= \frac{V_{G+} - V_{G-}}{I_{R+}} = \frac{V_{G+} - V_{G-}}{I_-} \\ &= \frac{V_{G+} - (-V_{G+})}{\frac{V_{G+}}{R_P} - \frac{1}{2}[V_{G+} - (-V_{G+})] \cdot g_{m,C}} = \frac{-V_{G-} - V_{G-}}{\frac{-V_{G-}}{R_P} - \frac{1}{2}[-V_{G-} - V_{G-}] \cdot g_{m,C}} \\ &= \frac{2}{\frac{1}{R_P} - g_{m,C}}, \end{aligned} \tag{4.3}$$

And thus the equivalent impedance of the active inductor is given by

$$\begin{aligned} Z(s) &= \frac{V_+ - V_-}{I_+} = \frac{V_+ - V_-}{I_-} = \frac{V_+ - V_-}{\frac{1}{2}(I_+ - I_-)} \\ &= \frac{2(V_+ - V_-)}{\frac{1}{2}[(V_+ - V_-) \cdot g_{m,F}] \cdot \frac{1}{C_{gy}s + \frac{1}{R_G}} \cdot g_{m,R}} \\ &= \frac{4C_{gy} \cdot s + 2\frac{1}{R_P} - 2g_{m,C}}{g_{m,F} \cdot g_{m,R}}, \end{aligned} \tag{4.4}$$

which is equivalent to an inductor serially connected with a variable resistor.

Based on the model in Fig. 4.3, a floating active inductor (FAI) cell is developed and its schematic is shown in Fig. 4.5. The functions and dimensions of the transistors in the schematic are summarised in Table. 4.1. The dimensions of the transistors are designed based on the con-

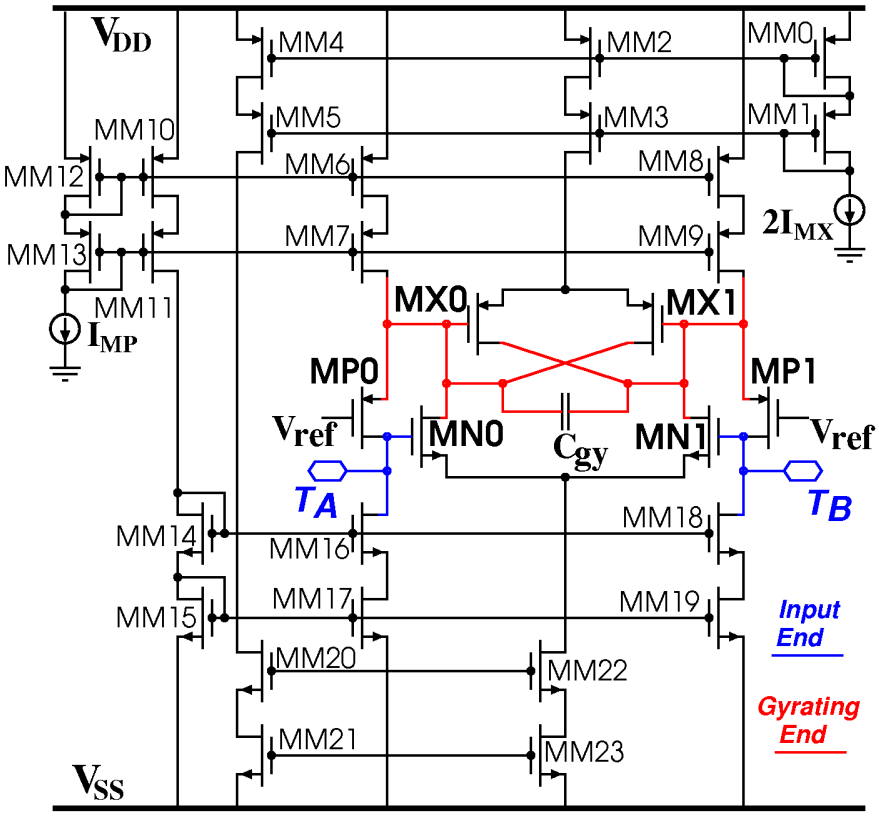


**Figure 4.5:** *Schematic of the FAI cell*

| | Transistor Type | Function | L ($\mu$m) | W ($\mu$m) |
|---|---|---|---|---|
| MN0 | NMOS | Forward transconductor | 3.5 | 100 |
| MN1 | NMOS | Forward transconductor | 3.5 | 100 |
| MP0 | PMOS | Reverse transconductor | 3.5 | 180 |
| MP1 | PMOS | Reverse transconductor | 3.5 | 180 |
| MX0 | PMOS | Compensation transconductor | 3.5 | 180 |
| MX1 | PMOS | Compensation transconductor | 3.5 | 180 |
| MM0 | PMOS | Current Mirror | 3.5 | 180 |
| MM1 | PMOS | Current Mirror | 3.5 | 180 |
| MM2 | PMOS | Current Mirror | 3.5 | 180 |
| MM3 | PMOS | Current Mirror | 3.5 | 180 |
| MM4 | PMOS | Current Mirror | 3.5 | 180 |
| MM5 | PMOS | Current Mirror | 3.5 | 180 |
| MM6 | PMOS | Current Mirror | 3.5 | 180 |
| MM7 | PMOS | Current Mirror | 3.5 | 180 |
| MM8 | PMOS | Current Mirror | 3.5 | 180 |
| MM9 | PMOS | Current Mirror | 3.5 | 180 |
| MM10 | PMOS | Current Mirror | 3.5 | 180 |
| MM11 | PMOS | Current Mirror | 3.5 | 180 |
| MM12 | PMOS | Current Mirror | 3.5 | 180 |
| MM13 | PMOS | Current Mirror | 3.5 | 180 |
| MM14 | NMOS | Current Mirror | 3.5 | 100 |
| MM15 | NMOS | Current Mirror | 3.5 | 100 |
| MM16 | NMOS | Current Mirror | 3.5 | 100 |
| MM17 | NMOS | Current Mirror | 3.5 | 100 |
| MM18 | NMOS | Current Mirror | 3.5 | 100 |
| MM19 | NMOS | Current Mirror | 3.5 | 100 |
| MM20 | NMOS | Current Mirror | 3.5 | 100 |
| MM21 | NMOS | Current Mirror | 3.5 | 100 |
| MM22 | NMOS | Current Mirror | 3.5 | 100 |
| MM23 | NMOS | Current Mirror | 3.5 | 100 |

**Table 4.1:** *Functions and dimensions of the transistors in FAI*

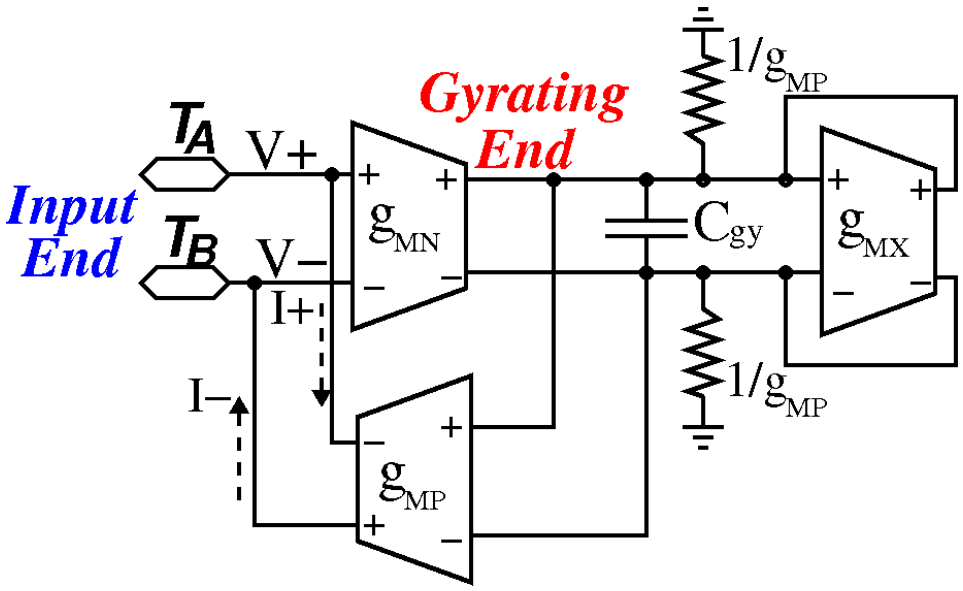


**Figure 4.6:** *Simplified representation of the FAI schematic.*

siderations of the operation mode, the noise and the mismatches factors, which will respectively be explained in details in the following.

The core components of the FAI cell are three differential transistor pairs: the NMOS transistor pair MN (MN0 and MN1) which functions as the forward tranconductor, the PMOS transistor pair MP (MP0 and MP1) which functions as the reverse transconductor, and the PMOS transistor pair MX (MX0 and MX1) which functions as the compensation transconductor. The other transistors in Fig. 4.5 are components of the current mirrors. Notably, while the differential pair MN and MX are based on the common-source structure, the differential pair MP is based on the common-gate structure. The sources of the differential pair MP add resistive loading at the gyrating end, as shown in Fig. 4.6. Therefore the equivalent impedance of the FAI is given by

$$Z(s) = \frac{4C_{gy} \cdot s + 2(g_{MP} - g_{MX})}{g_{MN} \cdot g_{MP}}. \tag{4.5}$$

The reason for using the common-gate structure for the MP pair is reflected by Eq. 4.5. The sources of the MP pair at the gyrating end provide the FAI with a constant resistance, which is to be cancelled by the variable equivalent input resistance of the MX pair. Thus the variable degree of cancellation between the resistance of MP and MX contributes to the quality factor tunability of the FAI cell.

The transistors in Fig. 4.5 are designed to operate in weak inversion mode so that the gate-source

transconductance is proportional to the transistor DC drain current:

$$g_m \approx \frac{1}{nU_T} \cdot I_D, \tag{4.6}$$

where $n$ is the slope factor, $U_T$ is the thermal voltage and $I_D$ is the transistor DC drain current [111]. The bulks of all the NMOS transistors in Fig. 4.5 are connected to $V_{SS}$ while the bulks of all the PMOS transistors are connected to $V_{DD}$. Consequently, the source-bulk transconductance due to body effect does not influence the transconductance of the MN and MX pairs where the transistor sources and bulks are connected together. By contrast, the MP transistor pair has separate source connections and thus the source-bulk transconductance should be considered. In weak inversion, the source-bulk transconductance is also approximately proportional to the transistor DC drain current [111]:

$$g_{mb} \approx \frac{n-1}{nU_T} \cdot I_D, \tag{4.7}$$

Thus the transconductance in Eq. 4.5 can be represented using currents[1]:

$$\begin{cases} g_{MX} = \frac{1}{nU_T} I_{MX}; \\ g_{MN} = \frac{1}{nU_T} I_{MX}; \\ g_{MP} = \frac{1}{nU_T} I_{MP} + \frac{n-1}{nU_T} I_{MP} = \frac{1}{U_T} I_{MP}. \end{cases} \tag{4.8}$$

Therefore Eq. 4.5 is rewritten as

$$Z(s) = \frac{4C_{gy}nU_T^2 \cdot s + 2U_T(nI_{MP} - I_{MX})}{I_{MP} \cdot I_{MX}}. \tag{4.9}$$

As mentioned above, the FAI cell can be modelled as an inductor in series with a resistor, the values of which are given by

$$\begin{cases} L_{FAI} = \frac{4C_{gy}nU_T^2}{I_{MP}I_{MX}} \\ R_{FAI} = \frac{2U_T(nI_{MP} - I_{MX})}{I_{MP}I_{MX}}. \end{cases} \tag{4.10}$$

The quality factor of FAI is adjustable by varying the difference between $nI_{MP}$ and $I_{MX}$. Eq. 4.10 indicates that the inductance of the FAI also varies when its quality factor is tuned; as will be shown in Section. 4.2, the correlation between the FAI inductance and quality factor fits

[1] As shown in Fig. 4.5 the currents in MN and MX are made equal through the current mirrors.

well with the relationship equation in Eq. 3.10 which is the basis for CF tuning of the cochlea filter.

Furthermore, the FAI becomes a pure inductor when $nI_{MP}$ equals $I_{MX}$, in which case the inductance becomes $\frac{4C_{gy}U_T^2}{I_{MP}^2}$. In the following text, the $I_{MP}$ is referred to as 'static current' which determines the maximum inductance of the FAI. Besides, the $I_{MX}$ is referred to as 'tuning current' and the ratio between $I_{MX}$ and $I_{MP}$ is called 'tuning factor' which is denoted as $x$ and determines the quality factor of the FAI. By using tuning factor $x$, Eq. 4.10 is rewritten as

$$\begin{cases} L_{FAI} = \frac{4C_{gy}nU_T^2}{x \cdot I_{MP}^2} \\ R_{FAI} = \frac{2U_T(n-x)}{x \cdot I_{MP}}. \end{cases} \tag{4.11}$$

As introduced above, the transistors in the FAI operate in weak inversion mode. This design option is based on two aspects of considerations. Firstly, as Eq. 4.6 tells, the transconductance is approximately proportional to DC current in weak inversion, and the FAI impedance can be concisely represented by the transistor current as shown in Eq. 4.10 and Eq. 4.11. In other words, the relationship between the FAI impedance and circuit biasing current is straightforward, which highly simplifies the FAI tuning. Secondly, as will be shown next, the transistor in strong inversion is not able to achieve the full range of audio frequencies. The mode of transistor operation is dependent on the inversion coefficient which is determined by

$$I_C = \frac{I_D}{I_{spec}} \text{ [112]}. \tag{4.12}$$

$I_{spec}$ is the specific current defined as

$$I_{spec} = 2n\beta U_T^2. \tag{4.13}$$

$\beta$ is the transistor transconductance parameter expressed as

$$\beta = \mu C_{ox} \frac{W}{L}, \tag{4.14}$$

where $\mu$ and $C_{ox}$ are process parameters which respectively refer to the the mobility constant and oxide capacitance per unit area; $W$ and $L$ are transistor channel width and length [112]. As defined in [112], the transistor operates in strong inversion when the inversion coefficient $I_C \gg 1$, and operates in weak inversion when $I_C \ll 1$. Besides, for transistors operating in strong inversion, the relationship between transistor gate-source transconductance and DC

| Power supply (V) | 3.3 |
|---|---|
| $\mu C_{ox}$ ($\mu A/V^2$) | NMOS:170; PMOS:58 |
| $C_{ox}$ (fF/$\mu$m$^2$) | 4.54 |
| n | $\approx$1.25 |
| $V_{TH}$ (V) | NMOS:0.59; PMOS:0.72 |
| ${K_F}^*$ | NMOS:$2.17e^{-26}$; PMOS: $3.396e^{-26}$ |
| ${A_F}^*$ | NMOS:1.507; PMOS: 1.461 |
| ${A_{VT}}^*$ ($mV \cdot \mu m$) | NMOS:9.5; PMOS: 14.5 |
| ${A_K}^*$ ($\% \cdot \mu m$) | NMOS:0.7; PMOS: 1.0 |

* $K_F$ and $A_F$ are noise parameters; $A_{VT}$ and $A_K$ are matching parameters;

**Table 4.2:** *Parameters in AMS 0.35 $\mu$m process*

drain current is given by

$$g_m \approx \beta(V_{GS} - V_{TH}) = \sqrt{2\beta I_D}\ [113]. \tag{4.15}$$

where $V_{GS}$ is the DC gate-source voltage and $V_{TH}$ is the threshold voltage [113]. Assume that the minimum value for $I_C$ is 10 for strong inversion, and thus the following expression stands:

$$g_m \geq \sqrt{40n}\beta U_T. \tag{4.16}$$

And based on Eq. 4.5, the inductance of the FAI is constrained by the following expression

$$L_{FAI} \leq \frac{C_{gy}}{10n\beta^2 U_T^2}. \tag{4.17}$$

Assume that the capacitors in the RLC ladders have similar capacitance as $C_{gy}$, and thus the estimated characteristic frequency of the RLC ladder is given by

$$\omega_c \simeq \frac{1}{\sqrt{L_{FAI}C_{gy}}} \geq \frac{\sqrt{10n}\beta U_T}{C_{gy}}. \tag{4.18}$$

Besides, based on Eq. 4.16 and Eq. 4.5, the following expression is derived:

$$\omega_c \simeq \frac{1}{\sqrt{L_{FAI}C_{gy}}} = \frac{\beta(V_{GS} - V_{TH})}{2C_{gy}} \leq \frac{\beta(V_{DD} - V_{SS} - V_{TH})}{2C_{gy}}. \tag{4.19}$$

The AustriaMicroSystems (AMS) 0.35 $\mu$m process is used to fabricate the chip, and its process

parameter values are summarised in Table. 4.2. The thermal voltage $U_T$ is given by

$$U_T = \frac{kT}{q}, \tag{4.20}$$

where $k$ is the Boltzmann constant, $T$ is thermal temperature and $q$ is electron charge; thus the approximate value for $U_T$ is thus 26 mV. The frequency limits in Eq. 4.17 and Eq. 4.19 are thereby rewritten as

$$\begin{cases} \text{For NMOS: } 1.56 \times 10^{-5} \cdot \frac{W}{L \cdot C_{gy}} \leq \omega_c \leq 2.3 \times 10^{-4} \frac{W}{L \cdot C_{gy}}; \\ \text{For PMOS: } 5.33 \times 10^{-6} \cdot \frac{W}{L \cdot C_{gy}} \leq \omega_c \leq 7.5 \times 10^{-5} \frac{W}{L \cdot C_{gy}}. \end{cases} \tag{4.21}$$

Eq. 4.21 indicates that only one order of frequency range can be covered, which is fairly limited compared with the $20 \sim 20000$ Hz audio frequency range. By contrast, for the transistors operating in weak inversion, the transconductance is dependent only on DC current and the audio frequency range can be covered by scaling down or up the currents.

### 4.1.3 Analysis of Circuit Non-idealities in the FAI cell

Fig. 4.6 is the simplified representation of the FAI schematic which does not include any circuit non-idealities. Naturally, there are always parasitics, noise and mismatches in the real circuits, which make the FAI operation deviate from what Eq. 4.10 predicts.

#### 4.1.3.1 Parasitics

The major parasitics in the FAI circuits are parasitic resistances and parasitic capacitances. The transconductors shown in Fig. 4.6 are ideal ones which have infinitely high input impedance and output impedance. Nevertheless, the output impedance of the differential pairs in Fig. 4.5 are determined by the drain-source resistance of the transistors which are never infinite due to the transistor channel modulation effect [111]. Moreover, the differential pairs MN and MX do not have infinitely high input impedance due to the parasitic capacitance at the transistor gate, neither does the differential pair MP due to the parasitic capacitance at the transistor source. Taking these parasitics into consideration, the FAI model is redrawn in Fig. 4.7. In weak inversion, the transistor parasitic capacitances are dominated by the gate-bulk capacitances [112], which is given by

$$C_P \approx C_{GB} \approx \frac{n-1}{n} C_{ox} W L. \tag{4.22}$$

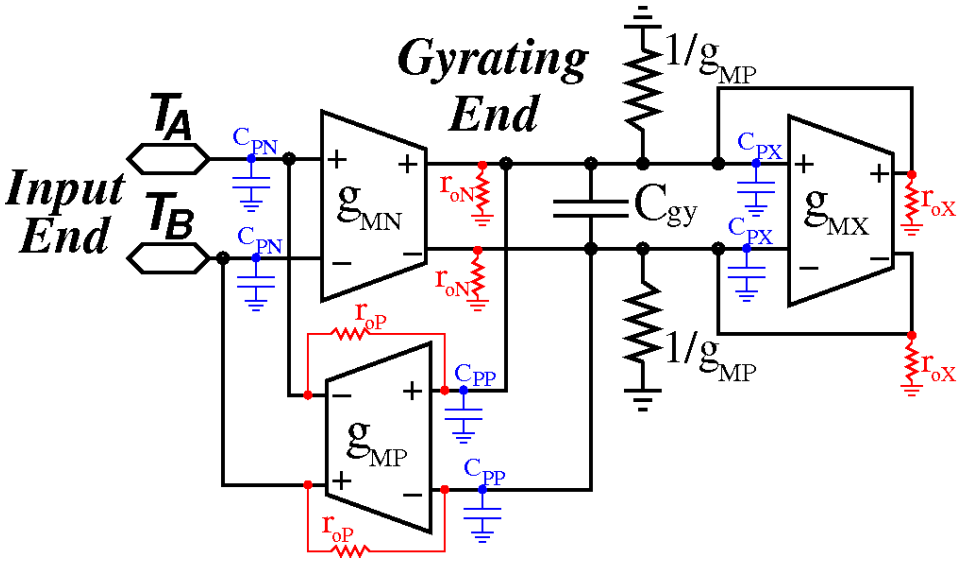


**Figure 4.7:** *Simplified representation of the FAI schematic considering parasitics.*

Based on the the transistor dimensions in Table. 4.1 and the process parameters in Table. 4.2, $C_{PX}$ and $C_{PP}$ are in the region of 0.572 pF while $C_{PN}$ is about 0.318 pF. The parasitic capacitances $C_{PX}$ and $C_{PP}$ are in parallel with the loading capacitance $C_{gy}$ and thus can be combined with $C_{gy}$. By contrast, $C_{PN}$ adds capacitive impedance to the FAI.

The parasitic resistances in the FAI are due to the transistor output (drain-source) resistance which is given by

$$r_o = \frac{1}{\lambda I_D}; \tag{4.23}$$

where $\lambda$ is the channel length modulation factor. The output resistances of the MN and MX pairs ($r_{oN}$ and $r_{oX}$) are in parallel with the source resistance of the MP pair ($1/g_{MP}$). Therefore, $r_{oN}$ and $r_{oX}$ are negligible as long as they are much higher than $1/g_{MP}$ (at least two-order higher). In fact, the ratio between them is given by

$$\frac{r_{oN}}{\frac{1}{g_{MP}}} = \frac{r_{oX}}{\frac{1}{g_{MP}}} = \frac{1}{\lambda I_{MX}} \cdot \frac{I_{MP}}{nU_T} = \frac{1}{\lambda \cdot x \cdot nU_T}. \tag{4.24}$$

The typical value of $\lambda$ is in the range of 0.005$\sim$0.05 $V^{-1}$ [114]. Assuming that the $\lambda$ is as large as 0.05 $V^{-1}$, the ratio in Eq. 4.24 becomes

$$\frac{r_{oN}}{\frac{1}{g_{MP}}} = \frac{r_{oX}}{\frac{1}{g_{MP}}} = \frac{615}{x}. \tag{4.25}$$

Furthermore, the tuning factor $x$ has to be smaller than the slope factor $n$ to avoid negative

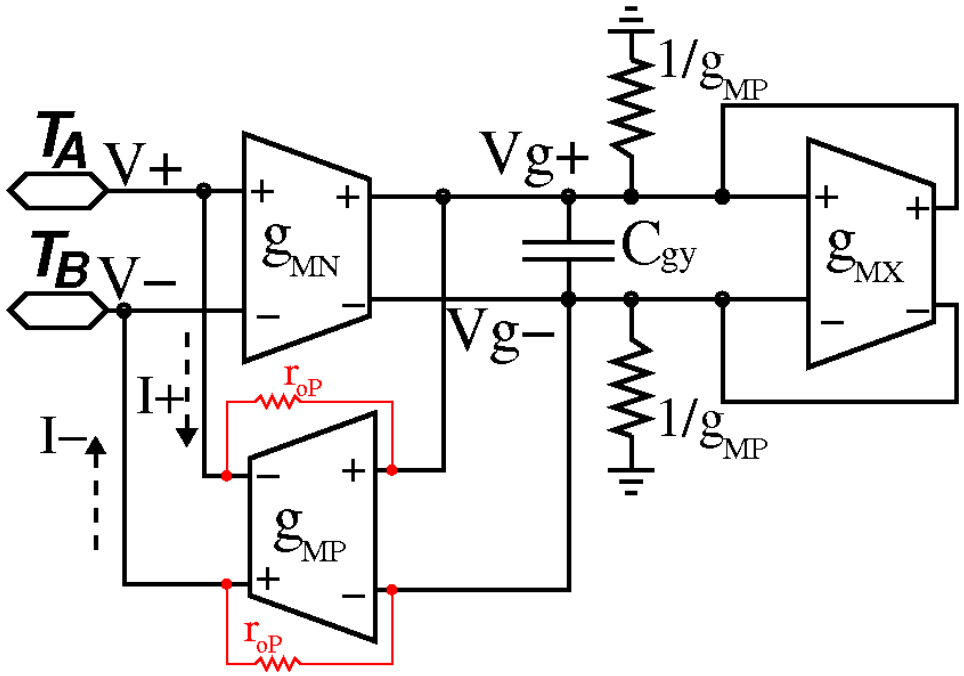


**Figure 4.8:** *Simplified representation of the FAI schematic considering only parasitic resistance of the MP pair.*

resistance in the FAI, and thus the minimum value for the resistance ratio in Eq. 4.25 is in the region of 500. Consequently, $r_{oN}$ and $r_{oX}$ are negligible.

The effects of parasitic resistance $r_{oP}$ on the FAI impedance is more complex. Considering only $r_{oP}$, as shown in Fig. 4.8, the following equations stand :

$$\begin{cases} (V_+ - V_-)g_{MN} + \frac{(V_+ - V_-) - (Vg_+ - Vg_-)}{r_{oP}} = (Vg_+ - Vg_-)(2C_{gy}s + g_{MP} - g_{MX}); \\ I_- + I_+ = (Vg_+ - Vg_-)g_{MP} + [(V_+ - V_-) - (Vg_+ - Vg_-)]/r_{op}; \\ I_+ = I_-. \end{cases} \quad (4.26)$$

And thus the equivalent impedance is given by

$$\frac{1}{Z(s)} = \frac{I_+}{V_+ - V_-} = \frac{I_-}{V_+ - V_-} = \frac{(g_{MN} + 1/r_{oP})(g_{MP} - 1/r_{op})}{4C_{gy}s + 2(g_{MP} - g_{MX}) + 2/r_{oP}} + 1/2r_{op}. \quad (4.27)$$

As explained above the transistor source-gate resistance is much higher than the transconductance, and thus $1/r_{oP}$ is negligible compared with $g_{MN}$ and $g_{MP}$. Thus Eq. 4.27 is rewritten as

$$\frac{1}{Z(s)} = \frac{g_{MN}g_{MP}}{4C_{gy}s + 2(g_{MP} - g_{MX}) + 2/r_{oP}} + 1/2r_{op}. \quad (4.28)$$

Therefore the equivalent model of the FAI with parasitic resistance and capacitance is illustrated

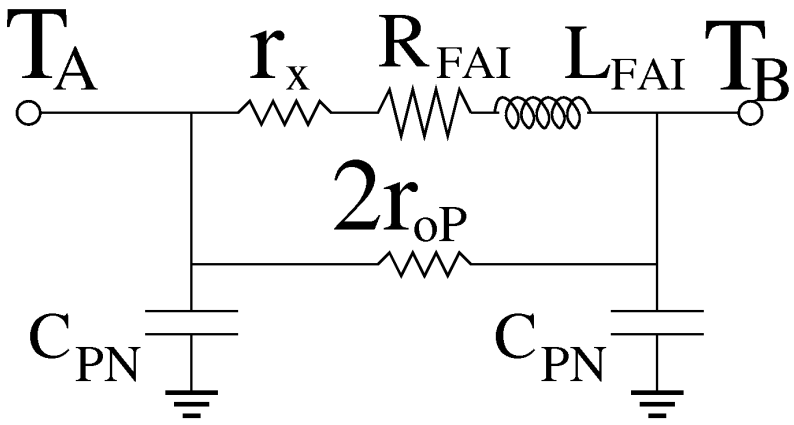


**Figure 4.9:** *The FAI model considering parasitics. ($r_x$ is equal to $2/g_{MN}g_{MP}r_{oP}$ as given by Eq. 4.28.)*

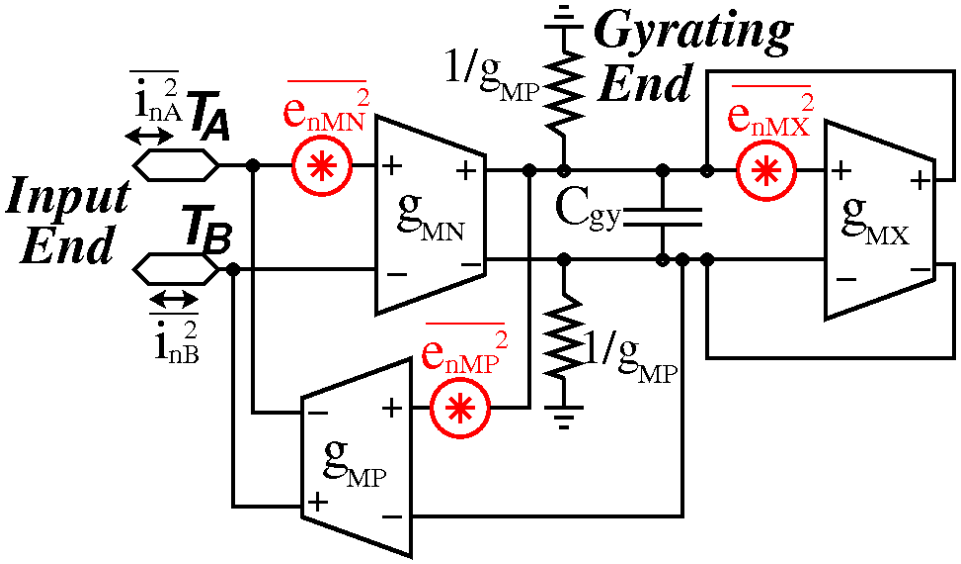


**Figure 4.10:** *Simplified representation of the FAI schematic considering noise.*

in Fig. 4.9.

#### 4.1.3.2 Noise

The noise model of the FAI is illustrated in Fig. 4.10, where $\overline{e_{nMN}^2}$, $\overline{e_{nMP}^2}$ and $\overline{e_{nMX}^2}$ are gate-referred voltage noise sources of the corresponding transistor pairs. Based on Fig. 4.10, the noise currents at the input end can be derived:

$$\overline{i_{nA}^2(\omega)} = \overline{i_{nB}^2(\omega)} = \frac{1}{2} \cdot g_{MP}^2 [\overline{e_{nMP}^2} + \frac{g_{MX}^2 \overline{e_{nMX}^2} + g_{MN}^2 \overline{e_{nMN}^2}}{(g_{MX} - g_{MP})^2 + 4\omega^2 C_{gy}^2}] \tag{4.29}$$

The major types of noise in MOS transistors are the thermal noise and the flicker noise [111, 112, 114]. The thermal noise is also called white noise which has constant noise power spectral density (PSD) across different frequencies. By contrast, the flicker noise is also called pink noise or $1/f$ noise which has reciprocal relationship between noise PSD and frequency. The relative dominance between these two types of noise is reflected by the transistor corner frequency. The transistor corner frequency is defined as the frequency at which the PSDs of these two types of noise equal with each other. According to the noise model provided by the foundry, the corner frequency can be expressed as a function of current and transistor dimensions:

$$\begin{cases} \text{For NMOS: } \omega_{corner} = \frac{3\pi K_F I_D^{A_F-1}}{4qC_{ox}L^2}; \\ \text{For PMOS: } \omega_{corner} = \frac{3\pi K_F I_D^{A_F-1}}{4qC_{ox}WL}, \end{cases} \tag{4.30}$$

where $K_F$ and $A_F$ are flicker noise parameters and the typical value of $A_F$ is between 1 and 2. The flicker noise will be dominant if the CF of circuits is lower than $\omega_{corner}$, while the thermal noise will be dominant vice versa. For ease of analysis, the transistor dimensions in the FAI are optimised such that $\omega_{corner}$ is always smaller than the CF of the cochlea filter. Optimisation method for the transistor dimensions will be elaborated in Section. 4.3.2.

According to the noise model provided by the foundry, the PSD of thermal noise current in a MOS transistor is given by

$$\overline{i_n^2(\omega)} = \frac{8kT}{3}(g_m + g_{mb} + g_{ds}), \tag{4.31}$$

where $g_m$ is the gate-source transconductance, $g_{mb}$ is the source-bulk transconductance due to body effect and $g_{ds}$ is the drain-source conductance which is the reciprocal of drain-source resistance and is negligible compared with $g_m$ as analysed above. By combining with Eq. 4.6 and Eq. 4.7, Eq.4.31 can be rewritten as:

$$\overline{i_n^2(\omega)} = \frac{8kTI_D}{3U_T}. \tag{4.32}$$

Consequently, the gate-referred noise sources are derived as

$$\begin{cases} \overline{e_{nMN}^2} = \frac{16kTI_{MX}}{3U_T} \cdot \frac{1}{g_{MN}^2}; \\ \overline{e_{nMX}^2} = \frac{16kTI_{MX}}{3U_T} \cdot \frac{1}{g_{MX}^2}; \\ \overline{e_{nMP}^2} = \frac{16kTI_{MP}}{3U_T} \cdot |\frac{j\omega C_{gy} - \frac{g_{MX}}{2}}{\frac{g_{MP}}{2} + (j\omega C_{gy} - \frac{g_{MX}}{2})}|^2 \cdot \frac{1}{g_{MP}^2} = \frac{16kTI_{MP}}{3U_T g_{MP}^2} \cdot \frac{4C_{gy}^2\omega^2 + g_{MX}^2}{(g_{MX} - g_{MP})^2 + 4C_{gy}^2\omega^2}. \end{cases} \tag{4.33}$$

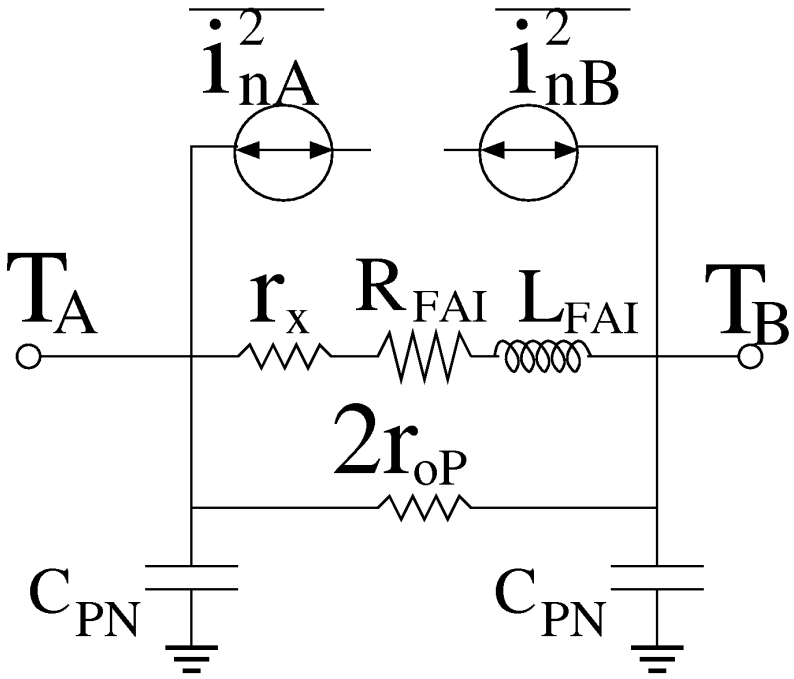


**Figure 4.11:** *FAI model considering noise and parasitics.*

Note that the MP pair receives source degeneration from $C_{gy}$ and MX pair, and thus its gate-referred noise has the modification term. Eq. 4.29 is thus rewritten as:

$$\begin{aligned}\overline{i_{nA}^2(\omega)} = \quad \overline{i_{nB}^2(\omega)} \quad &= \frac{8kT}{3U_T} \cdot \frac{(4C_{gy}^2\omega^2 + g_{MX}^2)I_{MP} + 2g_{MP}^2 I_{MX}}{(g_{MX} - g_{MP})^2 + 4C_{gy}^2\omega^2} \\ &= \frac{8kTI_{MP}}{3U_T} \cdot \frac{x^2 + 2n^2x + \frac{4C_{gy}^2 n^2 U_T^2 \omega^2}{I_{MP}^2}}{(x-n)^2 + \frac{4C_{gy}^2 n^2 U_T^2 \omega^2}{I_{MP}^2}}.\end{aligned} \tag{4.34}$$

The FAI model considering noise in addition to parasitics is illustrated in Fig. 4.11.

#### 4.1.3.3 Mismatch

Naturally, the operation of FAI is subject to transistor mismatch which causes circuit offsets. The mismatches can be classified into two categories: horizontal and vertical, according to different causes and consequences. Horizontal mismatch is the mismatch between transistors in differential pairs MP0-MP1, MN0-MN1 and MX0-MX1 which results in a DC current in the FAI running from port TA to TB. Taking the differential pair MN as example, as shown in Fig. 4.12, the mismatch between MN0 and MN1 results in a DC current running from port TA to port TB. The standard deviation of transistor current is given by

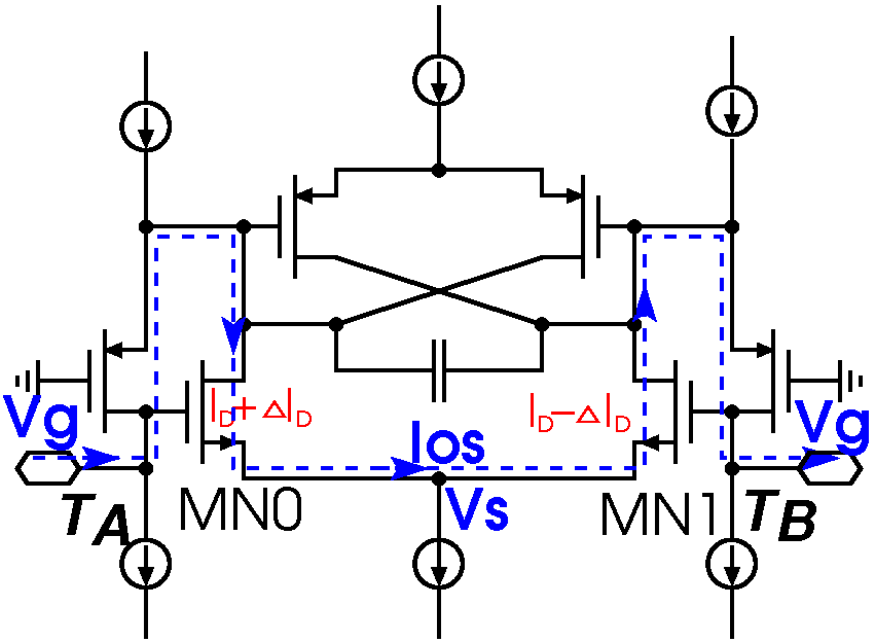


**Figure 4.12:** *FAI horizontal mismatch analysis*

$$\sigma(\frac{\Delta I_D}{I_D}) = \sqrt{\sigma^2(\frac{\Delta\beta}{\beta}) + (\frac{g_m}{I_D})^2\sigma^2(\Delta V_{th})}, \tag{4.35}$$

where $V_{th}$ is threshold voltage, $\frac{\Delta\beta}{\beta}$ is gain factor variation and $\Delta V_{th}$ is threshold voltage variation [112]. The standard deviation of these variations are dependent on transistor dimensions:

$$\begin{cases} \sigma(\frac{\Delta\beta}{\beta}) = \frac{A_K}{\sqrt{WL}}; \\ \sigma(\Delta V_{th}) = \frac{A_{VT}}{\sqrt{WL}}. \end{cases} \tag{4.36}$$

Based on Eq. 4.36, the $4\sigma$ limit of the offset current is given by

$$4\sigma(\frac{\Delta I_D}{I_D}) = 4\sqrt{\frac{{A_K}^2}{WL} + (\frac{1}{nU_T})^2\frac{A_{VT}}{WL}}, \tag{4.37}$$

whose value can be calculated using the matching parameters listed in Table. 4.2 and the transistor dimensions listed in Table. 4.1:

$$\begin{cases} \text{NMOS: } 4\sigma(\frac{\Delta I_D}{I_D}) = 6.25\%; \\ \text{PMOS: } 4\sigma(\frac{\Delta I_D}{I_D}) = 7.11\%; \end{cases} \tag{4.38}$$

The total offset currents from horizontal mismatch also include the mismatch from MP and

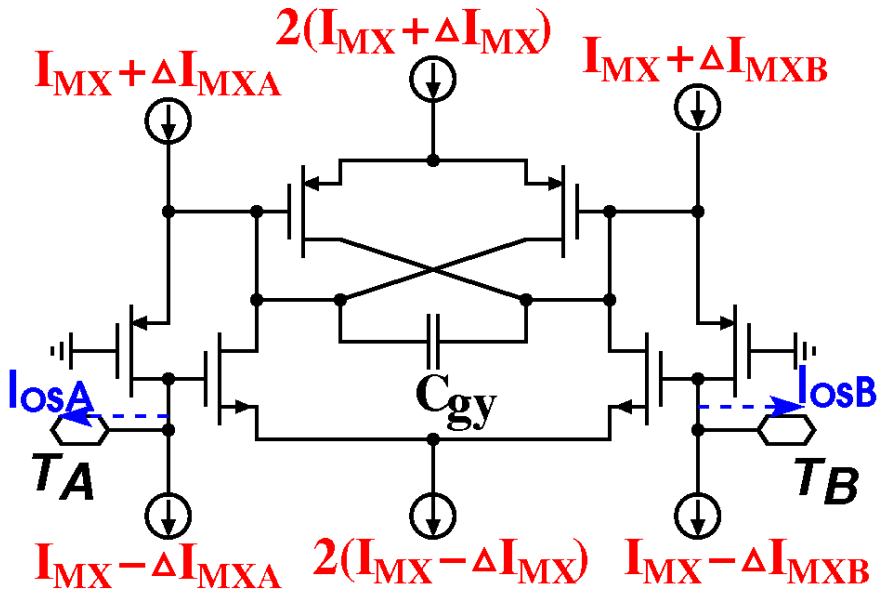


**Figure 4.13:** *FAI vertical mismatch analysis*

MX. And therefore the worst case horizontal mismatch is expressed as:

$$I_{osH} \leq 0.0711(I_{MP} + 2I_{MX}) \tag{4.39}$$

The vertical mismatch refers to the mismatch between the current sources in the upper side and the current sinks in the lower side. As shown in Fig. 4.13, the difference between the currents in the upper and lower side will flow out of the FAI through TA and TB. These two offset currents and their worst case values can be written as:

$$I_{osVA(B)} = 2\Delta I_{MPA(B)} + 2\Delta I_{MX} \leq 0.0711(2I_{MP} + 2I_{MX}). \tag{4.40}$$

Fig. 4.14 illustrates the FAI model considering the mismatch-induced offset currents in addition to noise and parasitics.

## 4.2 Cochlea Filter Design Based on FAI

According to Fig. 4.1(b), the RLC ladders based on the FAI cell are respectively built for the $2^{nd}$-order BPF, the $2^{nd}$-order LPF, and the $5^{th}$-order EF. The cascaded cochlea filter channel is shown in Fig. 4.15, which employs the fully differential architecture. The BPF is built by

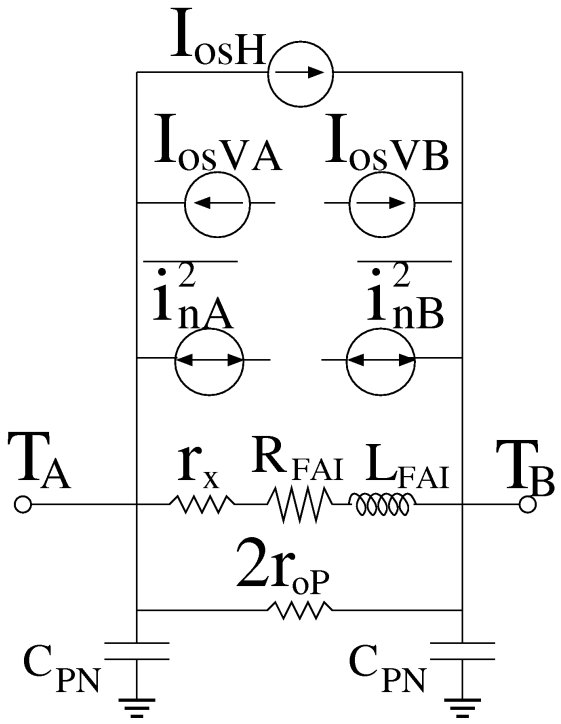


**Figure 4.14:** *FAI model considering the mismatch-induced offset currents in addition to noise and parasitics.*

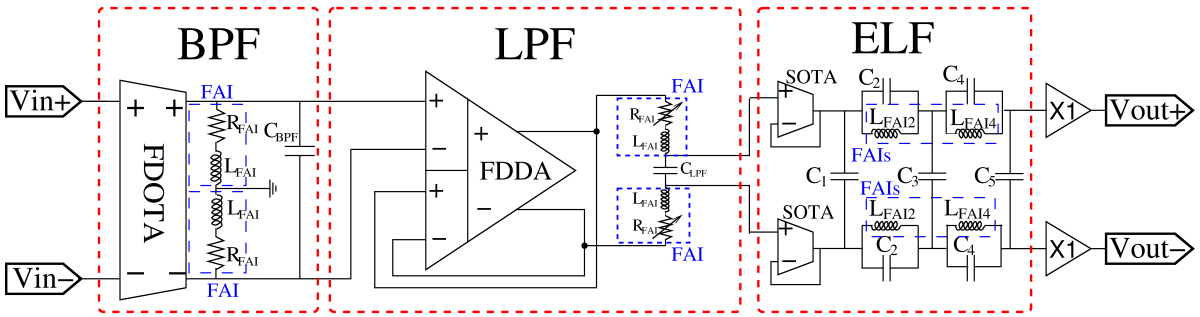


**Figure 4.15:** *Schematic of the cochlear filter channel*

loading a fully differential operational transconductance amplifier (FDOTA: Fig. 4.16) with two FAIs and a capacitor; the LPF is built upon FAI-Capacitor voltage divider with a fully differential difference amplifier (FDDA: Fig. 4.17) as input buffer; the ELF is built according to the filter design handbook [98] with single-end OTAs (OTA: Fig. 4.18) providing equivalent source resistances. There are totally eight FAIs in one channel; their $I_{MP}$ currents are made equal through current mirrors while their $I_{MX}$ currents are set separately. The denotations of the currents in the cochlea filter are listed in Table. 4.3. Besides, the FAIs in the BPF and LPF are all loaded with equal capacitance $C_0$, while $C_{BPF}$ is set as $1.2C_0$ and $C_{LPF}$ is set as $C_0$. More specifically, the value of $C_0$ is set as 5 pF. Besides, both $C_{BPF}$ and $C_{LPF}$ include the parasitic capacitances of the FAI as analysed in Section. 4.1.3.1.

| | BPF | LPF | EF |
|---|---|---|---|
| FAI static current ($I_{MP}$) | $I_{st}$ | $I_{st}$ | $I_{st}$ |
| FAI tuning current ($I_{MX}$) | $I_{BPF}$ | $I_{LPF}$ | $I_{ELF}$ |
| FDOTA DC current | $I_{FO}$ | - | - |
| FDDA DC current | - | $I_{FA}$ | - |
| SOTA DC current | - | - | $I_{SO}$ |

**Table 4.3:** *Denotions of currents in the cochlea filter*

### 4.2.1 BPF

The schematic of the FDOTA used in the BPF is illustrated in Fig. 4.16. The transistors MP0-1 form the differential pair and PMOS transistors are used to reduce flicker noise. The cascode transistors MP2-3 significantly increase the output resistance so that approximately all of the FDOTA output currents flow through the loaded FAIs. The transistors MP4-9 and MN0-5 respectively form the cascode current source and sink to bias the circuits. The transistors MP10-13 form the common-mode feedback (CMFB) so that the DC outputs of the FDOTA are stabilized at $V_{ref}$.

The dimensions of the transistors in Fig. 4.16 are listed in Table. 4.4. Long lengths of 3.5 $\mu$m are applied for all transistors to reduce channel modulation effects so that the transistor output resistances can be neglected. The differential pair MP0-1 are designed to be operating in weak inversion mode based on the same considerations as explained in the FAI design. The MP2-9 and MN0-5 are operating in moderate or strong inversion which has smaller transconductance and thus their contributions to the input-referred of FDOTA are negligible compared with MP0-1 [115]. Consequently, the MP0-1 has much higher aspect ratio than MP2-9 and

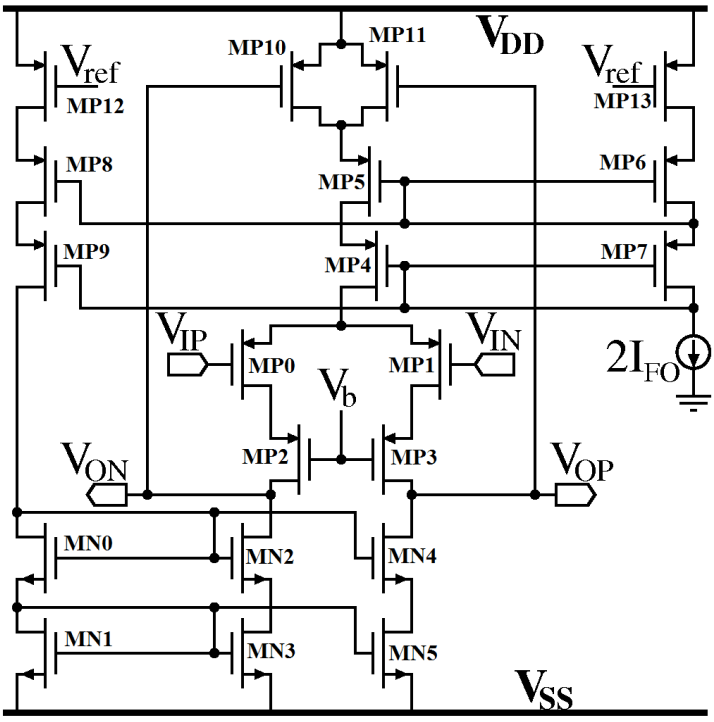


**Figure 4.16:** *Schematic of the fully differential OTA*

| | Transistor Type | Function | L ($\mu$m) | W ($\mu$m) |
|---|---|---|---|---|
| MP0-1 | PMOS | Differential Pair | 3.5 | 180 |
| MP2-3 | PMOS | Cascode | 3.5 | 22.5 |
| MP4-5 | PMOS | Current Mirror | 3.5 | 45 |
| MP6-9 | PMOS | Current Mirror | 3.5 | 22.5 |
| MN0-5 | NMOS | Current Mirror | 3.5 | 12.5 |
| MP10-13 | PMOS | Common-mode Feedback | 3.5 | 0.4 |

**Table 4.4:** *Functions and dimensions of the transistors in FDOTA*

MN0-5. MP10-13 are designed to have narrow width so that the CMFB has a high loop gain to effectively stabilise the DC output level of the FDOTA.

The transfer function of the BPF is given by

$$\begin{aligned} H_{BPF}(s) &= \frac{g_{m,FDOTA}}{2} \cdot \frac{2(L_{FAI}s + R_{FAI})}{2L_{FAI}C_{BPF}s^2 + 2R_{FAI}C_{BPF}s + 1} \\ &= \frac{I_{FO}}{2nU_TC_{BPF}} \cdot \frac{s + \frac{R_{FAI}}{L_{FAI}}}{s^2 + \frac{R_{FAI}}{L_{FAI}}s + \frac{1}{2L_{FAI}C_{BPF}}} \\ &= \frac{5I_{FO}}{12nU_TC_0} \cdot \frac{s + \frac{nI_{st} - I_{BPF}}{2nUTC_0}}{s^2 + \frac{nI_{st} - I_{BPF}}{2nUTC_0}s + \frac{5I_{st}I_{BPF}}{48nU_T^2C_0^2}}. \end{aligned} \quad (4.41)$$

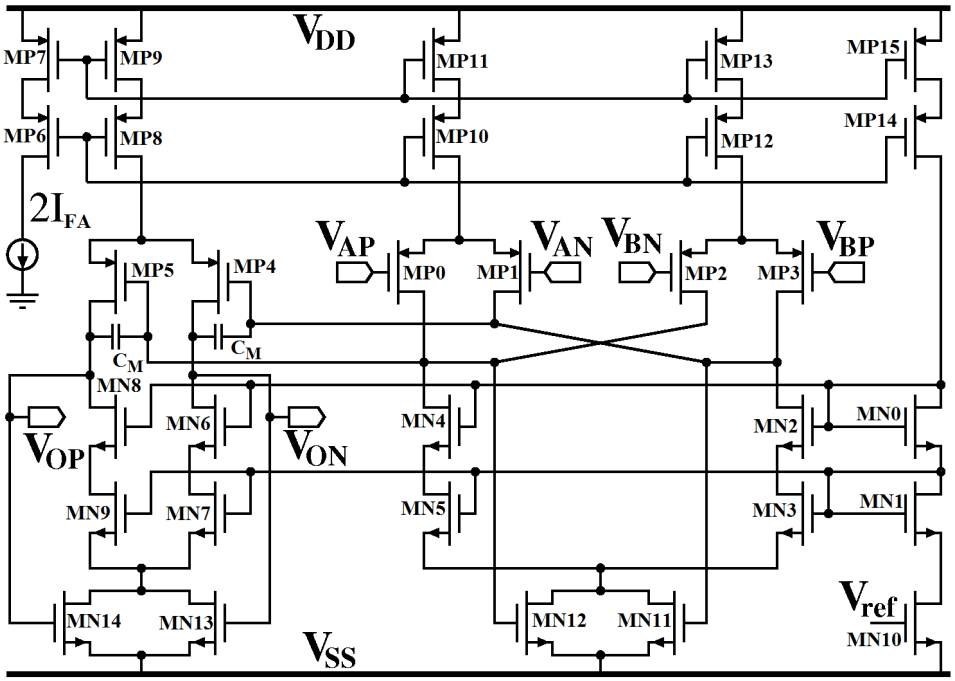


**Figure 4.17:** *Schematic of the FDDA*

By setting $I_{FO} = 2I_{st}$ and $I_{BPF} = I_{st}$, the following is derived:

$$H_{BPF}(s) = A_0 \cdot \frac{s + \frac{\omega_{BP}}{Q_{BP}}}{s^2 + \frac{\omega_{BP}}{Q_{BP}} s + \omega_{BP}^2}, \tag{4.42}$$

where

$$\begin{cases} A_0 = \frac{5I_{st}}{6nU_T C_0}; \\ \omega_{BP} = \frac{\sqrt{\frac{5}{48}} nI_{st}}{nU_T C_0}; \\ Q_{BP} = \frac{\sqrt{\frac{5}{12}} n}{n-1}. \end{cases} \tag{4.43}$$

Since the slope factor in the AMS 0.35 $\mu$m process is about 1.25, the following is derived:

$$\begin{cases} A_0 \approx 2.31\omega_{BP}; \\ Q_{BP} \approx 2.89, \end{cases} \tag{4.44}$$

which is in accordance with the settings for the cochlea filter model (Eq. 3.8).

### 4.2.2 LPF

The schematic of the FDDA used in the LPF is illustrated in Fig. 4.17. The FDDA is based on the two-stage configuration: the transistors MP0-3 form the dual differential pairs of the

input stage and the transistors MP4-5 form the differential pairs of the output stage. MP6-15 and MN0-9 are used to build the current mirrors and MN10-14 provide the common-mode feedback function. The $C_M$s are Miller compensation capacitors. The values of the $C_M$s are set as 0.5 pF, which are enough to keep the phase margin of the FDDA at 45° according to the simulation results in Cadence Spectre. As shown in Fig. 4.15, the FDDA is based on the unity-gain configuration and thus its gain should be high enough to buffer the voltage signal and protect it from being degraded by the FAI loads. The impedance of the FAI loads reaches minimum at the resonant frequency. According to Eq. 4.11 and assuming the tuning factor $x$ is set maximally at 0.999n, the minimum impedance of the FAI loads is can be calculated:

$$r_{min} \approx \frac{0.002U_T}{I_{st}}. \tag{4.45}$$

According to Eq. 4.43, the maximum value required for $I_{st}$ to cover the audio frequency range is roughly 10 nA. Assuming $I_{st}$ is set maximally at 20 nA, the minimum resistance of the FAI loads is thus roughly 260 $\mathrm{k}\Omega$. The unity-gain configured FDDA has input-output relationship expressed as

$$(v_{in} - v_{out}) \cdot g_{m1} r_{o1} g_{m2} = \frac{v_{out}}{r_{o2}} + \frac{v_{out}}{r_{min}}, \tag{4.46}$$

and thus

$$\frac{v_{out}}{v_{in}} = \frac{g_{m1} g_{m2} r_{o1} r_{o2} r_{min}}{g_{m1} g_{m2} r_{o1} r_{o2} r_{min} + r_{min} + r_{o2}}, \tag{4.47}$$

where $g_{m1}$ and $g_{m2}$ represent respectively the transconductances of the input-stage and the output-stage differential pairs and $r_{o1}$ and $r_{o2}$ represent the corresponding output resistances. $g_{m1} g_{m2} r_{o1} r_{o2}$ is the DC gain of the FDDA which is much higher than unity and thus $r_{min}$ is negligible compared with $g_{m1} g_{m2} r_{o1} r_{o2} r_{min}$. To make the FDDA an appropriate voltage buffer ($v_{out} \approx v_{in}$, the FDDA should be designed such that $r_{o2}$ is negligible compared with $g_{m1} g_{m2} r_{o1} r_{o2} r_{min}$ which means $g_{m1} g_{m2} r_{o1} r_{min}$ is much higher than unity. To maximise transistor current efficiency, the MP0-3 and MP4-5 are all designed to be operating in weak inversion and thus the following equation is derived:

$$g_{m1} g_{m2} r_{o1} = \frac{2I_{FA}}{nU_T} \cdot \frac{2m \cdot I_{FA}}{nU_T} \cdot \frac{1}{\lambda I_{FA}} = \frac{4mI_{FA}}{\lambda (nU_T)^2}, \tag{4.48}$$

| | Transistor Type | Function | L ($\mu$m) | W ($\mu$m) |
|---|---|---|---|---|
| MP0-3 | PMOS | Input-Stage Differential Pair | 3.5 | 90 |
| MP4-5 | PMOS | Output-Stage Differential Pair | 3.5 | 180 |
| MP6-7, MP10-15 | PMOS | Current Mirror | 3.5 | 22.5 |
| MP8-9 | PMOS | Current Mirror | 3.5 | 45 |
| MN0-9 | NMOS | Current Mirror | 3.5 | 12.5 |
| MN10-14 | NMOS | Common-mode Feedback | 3.5 | 0.4 |

**Table 4.5:** *Functions and dimensions of the transistors in FDDA*

where $m$ represents the ratio between the currents in MP4-5 and in MP0-3. By making $g_{m1}g_{m2}r_{o1}r_{min}$ two orders higher than unity, the following expression is derived

$$mI_{FA} \geq \frac{25\lambda(nU_T)^2}{r_{min}}. \tag{4.49}$$

Using the maximum $\lambda$ value, the minimum currents required to bias MP4-5 are thus 0.25 $\mu$A. To meet the weak inversion criterion, the aspect ratio MP4-5 is required to be at least 40:1, as shown in Table. 4.5. The currents in MP0-3, the $I_{FA}$ is set to be half of the currents in MP4-5 ($m$=2), as a compromise between the low power and low noise design and therefore, the aspect ratios of MP0-3 are also set to be half of those of MP4-5. The dimensions of the transistors in Fig. 4.17 are summarised in Table. 4.5. The long lengths of 3.5 $\mu$m are applied to reduce the channel modulation effects in the transistors.

As introduce above, the FDDA functions as a unity-gain buffer in the LPF; therefore the LPF transfer function is determined by the voltage division ratio between the FAIs and the capacitor $C_{LPF}$. The LPF transfer function is thus given by

$$H_{LPF}(s) = \omega_{LP}^2 \cdot \frac{1}{s^2 + \frac{\omega_{LP}}{Q_{LP}}s + \omega_{LP}^2}, \tag{4.50}$$

where

$$\begin{cases} \omega_{LP} = \frac{1}{4nU_TC_0}\sqrt{2nI_{st}I_{LPF}}; \\ Q_{LP} = \frac{1}{2(nI_{stat}-I_{LPF})}\sqrt{2nI_{st}I_{LPF}}. \end{cases} \tag{4.51}$$

Using the tuning factor $x$ to represent $I_{LPF}$, Eq. 4.51 is rewritten as follows

$$\begin{cases} \omega_{LP} = \frac{I_{st}}{4nU_TC_0}\sqrt{2nx}; \\ Q_{LP} = \frac{1}{2(n-x)}\sqrt{2nx}. \end{cases} \tag{4.52}$$

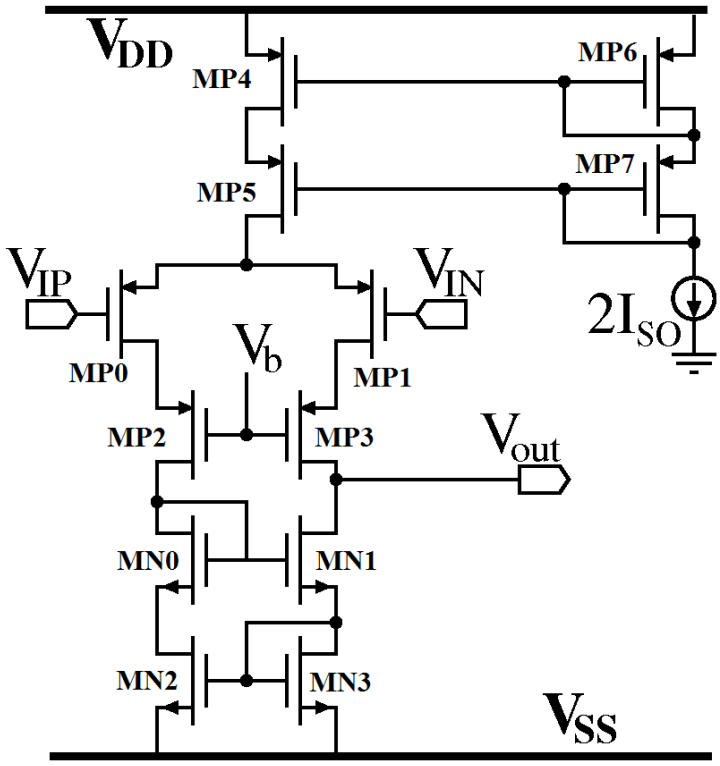


**Figure 4.18:** *Schematic of the single-end OTA*

| | Transistor Type | Function | L ($\mu$m) | W ($\mu$m) |
|---|---|---|---|---|
| MP0-1 | PMOS | Differential Pair | 3.5 | 22.5 |
| MP2-3 | PMOS | Cascode | 3.5 | 22.5 |
| MP4-7 | PMOS | Current Mirror | 3.5 | 45 |
| MN0-3 | NMOS | Active Load | 3.5 | 12.5 |

**Table 4.6:** *Functions and dimensions of the transistors in the single-end OTA*

Based on Eq. 4.43 and Eq. 4.52, the following equation is derived;

$$\begin{cases} \beta = \frac{\omega_{LP}}{\omega_{BP}} = \sqrt{1.2x}; \\ Q_{LPF} = \frac{0.866\beta}{1.5-\beta^2}, \end{cases} \tag{4.53}$$

which is in accordance with Eq. 3.10.

### 4.2.3 Elliptic Low-pass Filter (ELF)

As shown in Fig. 4.15, a pair of single-end OTA (SOTA) followers are used as the source resistances in the ELF. The schematic of the SOTA is illustrated in Fig. 4.18. The transistors in the SOTA also operate in weak inversion and the their functions and dimensions are summarised

in Table. 4.6. The widths of the differential pair are narrower compared with those in the FDOTA and the FDDA since the gain of the BPF and LPF in the filter channel makes the noise contribution of the SOTA far less significant. The equivalent resistance of the SOTA follower is given by

$$R_s = \frac{1}{g_{m,SOTA}} = \frac{nU_T}{I_{SO}} \tag{4.54}$$

The inductance and capacitance in the ELF are related with the value of $R_s$ as follows:

$$\begin{cases} L_{FAI,i} = \frac{L_{norm,i} \cdot R_s}{\omega_{-3dB}}; \\ C_i = \frac{C_{norm,i}}{R_s \cdot \omega_{-3dB}}, \end{cases} \tag{4.55}$$

where $\omega_{-3dB}$ is the -3 dB frequency; $L_{norm,i}$ and $C_{norm,i}$ are the normalised inductance and capacitance value which can be obtained from the filter design tables [98]. As stated in Chapter 3, $\omega_{-3dB}$ of the ELF is set as $\sqrt{2}\omega_{BP}$. Besides, $I_{SO}$ is set as $2I_{st}$ for ease of calculation. Therefore the values for the inductance and capacitance in the ELF are derived as[2]

$$\begin{cases} L_{FAI2} = 0.8551(\frac{nU_T}{I_{st}})^2 \frac{1}{\sqrt{n}} C_0; \\ L_{FAI4} = 1.113(\frac{nU_T}{I_{st}})^2 \frac{1}{\sqrt{n}} C_0; \end{cases} \tag{4.56}$$

$$\begin{cases} C_1 = 0.5252 \frac{1}{\sqrt{n}} C_0; \\ C_2 = 0.7651 \frac{1}{\sqrt{n}} C_0; \\ C_3 = 2.296 \frac{1}{\sqrt{n}} C_0; \\ C_4 = 1.373 \frac{1}{\sqrt{n}} C_0; \\ C_5 = 2.293 \frac{1}{\sqrt{n}} C_0. \end{cases} \tag{4.57}$$

Combining Eq. 4.10 and Eq. 4.56, the values for $C_{gy}$ in FAI2 and FAI4 are derived:

$$\begin{cases} C_{gy,FAI2} = 0.2138(\frac{I_{ELF}}{I_{st}})\sqrt{n} C_0; \\ C_{gy,FAI4} = 0.2783(\frac{I_{ELF}}{I_{st}})\sqrt{n} C_0. \end{cases} \tag{4.58}$$

According to Eq. 4.10, $I_{ELF}$ should be set as $nI_{st}$ so that the FAI is a pure inductor. Nevertheless, to leave sufficient margin for stability, $I_{ELF}$ is set as $1.2I_{st}$. As $n$ is about 1.25, the

[2]Detailed calculations are given in Appendix A.1

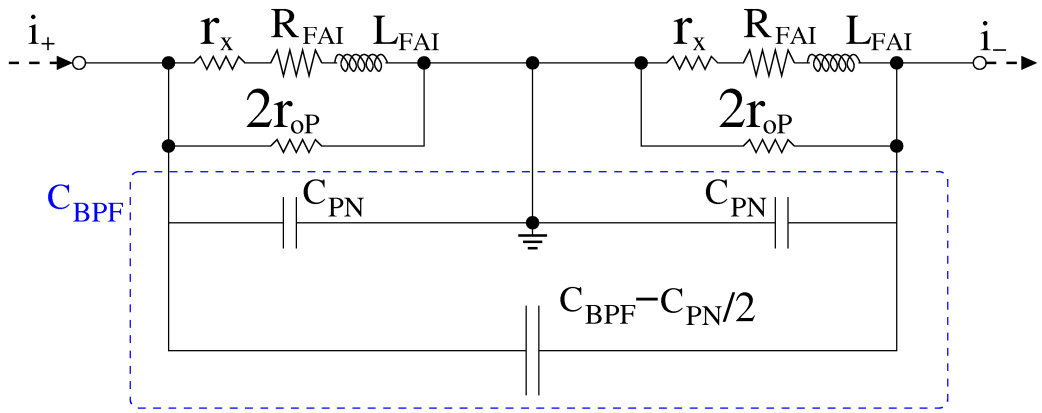


**Figure 4.19:** *Parasitics in the BPF*

capacitor values are rewritten as follows

$$\begin{cases} C_{gy,FAI2} = 0.2869C_0 \\ C_{gy,FAI4} = 0.3734C_0 \\ C_1 = 0.4698C_0 \\ C_2 = 0.6843C_0 \\ C_3 = 2.054C_0 \\ C_4 = 1.228C_0 \\ C_5 = 2.051C_0 \end{cases} \tag{4.59}$$

Note that the capacitance in Eq. 4.59 includes the parasitic capacitance analysed in Section. 4.1.3.1.

## 4.3 Non-ideality Analysis of the Cochlea Filter

The effects of circuit non-idealities on the cochlea filter are analysed, following the analysis results of FAI cell in Section. 4.1.3.

### 4.3.1 Parasitics

As stated above, the parasitic capacitances of the FAI have been combined with the corresponding capacitors in Fig. 4.15. For example, as shown in Fig. 4.19, the actually loaded capacitance in the BPF is $C_{BPF}$ subtracted by capacitance of the parasitics. Note that in Fig. 4.19, the FDOTA is not shown but its outputs are represented by $i_+$ and $i_-$. Following Eq. 4.28, the

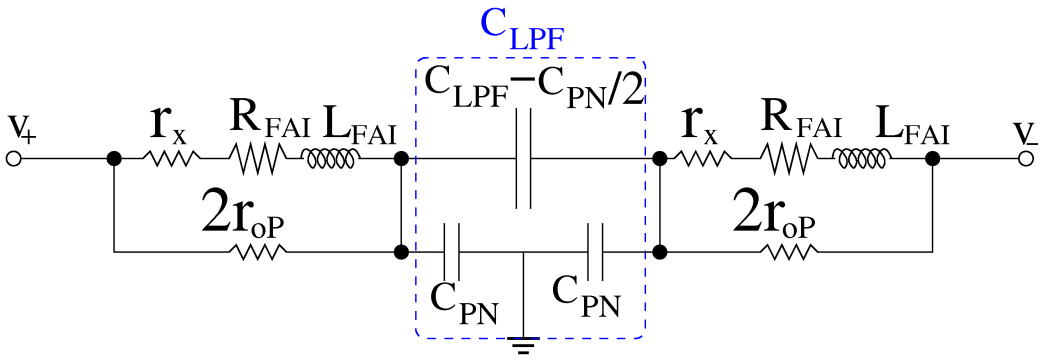


**Figure 4.20:** *Parasitics in the LPF*

parasitic resistance values in Fig. 4.19 are given by

$$\begin{cases} 2r_{oP} = \frac{2}{\lambda I_{st}}; \\ r_x = \frac{2}{g_{MP}g_{MN}r_{oP}} = \frac{2\lambda n U_T^2}{I_{st}}. \end{cases} \tag{4.60}$$

As stated above, $\lambda U_T$ is far less than unity and the maximum in-band frequency of the cochlea filter is $\sqrt{2}\omega_{LQ}$. Therefore the following relationship inequations between the resistances in Fig. 4.19 stand:

$$\begin{cases} r_x \ll R_{FAI} = \frac{2U_T(n-1)}{I_{st}}; \\ |R_{FAI} + j\omega L_{FAI}| \leq \sqrt{[\frac{2U_T(n-1)}{I_{st}}]^2 + (\sqrt{2}\omega_{LQ}\frac{4C_0 n U_T^2}{I_{st}^2})^2} \approx \frac{2.1U_T}{I_{st}} \ll 2r_{oP}. \end{cases} \tag{4.61}$$

Consequently the parasitic resistances in the BPF are negligible.

Fig. 4.20 illustrates the parasitics in the LPF. $v_+$ and $v_-$ represent the output of the FDDA-based buffer. As stated above, the parasitic capacitances are combined in $C_{LPF}$. The values of the parasitic resistances are given by

$$\begin{cases} 2r_{oP} = \frac{2}{\lambda I_{st}}; \\ r_x = \frac{2}{g_{MP}g_{MN}r_{oP}} = \frac{2\lambda n U_T^2}{xI_{st}}. \end{cases} \tag{4.62}$$

If the minimum tuning factor $x$ is 0.5, the following inequations stand:

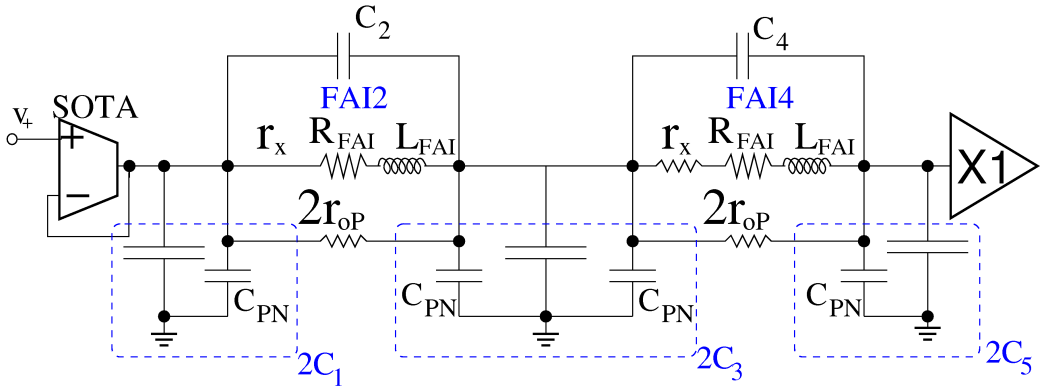


**Figure 4.21:** *Parasitics in the ELF.*

$$\begin{aligned}\frac{2r_{oP}}{|r_x+R_{FAI}+j\omega L_{FAI}|} &\geq \frac{\frac{2}{\lambda I_{st}}}{|\frac{2\lambda nU_T^2}{xI_{st}}+\frac{2U_T(n-x)}{xI_{st}}+j\sqrt{2}\omega_{LQ}\cdot\frac{4C_0nU_T^2}{xI_{st}{}^2}|}\\ &\approx \frac{x}{\lambda U_T\sqrt{(n-x)^2+\frac{5}{6}n}}\\ &\geq \frac{1}{2.54\lambda U_T}\\ &\gg 1;\end{aligned} \tag{4.63}$$

Consequently the shunt parasitic resistance $2r_{oP}$ is negligible. Considering the series parasitic resistance $r_x$, the LPF transfer function becomes

$$H_{LPF}(s)=\omega_{LP}^2\cdot\frac{1}{s^2+\frac{\omega_{LP}}{Q_{LP}}s+\omega_{LP}^2}, \tag{4.64}$$

where

$$\begin{cases}\omega_{LP}=\frac{1}{\sqrt{2C_{LPF}L_{FAI}}}=\frac{I_{st}}{4nU_TC_0}\sqrt{2nx}\\ Q_{LP}=\frac{\sqrt{L_{FAI}}}{\sqrt{2C_{LPF}}(R_{FAI}+r_x)}=\frac{\sqrt{2nx}}{2n(1+\lambda U_T)-2x}\end{cases} \tag{4.65}$$

Therefore, $r_x$ does not change the resonant frequency of the LPF, but reduces its Q factor. Nevertheless, since $\lambda U_T$ is far less than unity, the effect of $r_x$ on $Q_{LP}$ is negligible.

The ELF with parasitics is shown in Fig. 4.21. For simplicity, only one branch of the differential structure is shown. The parasitic resistance is also negligible since

$$\begin{cases}r_x \ll R_{FAI2}=R_{FAI4}=\frac{2U_T(n-1.2)}{1.2I_{st}};\\ |R_{FAI2}+j\omega L_{FAI}|\leq\sqrt{[\frac{2U_T(n-1)}{I_{st}}]^2+(\sqrt{2}\omega_{LQ}\cdot 0.5551\frac{n\sqrt{n}U_T^2C_0}{I_{st}^2})^2}\approx\frac{0.73U_T}{I_{st}}\ll 2r_{oP};\\ |R_{FAI4}+j\omega L_{FAI}|\leq\sqrt{[\frac{2U_T(n-1)}{I_{st}}]^2+(\sqrt{2}\omega_{LQ}\cdot 1.113\frac{n\sqrt{n}U_T^2C_0}{I_{st}^2})^2}\approx\frac{0.91U_T}{I_{st}}\ll 2r_{oP}.\end{cases} \tag{4.66}$$

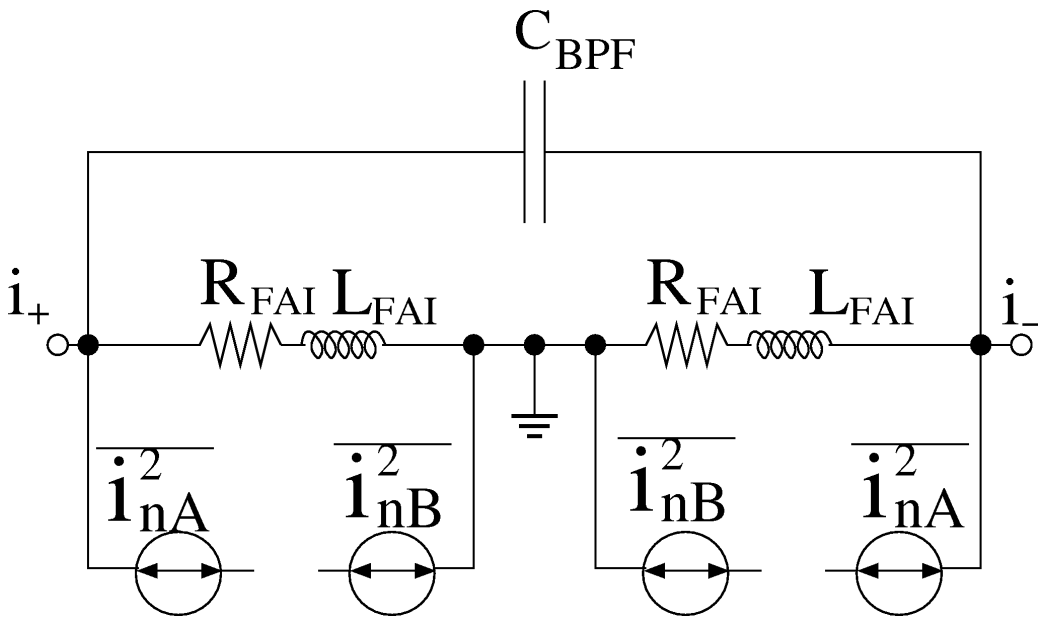


**Figure 4.22:** *FAI noise in the BPF.*

### 4.3.2 Noise

As stated in Section. 4.1.3.2, the CF of the cochlea filter is assumed to be higher than the noise corner frequency. Based on Eq. 4.30 and Eq. 4.43, the following equations stand:

$$\begin{cases} ForNMOS: \omega_{corner} = \frac{3\pi K_F I_{st}^{A_F-1}}{4qC_{ox}L^2} = \frac{3\pi K_F (3.46\omega_{LQ}U_T C_0)^{A_F-1}}{4qC_{ox}L^2}; \\ ForPMOS: \omega_{corner} = \frac{3\pi K_F I_{st}^{A_F-1}}{4qC_{ox}WL} = \frac{3\pi K_F (3.46\omega_{LQ}U_T C_0)^{A_F-1}}{4qC_{ox}WL}. \end{cases} \tag{4.67}$$

Thus based on the transistor dimensions given in Table. 4.1, the noise parameter values in Table. 4.2 and the 5 pF setting for $C_0$, the following is derived:

$$\begin{cases} \text{NMOS: } \frac{\omega_{corner}}{\omega_{LQ}} \approx 3.15\omega_{LQ}^{(-0.493)}; \\ \text{PMOS: } \frac{\omega_{corner0}}{\omega_{LQ}} \approx 0.124\omega_{LQ}^{(-0.539)}. \end{cases} \tag{4.68}$$

Apparently $\omega_{LQ}$ is higher than 10 Hz and thus

$$\begin{cases} \text{NMOS: } \frac{\omega_{corner}}{\omega_{LQ}} < 1.01 \\ \text{PMOS: } \frac{\omega_{corner0}}{\omega_{LQ}} < 0.0358 \end{cases} \tag{4.69}$$

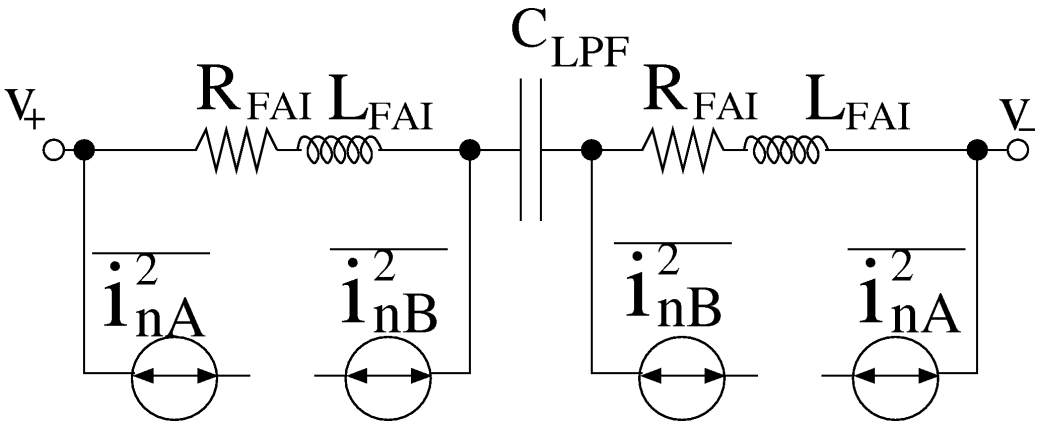


**Figure 4.23:** *FAI noise in the LPF*

Consequently, the assumption of the noise analysis in Section. 4.3.2 is valid. For simplicity, the Eq. 4.34 is rewritten as follows

$$\overline{i_{nA}^2(\omega)} = \overline{i_{nB}^2(\omega)} = 8.26\sqrt{n}kTC_0\omega_{LQ} \cdot \frac{x^2 + 2n^2x + 0.521\frac{\omega^2}{\omega_{LQ}^2}}{(x-n)^2 + 0.521\frac{\omega^2}{\omega_{LQ}^2}}. \tag{4.70}$$

so that the noise current in FAI is represented using $\omega_{LQ}$. Eq. 4.71 can be normalised as follows

$$\overline{i_{nA}^2(\xi)} = \overline{i_{nB}^2(\omega)} = 8.26\sqrt{n}kTC_0\omega_{LQ} \cdot \frac{x^2 + 2n^2x + 0.521\xi^2}{(x-n)^2 + 0.521\xi^2}, \tag{4.71}$$

where $\xi$ denotes $\frac{\omega}{\omega_{LQ}}$.

Fig. 4.22 shows the FAI noise sources in the BPF. The FAIs both have one end shorted to ground so that the noise currents $\overline{i_{nB}^2(\omega)}$ are released. Therefore based on Eq. 4.34 the input referred noise of the BPF is given by

$$\overline{V_{niBPF}^2(\xi)} = \frac{2\overline{i_{nA}^2(\omega)}}{g_{m,FDOTA}^2} = 0.6(\frac{kT}{C_0\omega_{LQ}})(\frac{\xi^2 + 7.92}{\xi^2 + 0.12}). \tag{4.72}$$

Fig. 4.20 shows the FAI noise sources in the LPF. Since the FDDA buffer has low output impedance, the noise currents $\overline{i_{nA}^2(\omega)}$ cause little noise voltage in the LPF output. The input referred noise of the LPF is given by

$$\overline{V_{niLPF}^2(\xi)} = 2\overline{i_{nB}^2(\omega)} \cdot |R_{FAI} + j\omega L_{FAI}|^2 = \frac{5.51\sqrt{n}kT}{x^2C_0\omega_{pc}}(x^2 + 2n^2x + 0.521\xi^2). \tag{4.73}$$

The ELF is the last stage of the cochlea filter. Since the BPF and LPF provide all the gain for the cochlea filter, the noise from elliptic filter is far less significant when referred at the input of the cochlea filter. Therefore, neglecting the noise from the ELF, the input referred noise density of the cochlea filter channel is the sum of the BPF input referred noise and the LPF input referred noise divided by the gain of BPF. Combining Eq. 4.42, Eq. 4.43, Eq. 4.72 and Eq. 4.73, the input referred noise of the cochlea filter is given by

$$\overline{V_{ni}^2(\xi)} = \frac{kT}{\omega_{LQ}C_0}[\frac{1.15(x^2+3.125x+0.521\xi^2)(\xi^4-1.88\xi^2+1)}{x^2(\xi^2+0.12)} + \frac{0.6(\xi^2+7.92)}{\xi^2+0.12}]. \tag{4.74}$$

And the integrated input-referred noise is calculated by

$$\begin{aligned} V_{inoise}^2 &= \int_0^{\sqrt{2}} \overline{V_{ni}^2(\xi)} d\xi \\ &= \frac{kT}{\omega_{LQ}C_0}(27.3 + \frac{26.4}{x} + \frac{0.27}{x^2}) \end{aligned} \tag{4.75}$$

Eq. 4.75 indicates that the integrated input-referred noise of the cochlea filter decreases with increasing CF and tuning factor.

### 4.3.3 Mismatch

Fig. 4.24 shows the FAI offset currents in the BPF. The FAIs have one port shorted to ground. Similarly, the FAIs in the LPF have one port connected to the low-impedance output of the FDDA. Therefore in the BPF and LPF, the $I_{osH}$ and $I_{osVB}$ are released. By contrast, the $I_{osVA}$ flow through the FAI and causes a DC voltage shift at the output. Based on Eq. 4.40, the worst-case DC offset is given by

$$V_{os} \leq 2I_{osVA} \cdot R_{FAI} \leq 7.4mV; \tag{4.76}$$

The FAIs in the ELF should be analysed separately. The FAI2s have one port connected to the OTA followers while the FAI4s have one port connected to the other port of FAI2s. Thus $I_{osH}$ and $I_{osV}$ of both FAI2 and FAI4 flow through the OTA follower and cause the DC shift given by

$$V_{os} \leq (I_{osH} + 2I_{osV})nU_T/I_{st} \leq 28.2mV; \tag{4.77}$$

Besides, the offset currents in FAI4 flow through FAI2 in addition to one branch of $I_{osV}$ of the

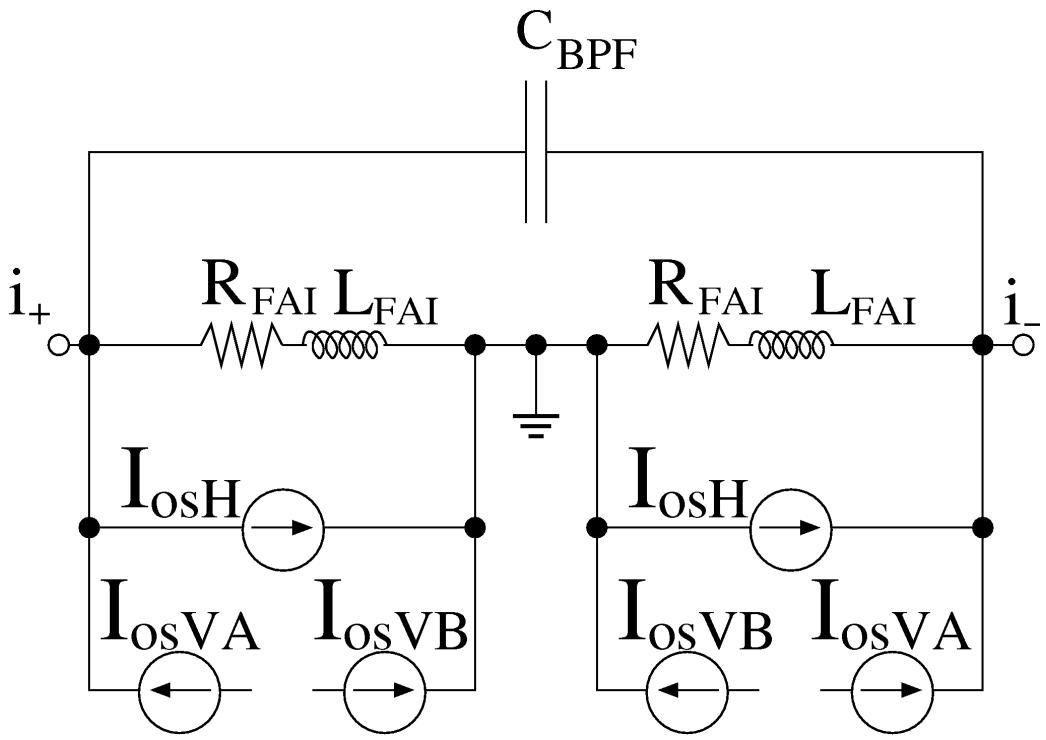


**Figure 4.24:** *Mismatch-induced offset currents in the BPF*

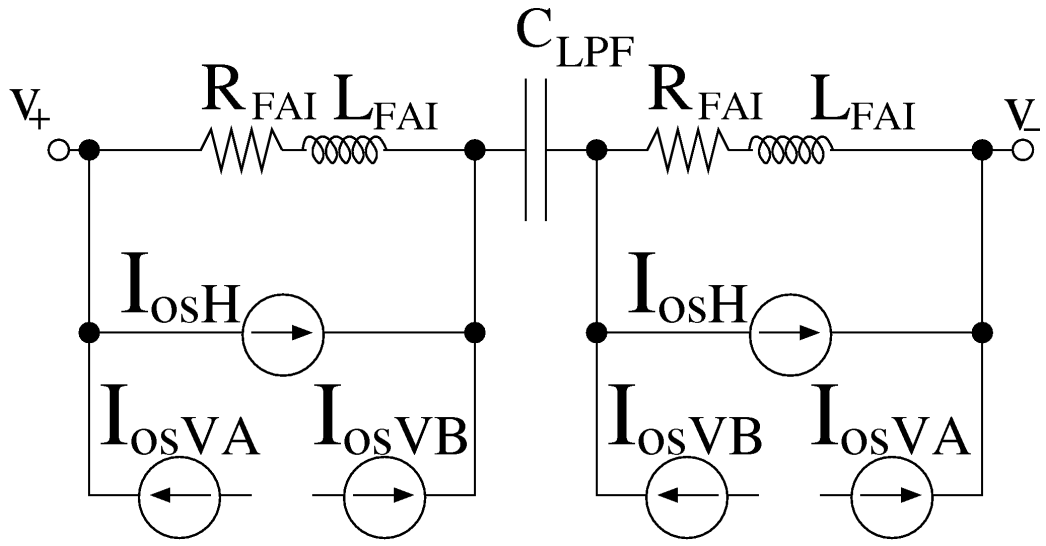


**Figure 4.25:** *Mismatch-induced offset currents in the LPF*

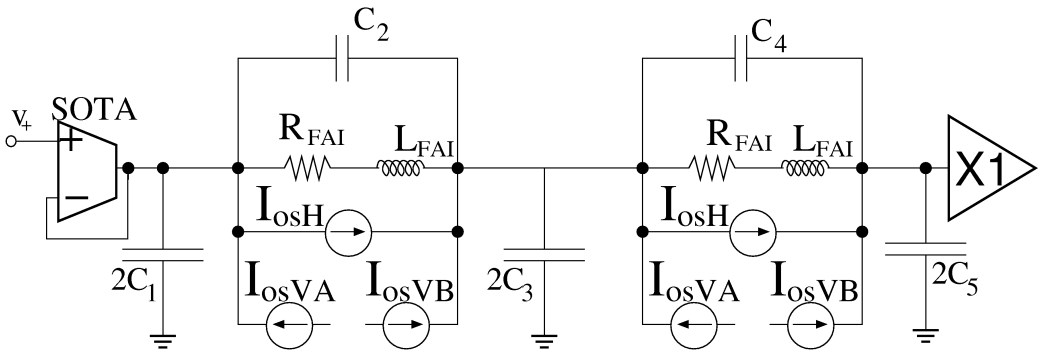


**Figure 4.26:** *Mismatch-induced offset currents in the ELF*

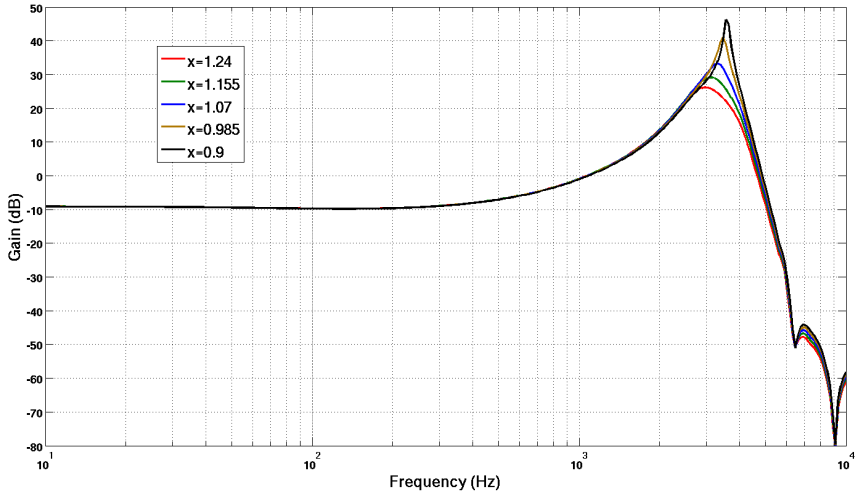


**Figure 4.27:** *Simulated cochlea filter frequency response with worst-case DC offsets*

FAI2 itself and cause the DC shift given by

$$V_{os} \leq (I_{osH} + 3I_{osV})R_{FAI2} \leq 1.88mV; \tag{4.78}$$

In the end, one branch of $I_{osV}$ flows through FAI4 and causes the DC shift given by

$$V_{os} \leq I_{osV}R_{FAI4} \leq 0.678mV. \tag{4.79}$$

The cochlea filter is verified using the Cadence Spectre simulator by adding the above worst-case DC offsets. The simulated filter frequency response is shown in Fig. 4.27, which proves that the cochlea filter is still able to function properly against the above DC offsets.

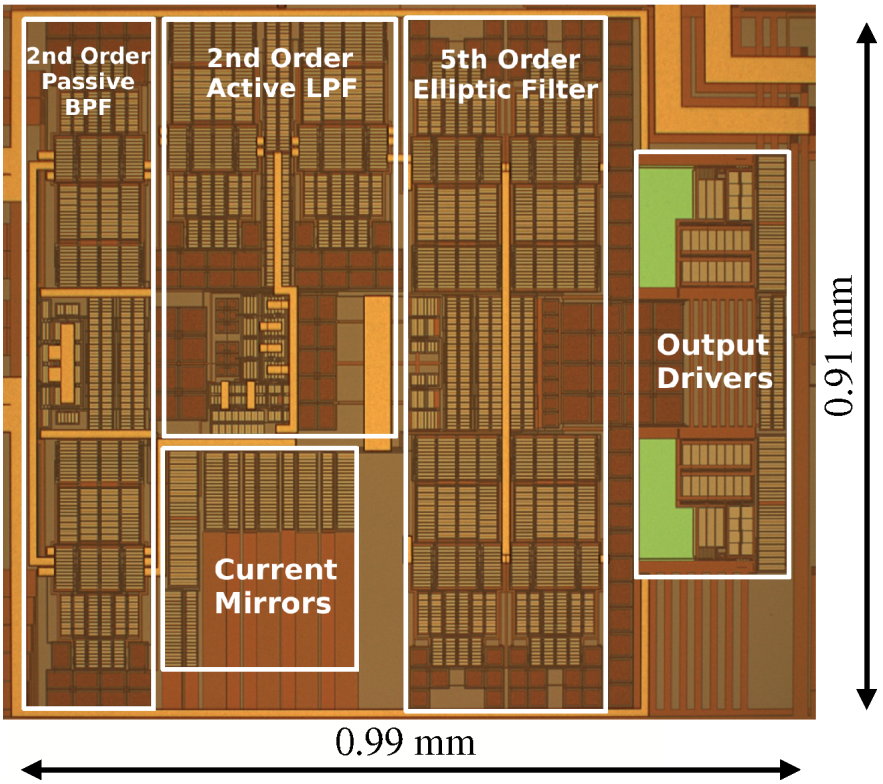


**Figure 4.28:** *Chip micrograph showing the cochlea filter*

## 4.4 VLSI Implementation

Based on the design introduced above, a cochlea filter channel is fabricated using AMS 0.35$\mu$m 2-poly 4-metal process, as shown in Fig. 4.28. The size of the cochlea filter is less than 1 $mm^2$. Therefore the one-third octave scale filter bank proposed in Chapter 3 is expected to occupy roughly 30$mm^2$, which is reasonable for standard CMOS technologies.

The block diagram of the chip structure is shown in Fig. 4.29. The on-chip biasing current is down to pico-amp level for low frequency channels and therefore the current mirrors with 1:100 ratio are employed to improve the precision of off-chip current settings and measurements. As illustrated in Fig. 4.15, the output drivers are used to interface the cochlea filter with the I/O pads and the off-chip devices. The characterisation results of the chip are detailed in the next chapter.

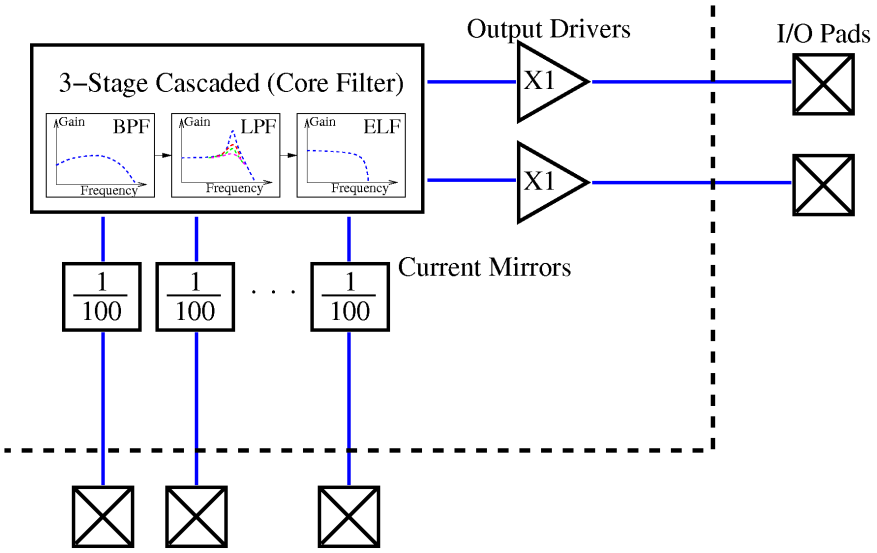


**Figure 4.29:** *Block diagram of the chip structure*

## 4.5 Summary

The implementation of the proposed cochlea filter using analogue VLSI circuits is detailed in this chapter. The filter transfer function is realised using the active RLC ladders. A floating active inductor (FAI) cell is developed which has the following features:

- it has floating terminals, which is strictly required to implement the elliptic low-pass filter (ELF).
- it employs transistors operating in weak inversion mode so that its impedance is concisely represented by the transistor currents as shown by Eq. 4.10. This reduces the design complexity: the same FAI circuits are reused throughout the cochlea filter design and the different inductance requirements can be simply addressed by setting appropriate currents.
- its equivalent impedance consists of a variable resistance in addition to the inductance, which means it is an inductor with variable quality factor. This feature makes it feasible to realise the CF tuning mechanism of the cochlea filter.

Briefly speaking, the FAI cell is highly feasible for the cochlea filter implementation.

Comprehensive analysis is performed on the circuit non-idealities including the parasitics, noise and mismatches. The effects of these circuit non-idealities on the cochlea filter operation and

performance are investigated, and the transistor dimensions have been optimised accordingly to minimise these effects.

In the end, an analogue VLSI chip is fabricated to verify the circuit function and performance. The chip results will be detailed in the next chapter.

# Chapter 5
# Experimental Results from the Cochlea Filter Chip

This chapter presents the experimental results from the prototype chip of the cochlea filter. The chip results are compared with the physiological results of biological cochlea following a similar routine as that in Chapter 3. Besides, the chip results regarding noise, harmonic distortion, intermodulation distortion and real acoustic signal testing are also provided and discussed.

## 5.1 Experimental Setup

A prototype PCB and a PXI platform are built to characterise the cochlea filter chip . The experimental setup is illustrated in Fig. 5.2. A PXI system (from National Instruments) is established for automated testing. The NI PXI-1042Q chassis is assembled with the PXI-8360 module for laptop remote control, the PXI-4110 module to provide appropriate DC power supply, the PXI-6723 analogue output module to generate electrical inputs, the PXI-4462 module for data acquisition (DAQ) and the PXI-7851R multifunction RIO module to control the current sources on the PCB and thus the biasing currents of the cochlea filter. By changing biasing currents, the cochlea filter can be configured to operate in different frequency bands. Besides, a MEMS microphone (ADMP401) is integrated on the PCB so that the cochlea filter can be tested with real sound inputs. Details about the LabVIEW program used to characterise the chip can be found in Appendix A.2

The static current of the cochlea filter $I_{st}$ is set with different values from 37.14 pA to 9.915 nA so as to make the filter operate in nine frequency regions corresponding to octave audio bands from 31 Hz to 8 kHz. The BPF current $I_{BPF}$ is set where $\omega_{LQ}$ is approximately 10$\sim$20$\%$ smaller than the corresponding octave frequency value. The LPF current $I_{LPF}$ is set in the region from where $\omega_{HQ}$ overlays with $\omega_{LQ}$ (LQ mode), to where the LPF peak gain is maximised before the system start to oscillate (HQ mode). The ELF current $I_{ELF}$ is set as $1.2I_{st}$

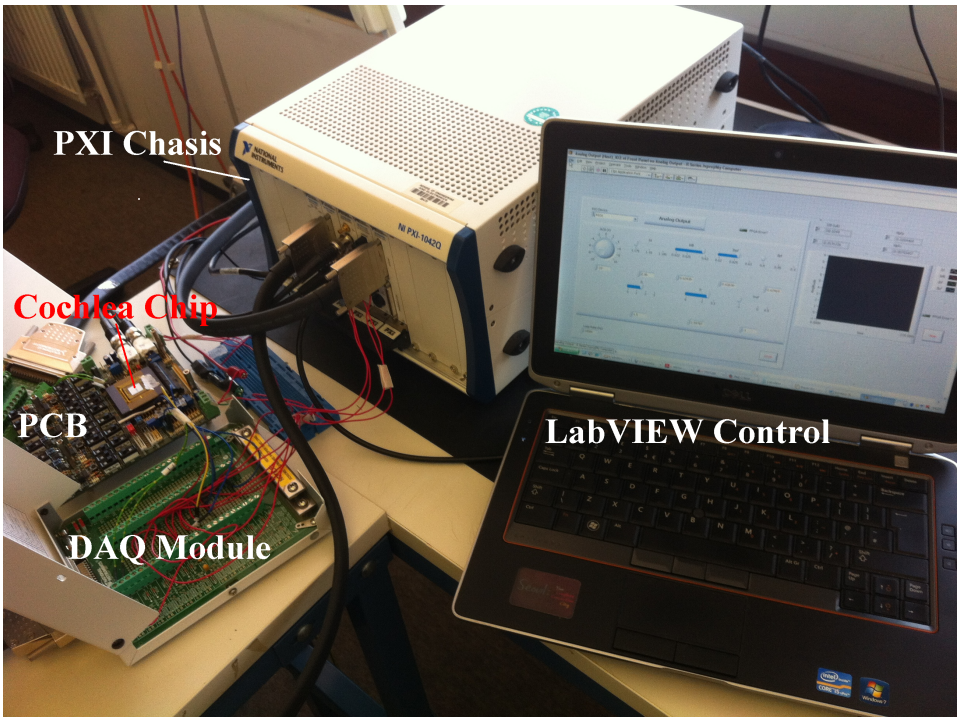


**Figure 5.1:** *NI PXI-based testing system*

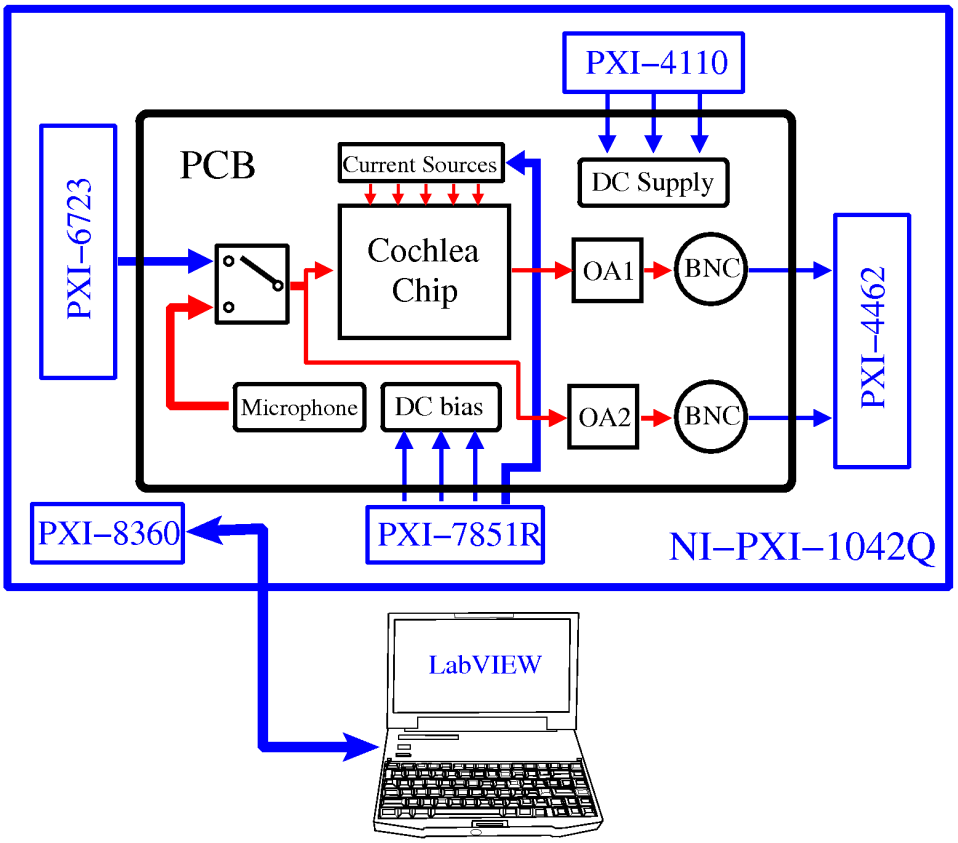


**Figure 5.2:** *Testing system block diagram*

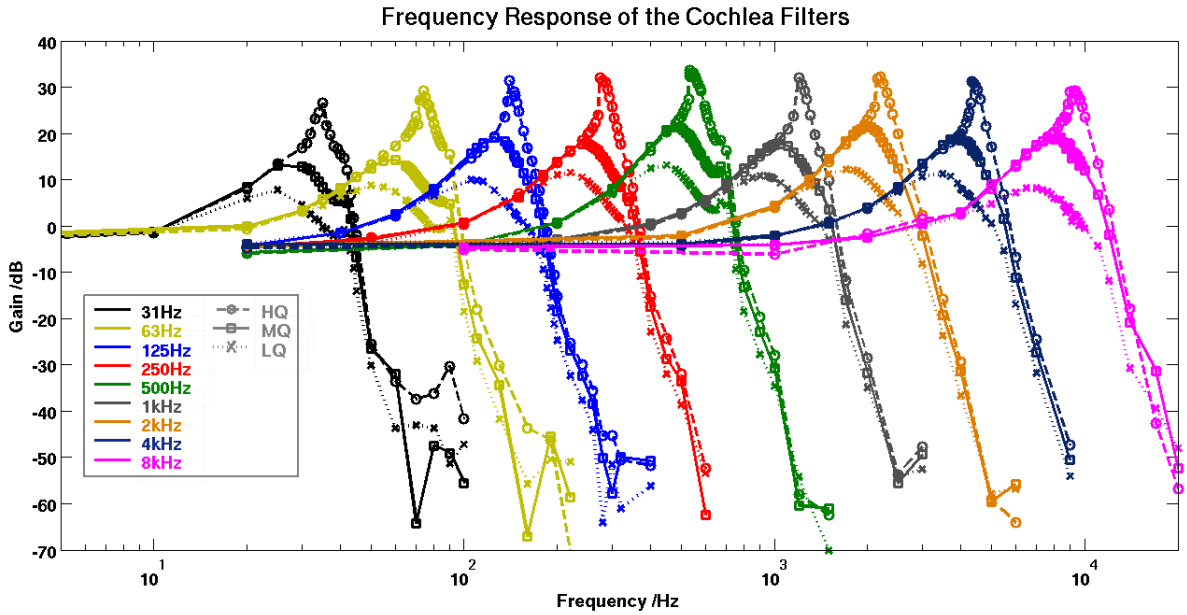


**Figure 5.3:** *Measured frequency responses of 9 cochlea filters covering octave audio bands from 31 Hz to 8 kHz.*

as explained in Section 4.1.

## 5.2 Measured Chip Results

### 5.2.1 Frequency Response

| Animal Type | $S_1$ (dB/dec) | Max. $S_2$ (dB/dec) | Max. $S_3$ (dB/dec) | $\omega_{LQ}$ (Hz) | $Max.\omega_{HQ}$ (Hz) | PGDR (dB) | Max. $Q_10$ |
|---|---|---|---|---|---|---|---|
| Filter1 | 27.2 | 97.1 | -336.2 | 25 | 35 | 18.8 | 3.55 |
| Filter2 | 24.6 | 119.8 | -274.2 | 53 | 74 | 20.4 | 3.81 |
| Filter3 | 20.6 | 88.5 | -301.8 | 105 | 140 | 21.5 | 3.24 |
| Filter4 | 22.1 | 118 | -290.9 | 220 | 275 | 20.6 | 3.85 |
| Filter5 | 22.8 | 113.6 | -230.5 | 430 | 545 | 20.5 | 3.47 |
| Filter6 | 23.1 | 90 | -391.4 | 0.9k | 1.2k | 21.3 | 3.49 |
| Filter7 | 22.6 | 116.8 | -238.5 | 1.7k | 2.2k | 20.0 | 3.57 |
| Filter8 | 22.2 | 93.5 | -272.1 | 3.5k | 4.4k | 20.0 | 3.26 |
| Filter9 | 11.8 | 67.3 | -268.4 | 7.1k | 9.2k | 21.1 | 2.64 |

**Table 5.1:** *Specifications of magnitude frequency response from the cochlea filter chip, following the criteria listed in Table. 2.1.*

Frequency responses of the nine filter bands in magnitude are measured and plotted in Fig. 5.3.

Apart from the LQ and HQ modes mentioned above, responses of the cochlea filters in medium Q (MQ) mode are also measured, where $I_{LPF}$ is adjusted so that the CF of the entire filter locates approximately at the corresponding octave frequency value. Comparing with biology, the LQ, MQ and HQ filter modes respectively correspond to cochlea response with high intensity, normal intensity and low intensity sound stimulus.

Although the gain of the cochlea filter is not as high as the model results shown in Fig. 3.4 due to the compression effect of transistors in weak inversion, the gentle and constant low-frequency tail, the selective and variable CF response and the ultra-steep roll-off are observed in all of the filters shown in Fig. 5.3. Table. 5.1 lists the frequency response specifications to compare with the biological cochlea and the filter model results given in Table. 2.1 and Table. 3.2. Table. 5.2 compares the results of this work with the previous ones (the minimum and maximum values in Table. 5.1 have been excluded). Besides more detailed specifications are summarised in Table 5.3.

| | | | Application | $S_1$ (dB/dec) | Max. $S_2$ (dB/dec) | Max. $S_3$ (dB/dec) | Max. $\omega_{HQ}$ / $\omega_{LQ}$ | PGDR (dB) | Max. $Q_{10}$ |
|---|---|---|---|---|---|---|---|---|---|
| Biological Cochlea | | | - | 20[9] ~47.8[8] | 49.8[7] ~274[10] | -472[7] ~-236[11] | 1.4[10] ~ 1.6[11] | 20[11] ~40[1, 10] | 2.21[7] ~6.93[7, 10] |
| Travelling-Wave Architectures | 1-D | [16] | General | ≈0 | 17.2 | 101.9 | - | - | 1.01 |
| | | [67] | General | - | 20 | -94.3 | - | - | 1.04 |
| | | [69] | General | - | 20 | -120 | - | - | 1.12 |
| | | [70]* | CI | 0 | 5 | -40 | - | - | 0.56 |
| | | [72] | General | - | 20 | -120 | - | - | 1.12 |
| | | [73]* | General | **19.9** | **76.4** | -181.2 | 2.46 | **46** | **2.53** |
| | | [17] | General | ≈0 | **67** | -175.5 | 1.4 | **34** | **2.32** |
| | | [74]* | CI | 0 | 18 | -60 | - | - | 0.84 |
| | | [75] | General | - | 14.6 | -20 | - | - | 0.34 |
| | | [20] | General | 0 | **57.3** | -34.1 | 0.57 | 7.5 | 0.77 |
| | 2-D | [83] | General | - | 30 | **-215.8** | - | - | 1.54 |
| | | [29] | ASR | **19.9** | **60.3** | -106 | 0.9 | **28** | 1.79 |
| | | [18] | General | ≈5 | 28.9 | -66.4 | 2.67 | 16 | 1.04 |
| | | [19] | General | ≈10 | 83 | -179.4 | 1 | **24** | **2.7** |
| Parallel Cochlea Filter Banks | Gamma-tone | Original[22]* | CASA | - | **85.8** | **235** | - | - | **2.96** |
| | | APGF[92]* | CASA | - | **106.9** | **-298.4** | - | - | **3.65** |
| | | OZGF[95] | General | **17** | **232.5** | **-299** | 1 | **70** | **5.74** |
| | Basic Filters | [26] | CI | - | 33.2 | -39.6 | - | - | 0.78 |
| | | [27] | CI | - | 30.6 | -42.9 | - | 17.1 | 0.81 |
| | 3-Stage Cascade | This Work | General | **22.2 ~24.6** | **88.5 ~118** | **238.5 ~336.2** | **1.25 ~1.39** | **20.0 ~21.3** | **3.24 ~3.81** |

*Simulated Results

**Table 5.2:** *Comparison of frequency response between the biological cochlea, the previous cochlea filter models and this work. The data which match or roughly match with biology have been highlighted.*

| | | CF * | CF Variation | -3 dB BW * | ERB * | $I_{stat}$ | $x$ | PG * | PG Variation | Q factor | Roll-off Slope |
|---|---|---|---|---|---|---|---|---|---|---|---|
| Filter1 | LQ | 25Hz | -19.3% ∼+12.9% | 12.4Hz | 14.3Hz | 37.14pA | 0.68 | 7.736dB | 18.8dB | 2.08 | 125.5dB/dec |
| | MQ | 31 Hz | | 9.8Hz | 14.8Hz | | 1.07 | 12.48dB | | 3.16 | 189.3 dB/dec |
| | HQ | 35Hz | | 2.2Hz | 3.97Hz | | 1.39 | 26.53 dB | | 15.9 | 336.2dB/dec |
| Filter2 | LQ | 53Hz | -15.9% ∼+17.5% | 25.1Hz | 32.5Hz | 78.41pA | 0.68 | 8.787dB | 20.4dB | 2.11 | 110.8dB/dec |
| | MQ | 63Hz | | 19.2Hz | 27.5Hz | | 0.95 | 14.26dB | | 3.28 | 159.2dB/dec |
| | HQ | 74Hz | | 3.8Hz | 7.87Hz | | 1.45 | 29.14dB | | 19.5 | 274.2dB/dec |
| Filter3 | LQ | 105Hz | -16% ∼+12% | 46Hz | 54.3Hz | 143.7pA | 0.82 | 9.971dB | 21.5dB | 2.28 | 124.1dB/dec |
| | MQ | 125Hz | | 33Hz | 41.8Hz | | 1.26 | 19.07dB | | 3.79 | 183.9dB/dec |
| | HQ | 140Hz | | 7.2Hz | 11.0Hz | | 1.48 | 31.51dB | | 19.4 | 301.8dB/dec |
| Filter4 | LQ | 220Hz | -12% ∼+10% | 90Hz | 106Hz | 279.1pA | 0.92 | 11.52dB | 20.6dB | 2.44 | 132.4dB/dec |
| | MQ | 250Hz | | 70Hz | 88.1Hz | | 1.23 | 17.72dB | | 3.57 | 172.4dB/dec |
| | HQ | 275Hz | | 18Hz | 24.6Hz | | 1.53 | 32.10dB | | 15.3 | 290.9dB/dec |
| Filter5 | LQ | 430Hz | -12.2% ∼+11.2% | 160Hz | 203Hz | 554.0pA | 0.88 | 13.14dB | 20.5dB | 2.69 | 110.6dB/dec |
| | MQ | 490Hz | | 115Hz | 162Hz | | 1.26 | 21.32dB | | 4.26 | 161.9dB/dec |
| | HQ | 545Hz | | 39Hz | 53.4Hz | | 1.55 | 33.64dB | | 14.0 | 240.5dB/dec |
| Filter6 | LQ | 0.9kHz | -14.3% ∼+14.3% | 410kHz | 484Hz | 1.189nA | 0.89 | 10.79dB | 21.3 dB | 2.20 | 116.3 dB/dec |
| | MQ | 1.05kHz | | 350kHz | 386Hz | | 1.24 | 17.74dB | | 3.00 | 160.9dB/dec |
| | HQ | 1.2kHz | | 75Hz | 101Hz | | 1.55 | 32.07dB | | 16.0 | 391.4dB/dec |
| Filter7 | LQ | 1.7kHz | -15% ∼+10.8% | 0.65kHz | 0.864kHz | 2.156nA | 0.88 | 12.23 dB | 20.0dB | 2.62 | 114.6dB/dec |
| | MQ | 2kHz | | 0.55kHz | 0.629kHz | | 1.31 | 21.38dB | | 3.64 | 166.8dB/dec |
| | HQ | 2.2kHz | | 0.15kHz | 0.238 kHz | | 1.54 | 32.22dB | | 14.7 | 238.5dB/dec |
| Filter8 | LQ | 3.5kHz | -10.3% ∼+12.8% | 1.27kHz | 1.69kHz | 4.291nA | 0.91 | 11.28dB | 20.0dB | 2.76 | 120.7dB/dec |
| | MQ | 3.9kHz | | 1.05kHz | 1.33kHz | | 1.29 | 18.95dB | | 3.71 | 160.6dB/dec |
| | HQ | 4.4kHz | | 0.24kHz | 0.375kHz | | 1.55 | 31.26dB | | 18.3 | 272.1dB/dec |
| Filter9 | LQ | 7.1kHz | -14.5% ∼+10.8% | 3.15kHz | 4.01kHz | 9.915nA | 0.68 | 8.152dB | 21.1dB | 2.25 | 123.6dB/dec |
| | MQ | 8.3kHz | | 2.5kHz | 2.94kHz | | 1.20 | 19.03 dB | | 3.32 | 176.0dB/dec |
| | HQ | 9.2kHz | | 0.87kHz | 1.28 kHz | | 1.55 | 29.23 dB | | 10.6 | 268.4dB/dec |

*CF = CF; -3 dB BW = -3 dB Bandwidth; ERB = Equivalent Rectangular Bandwidth; PG = Peak Gain.

**Table 5.3:** *Frequency response specifications of the cochlea filter in different configurations*

### 5.2.2 Phase Response

Fig. 5.4 shows the phase response of the cochlea filter with different CFs. Besides, the comparisons between LQ, MQ and HQ responses in 31 Hz and 8 kHz are shown in Fig. 5.6. As expected, in all filters the CF phase lag is approximately 0.4 cycles in the LQ mode and in the region of 1 cycle in the HQ mode. As shown in Fig. 5.6, the slope of the phase-frequency curve becomes steeper when frequency moves from low to high. The HQ phase response has a much steeper slope around CF than LQ response, and thus the HQ phase lag is lower than LQ for frequencies below CF but is higher for frequencies above CF.

### 5.2.3 Group Delay

Fig. 5.7 shows the maximum group delay in unit of periods across different CFs. As expected, the group delay increases from LQ to HQ mode. The maximum group delays in LQ and MQ modes are approximately 5 periods while the maximum group delay in HQ mode is in the region of 10 periods. The LQ group delay is higher than the model value probably due to the non-perfection of the ELF. As shown in Fig. 5.8, the peak of group delay from ELF is more prominent than that in the model figure (Fig. 3.8). The non-accuracy of inductance and capacitance is the main reason for the increase of ELF group delay. However, the maximum group delay in HQ response agrees well with the model value as the dominant delay results from the LPF instead of the ELF. The comparison of HQ maximum group delay with human cochlea is shown in Fig. 5.9.

### 5.2.4 Critical Bandwidth

An equivalent rectangular band-pass filter model is illustrated in Fig. 5.10, which reflects the critical band and frequency discrimination feature of the designed cochlea filters. The calculated equivalent rectangular bandwidth (ERB) and measured -3dB bandwidth of the cochlea filters are plotted versus corresponding CF in Fig. 5.11, together with the approximated bandwidth of human auditory filters derived from the formula given by Glasberg and Moore [87] for comparison. It shows that -3dB bandwidth is generally narrower than the ERB, but their discrepancy is not significant. The exact bandwidth values are listed in Table. 5.3. It is observed from Fig. 5.11 that the ERB curve derived by Glasberg and Moore from psycho-acoustical research lies in-between the ERB curves of the MQ and HQ modes. However as the cochlea filter

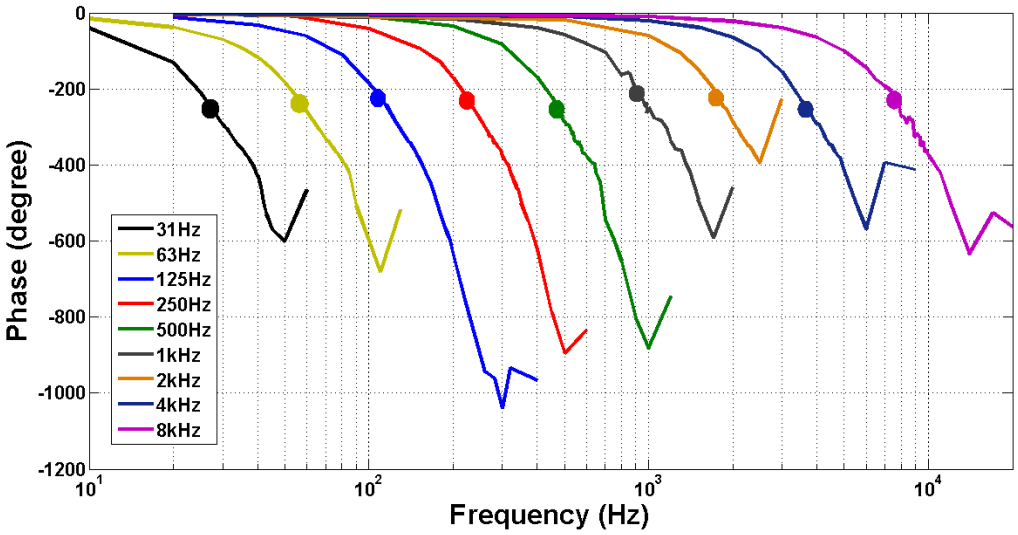


**(a)** LQ Phase Response

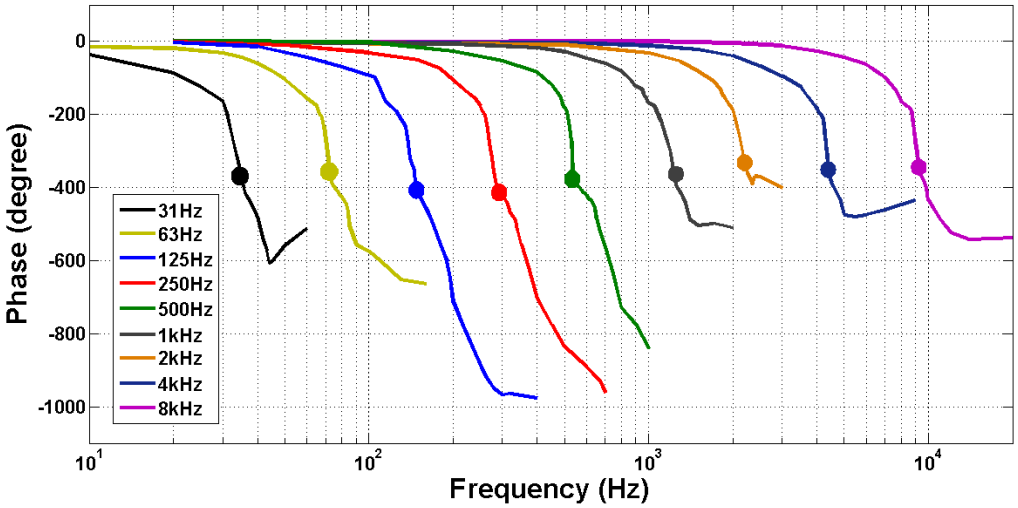


**(b)** HQ Phase Response

**Figure 5.4:** *Phase response of the cochlea filter with different CFs. The circles represents the location of the CFs.*

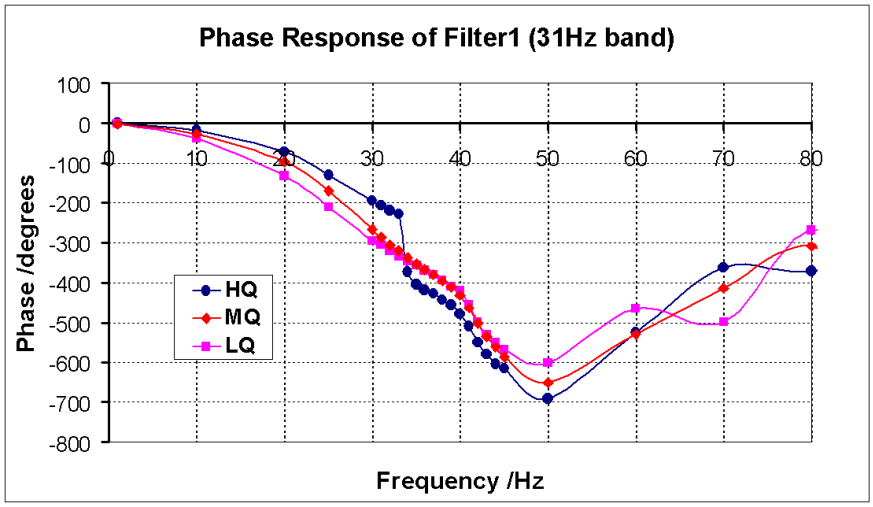


**Figure 5.5:** *Measured phase response of the 31 Hz band.*

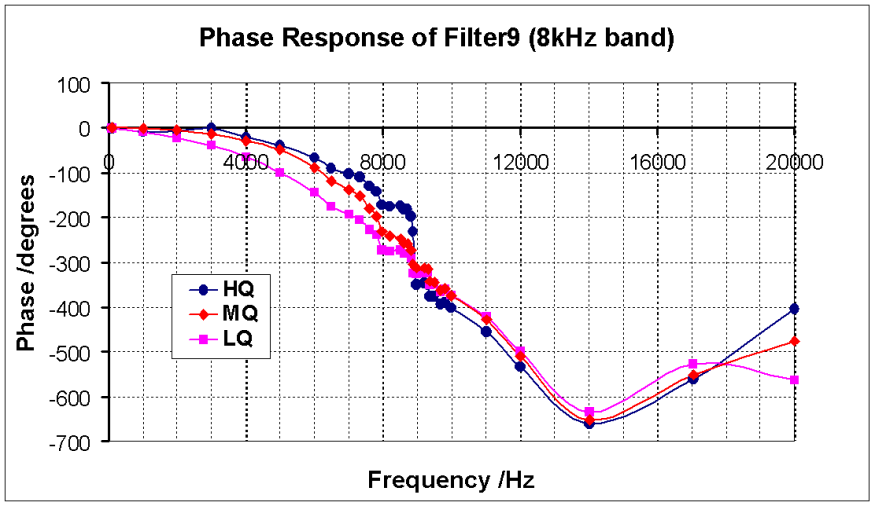


**Figure 5.6:** *Measured phase response of the 8 kHz band.*

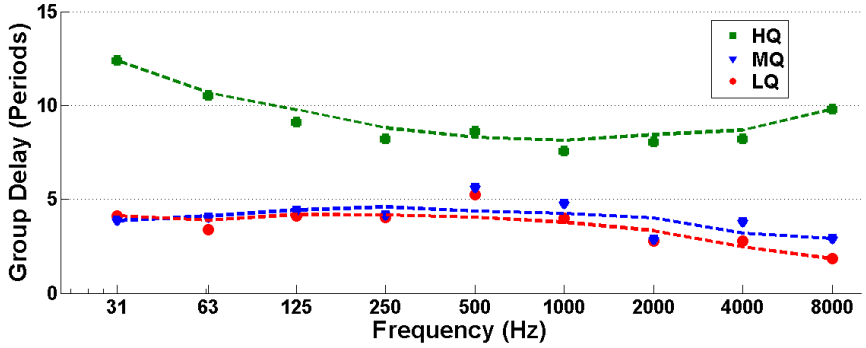


**Figure 5.7:** *Measured maximum group delay across different CFs.*

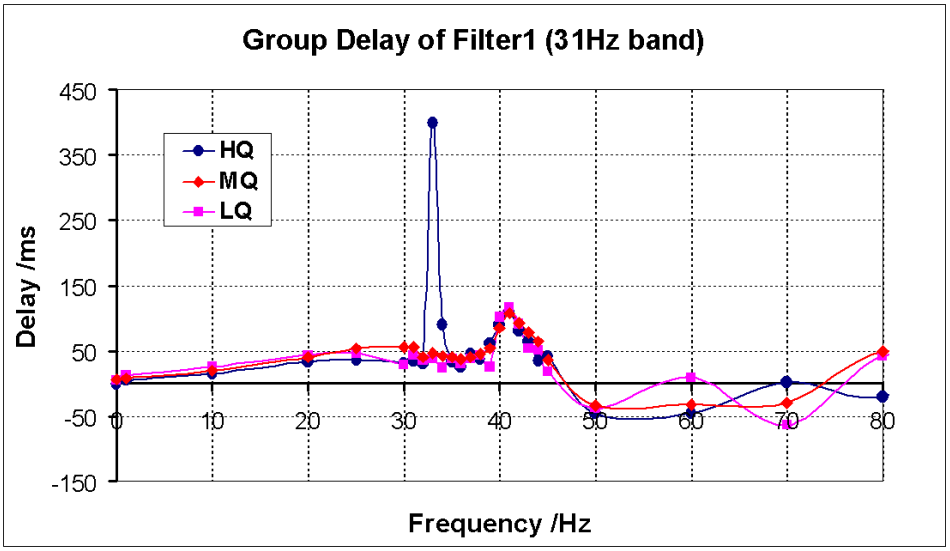


**Figure 5.8:** *Measured group delay from the 31 Hz band.*

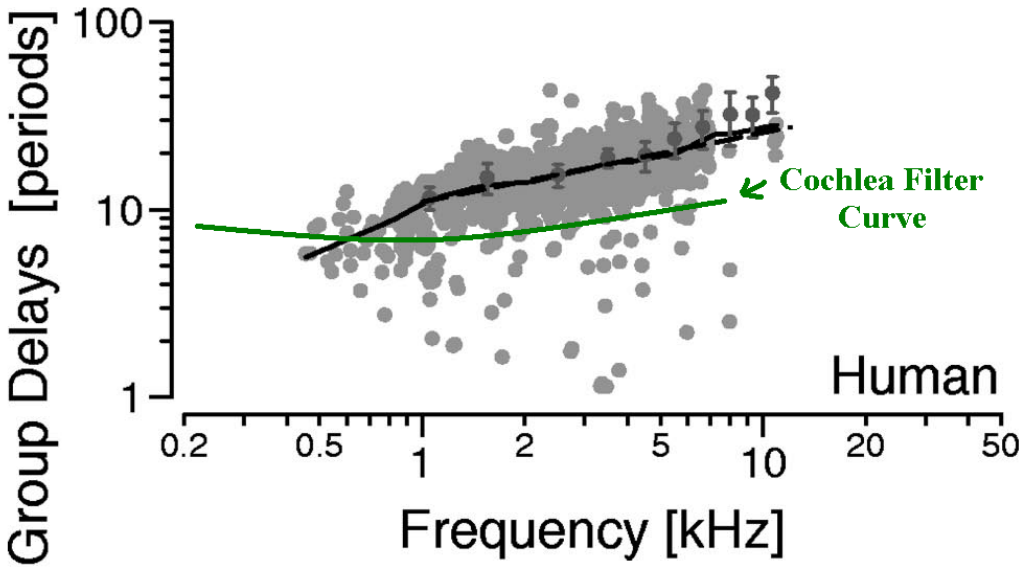


**Figure 5.9:** *The HQ maximum group delay curve in comparison with physiologically measured results from human cochlea. (The figure is adapted from the Fig. 5 in [102].)*

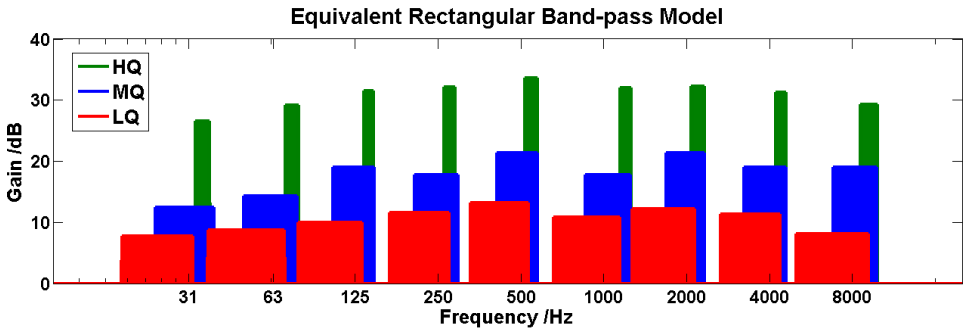


**Figure 5.10:** *Equivalent rectangular band-pass model of the cochlea filters*

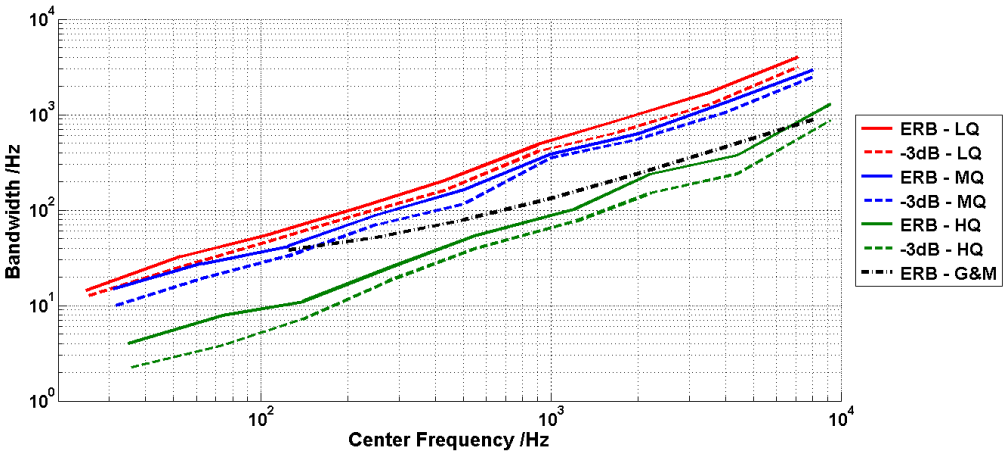


**Figure 5.11:** *ERB and -3 dB bandwidth of the cochlea filters versus CFs in comparison with approximated ERB of human auditory filters*

can be continuously tuned, it is possible to find a condition between the MQ and HQ modes where the ERB versus CF curve corresponds with better agreement to psycho-acoustical results [87].

### 5.2.5 Impulse Response

Impulse responses of the cochlea filter in 31 Hz and 8 kHz bands are shown in Fig 5.12, together with the decomposed responses from the three sub-filters. The time intervals ($t_{d1}$, $t_{d2}$) between adjacent peaks are labelled, which represent the ringing periods. The decrease of ringing periods observed in the 31 Hz filter and the HQ response of the 8 kHz filter demonstrates the expected frequency glides effects. However, this effect is not obvious in the LQ response of the 8 kHz filter and the reason is found in the decomposed impulse responses plot, which shows that the LPF response settles even faster than the other two sub-filters.

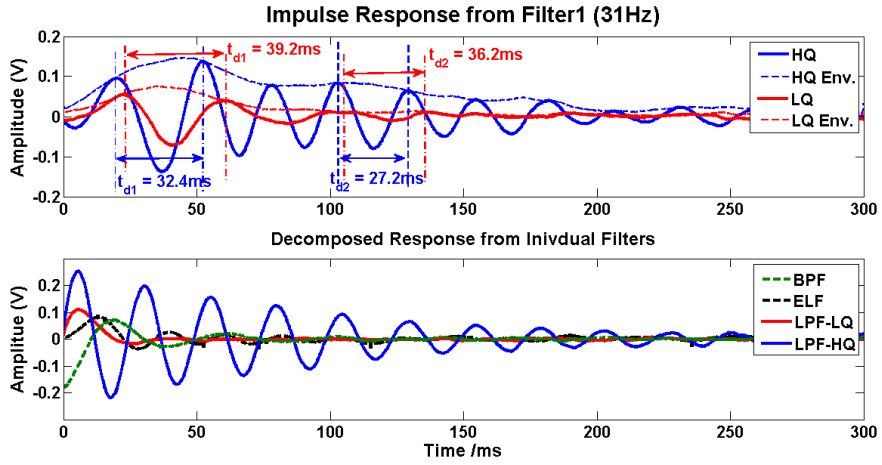


**(a)**

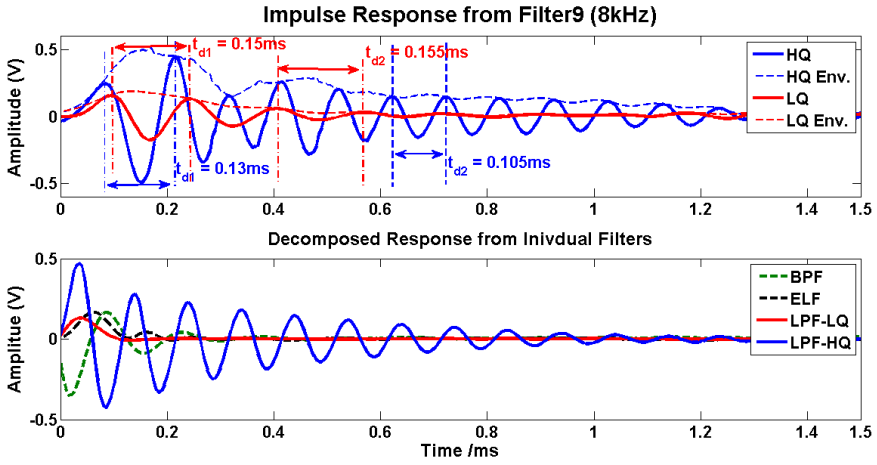


**(b)**

**Figure 5.12:** *Measured impulse response from the 31 Hz and 8 kHz band cochlea filters*

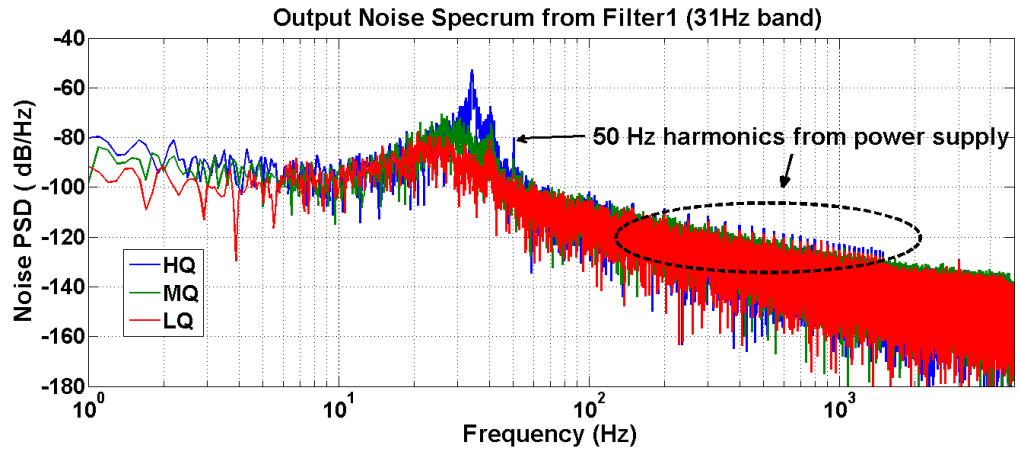


**(a)**

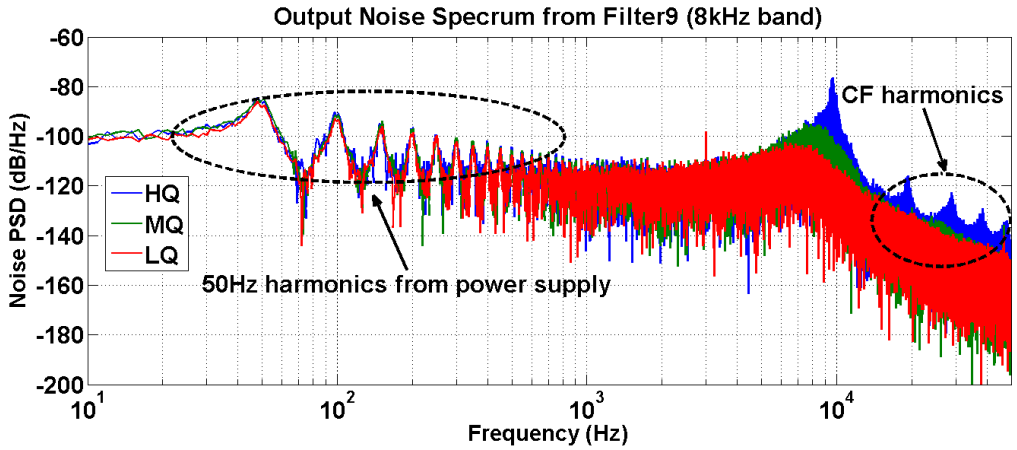


**(b)**

**Figure 5.13:** *Measured output noise spectrum from the 31 Hz and 8 kHz band filters*

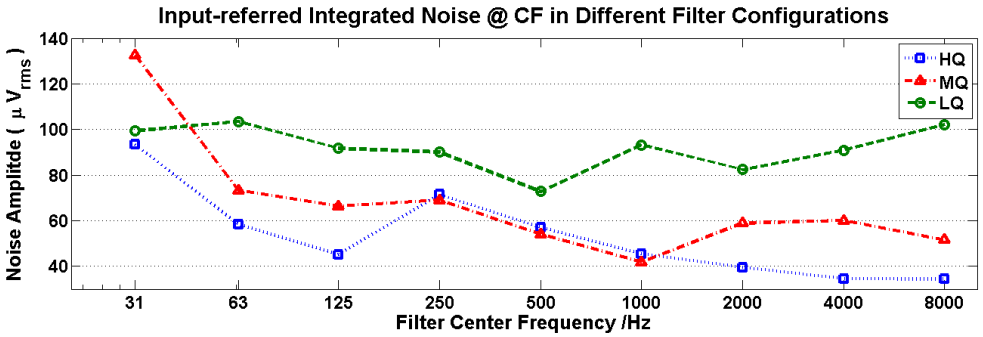


**Figure 5.14:** *Plot of measured input referred noise versus CF*

### 5.2.6 Noise Measurement

The different noise shapes of the LQ, MQ and HQ modes in Fig. 5.13 verify the frequency response characteristics of the proposed cochlea filter from another angle. The 50 Hz harmonics shown are due to the ripples of power supply. Besides, the noise spectrum of the HQ mode of 8 kHz band has prominent peaks at CF harmonics. This indicates that the 8 kHz band has even more harmonic distortion than the 31 Hz band especially in the HQ mode. As shown in Table. 5.3, the DC current in FAI scales with CF. Therefore, the operation of transistors in the FAI moves from weak inversion towards moderate inversion when CF increases. However, the DC operating points of the filter are designed based on the weak inversion assumption, and the circuit linearity will be affected by the DC variation. Besides, the CF harmonics should be well attenuated by the elliptic filter in theory. However, the transistor in moderate inversion has lower $gm/I_D$ compared with weak inversion which makes the FAI inductance deviate from designed values and consequently degrade the elliptic filter performance. The harmonic distortion issue will be discussed further in Section. 5.2.7.

The input-referred noise densities at the CFs of the 9 filter bands are illustrated in Fig. 5.14. Compared with the noise prediction function of Eq. 4.75, the measured results in MQ and HQ modes agree that the input referred noise decreases for higher CFs. However, LQ mode shows noise has little variation from low to high frequencies, probably because the filter selectivity is not high enough to overcome the added power supply harmonics from the increase of filter bandwidth. Besides, Fig. 5.14 proves that the increase of tuning factor $x$ results in lower input referred noise. An exception is the 31 Hz band whose MQ response has even wider ERB than the LQ response as shown in Table. 5.3.

### 5.2.7 Total Harmonic Distortion (THD) and Signal-to-Noise and Distortion Ratio (SINAD)

Fig. 5.15 shows the plots of THD and SINAD against input level based on the measured results from the 31 Hz and 8 kHz bands. The SINAD of both filters generally maintain above the 12dB SINAD threshold for intelligent hearing before THD reaches the edge of 5% limit. The HQ mode has most significant harmonic distortion due to high LPF gain and thus high signal amplitude at the elliptic filter input. As predicted in the noise spectrum (Fig. 5.13(b)), the 8 kHz band has more harmonic distortion than the 31 Hz band. Based on the 5% THD limit, the maximum input level is plotted against filter CFs, so is the maximum SINAD. Fig. 5.16 shows

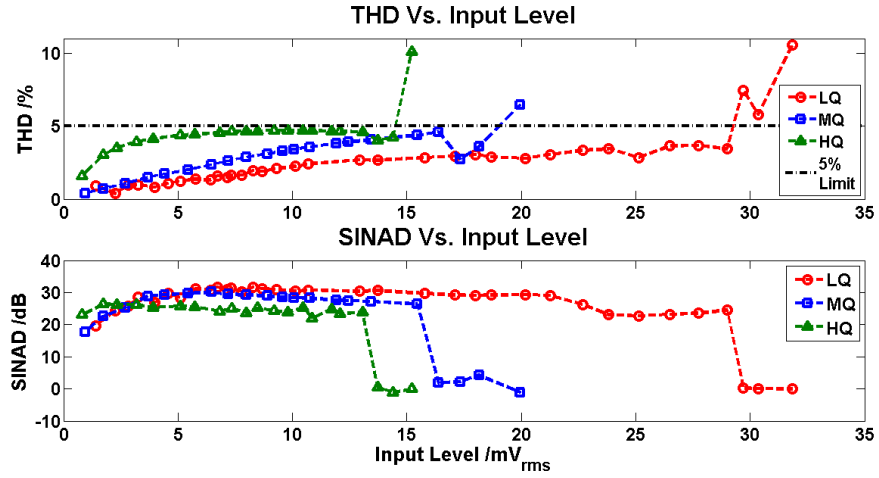


**(a)** 31 Hz

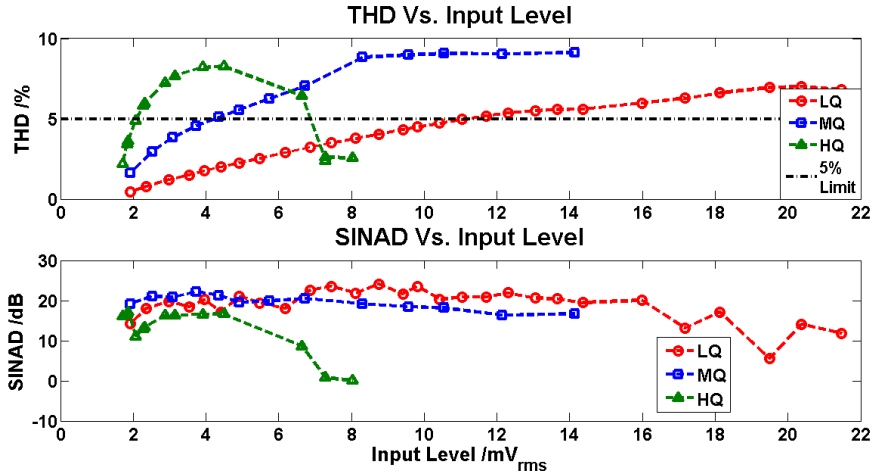


**(b)** 8 kHz

**Figure 5.15:** *Measured THD and SINAD plots versus input level from (a) 31 Hz and (b) 8 kHz band filters*

the filter linearity tends to degrade in higher frequencies.

### 5.2.8 Two-tone Inter-modulation Test

The two -tone inter-modulation distortion test is performed and the results are shown in Fig. 5.17. The third-order inter-modulation product $2f_1 - f_2$ appears to be the most prominent distortion component because it is designed to coincide with the filter CF. The inter-modulation distortion is also found in the biological cochlea, which proves that the biological hearing system can tolerate the 17$\sim$24dB worst-case spurious free dynamic range (SFDR) [116]. Fig. 5.18 plots the filter maximum input range measured using the 17dB SFDR limit. It shows in most of the

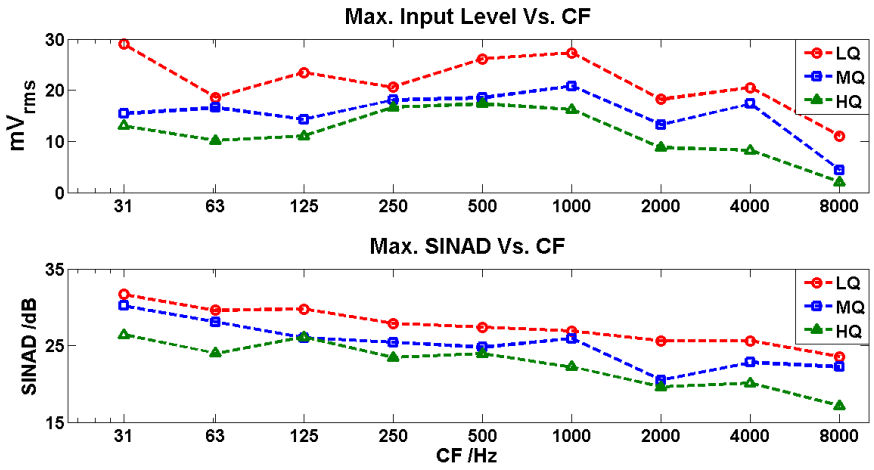


**Figure 5.16:** *Measured maximum input range and SINAD across different CFs*

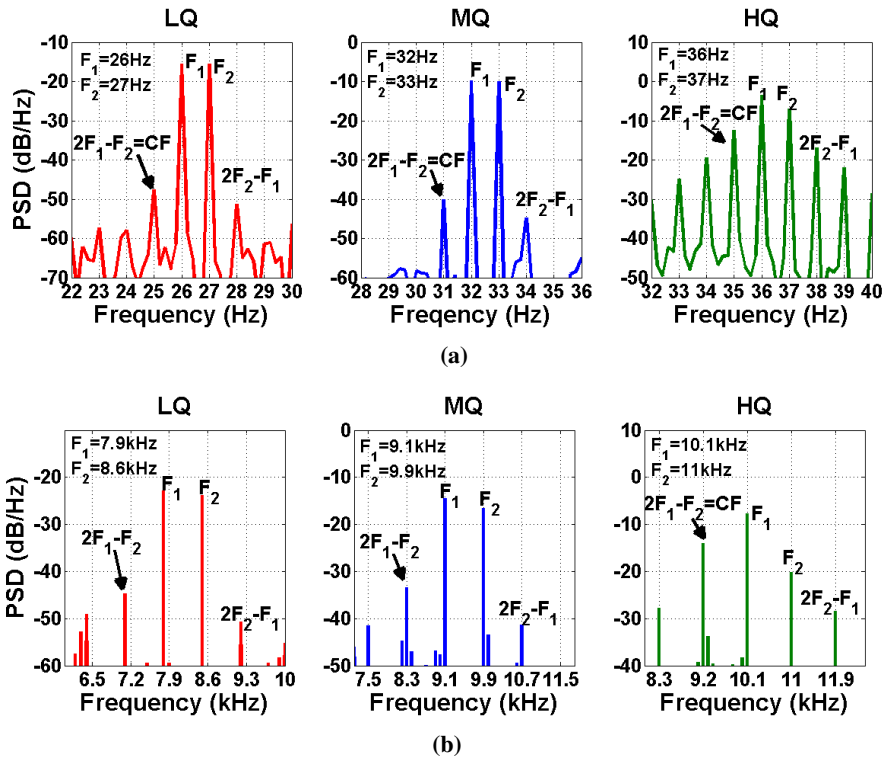


**Figure 5.17:** *Two-tone inter-modulation distortion measured from (a) 31 Hz and (b) 8 kHz band filters. Two signals in equal amplitude (10mV) with primary frequencies $f_1$ and $f_2$ such that $2f_1 - f_2 = CF$ are applied to the cochlea filter.*

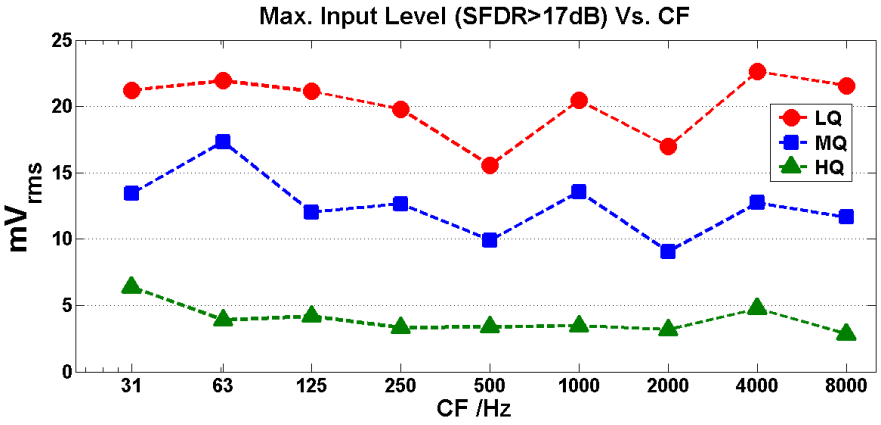


**Figure 5.18:** *Maximum input range measured across different CFs using the 17 dB SFDR limit.*

frequency bands the maximum input range is further reduced compared with the results based on the 5% THD limit. Nevertheless, the input range of the 8 kHz band appears even higher than the results in Fig. 5.16 and there is no significant degradation compared with the other bands. The distortion products of interest in the inter-modulation measurement are in-band signals while the CF harmonics measured in the THD test are out-of-band signals. Therefore, the discrepancy of results indicates that the high harmonic distortion measured in the 8 kHz band is probably due to the degraded stop-band attenuation.

### 5.2.9 Testing with Acoustic Signals

A segment of acoustic signal (mixed sounds from musical instruments of the horn and bass drum) is applied to the cochlea filter. The spectrogram of the signal is shown in Fig. 5.19. Since the signal amplitude has been reduced to be compatible with the linear range of the cochlea filters, the actual input signal is mixed with quantisation noise. As the frequencies around 63 Hz, 1 kHz and 2 kHz have highest intensity, the cochlea filter is tested in these three frequency bands accordingly and the results are shown in Fig. 5.20; the output combinations of the three channels are shown in Fig. 5.21. The results prove the frequency selectivity of the cochlea filters and show that the quantisation noise has been attenuated, especially by the filters in HQ mode.

Nevertheless, as shown in Fig. 5.20, the noise around CF is selectively amplified rather than the signal in the HQ output of the 1 kHz band. This is due to the fact that the cochlea filter

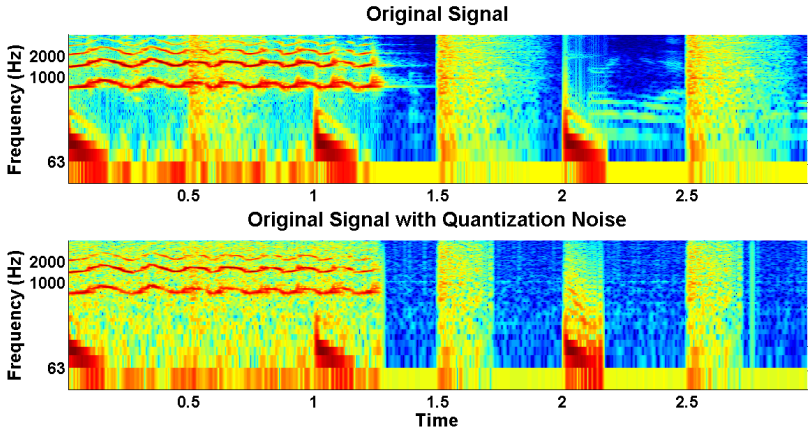


**Figure 5.19:** *Spectrogram of the input acoustic signal. The signal is applied together with the quantisation noise from the 13-bit DAC in the NI-6732 analog output.*

currently does not have the capability to distinguish between the signal and the noise. This problem can be potentially solved by adding the SNR estimation mechanism [30]. Besides, the results show that the octave distribution of filter CFs is inadequate for high performance audio signal processing. As for future applications, more sophisticated distributions like one third octave or bark scale will be employed.

### 5.2.10 Others

Table 5.4 lists the measured specifications of the cochlea filter chip. Note that the power dissipation of the FDDA and the output buffers does not scale with filter CF. As a result, the power dissipation of the 31 Hz filter is only one-third less than that of the 8 kHz filter. Table. 5.5 summarises the scores in terms of auditory filter model following the criteria given by Lyon [117]. The cochlea filter has not been integrated with ATC block in hardware, but as the input-dependent function has been proven by the Simulink simulation results in Chapter 3 , a potential '+' credit is given in the 'dynamic' criterion.

## 5.3 Summary

The experimental results of the cochlea filter chip is presented in this chapter. The highlights are summarised as follows

- As predicted by the filter model in Chapter 3, the filter has highly faithful frequency

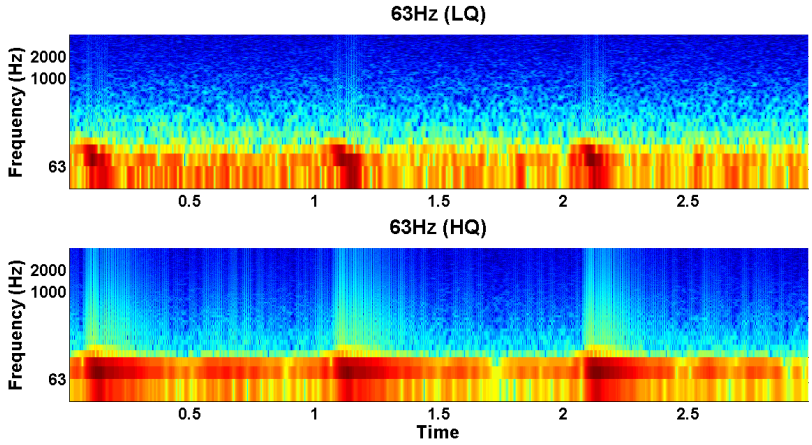


**(a)** 63Hz band

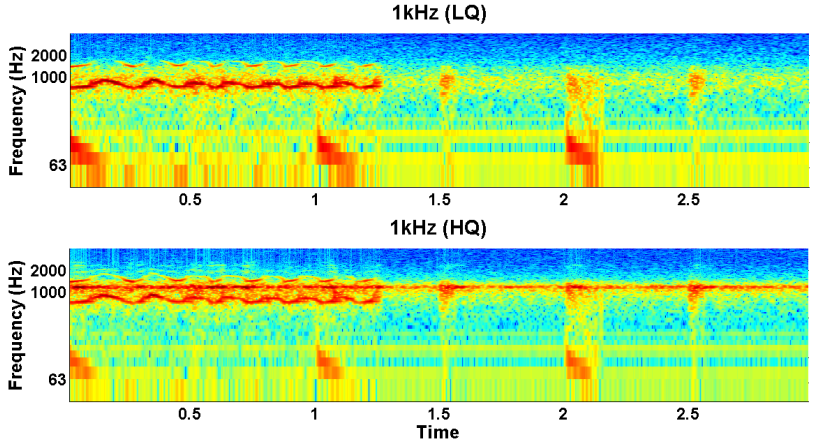


**(b)** 1kHz band

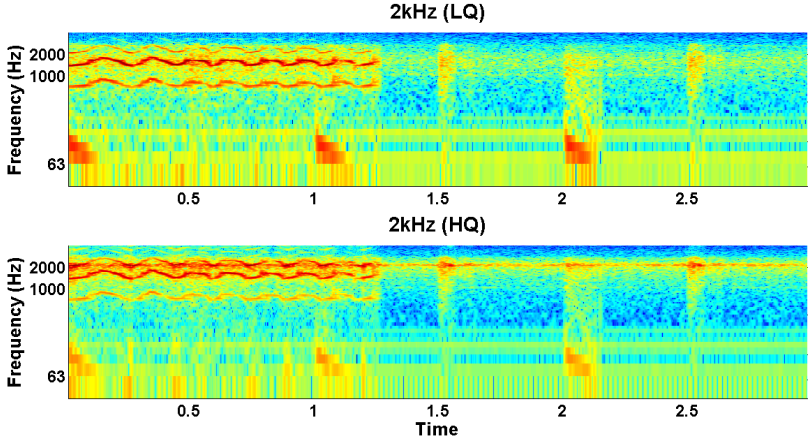


**(c)** 2kHz band

**Figure 5.20:** *Measured time-frequency spectrogram of outputs from the cochlea filters in response to mixed acoustic signals of roaring horn and bass drum.*

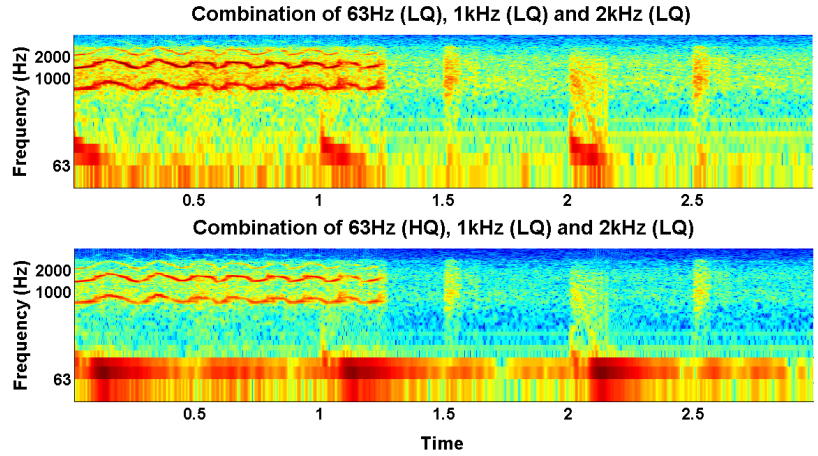


**(a)**

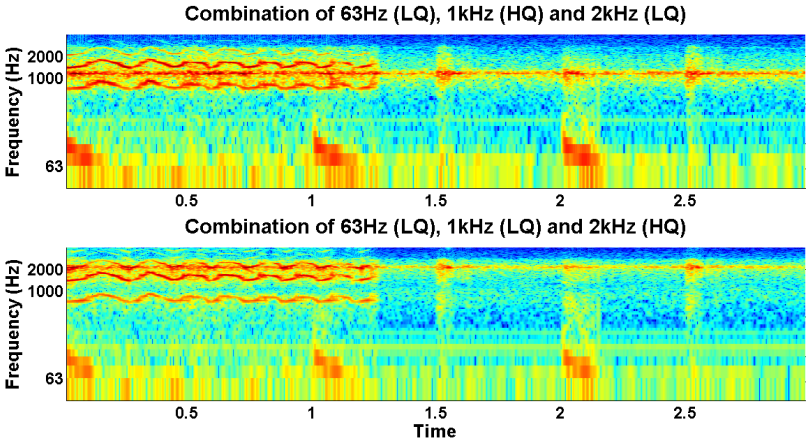


**(b)**

**Figure 5.21:** *Combination of the three band outputs.*

| | |
|---|---|
| Fabrication process | AMS 0.35 $\mu$m 3.3V 2P4M |
| Channel area | $0.9mm^2$ (0.99mm X 0.91mm) |
| CF | 31 Hz$\sim$8 kHz |
| Power dissipation | 59.5$\mu$W @31 Hz;<br>90.0$\mu$W @8 kHz. |
| Peak gain variation | 18.8dB @31 Hz;<br>21.1dB @8 kHz. |
| Cut-off slope | 125.5dB/dec(LQ) $\sim$ 336.2dB/dec(HQ) @31 Hz;<br>123.6dB/dec(LQ) $\sim$ 268.4dB/dec(HQ) @8 kHz. |
| Phase delay @CF | 210.5degree(LQ) $\sim$ 373.1degree(HQ) @31 Hz;<br>204.8degree(LQ) $\sim$ 347.4degree(HQ) @8 kHz. |
| Min. input noise | 93.34$\mu V_{rms}$ @31 Hz;<br>34.32$\mu V_{rms}$ @8 kHz. |
| Max. input swing<br>(THD$<5\%$) | 82.0 $mV_{p-p}$ @31 Hz;<br>31.2 $mV_{p-p}$ @8 kHz. |
| Max. input swing<br>(SFDR>17dB) | 60 $mV_{p-p}$ @31 Hz;<br>61 $mV_{p-p}$ @8 kHz. |
| SINAD | 26.38dB (HQ) $\sim$ 31.67dB (LQ) @31 Hz;<br>17.13 dB (HQ) $\sim$ 23.56dB (LQ) @8 kHz. |
| Expected dynamic<br>range with AQC * | 49.8dB @31 Hz;<br>50.2dB @8 kHz. |

*The lower bound is determined by the HQ input-referred noise and the upper bound is determined by the LQ linear range.

**Table 5.4:** *Summary of Chip Specifications*

response as the biological cochlea: it replicates the gentle and constant response in low-frequency band, variable and selective CF response and the sharp transition from pass-band into stop-band. Besides, the similarities in phase response, group delay and impulse response are also proven by the chip results.

- The filter is able to operate at CFs from as low as 31 Hz to as high as 8 kHz. Experimental results show that the filter operation does obviously not degrade in deep low frequencies.

- Filter efficiency has been improved by the specialised triple-stage design, to the extent that:

| | | | |
|---|---|---|---|
| 1. Simple | laplace domain | 6. Stable tail | + |
| 2. BW control | + | 7. Runnable | + |
| 3. Peak/skirts | + | 8. Waves | * (partial) |
| 4. Asymmetry | + | 9. Impulse resp. | + |
| 5. Gain Variation | + | 10. Dynamic | + (potentially) |

**Table 5.5:** *Scores as an Auditory Filter Model [117]*

  - The active behaviour observed in biology is emulated by tuning only one circuit parameter (tuning factor $x$), and positions of only one pair of poles (poles of LPF) are shifted in tuning. The reduced tuning complexity will prospectively improve the system robustness and dynamic performance of when the filter is integrated with ATC.
  - In previous second-order section based filters, the biologically-realistic 330dB/dec roll-off requires the filter order to be at least 16 [94]. The same steepness is achieved in this $9^{th}$ order design by using a sharp cut-off elliptic filter. The lower filter order leads to less power consumption and smaller chip area for each channel, and thus a larger number of channels can be implemented in a parallel filter bank, which will prospectively increase the functionality of the future cochlea system shown in Fig. 1.3.

Nevertheless, the experimental results also suggest a couple of improvements are necessary in the future such as:

- The filter dynamic range is constrained by the limited linear range of the tanh transconductance in the FAIs. Linearisation techniques such as multi-tanh [118] may be investigated in the future.
- Other mechanisms including local control (AQC) and signal-noise distinguishing mechanism should be integrated with the filter as the next step.

# Chapter 6
# MEMS Interface Circuit Towards a MEMS-CMOS Cochlea Filter

In this chapter, the possibilities of an alternative approach to implement the cochlea filter employing MEMS technology are investigated. A novel MEMS interface circuit is developed to address a key challenge in such approach. The circuit design method is elaborated and the experimental results from the prototype chip are provided and discussed.

## 6.1 Introduction

Implementation of cochlea-like sensors using MEMS technology has become an emerging research topic during the past decade [56, 119–121]. The basis of a MEMS cochlea sensor is an array of acoustic resonators such as the 'fishbone' structure [56], the cantilever array structure [119], the beam-membrane structure [120] and the resonant gate transistors [121]. Generally, the resonant structures are based on long beams as shown in Fig. 6.1. In a MEMS-based cochlea system, the frequency separation is performed mechanically rather than electronically, which results in a number of advantages such as higher stability and less power consumption. Although the MEMS acoustic resonators are still far from the characteristics of the biological cochlea, their proven band-pass functions have already made them a sufficient substitute for the BPF of the cochlea filter proposed in this thesis.

To implement a MEMS-CMOS cochlea filter, the interface circuitry is required to convert the motion of the MEMS structure into electrical signals. The most commonly used MEMS interface technique is the capacitive sensing method. As shown in Fig. 6.2, a sensing capacitor $C_m$ is formed by the sensing structure and the bottom electrodes. The sensing structure is biased with a DC voltage $V_b$ and the bottom electrodes are grounded through a high-impedance path. Therefore, the charge of $V_b \cdot C_m$ is stored on the sensing capacitance. Since the ground path has high impedance, the charge on $C_m$ keeps approximately constant when the sensing capacitance varies and thus the capacitance variation is converted to the voltage output ($V_s$) which is fed to

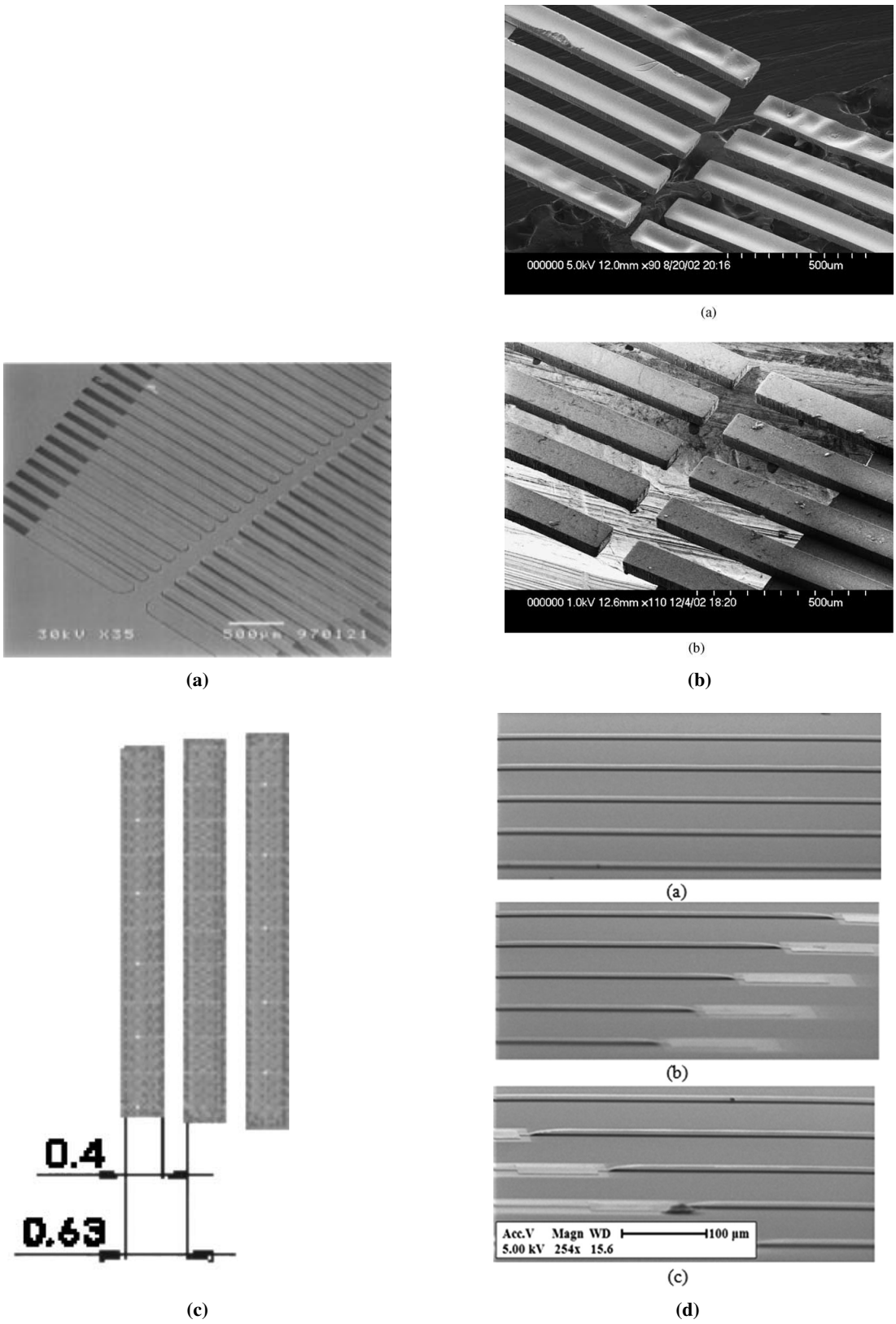


**Figure 6.1:** *The long beam structures in the MEMS acoustic resonators. Fig. 6.1(a) is taken from [56]; Fig. 6.1(b) is taken from [119]; Fig. 6.1(c) is taken from [120]; Fig. 6.1(d) is taken from [121]*

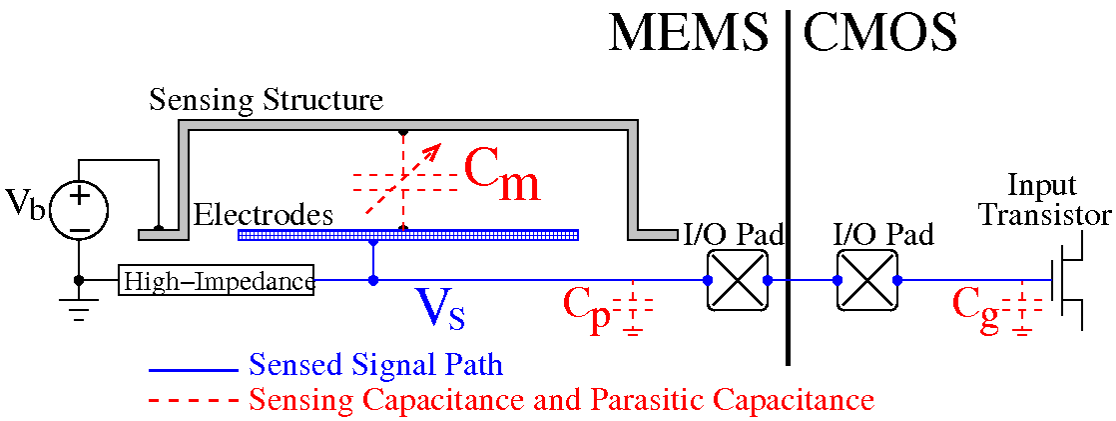


**Figure 6.2:** *Capacitive sensing technique.*

the CMOS transistors. $V_s$ is given by

$$V_s = \frac{V_b \cdot \Delta C_m}{C_m + C_p + C_g}. \tag{6.1}$$

where $C_p$ represents the parasitic capacitance due to I/O pads and wire connections and $C_g$ represents the input capacitance of the CMOS circuits. Since the beam-type MEMS acoustic resonators have long and slim shape, their sensing capacitance will be very small. Therefore the output voltage will be significantly degraded by the parasitic capacitance as Eq. 6.1 indicates. As a result, a high-gain amplifier is required for signal amplification. Also, the noise from the CMOS circuits has to be attenuated to maintain a feasible threshold of signal detection.

During the past decade, sensing techniques for MEMS inertial sensors with tens to hundreds of femtofarad sensing capacitance have been developed [122–125]. These works improve the sensor sensitivity by taking advantage of the differential sensing capacitance in the inertial sensors based on which a capacitive Wheatstone bridge is built. By virtue of the balanced bridge structure, the sensing capacitance variation can be directly modulated by applying an AC biasing voltage. Since the sensor signal modulation is performed prior to interfacing with CMOS circuits, all the low-frequency circuits noise can be effectively attenuated with the chopper-stabilisation mechanism. However, the differential structure has not been applicable for acoustic sensors which require open cavities for sound detection. As a result, the modulation can only be performed after the signal is read-out and a source-follower buffer is required to shield the sensor from modulation spurs [126, 127]. Compared with the amplifier, the source-follower has an advantage of less input capacitance which improves the sensitivity. Nevertheless, due to the

unity-gain characteristic, the source-follower performs no attenuation of the noise in later-stage circuits.

All of the above-mentioned works concentrate on signal amplification and noise reduction. Efforts have been made to reduce the parasitic capacitance $C_g$ in Eq. 6.1 [123, 125–127], but the signal degradation induced by $C_p$ is not addressed. Generally speaking, the reported interface circuits thus far similarly follow a high-degradation high-amplification process, which is apparently not power efficient.

In this chapter, a capacitive interface which follows a low-degradation low-amplification process is introduced. A circuit which is able to cancel the parasitic capacitance is developed to reduce signal degradation so that the gain requirement for the later-stage amplifier is lowered. The parasitic-cancellation mechanism does not require extra power and thus the system power efficiency is significantly improved. The chopper-stabilisation technique is also employed to reduce low-frequency noise and circuit offsets. The circuit design is elaborated in Section 6.2. The experimental results from the prototype VLSI chip are discussed in Section 6.3. The chip is fabricated using the same AMS 0.35 $\mu$m process as the cochlea filter chip in Chapter 5.

## 6.2 Power-Efficient Capacitive Interface Circuits with Parasitic-Cancellation and Chopper-stabilisation

### 6.2.1 System Structure

As shown in Figure. 6.3, the proposed interface circuit consists of a parasitic-cancellation (PC) circuit and a chopper-stabilised amplifier. The PC circuit has two functions. Firstly, as indicated by its name, the PC circuit cancels the parasitic capacitance shown in Fig. 6.2 and improves the sensitivity of the MEMS sensor. Secondly, the PC circuit functions as a buffer to protect the sensor from the effects of charge injection and clock feed-through caused by the choppers. The chopper-stabilised amplifier provides gain to the sensed signal. The two choppers are controlled by the same clock signal and operate respectively as the modulator and the demodulator. The chopper-stabilisation scheme is used to reduce the low-frequency noise and DC offsets of the amplifier.

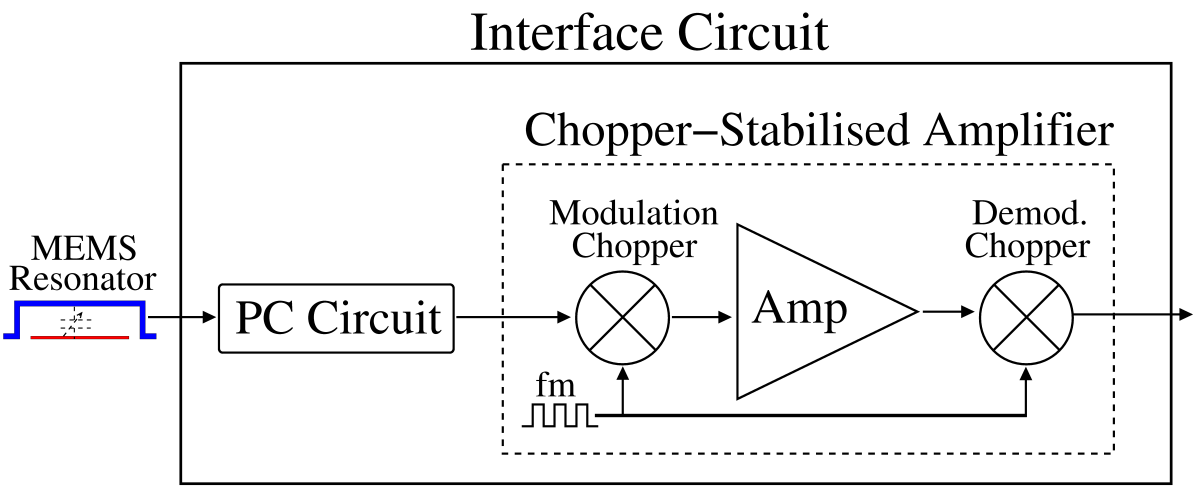


**Figure 6.3:** *System structure of the proposed interface circuit*

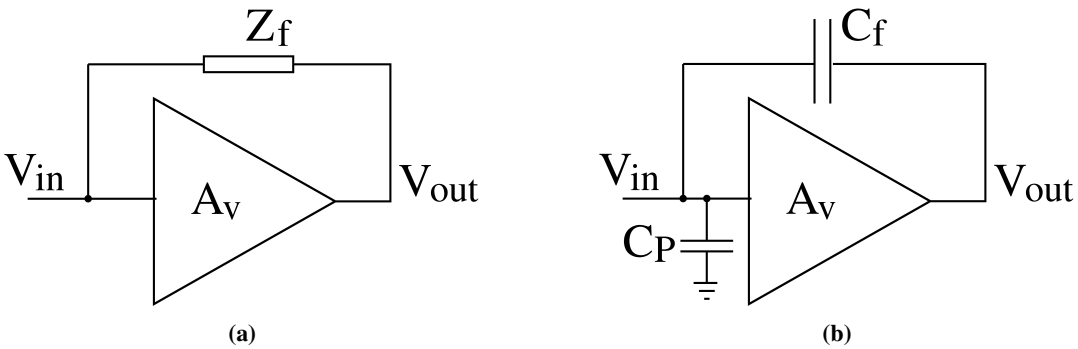


**Figure 6.4:** *Positive feedback structure to generate equivalent negative input impedance.*

### 6.2.2 Parasitic-cancellation Circuits

#### 6.2.2.1 Principle of parasitic-cancellation using negative impedance

The proposed PC circuit cancels the parasitic capacitance using a negative input impedance method. According to the Miller theorem, the negative impedance can be obtained using the positive feedback structure shown in Fig. 6.4(a). The output of the gain stage is positively fed-back to its input through an impedance element $Z_f$. The equivalent input impedance of the circuit is thus given by

$$Z_i = \frac{Z_f}{1 - A_v}. \tag{6.2}$$

Therefore the input impedance becomes negative when the gain exceeds unity. This principle can be applied for cancellation of the parasitic capacitance. As shown in Fig. 6.4, $C_p$ represents the parasitic capacitance at the input of the gain stage and $C_f$ represents the feedback

capacitance. Based on Miller theorem, the equivalent input impedance of the circuit is given by

$$Z_i(s) = \frac{1}{sC_p - sC_f \cdot (A_v - 1)} = \frac{1}{s[C_p - (A_v - 1)C_f]}. \tag{6.3}$$

The parasitic capacitance is reduced by $(A_v - 1)C_f$. For stability issue, Eq. 6.3 should always be positive and thus $(A_v - 1)C_f$ should always be smaller than $C_p$.

#### 6.2.2.2 Parasitic-cancellation circuit design

The schematic of the parasitic-cancellation circuit is shown in Fig. 6.5(a). All transistors operate in saturation region. The core components of the circuit are two pairs of PMOS transistors, $MP_A$ and $MP_B$. The other transistors in Fig. 6.5(a) are all components of the current mirrors. The simplified representation of the circuit is shown in Fig. 6.5(b). The $MP_A$ transistors are input transistor pair based on the common-drain configuration. The cross-connected $MP_B$ transistors function as the active loads. The two pairs of transistors form a fully differential cross-connected source-follower topology. The PMOS transistors are used due to their lower flicker noise compared with the NMOS transistors. Also, since the PMOS transistors are fabricated in the N-Well, the separate bulk connections are possible; the bulks of the transistors $MP_A$ and $MP_B$ are respectively connected to their sources so that the body effect is negligible.

The DC gain of the circuit is given by

$$A_v = \frac{V_{OP} - V_{ON}}{V_{IP} - V_{IN}} = \frac{gm_A}{gm_A - gm_B}, \tag{6.4}$$

where $gm_A$ and $gm_B$ respectively represent the transconductance of $MP_A$ and $MP_B$. As shown in Fig. 6.5, the bias current for $MP_A$ is $I_0$ and the bias current for $MP_B$ is $I_0 - I_X$. The dimensions of $MP_A$ and $MP_B$ are made identical for ease of analysis. Since low output impedance is required for the circuit, the transistors $MP_A$ are designed to operate in strong inversion. The current $I_X$ is designed to be tunable from 0 to $I_0$ and the operation of transistors $MP_B$ spans from strong to weak inversion. Therefore, the EKV model [112] which has uniform expression for different inversion regions is selected to perform circuit analysis as follows.

In EKV model, the transconductance of transistors in saturation region is given by

$$gm = 2n\mu\frac{W}{L}U_T q_s, \tag{6.5}$$

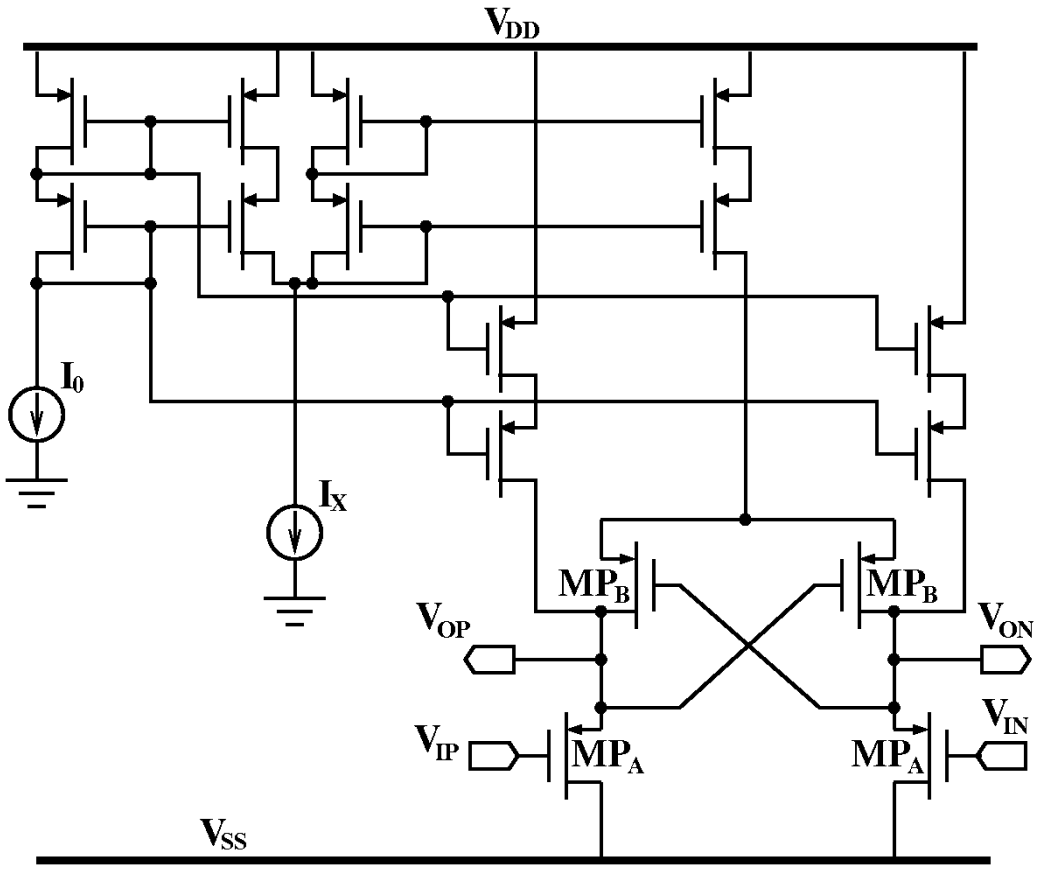


**(a)** Full Schematics

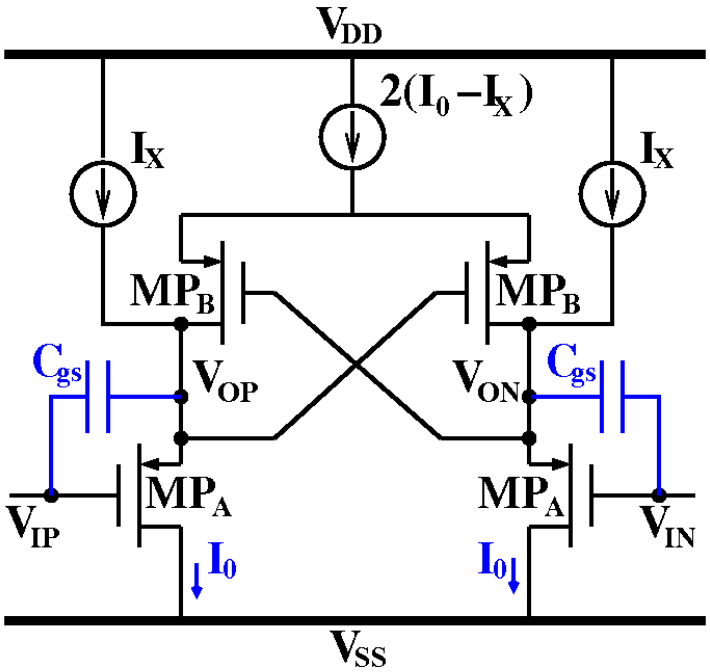


**(b)** Simplified Representation

**Figure 6.5:** *Schematic of the parasitic-cancellation circuit*

where $q_s$ is the normalised charge at the source. $q_s$ is determined by the transistor current:

$$q_s = \frac{\sqrt{4i_f + 1} - 1}{2}, \tag{6.6}$$

where $i_f$ represents the normalised transistor forward current defined by

$$i_f = \frac{I_D}{2n\mu C_{ox}\frac{W}{L}U_T^2} \text{ [112]}. \tag{6.7}$$

$i_f$ is far greater than unity when transistors operate in strong inversion and is far smaller than unity when transistors operate in weak inversion. Based on Eq. 6.5, Eq. 6.6 and Eq. 6.7, the gain of the PC circuit can be represented using current:

$$A_v = \frac{2i_0 - \sqrt{i_0} + \sqrt{i_0 - i_x + \frac{1}{4}} - 2\sqrt{i_0}\sqrt{i_0 - i_x + \frac{1}{4}}}{2i_x}, \tag{6.8}$$

where $i_0$ and $i_x$ are respectively the normalised form of $I_0$ and $I_X$. When $MP_B$ operates in weak inversion, $i_0 - i_x$ is far less than unity and thus

$$A_v \approx \frac{2i_0 - 2\sqrt{i_0} + \frac{1}{2}}{2i_x} \approx \frac{i_0}{i_x} = \frac{I_0}{I_X}. \tag{6.9}$$

When $MP_A$ operates in strong inversion, $i_0 - i_x$ is far greater than unity and thus

$$\begin{aligned} A_v &\approx \frac{2i_0 - \sqrt{i_0} + \sqrt{i_0 - i_x} - 2\sqrt{i_0}\sqrt{i_0 - i_x}}{2i_x} \\ &\approx \frac{i_0}{i_x}(1 - \sqrt{1 - \sqrt{i_x}i_0}) = \frac{I_0}{I_X}(1 - \sqrt{1 - \frac{I_X}{I_0}}). \end{aligned} \tag{6.10}$$

Therefore, the derivative of $A_v$ against $\frac{I_0}{I_X}$ decreases when $MP_B$ shifts from weak to strong inversion.

The transistors have intrinsic capacitance $C_{gs}$ between the gate and the source [112–115]. As shown in Fig. 6.5(b), $C_{gs}$ forms a positive feedback loop from the output to the input. According to Eq. 6.2, the equivalent input capacitance of the circuit is given by

$$C_g = -C_{gs} \cdot (A_v - 1). \tag{6.11}$$

Therefore the circuit is able to cancel the parasitic capacitance when interfacing MEMS res-

onators. According to Eq. 6.1, the sensed output voltage is given by

$$V_s = \frac{V_b \cdot \Delta C_m}{C_m + C_p + C_g} = \frac{V_b \cdot \Delta C_m}{C_m + [C_p - (A_v - 1)C_{gs}]}. \tag{6.12}$$

Note that the output from the PC circuit is given by

$$V_o = V_s \cdot A_v = \frac{A_v V_b \cdot \Delta C_m}{C_m + [C_p - (A_v - 1)C_{gs}]}. \tag{6.13}$$

The output reaches maximum when $A_v$ equals $\frac{C_p}{C_{gs}} + 1$ so that $C_p$ is fully cancelled. The output in this case is given by

$$V_{o,MAX} = \frac{V_b \cdot \Delta C_m (\frac{C_p}{C_{gs}} + 1)}{C_m}. \tag{6.14}$$

$A_v$ is designed to be variable by tuning the current $I_X$. As a result the negative capacitance can be adjusted to match the parasitic capacitance. There are two advantages in this tuning design. Firstly, both the DC operating point and the output resistance of the circuit are determined by the transconductance of $MP_A$. As the current in $MP_A$ keeps constant, neither the DC operating point nor the driving ability of the circuit is affected when $I_X$ varies. Therefore this tuning mechanism has fairly high flexibility. Secondly, the power consumption of the circuit is dependent on $I_0$ rather than $I_X$. Therefore the increase of sensed signal and gain does not result in any extra power consumption, which to a large extent benefits the power efficiency of the entire interface circuit. This issue will be further discussed in Section. 6.2.5.1.

The transistor dimensions are determined based on two factors, the noise and the capacitance. As shown in Fig. 6.3, the PC circuit is the first stage of the interface circuit, and unlike the amplifier, its low-frequency noise cannot be attenuated by chopper-stabilisation. Consequently, the noise of the PC circuit is critical for the overall noise performance of the interface circuit. As analysed in [127], the circuit noise can be optimised by choosing appropriate transistor dimensions. Based on the EKV model [112], the transistor thermal noise and flicker noise are respectively given by

$$\frac{\overline{V_{ntherm}^2}}{\Delta f}(f) = 4kT\frac{{G_{nD}}^2}{gm}, \tag{6.15}$$

$$\frac{\overline{V_{n1/f}^2}}{\Delta f}(f) = \frac{K_F}{C_{ox}^2 WLf}, \tag{6.16}$$

where $G_{nD}$ is transistor thermal noise conductance, $K_F$ is the flicker noise coefficient and $f$ is

frequency. $G_{nD}$ is determined by

$$G_{nD} = \frac{n\beta U_T}{3} \cdot \frac{4q_s^2 + 3q_s}{q_s + 1} \tag{6.17}$$

According to Eq. 6.6 and Eq. 6.7, Eq. 6.15 can be rewritten as

$$\frac{\overline{V_{ntherm}^2}}{\Delta f}(f) = \frac{2n^2 kT}{3I_D}\left(2\sqrt{\frac{2I_D L}{n\mu C_{ox} W} + U_T^2} + U_T\right). \tag{6.18}$$

According to Eq. 6.18, low thermal noise results from wide transistor width and short length, while according to Eq. 6.16, low flicker noise results from wide transistor width and long length.

Besides, to increase the maximum output of the PC circuit, the capacitance $C_{gs}$ should be decreased according to Eq. 6.14. $C_{gs}$ is related with the transistor dimension in the following equation

$$C_{gs} = WLC_{ox} \cdot \frac{q_s}{3} \cdot \frac{2q_s + 3}{(q_s + 1)^2} = \frac{WLC_{ox}}{3}[2 - \frac{1}{q_s + 1} - \frac{1}{(q_s + 1)^2}]\ [112]. \tag{6.19}$$

Based on Eq. 6.6 and Eq. 6.7, the equation is rewritten using $i_f$ as

$$C_{gs} = \frac{2n\mu U_T^2 W^2 \cdot i_f}{3I_D}[2 - \frac{2}{\sqrt{4i_f + 1} + 1} - \frac{1}{(\sqrt{4i_f + 1} + 1)^2}]. \tag{6.20}$$

Thus small $C_{gs}$ results from narrow transistor width and low $i_f$ which prefers short transistor length as Eq. 6.7 indicates.

| | W | L |
|---|---|---|
| Low flicker noise | ↑ | ↑ |
| Low thermal noise | ↑ | ↓ |
| Small $C_{gs}$ | ↓ | ↓ |

**Table 6.1:** *Optimisation of transistor dimensions for noise and capacitance.*

Above analysis is summarised in Table. 6.1. To make compromise between thermal noise, flicker noise and capacitance, the combination of wide width and short length is selected since both of them are preferred for 2 out of the 3 criteria. In practice, the transistor width is set as 280 $\mu$m and the transistor length is set as 0.35 $\mu$m.

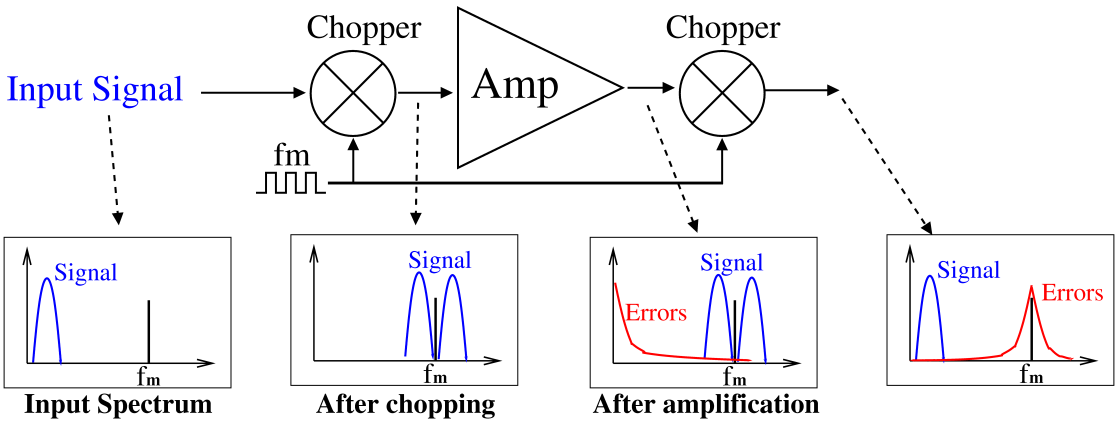


**Figure 6.6:** *Principle of chopper-stabilisation technique for low-frequency error elimination*

### 6.2.3 Chopper-Stabilised Amplifier

The chopper-stabilisation technique is commonly used to reduce flicker noise and circuit offsets [113]. Both the flicker noise and circuit offsets are low-frequency circuit errors, and thus their negative effects are especially significant on low frequency audio circuits. The principle of chopper-stabilisation is to remove low-frequency circuit errors from signals using a pair of chopper modulators. As shown in Figure. 6.6, the signal spectrum is shifted to the modulation frequency before amplification and thus refrained from the low frequency errors of the amplifier; after the second modulation, the signal is recovered while the low frequency errors are shifted to the modulation frequency. As a result, the signal and the errors are separated.

The schematic of the chopper-stabilised amplifier is shown in Fig. 6.7. As high gain is not required, a single-stage amplifier is used. The choppers are built using complementary MOS switches where a PMOS transistor and a NMOS transistor are connected in parallel. The PMOS and NMOS transistors have opposite charge injections which cancel with each other so that the charge injection effect of the switch is significantly reduced [115]. Each chopper consists of two pairs of switches, a forward pair and a cross pair. The forward pair is controlled by clock signal $CLK+$ and the cross pair is controlled by $CLK-$. $CLK+$ and $CLK-$ are required to be non-overlapping to avoid metastability. The circuit shown in Fig. 6.8 is used to generate the non-overlapping clock signals.

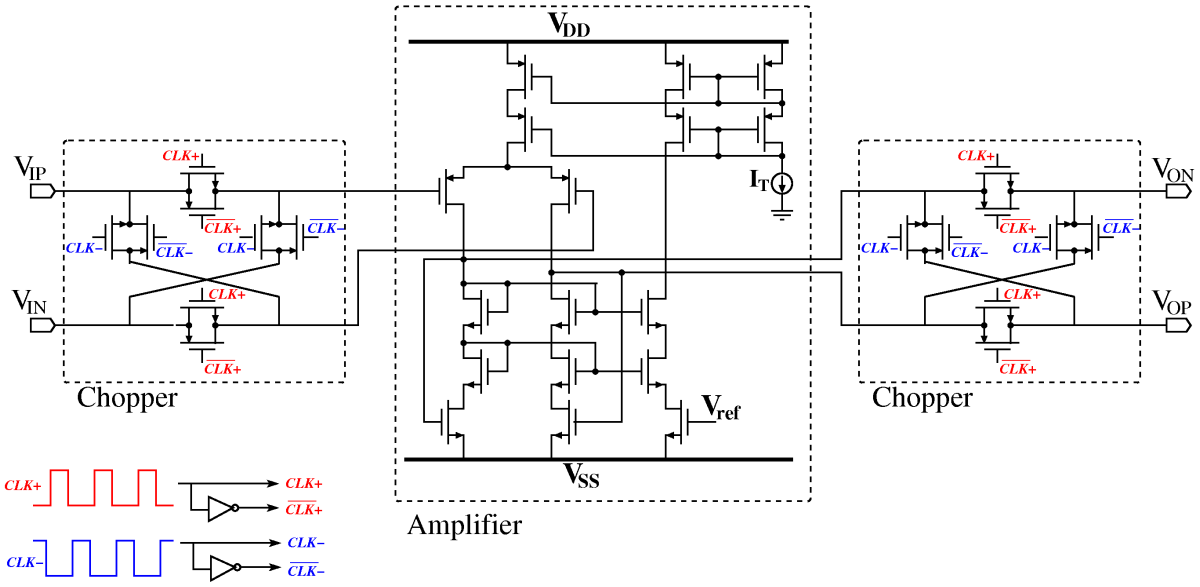


**Figure 6.7:** *Schematic of the chopper-stabilised amplifier*

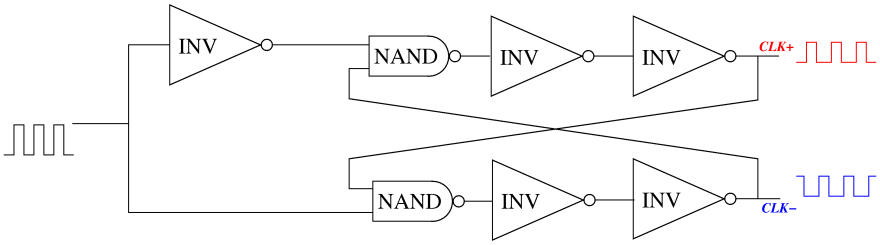


**Figure 6.8:** *Non-overlapping clock generator based on NAND gate and inverter.*

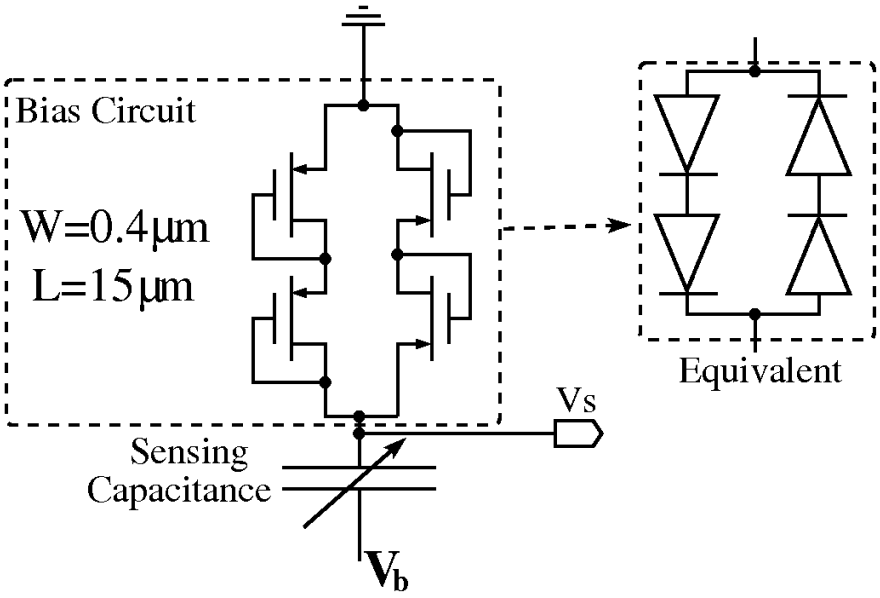


**Figure 6.9:** *Sensor bias circuit.*

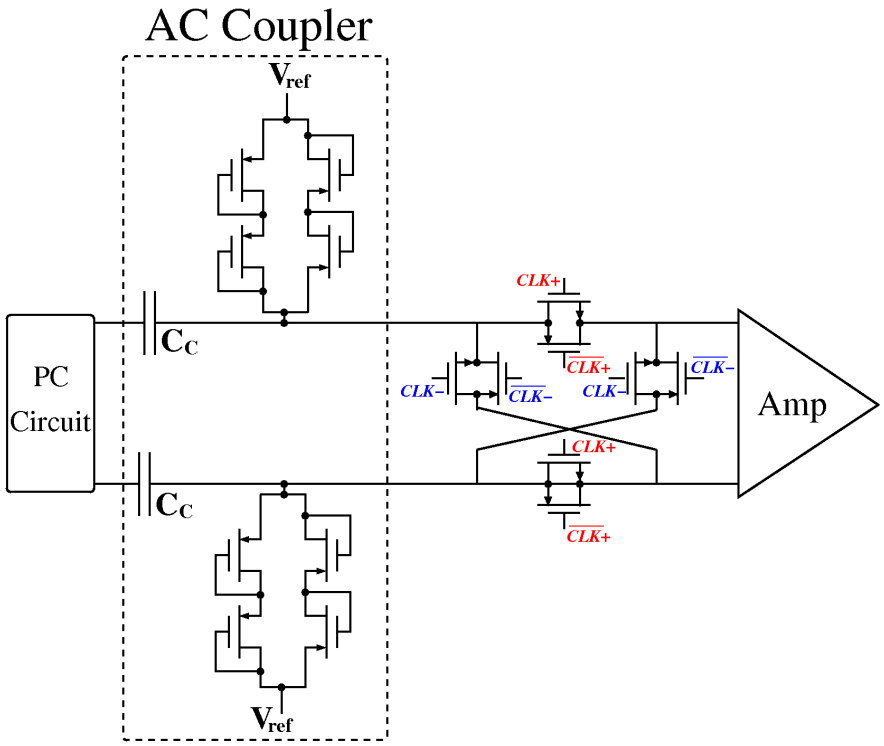


**Figure 6.10:** *The AC coupler circuit between the PC circuit and the chopper-stabilised amplifier.*

### 6.2.4 Other Circuits

A sensor bias circuit is required to provide the high-impedance ground path shown in Fig. 6.2. To ensure that the charge keeps approximately constant when sensing capacitance varies, the time constant of the RC circuit formed by the sensing capacitance and the AC resistance of the bias circuit has to be longer than the sensor vibration period. The sensing capacitance of the MEMS resonator is expected to be less than 1 pF and thus the biasing resistance has to be higher than 10 GΩ. As shown in Fig. 6.9, the diode-connected transistors are used to build such sensor bias circuit. The circuit operates equivalently as a cross-coupled double diode pair. The cross-coupled structure ensures that the DC voltage is passed through to the sensing capacitance while the AC signal is blocked when the sensed voltage is much lower than the diode threshold. To increase resistance, the transistors are optimised into narrow width and long length shape. Besides, two transistors are serially connected to further increase the resistance. The simulation in Cadence Spectre shows that such bias circuit has an AC resistance of roughly 500 GΩ, which sufficiently meets the requirement.

The same diode-connected transistors are used to build an AC coupler circuit between the PC

circuit and the chopper-stabilised amplifier as shown in Fig. 6.10. $C_c$ is the AC coupling capacitor and the diode-connected transistors provide the input DC bias for the chopper-stabilised amplifier. The purpose of the AC coupler is to block the DC offset from the PC circuit which otherwise will cause errors and instability in later-stage circuits. To avoid loading effects from the input capacitance of the chopper-stabilised amplifier, $C_c$ is set with high capacitance (80 pF).

### 6.2.5 System-Level Analysis

Compared with typical designs [122–127], the major improvement in the proposed interface circuit is the employment of the parasitic-cancellation circuit. This section is going to analyse how the PC circuit improves the system-level performance of the overall interface circuit regarding power efficiency and noise.

#### 6.2.5.1 Power Efficiency

As stated above, the PC circuit significantly increases the sensitivity of capacitive sensors. In the typical design based on the simple unity-gain buffer, the voltage output from the buffer is given by Eq. 6.1. As Eq. 6.13 indicates, the output level is increased by at least a factor of $\frac{A_v \cdot (C_m+C_p)}{C_m+C_p-(A_v-1)C_{gs}}$ in this design. Under the extreme circumstance that the parasitic capacitance is fully cancelled, the output level is increased by a factor of $(\frac{C_p}{C_{gs}}+1) \cdot \frac{C_m+C_p}{C_m}$ as suggested by Eq. 6.14. The $C_{gs}$ reaches maximum value of $\frac{2C_{ox}WL}{3}$ when transistor operates in deep strong inversion where $i_f$ in Eq. 6.20 is far less than unity [112]. According to the selected transistor dimensions and the process parameters, the maximum $C_{gs}$ is in the region of 0.3 pF. Based on the assumption that the sensing capacitance of MEMS resonator is 0.5 pF and the parasitic capacitance $C_p$ is 5 pF, the proposed PC circuit increases the output level by at least 45 dB. As a result, the gain requirement for the chopper-stabilised amplifier is reduced by 45 dB, so is the gain-bandwidth product (GBW) requirement. The relationship between amplifier GBW and power consumption is approximated by

$$P = K \cdot GBW^2 C_L^2/(W/L) \tag{6.21}$$

where $K$ is a lumped amplifier constant and $C_L$ is the load capacitor [125]. According to Eq. 6.21, the amplifier is required to consume 38000 times more power to achieve 45 dB extra

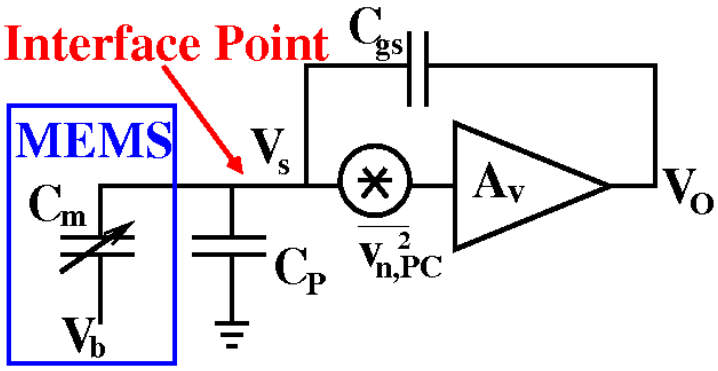


**Figure 6.11:** *Simplified circuit model at the MEMS interface end.* $\overline{v_{n,PC}^2}$ *represents the input-referred noise of the PC circuit.*

gain. Even if using cascaded-amplifier approach, more power consumption is still required since extra amplifier needs to be added. Notably, the PC circuit does not consume any extra power to increase the signal level as explained above. Therefore, the PC circuit significantly improves the overall power efficiency of the interface circuits.

#### 6.2.5.2 Noise Performance

Fig. 6.11 shows the circuit model at the MEMS interface end. The AC output $v_o$ is derived based on Fig. 6.11:

$$v_o = \frac{A_v(C_m + C_p + C_{gs})}{C_m + C_p + C_{gs}(1 - A_v)} \cdot (V_b \cdot \frac{\Delta C_m}{C_m + C_p + C_{gs}} \mp \sqrt{\overline{v_{n,PC}^2}}). \tag{6.22}$$

The equivalent signal-flow graph is illustrated in Fig. 6.12(a); the signal-to-noise ratio (SNR) of the PC circuit output is given by

$$SNR = \frac{(V_b \cdot \frac{\Delta C_m}{C_m + C_p + C_{gs}})^2}{\overline{v_{n,PC}^2}}. \tag{6.23}$$

The PC circuit is in source-follower configuration and its input-referred noise is given by

$$\overline{v_{n,PC}^2} = \overline{v_{nA}^2} + \frac{\overline{i_{nB}^2}}{gm_A^2}, \tag{6.24}$$

where $\overline{v_{nA}^2}$ represents the noise voltage power of the input transistor $MP_A$ and $\overline{i_{nB}^2}$ represents the noise current power of the load transistor $MP_B$ [115]. If the PC circuit has unity gain and thus no parasitic cancellation is performed, the current in $MP_B$ is close to zero and its noise

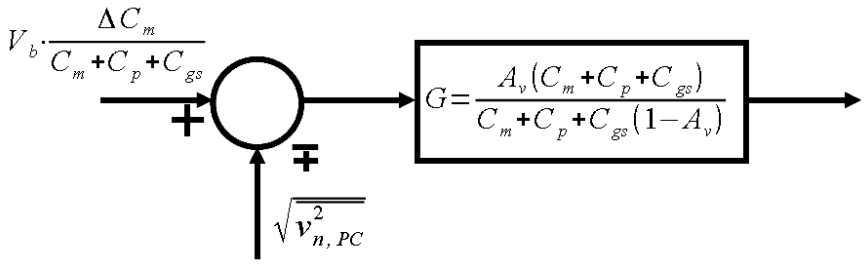


**(a)** Equivalent Signal-Flow Graph of the PC circuit with Noise

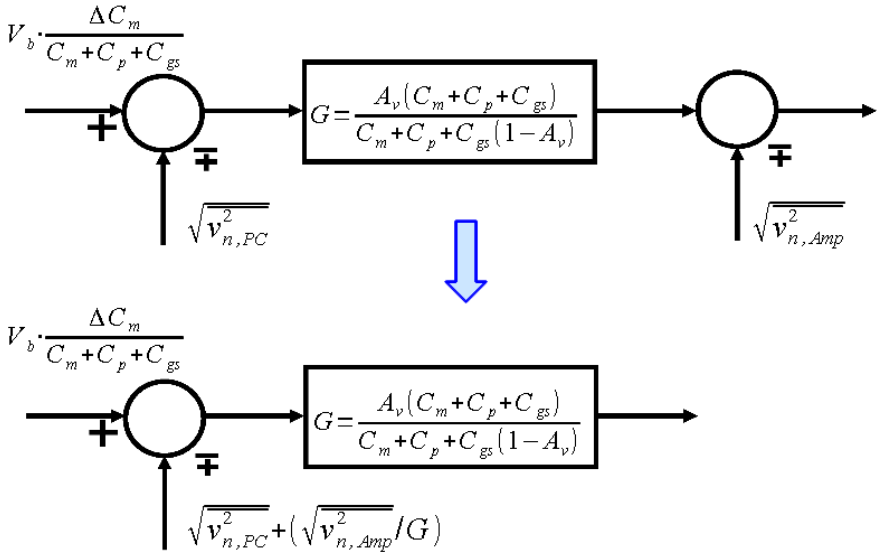


**(b)** Equivalent Signal-Flow Graph Considering Noise from the Amplifier

**Figure 6.12:** *Signal-flow graph representation of the PC circuit.* $\overline{v^2_{n,Amp}}$ *represents the noise from the amplifier.*

contribution is negligible compared with $MP_A$ and thus $\overline{v_{n,PC}^2}$ roughly equals $\overline{v_{nA}^2}$. Under the circumstance that the parasitic capacitance is fully cancelled, the current in $MP_B$ is close to the current in $MP_A$. Since $MP_A$ and $MP_B$ have identical dimension, their noise contribution are roughly the same and thus $\overline{v_{n,PC}^2}$ equals $2\overline{v_{nA}^2}$. Therefore, the SNR of the PC circuit is degraded by half when the parasitic capacitance is fully cancelled. Nevertheless, the gain of the PC circuit results in attenuation of the noise from the chopper-stabilised amplifier, as shown in Fig. 6.12(b). When PC circuit has no parasitic cancellation, the overall SNR is roughly given by

$$SNR = \frac{(V_b \cdot \frac{\Delta C_m}{C_m+C_p+C_{gs}})^2}{\overline{v_{nA}^2} + \overline{v_{n,Amp}^2}}. \tag{6.25}$$

When the parasitic capacitance is fully cancelled, the noise from the amplifier is negligible and the overall SNR is roughly given by

$$SNR = \frac{(V_b \cdot \frac{\Delta C_m}{C_m+C_p+C_{gs}})^2}{2\overline{v_{nA}^2}}. \tag{6.26}$$

Consequently, the parasitic-cancellation has approximately no effect on system SNR when the input-referred noise of the PC circuit and the chopper-stabilised amplifier are equal. However, the SNR is maximally reduced by 3 dB if the noise of the chopper-stabilised amplifier is much less than that of the PC circuit. The principle of this design is to use parasitic-cancellation to reduce signal degradation and thus reduce the gain and power of the chopper-stabilised amplifier. The reduction of power in the chopper-stabilised amplifier increases its noise. According to Eq. 6.25 and Eq. 6.26, the parasitic-cancellation improves the system SNR when the chopper-stabilised amplifier becomes more noisy than the PC circuit. Therefore, the improvement of noise performance from the parasitic-cancellation is concurrent with the improvement of power efficiency.

## 6.3 VLSI Implementation and Chip Results

### 6.3.1 VLSI Chip and Experimental Setup

The proposed interface circuit is implemented in an analogue VLSI chip which is fabricated using AMS 0.35 $\mu$m standard CMOS process. The chip micrograph is shown in Fig. 6.13. To characterise the chip, a prototype PCB is developed as shown in Fig. 6.14. The equivalent circuit model of a capacitive sensor is shown in Fig. 6.15 where the sensing capacitance is rep-

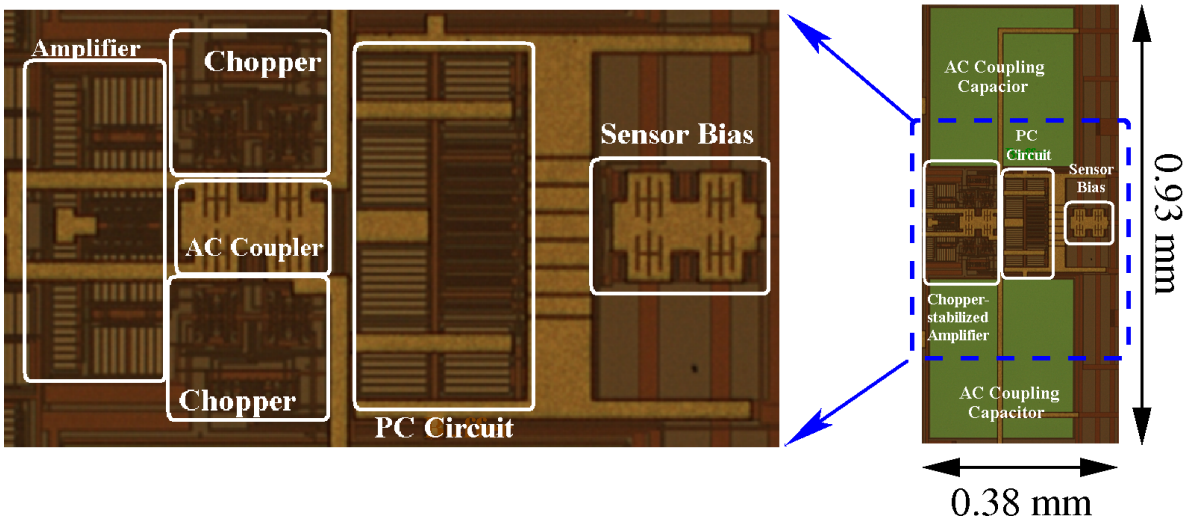


**Figure 6.13:** *Chip micrograph of the interface circuit*

resented by a constant capacitor and the capacitance variation is represented by an AC voltage source. The output of the AC voltage source is given by

$$v_{ac} = \frac{V_b \Delta C_m}{C_m}. \tag{6.27}$$

The 1 pF capacitor array in Fig. 6.14 is used to model the sensing capacitance of the MEMS resonator. By switching between parallel and serial configurations, the total capacitance can be adjusted from 5 pF down to 200 fF. As shown in Fig. 6.16, although a differential sensing structure is not applicable in acoustic sensors, the differential sensor output can still be generated using the pseudo-differential capacitive sensing approach where two identical capacitive sensors are biased with reverse voltage [128]. Therefore the capacitance pair is used to test the interface circuit with differential input signals as shown in Fig. 6.17.

The reconfigurable current sources in Fig. 6.14 are used to provide $I_0$ and $I_X$ for the PC circuit. The other current sources in Fig. 6.14 are used to bias the rest of circuits on the chip. An off-chip function generator is used to generate the 100 kHz square wave signal which is applied for the chopper switch control. The output of the interface chip is analysed using the same LabVIEW system as that in the cochlea filter chip characterisation. More details about the LabVIEW program used to characterise this chip can be found in Appendix A.2

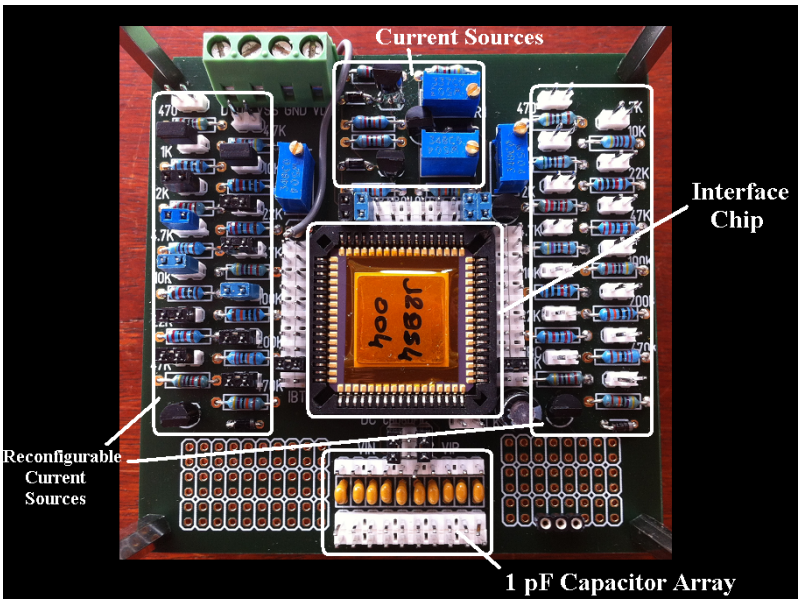


**Figure 6.14:** *Prototype PCB for chip characterisation*

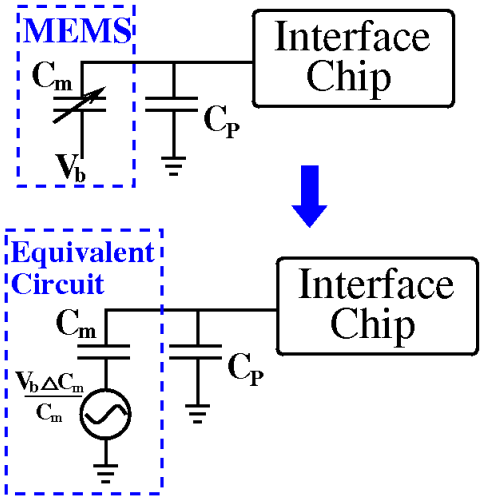


**Figure 6.15:** *Equivalent circuit model for the MEMS capacitive sensor.*

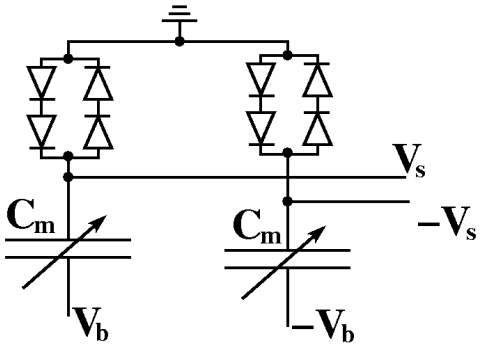


**Figure 6.16:** *Pseudo-differential capacitive sensing method.*

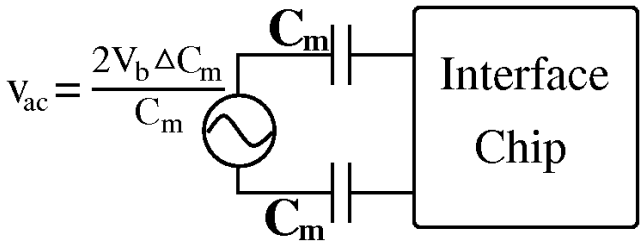


**Figure 6.17:** *Equivalent circuit model for the pseudo-differential capacitive sensing method.*

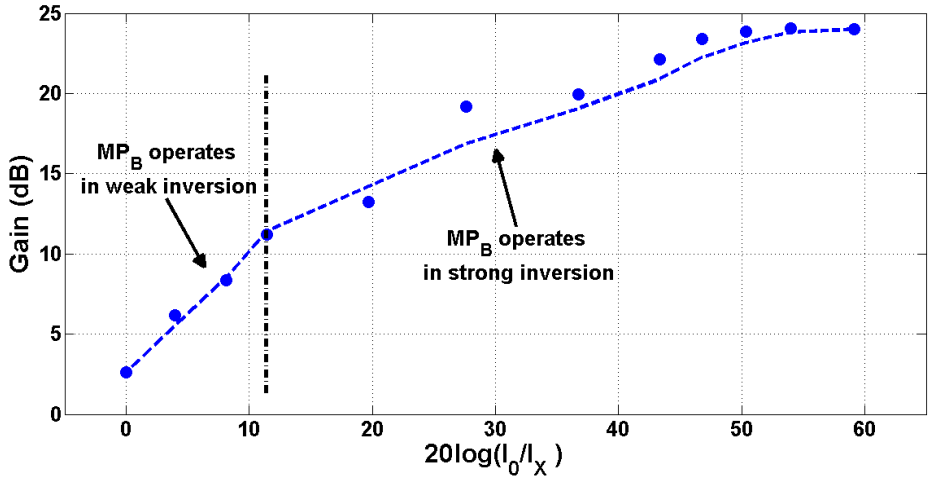


**Figure 6.18:** *Measured gain of the PC circuit versus* $\frac{I_0}{I_X}$.

### 6.3.2 Experimental Results

#### 6.3.2.1 Gain Variation of the PC circuit

The PC circuit is tested with the 500 Hz, 3 mV amplitude sinusoidal input signal. $I_0$ is set constantly as 5 $\mu$A and $I_X$ is adjusted from 7 nA to 5 $\mu$A. Figure. 6.18 illustrates the log-log plot of the measured gain of the PC circuit against $\frac{I_0}{I_X}$. The transistor $MP_B$ operates in weak inversion when $\frac{I_0}{I_X}$ is small and shifts to strong inversion when $\frac{I_0}{I_X}$ grows large. The results in Fig. 6.18 agree with Eq. 6.9 and Eq. 6.10: the gain of the PC circuit linearly increases with $\frac{I_0}{I_X}$ when $MP_B$ operates in weak inversion and the slope of gain growth becomes compressed when $MP_B$ shifts into strong inversion.

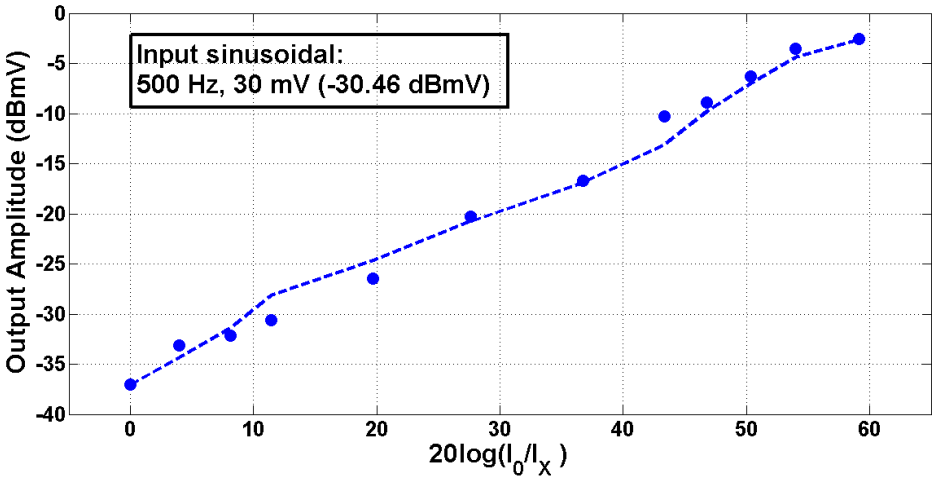


**(a)** Measured Growth of Output Amplitude with $\frac{I_0}{I_X}$

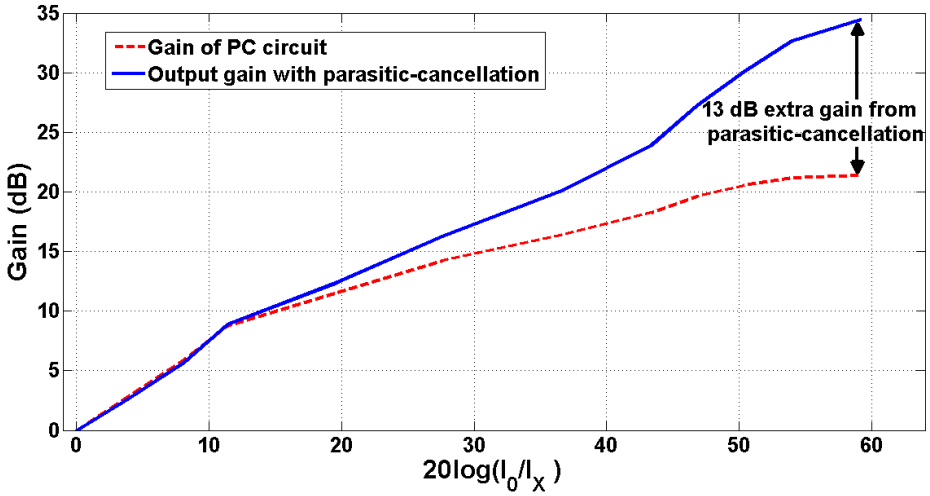


**(b)** Comparison with the Curve in Fig. 6.18

**Figure 6.19:** *Measured output amplitudes from the capacitive interfacing experiments.*

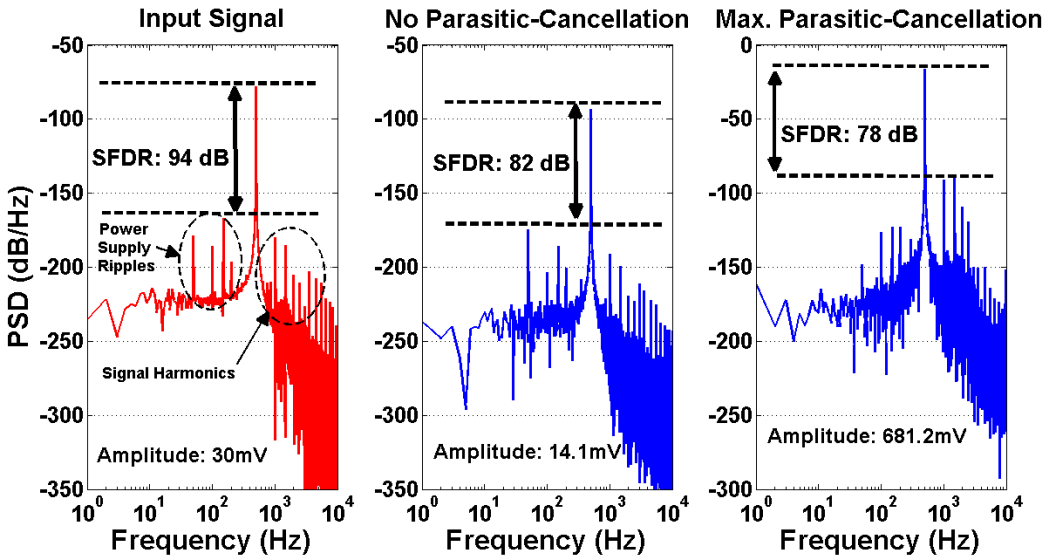


**Figure 6.20:** *Input and output spectrum from the capacitive interfacing experiments.*

#### 6.3.2.2 Capacitive Interfacing Experiment and Effects of parasitic-cancellation

The circuit model shown in Fig. 6.15 is used to test the capacitive read-out function of the interface circuit. A pair of 0.5 pF capacitance is used to model the sensing capacitance and a differential sinusoidal voltage signal with 500 Hz frequency and 30 mV amplitude is applied as $v_{ac}$. This input setting is equivalent to a 7.5 fF maximum capacitance variation from a pair of $\pm 1V$-biased MEMS sensors with 0.5 pF sensing capacitance. The same current settings are applied as that in Section. 6.3.2.1. The output amplitude of the interface chip is plotted against $\frac{I_0}{I_X}$ as shown in Fig. 6.19(a). The PC circuit provides about 35 dB higher gain compared with the unity-gain buffer ($\frac{I_0}{I_X}$=1). As shown in Fig. 6.19(b), the output amplitude is normalised by the minimum output and compared with the curve in Fig. 6.18 within the same coordinate. The comparison shows that the parasitic-cancellation mechanism contributes an extra 13 dB gain. The 35 dB gain is less than the expected (45 dB) probably because the actual parasitic capacitance $C_p$ is smaller then the assumed 5 pF value.

Fig. 6.20 illustrates the spectrum of the input signal and the interface chip output under the two extreme circumstances: the minimum and maximum $\frac{I_0}{I_X}$. As shown in Fig. 6.19(b), there is no parasitic-cancellation for under the minimum $\frac{I_0}{I_X}$ condition and there is maximum parasitic-cancellation under the maximum $\frac{I_0}{I_X}$ condition. The spectrum in Fig. 6.20 shows that the spurious-free dynamic range (SFDR) is slightly reduced by maximum parasitic-cancellation. Furthermore, in the input signal and the output signal when no parasitic-cancellation is applied,

the most prominent spurious component results from the power supply ripples; by contrast, the most prominent spurious component in the maximum parasitic-cancellation output results from the signal harmonics. This shows that the parasitic-cancellation improves the spurious attenuation in lower frequencies but also results in more circuit non-linearity due to the increase of signal amplitude.

The THD, SNR and SINAD of the outputs are respectively plotted against $\frac{I_0}{I_X}$ in Fig. 6.21. As predicted by Fig. 6.20, the THD generally becomes higher when $\frac{I_0}{I_X}$ increases. The SNR is reduced by about 3$\sim$4 dB when $\frac{I_0}{I_X}$ reaches maximum. As analysed in Section. 6.2.5.2, this shows that the input-referred noise of the chopper-stabilised amplifier is much less than that of the PC circuit, which probably results from the effective flicker noise removal by the chopper-stabilisation. The SNR peaks with moderate $\frac{I_0}{I_X}$ where the noise attenuation on the chopper-stabilised amplifier dominates the noise increase of the PC circuit. Compared with the input SNR, the noise figure of the interface circuit is in the region of 3.5$\sim$10.5 dB. The SINAD follows similar trend with SNR curve, but the degradation in high $\frac{I_0}{I_X}$ region is slightly more significant since the harmonic distortion effect is included.

#### 6.3.2.3 Examination of the Chopper-stabilisation Scheme

Two experiments are performed to examine the effectiveness of the chopper-stabilisation (CHS) scheme: the output noise spectrum of the interface chip with and without CHS are measured and compared in Fig. 6.22; the output waveforms in response to 500 Hz, 20 mV sinusoidal input are compared in Fig. 6.23 to show the offset elimination effect. The output noise is measured by grounding the input of the interface chip and analysing the output waveform. The total noise is calculated by performing mean-square-root operation on the output waveform. The result without CHS is obtained by connecting the chopper control signal to $V_{DD}$ so that the forward choppers are always on while the cross choppers are always off. The comparison in Fig. 6.22 shows that the low frequency noise is significantly reduced. Also, the ripples from power supply are attenuated because the reduced offset from chopper-stabilisation improves the common-error cancellation of the fully differential circuits. The effectiveness of offset elimination is proven in Fig. 6.23.

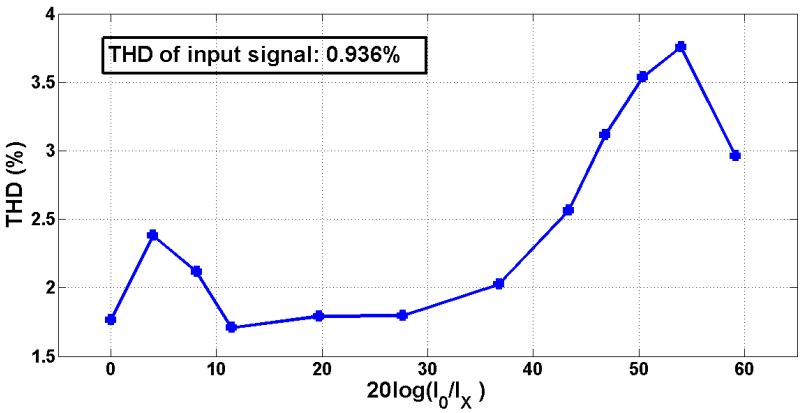


**(a)** Growth of THD with $\frac{I_0}{I_X}$

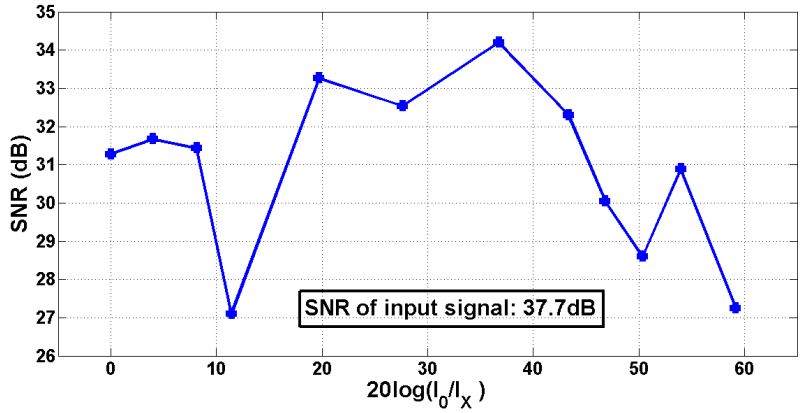


**(b)** Growth of SNR with $\frac{I_0}{I_X}$

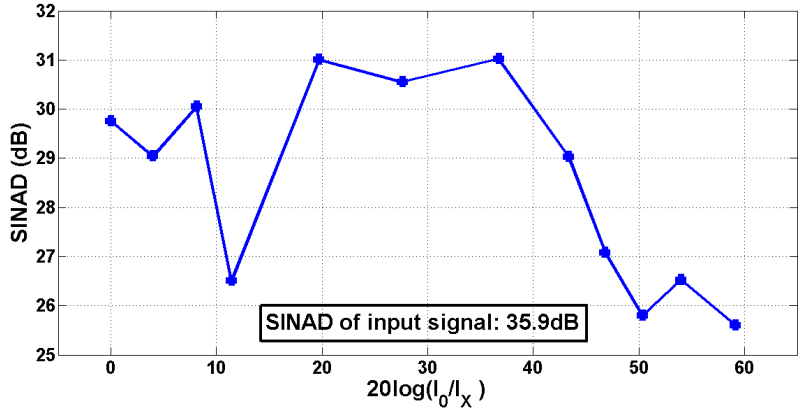


**(c)** Growth of SINAD with $\frac{I_0}{I_X}$

**Figure 6.21:** *Measured THD, SNR and SINAD from the capacitive interfacing experiments.*

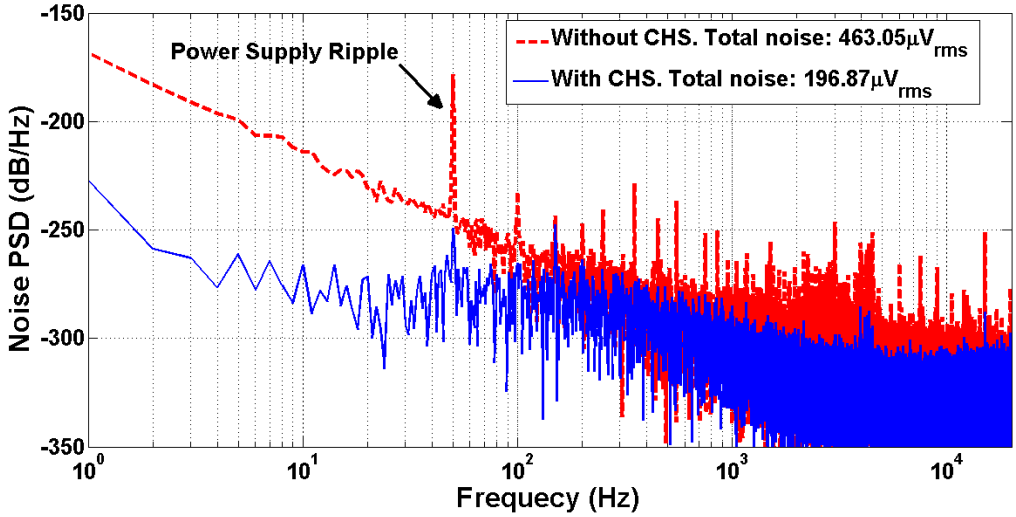


**Figure 6.22:** *Output noise spectrum with and without chopper-stabilisation.*

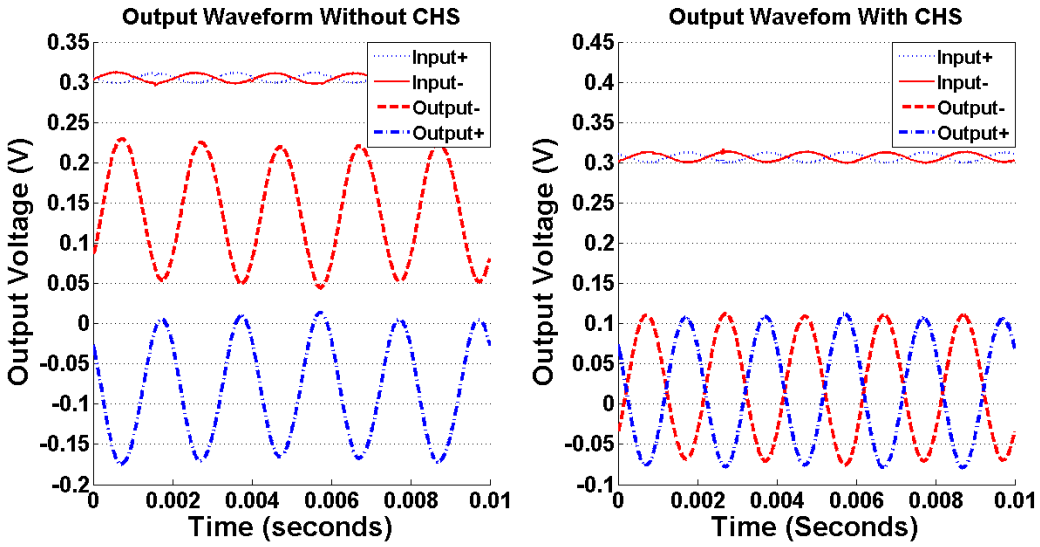


**Figure 6.23:** *Output waveforms in response to sinusoidal input with and without chopper-stabilisation.*

| Total Power | PC circuit | Chopper-stabilised Amplifier | Clock Generator & Others |
|---|---|---|---|
| 165.2 $\mu$W | 35.45 $\mu$W | 92.06 $\mu$W | 37.67 $\mu$W |

**Table 6.2:** *Summary of power consumption*

| Fabrication process | AMS 0.35 $\mu$m 3.3V 2P4M |
|---|---|
| Occupation Area | 0.35 $\mathrm{mm}^2$ |
| Equivalent capacitive sensor specifications | |
| Sensing capacitance | $2 \times 0.5$ pF |
| Bias Voltage | $\pm 1$ V |
| Maximum Capacitance Variation | 7.5 fF |
| Output Amplitude | 745 mV (max. parasitic-cancellation);<br>14.1 mV (without parasitic-cancellation). |
| THD | 2.96% (max. parasitic-cancellation);<br>1.77% (without parasitic-cancellation). |
| SNR | 27.26 dB (max. parasitic-cancellation);<br>31.28 dB (without parasitic-cancellation). |
| Noise Figure | 10.4 dB (max. parasitic-cancellation);<br>6.4 dB (without parasitic-cancellation). |
| SINAD | 25.61 dB (max. parasitic-cancellation);<br>29.76 dB (without parasitic-cancellation). |
| SFDR | 78 dB (max. parasitic-cancellation);<br>82 dB (without parasitic-cancellation). |
| Power Consumption | 165.2 $\mu$W |

**Table 6.3:** *Specifications summary of the interface chip*

#### 6.3.2.4 Power Consumption

The power consumption of the interface chip is summarised in Table. 6.2. As shown in Fig. 6.19(a), the PC circuit contributes to 35 dB extra gain compared with the typical unity-gain buffer. Therefore, without the parasitic-cancellation, an extra amplifier with 35 dB gain is required. In fact, the measured gain of the chopper-stabilised amplifier in this design is 29.6 dB which consumes 92.06 $\mu$W power. Therefore, the parasitic-cancellation scheme saves at least 92.06 $\mu$W power consumption.

## 6.4 Summary

In this chapter, a power-efficient MEMS capacitive interface circuit with parasitic-cancellation and chopper-stabilisation is introduced. The circuit is especially suitable for sensors with small sensing capacitance because it addresses the signal degradation issue by effectively cancelling

the parasitic capacitance at the circuit input. The interface circuit follows a low-degradation low-amplification process, which has better power-efficiency compared with the high-degradation high-amplification process in typical designs. Besides, the chopper-stabilisation technique effectively reduces the low-frequency noise and circuit offsets which improves the precision and stability of the interface circuit. The function of the interface circuit is proven in the experimental results of the prototype VLSI chip. The chip specifications of the interface circuit are summarised in Table. 6.3.

The interface circuit theoretically has the capability to efficiently read-out signals from MEMS cochlea-like acoustic resonators which have very small sensing capacitance. Therefore, a MEMS-CMOS implementation of the cochlea filter proposed in this thesis will be possible in the future.

# Chapter 7
# Conclusion and Future Work

## 7.1 A Review of the Objectives

As stated in Chapter 1.2, the core objective of this work is to develop a biomimetic cochlea filter which closely resembles the biological cochlea response and is highly feasible for low-power and compact-size analogue VLSI implementation. This objective has been fulfilled in this thesis, since the presented filter meets all the aforementioned criteria:

- The chip results in Fig. 5.3, Table. 5.1 and Table. 5.3 demonstrate that the filter response around CF is highly tunable: the peak gain has 18.8$\sim$ 21.5 dB wide range of variation; the Q factor also increases with the peak gain, and the maximum $Q_{10}$ factor reaches 3.85; the CF shifts accordingly with the variation of peak gain and Q factor, which is similar as the biological cochlea.
- As shown in Fig. 5.3, the frequency response curve in low frequencies has a gentle rising slope and keeps constant while the CF response varies.
- The roll-off slope towards stop-band reaches maximally 391.4 dB/dec, which is comparable with the biological cochlea. Thus the filter has a highly asymmetric shape of frequency response: a gentle low-frequency tail and an ultra-steep stop-band roll-off.
- As reflected by the pole-zero plot in Fig. 3.3, the filter has minimum-phase property. Consequently the phase response and group delay of the filter are also biologically faithful, which is proven by the chip results in Fig. 5.6 and Fig. 5.7.
- The filter is easy to realise using analogue VLSI circuits, since its Laplace-domain representation (Eq. 3.11) can be simply translated to the pole-zero form.
- The CF tuning of the filter depends on only one variable parameter, the tuning factor $x$, which achieves the three aspects of CF tuning (peak gain, Q factor and CF shift) all together. The simplified tuning complexity leads to improved tuning accuracy and reduced risk of circuit instability.

- As shown in Table. 5.4, the cochlea filter consumes 59.5$\sim$90 $\mu$W power and occupies less than 1 $mm^2$ chip area. Thus a budget of 2$\sim$3 mW power and 30 $mm^2$ area is sufficient to implement a third-octave distributed cochlea filter bank.

- The non-ideal factors such as the parasitics, noise and transistor mismatches are comprehensively analysed in Chapter 4 and the dimensions of transistors in the cochlea filter circuits have been designed to minimise their effects. The numeric results given above are all measured from the chip, which proves that the filter operation is robust against these non-ideal factors.

Nevertheless, the experiment results also indicate that the filter can be improved in the following aspects:

- The peak gain tuning range and maximum $Q_{10}$ factor matches the lower bound of the physiological results. To further enhance the biological comparability and the performance, future implementations of the filter would target at a peak gain tuning range of 30 $\sim$ 40 dB and a maximum $Q_{10}$ factor greater than 5.

- In this design, the power consumption of the FDDA and the output drivers does not scale with filter CF; as a result, the overall filter power consumption only reduces to 59.5 $\mu$W in the 31 Hz band. In fact, the filter with lower CF has narrower signal bandwidth and thus the bandwidth requirement for the FDDA and the output drivers is reduced. Consequently, the power consumption of the FDDA and the output drivers should be designed to scale with CF in the future so that the filter power consumption can be further decreased.

- The mismatch analysis in this work concentrates on the circuit offsets. However, the effects of the transistor mismatch on the power supply rejection performance has not been adequately addressed. As reflected in the chip results, the 50 Hz power supply ripples have significantly negative effects on the filter performance. Therefore, the power supply rejection ratio should be listed as an important specification of design objective in the future.

- As also shown in the chip results, the filter linear range is constrained by the tanh transconductance of the FAI cells. A prospective solution for this issue is to apply the linearisation techniques such as the multi-tanh method [118] to the FAI cells.

## 7.2 A Summary of the Contribution to Knowledge

As stated in the previous section, the objective of developing a biomimetic cochlea filter which faithfully resembles the biological cochlea response and is highly feasible for analogue VLSI implementation is achieved in this thesis. While the existing cochlea models focus on emulating the anatomical structure and hydrodynamics of the biological cochlea, this work takes an alternative approach by directly matching the filter response with the physiological data; this is the key factor that makes the proposed filter capable of replicating closely the frequency response characteristics of the biological cochlea. Moreover, the biological fidelity of the filter is also examined in an extensive range of aspects including the phase response, group delay and impulse response. Eventually, all these aspects of fidelities are verified by the chip results. To the best of the author's knowledge, there have been no other cochlea filter or cochlea model implementations that are able to match the biological cochlea in so many aspects.

The biological fidelity feature of the presented filter makes it promising for a variety of future hearing applications. Firstly, it provides a solution for spectral decomposition in the next generation cochlea implant products that require a closer mimicking of the signal processing in the biological cochlea. Secondly, it can be used to generate cochleagrams for CASA-based sound processing systems; compared with the existing filters, it will prospectively contribute to a closer emulation of the auditory scene analysis that occurs in the biological auditory system and it will be advantageous for portable or wearable applications due to its feasibility for low-power and compact-size analogue VLSI implementation. Besides, a biologically faithful artificial hearing system can be built upon the presented filters, which will probably become a conducive platform to perform hearing research and build intelligent machine hearing systems in the future.

Also, most of the design objectives listed in Section 1.2 are common challenges for the analogue VLSI implementation of cochlea-inspired systems, and therefore the solutions provided in this thesis will be constructive for future relevant works.

Additionally, Chapter 6 investigates the possibilities of implementing the cochlea filter using the MEMS acoustic resonators. A novel capacitive interface circuit is developed to address the MEMS interface challenge for such implementation. As proven by the chip results, the circuit is able to cancel the parasitic capacitance at the MEMS-CMOS interface, which significantly improves the sensitivity of signal read-out from the low-capacitance MEMS resonators. With

this interface circuit, a MEMS-CMOS implementation of the cochlea filter will be possible in the future. Moreover, the circuit provides a power-efficient solution for the problem of signal read-out from MEMS sensors with low sensing capacitance, which will be commonly useful in many other MEMS sensor applications.

## 7.3 Future Work

Firstly, the improvements listed in Section 7.1 should be addressed in the future. Besides, as introduced in Fig. 4.1.1, an alternative approach to realise the cochlea filter using biquad-integrator cascade can be implemented. In this thesis, the FAI-based active RLC implementation is selected to reduce design complexity. However, it would be worth comparing the two approaches based on their chip performances in the future.

The cochlea filter introduced in this thesis represents a fundamental work for a biologically-inspired hearing system shown in Fig. 1.3. The next step is to integrate the filter with the ATC block (the local control unit in Fig. 1.3). In Chapter 3, the ATC block is built in Simulink only as a proof of concept, while its hardware implementation is not covered in this thesis but left open for future investigations. Subsequently, a cochlea filter bank will be implemented and integrated with the spike codec and neuromorphic processing units. Eventually, the complete system in Fig. 1.3 will be built for future research.

A new type of stimulation strategy will be developed if the filter is to be used in cochlea implants, since the existing stimulation strategies are designed for basic band-pass filters. Besides, the cochlea filter has demonstrated the capability of generating cochleagrams in Chapter 3, and in the future it will be of interest to investigate whether and how this filter is going to improve the performance in practical audio signal processing tasks such as speech recognition or sound identification.

# Appendix A
# **Appendices**

## A.1 Derivations

### Relationship between $S_2$ slope and Q factor of the cochlea filter

The Q factor of a filter is given by

$$Q = \frac{\mathrm{CF}}{3\,\mathrm{dB\ Bandwidth}} = \frac{\mathrm{CF}}{\mathrm{CF}\cdot 10^{3/\mathrm{S_0}} - \mathrm{CF}\cdot 10^{-3/\mathrm{S_0}}}, \tag{A.1}$$

where $S_0$ is the slope steepness. Therefore, the $49.8 \sim 274$ dB/dec $S_2$ slope of the biological cochlea is approximately mapped with the $3.6 \sim 19.8$ Q factor.

### Derivation of capacitance/inductance values in the ELF

The design table for elliptic filters is shown in Fig. A.1. According to the design parameters in Table. 3.1, the following values are selected:

$$\begin{cases} L_{norm,2} = 0.7806 = L_{FAI,2}\cdot\frac{\omega_{-3dB}}{R_s}; \\ L_{norm,4} = 1.0162 = L_{FAI,4}\cdot\frac{\omega_{-3dB}}{R_s}; \\ C_{norm,1} = 0.2377 = 2C_1\cdot\omega_{-3dB}R_s; \\ C_{norm,2} = 0.1746 = C_2\cdot\omega_{-3dB}R_s; \\ C_{norm,3} = 1.0478 = 2C_3\cdot\omega_{-3dB}R_s; \\ C_{norm,4} = 0.3134 = C_4\cdot\omega_{-3dB}R_s; \\ C_{norm,5} = 1.0465 = 2C_5\cdot\omega_{-3dB}R_s. \end{cases} \tag{A.2}$$

Since the following equations stand:

$$\begin{cases} \frac{\omega-3dB}{R_s} = \frac{\sqrt{2}\omega_{BP}}{\frac{nU_T}{2I_{st}}} = 0.913\frac{\sqrt{n}I_{st}^2}{(nU_T)^2C_0} \\ \omega{-}3dB\cdot R_s = \sqrt{2}\omega_{BP}\cdot\frac{nU_T}{2I_{st}} = 0.228\frac{\sqrt{n}}{C_0}, \end{cases} \tag{A.3}$$

the results in Eq. 4.57 and Eq. 4.56 are derived.

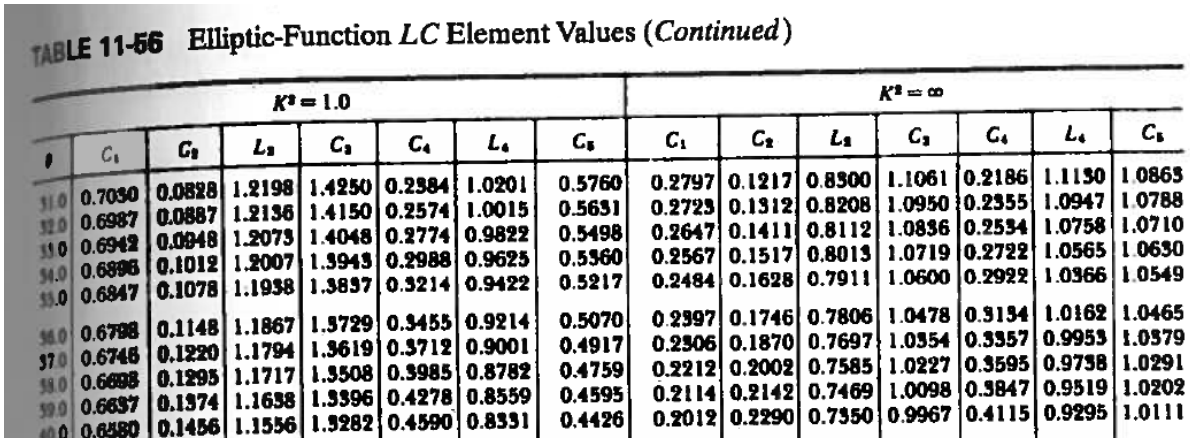

TABLE 11-56 Elliptic-Function *LC* Element Values (*Continued*)

| | $K^2 = 1.0$ | | | | | | | $K^2 = \infty$ | | | | | | |
|---|---|---|---|---|---|---|---|---|---|---|---|---|---|---|
| θ | $C_1$ | $C_2$ | $L_3$ | $C_3$ | $C_4$ | $L_4$ | $C_5$ | $C_1$ | $C_2$ | $L_3$ | $C_3$ | $C_4$ | $L_4$ | $C_5$ |
| 31.0 | 0.7030 | 0.0828 | 1.2198 | 1.4250 | 0.2584 | 1.0201 | 0.5760 | 0.2797 | 0.1217 | 0.8300 | 1.1061 | 0.2186 | 1.1130 | 1.0865 |
| 32.0 | 0.6987 | 0.0887 | 1.2136 | 1.4150 | 0.2574 | 1.0015 | 0.5631 | 0.2725 | 0.1312 | 0.8208 | 1.0950 | 0.2355 | 1.0947 | 1.0788 |
| 33.0 | 0.6942 | 0.0948 | 1.2073 | 1.4048 | 0.2774 | 0.9822 | 0.5498 | 0.2647 | 0.1411 | 0.8112 | 1.0836 | 0.2534 | 1.0758 | 1.0710 |
| 34.0 | 0.6896 | 0.1012 | 1.2007 | 1.3943 | 0.2988 | 0.9625 | 0.5360 | 0.2567 | 0.1517 | 0.8013 | 1.0719 | 0.2722 | 1.0565 | 1.0630 |
| 35.0 | 0.6847 | 0.1078 | 1.1938 | 1.3837 | 0.3214 | 0.9422 | 0.5217 | 0.2484 | 0.1628 | 0.7911 | 1.0600 | 0.2922 | 1.0366 | 1.0549 |
| 36.0 | 0.6798 | 0.1148 | 1.1867 | 1.3729 | 0.3455 | 0.9214 | 0.5070 | 0.2397 | 0.1746 | 0.7806 | 1.0478 | 0.3134 | 1.0162 | 1.0465 |
| 37.0 | 0.6746 | 0.1220 | 1.1794 | 1.3619 | 0.3712 | 0.9001 | 0.4917 | 0.2306 | 0.1870 | 0.7697 | 1.0354 | 0.3357 | 0.9953 | 1.0379 |
| 38.0 | 0.6693 | 0.1295 | 1.1717 | 1.3508 | 0.3985 | 0.8782 | 0.4759 | 0.2212 | 0.2002 | 0.7585 | 1.0227 | 0.3595 | 0.9738 | 1.0291 |
| 39.0 | 0.6637 | 0.1374 | 1.1638 | 1.3396 | 0.4278 | 0.8559 | 0.4595 | 0.2114 | 0.2142 | 0.7469 | 1.0098 | 0.3847 | 0.9519 | 1.0202 |
| 40.0 | 0.6580 | 0.1456 | 1.1556 | 1.3282 | 0.4590 | 0.8331 | 0.4426 | 0.2012 | 0.2290 | 0.7350 | 0.9967 | 0.4115 | 0.9295 | 1.0111 |

**Figure A.1:** *Filter design table for elliptic filters. Image is take from [98]*

## A.2 Program Codes

### MATLAB code for generation of the cochleagram

```
%Plot cochleagram;
%End time 'te' should be set prior to the program;
%Color limit 'clims' should be set prior to the program;
%The output waveform from the cochlea bank has been saved in
%'bank'.

h=figure;

 %Expand the 32 channels outputs to 94 channels;
n=size(bank);
n=n(2);
ENV=double(zeros(32*3-2,n));

%Extract the envelope of the original outputs
%using Hilbert transform;
for x=1:32
    ENV(3*x-2,:)=hilbertenv(bank(x,:),44100);
end

%Extra two channels are interpolated by taking geometric
%means between two adjecent channles in the original outputs
for x=1:23
```

```
23:     ENV(3*x-1,:)=(ENV(3*x-2,:).^2.*ENV(3*x+1,:)).^(1/3);
24: end
25: for x=1:23
26:     ENV(3*x,:)=(ENV(3*x+1,:).^2.*ENV(3*x-2,:)).^(1/3);
27: end
28:
29: %Calculate maximum output for normalisation;
30: m=max(max(ENV));
31: %Generate cochleagram;
32: imagesc(bank(1,:),[1 70], 20*log10(ENV/m),clims);
33:
34: %Graphic settings;
35: colormap(jet(4096));
36: colorbar
37: set(gca,'YDir','normal');
38: xlim([0 te]);
39: ylim([1 70]);
40: set(gca,'YTick',[3 12 21 30 39 48 57 66])
41: set(gca,'YTickLabel',{'125','250','500','1000','2000','4000','8000','16000'})
42: xlabel('Time␣(Seconds)')
43: ylabel('Frequency␣(Hz)')
44: set(0,'DefaultAxesFontSize',16)
45: set(0,'DefaultAxesfontWeight','bold')
46: set(0,'DefaultTextFontSize',20)
47: set(0,'DefaultTextfontWeight','bold')
48: saveas(h,'cgram','fig');
49: saveas(h,'cgram','png');
```

### LabVIEW program for VLSI testing

The LabVIEW program used to characterise the frequency response of the cochlea filter chip is illustrated in Fig. A.2 and Fig. A.3, where Fig. A.2 shows the front panel and Fig. A.3 shows the program block diagram. Similarly, the LabVIEW program used to characterise the interface chip is illustrated in Fig. A.2 and Fig. A.3

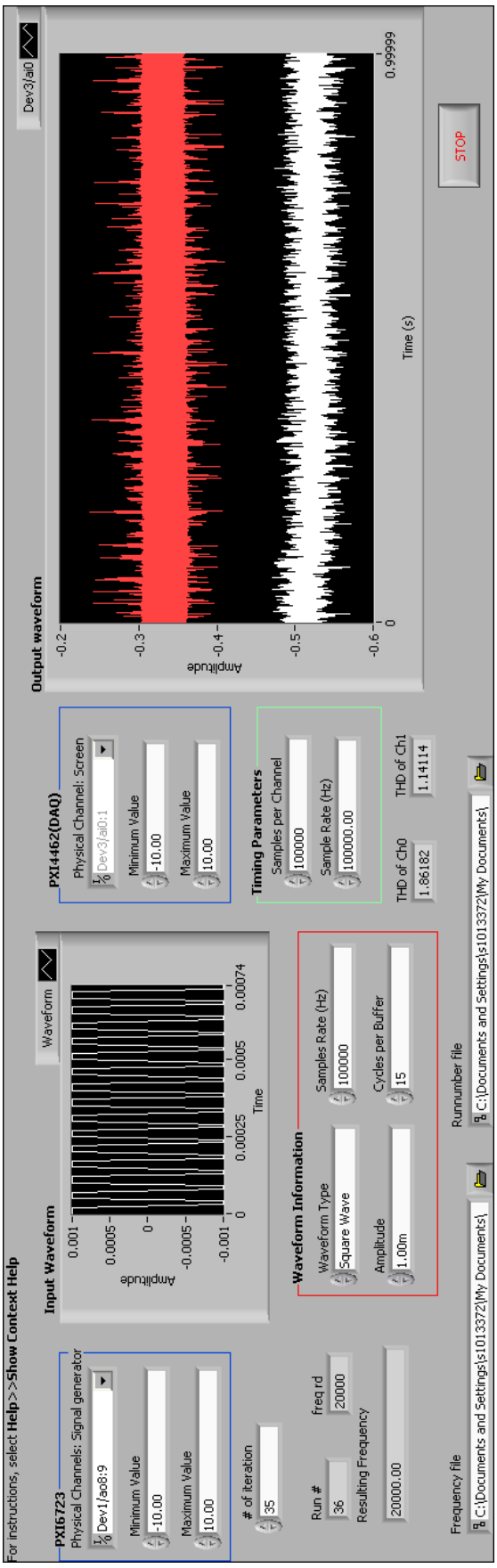


**Figure A.2:** *Front panel of the LabVIEW program for cochlea filter chip characterisation*

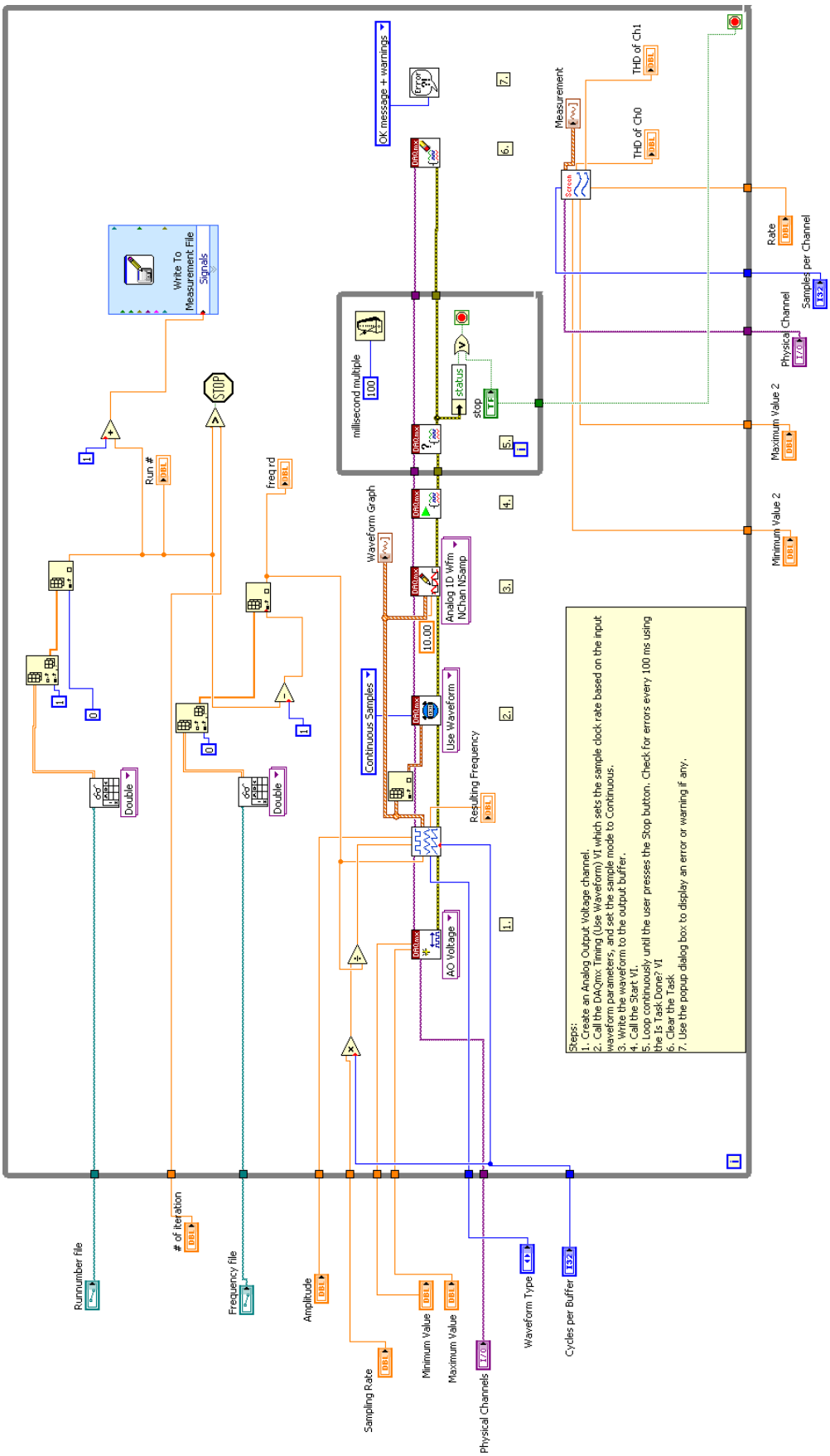


**Figure A.3:** *Block diagram of the LabVIEW program for cochlea filter chip characterisation*

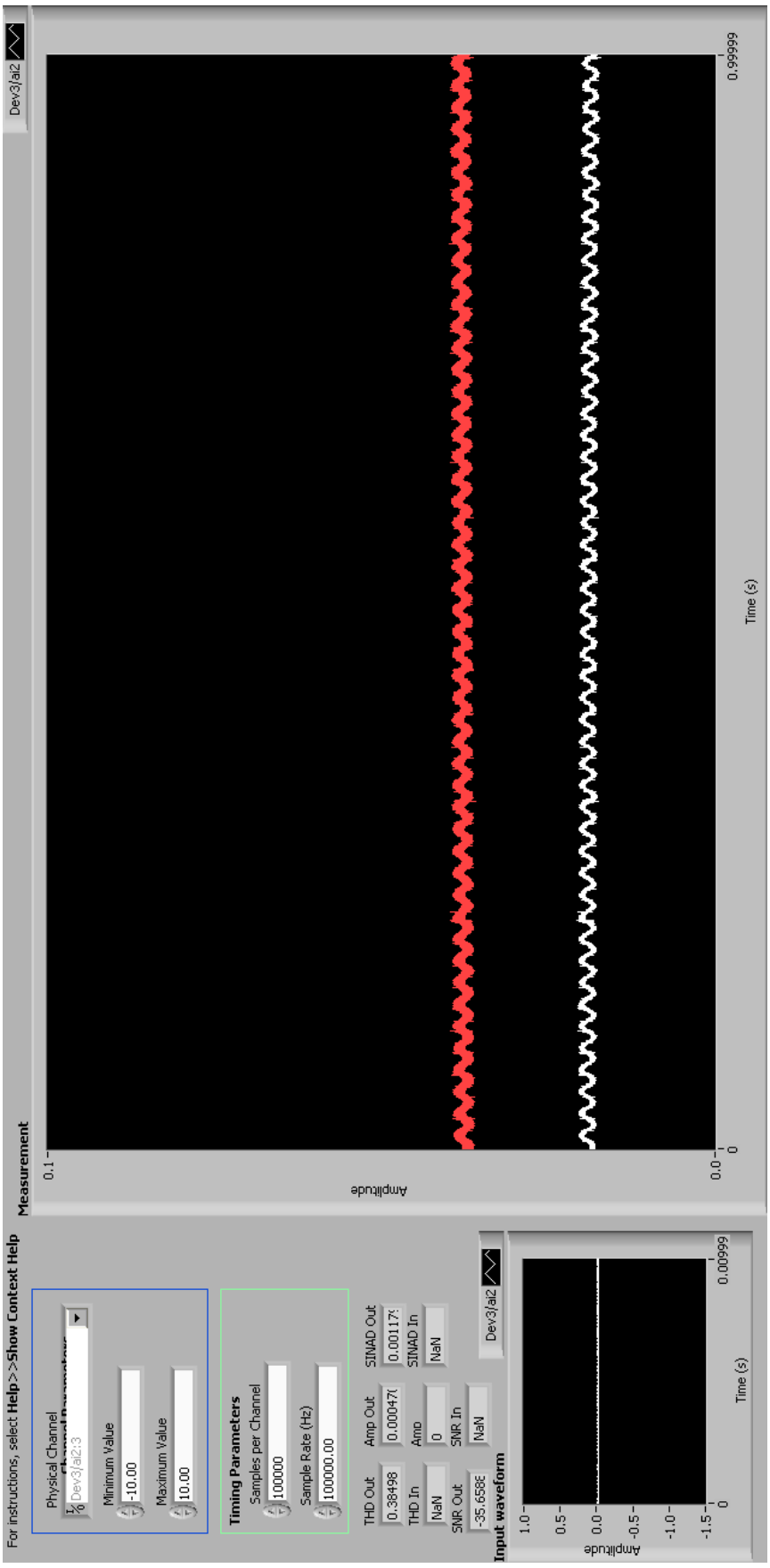


**Figure A.4:** *Front panel of the LabVIEW program for interface chip characterisation*

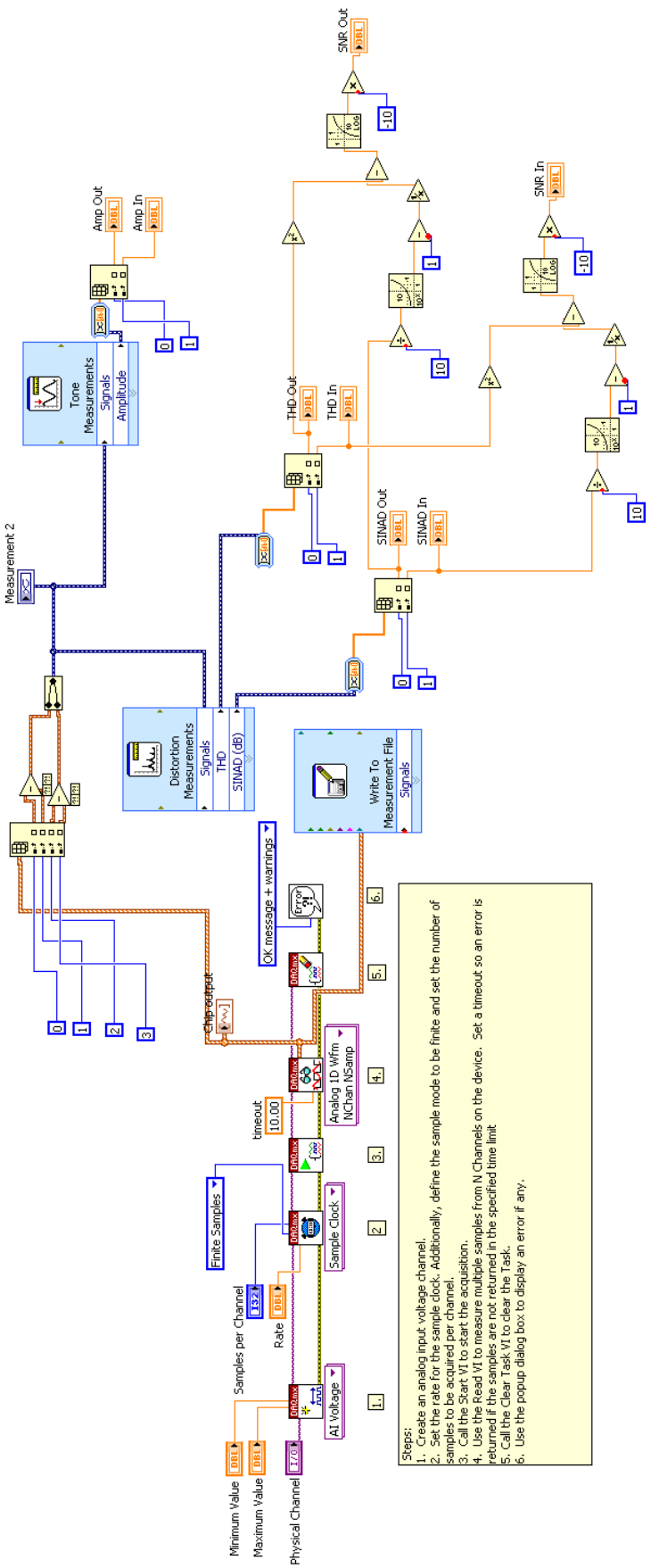


**Figure A.5:** *Block diagram of the LabVIEW program for interface chip characterisation*

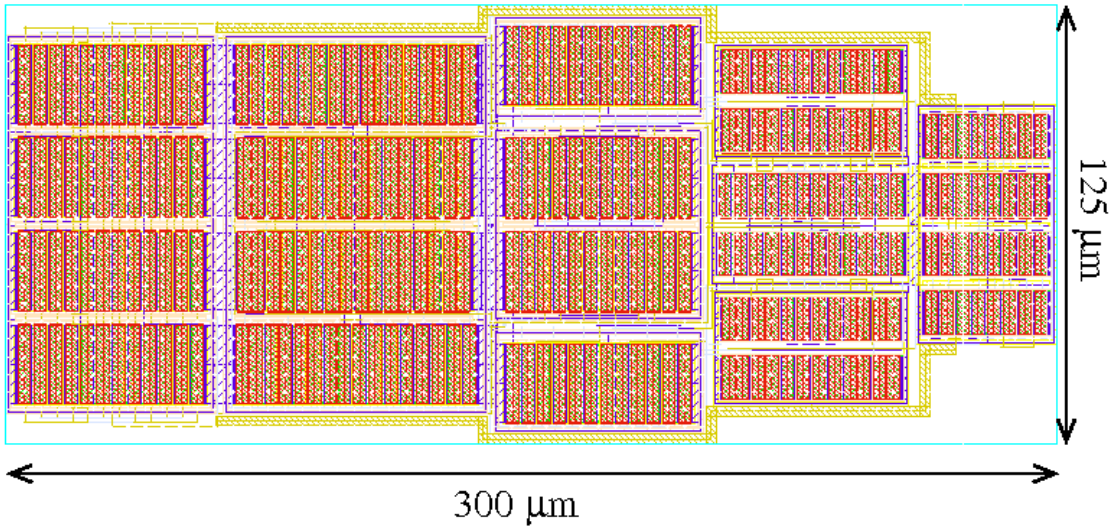


**Figure A.6:** *Layout of the FAI cell.*

## A.3 Circuit Layouts

The layouts of the elementary circuit blocks introduced in this thesis including the FAI, fully differential OTA, FDDA, single-end OTA, parasitic-cancellation circuit, chopper, sensor bias circuit and the amplifier used in the interface circuits are shown in the following figures.

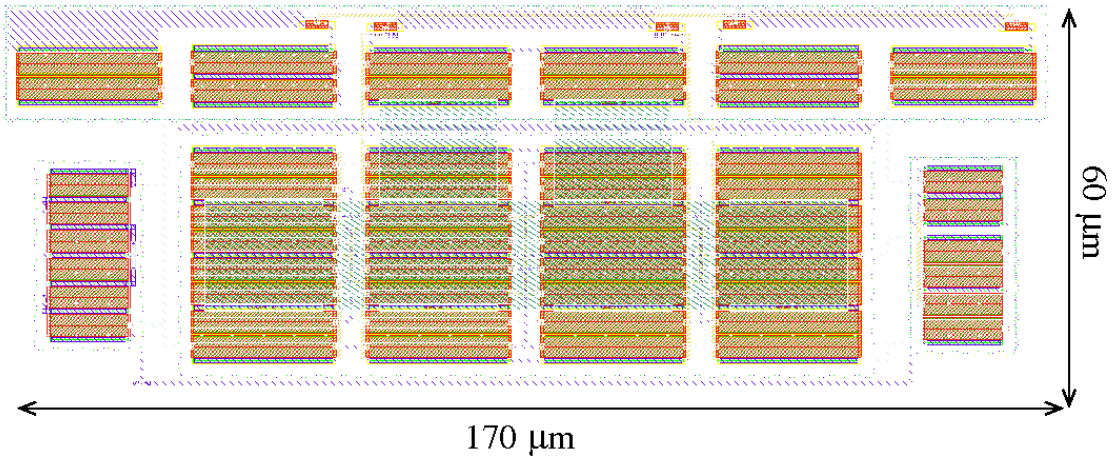


**Figure A.7:** *Layout of the fully differential OTA.*

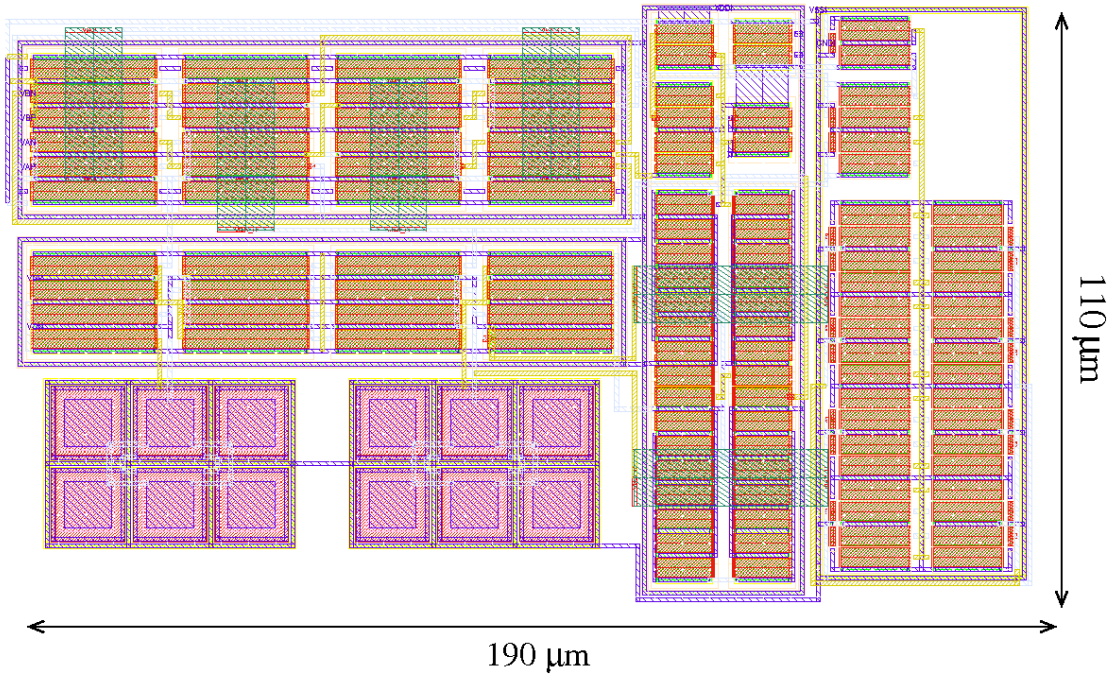


**Figure A.8:** *Layout of the FDDA.*

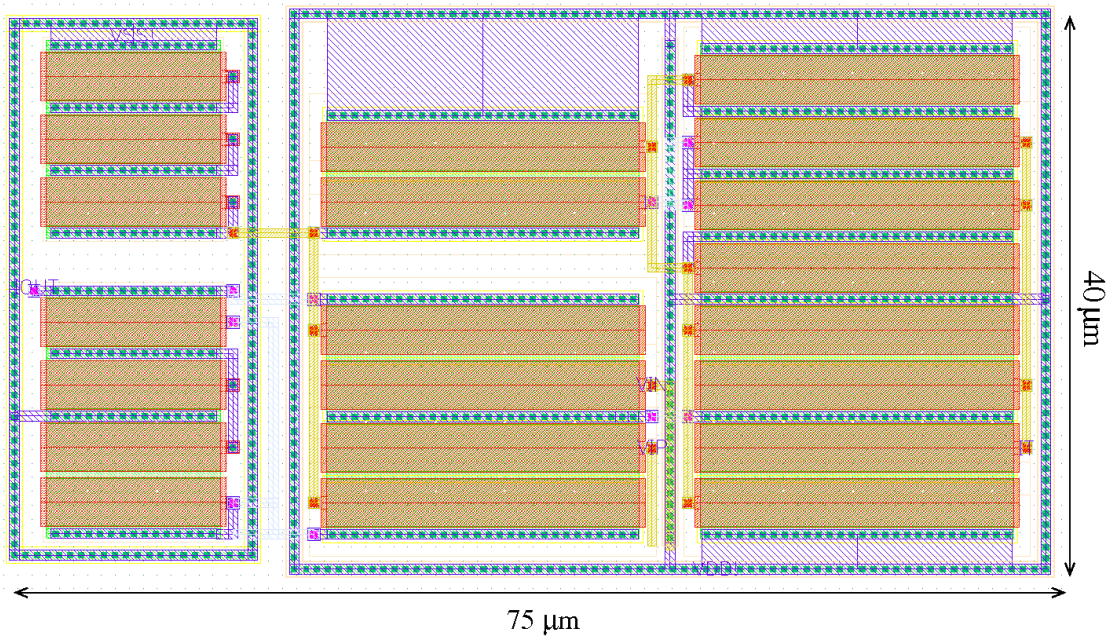


**Figure A.9:** *Layout of the single-end OTA.*

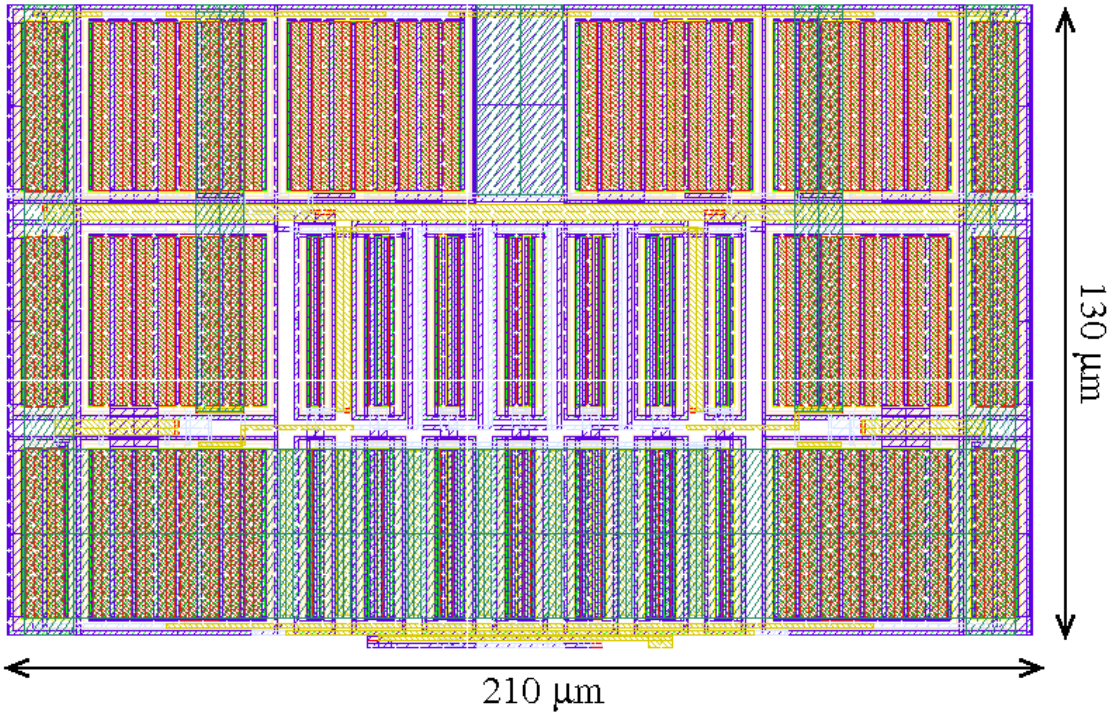


**Figure A.10:** *Layout of the parasitic-cancellation circuit.*

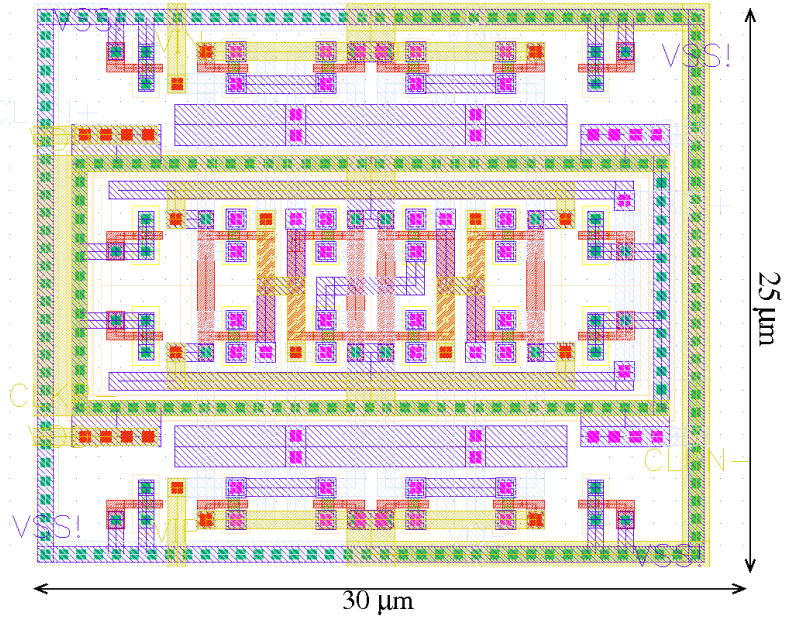


**Figure A.11:** *Layout of the chopper.*

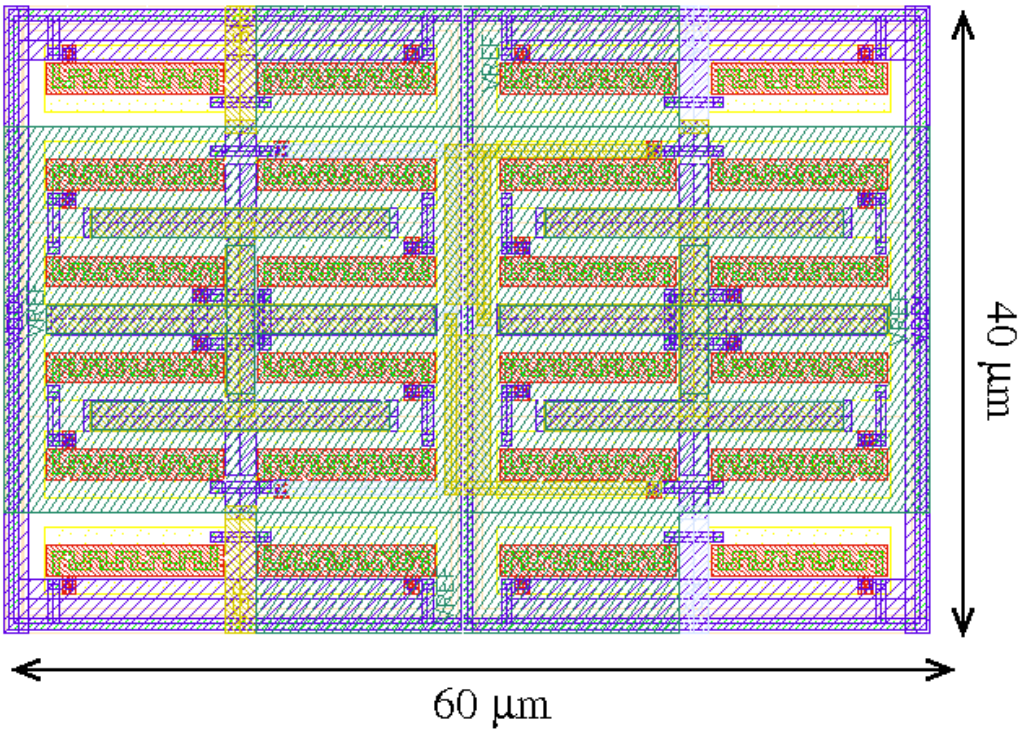


**Figure A.12:** *Layout of the sensor bias circuit.*

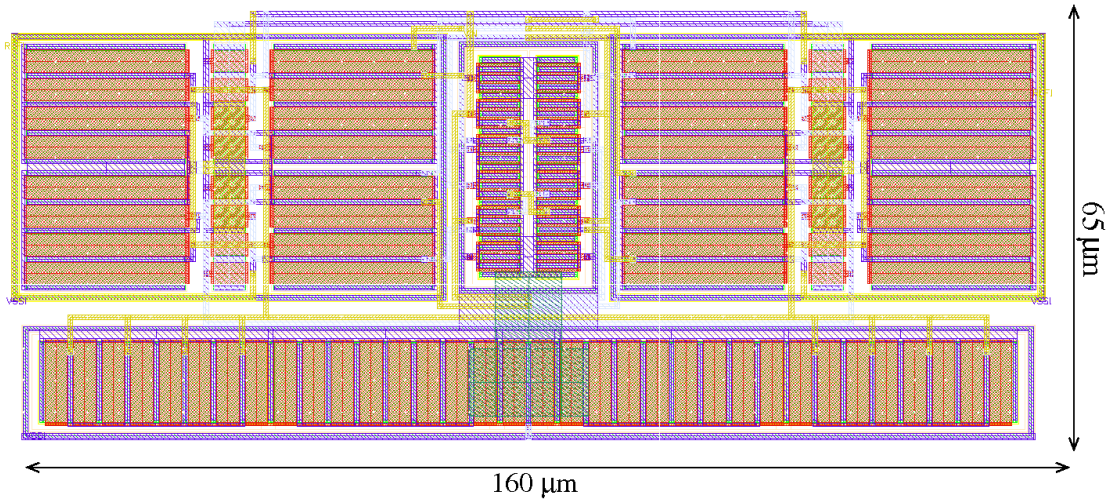


**Figure A.13:** *Layout of the amplifier used in the interface circuit.*

# Appendix B

# A List of Publications

Several research publications have been generated from this work. They are listed below

- **Shiwei Wang**, T. J. Koickal, A. Hamilton, R. Cheung and L. Smith, "A bio-realistic analog CMOS cochlea filter with high tunability and ultra-steep roll-off," accepted by *IEEE Trans. Biomed. Circuits Syst.*, 2014. DOI:10.1109/TBCAS.2014.2328321.

- **Shiwei Wang**, T. J. Koickal, A. Hamilton, E. Mastropaolo, R. Cheung, A. Abel and L. Smith, "A power-efficient capacitive read-out circuit with parasitic-cancellation for MEMS cochlea sensors ," under review by *IEEE Trans. Biomed. Circuits Syst.*, 2014.

- **Shiwei Wang**, T. J. Koickal, A. Hamilton, E. Mastropaolo, R. Cheung and L. Smith, "A floating active inductor based CMOS cochlea filter with high tunability and sharp cut-off," *Proc. IEEE Symp. on Circuits and Systems*, pp. 193-196, 2013.

- **Shiwei Wang**, T. J. Koickal, A. Hamilton, E. Mastropaolo, R. Latif, R. Cheung, M. Newton and L. S. Smith, "A low-noise interface circuit for MEMS cochlea-mimicking acoustic sensors," *Proc. IEEE Symp. on Circuits and Systems*, pp.1151-1154, 2012.

- T. J. Koickal, R. Latif, L. Gouveia, E. Mastropaolo, **Shiwei Wang**, A. Hamilton, R. Cheung, M. Newton and L. S. Smith, "Design of a spike event coded RGT microphone for neuromorphic auditory systems ," *Proc. IEEE Symp. on Circuits and Systems*, pp. 2465 - 2468 , 2011.

This article has been accepted for inclusion in a future issue of this journal. Content is final as presented, with the exception of pagination.



# A Bio-Realistic Analog CMOS Cochlea Filter With High Tunability and Ultra-Steep Roll-Off

Shiwei Wang, *Student Member, IEEE*, Thomas Jacob Koickal, Alister Hamilton, Rebecca Cheung, *Senior Member, IEEE*, and Leslie S. Smith, *Senior Member, IEEE*

***Abstract*—This paper presents the design and experimental results of a cochlea filter in analog very large scale integration (VLSI) which highly resembles physiologically measured response of the mammalian cochlea. The filter consists of three specialized sub-filter stages which respectively provide passive response in low frequencies, actively tunable response in mid-band frequencies and ultra-steep roll-off at transition frequencies from pass-band to stop-band. The sub-filters are implemented in balanced ladder topology using floating active inductors. Measured results from the fabricated chip show that wide range of mid-band tuning including gain tuning of over 20dB, Q factor tuning from 2 to 19 as well as the bio-realistic center frequency shift are achieved by adjusting only one circuit parameter. Besides, the filter has an ultra-steep roll-off reaching over 300 dB/dec. By changing biasing currents, the filter can be configured to operate with center frequencies from 31 Hz to 8 kHz. The filter is $9^{th}$ order, consumes $59.5 \sim 90.0\ \mu$W power and occupies $0.9\ \mathrm{mm}^2$ chip area. A parallel bank of the proposed filter can be used as the front-end in hearing prosthesis devices, speech processors as well as other bio-inspired auditory systems owing to its bio-realistic behavior, low power consumption and small size.**

***Index Terms*—Analog VLSI, auditory filter, bio-inspired circuits, CMOS cochlea, floating active inductor.**

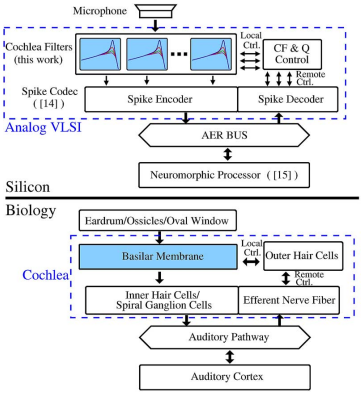


Fig. 1. Position of this work in a bio-inspired auditory system, in comparison with system-level diagram of biological auditory system.

## I. Introduction

THE cochlea in the inner ear of mammals has remarkable filter functions. It converts sound pressure into multi-channels of band-passed outputs, where the sensitivity of each channel is dynamically tuned according to the input intensity and the out-of-band frequency components are greatly suppressed with an ultra-steep roll-off at the stop-band [1]. These filtering features of cochlea make it capable of adapting to wide dynamic range of sound input and performing high-resolution frequency decomposition. In recent years, many bio-inspired systems employing filters that emulate the cochlea filter functions have been implemented, which are used in a variety of applications including hearing prosthetic devices [2]–[4], speech/sound recognition systems [5]–[10] as well as RF spectrum analyzers [11] and channel multiplexers [12]. In this work, we aim to build a cochlea filter in analog VLSI which closely resembles the frequency response of biological cochlea. The use of analog circuitry for front-end signal processing improves power-efficiency [13] (see position of the cochlea filters in Fig. 1). Besides, the progressive results from physiological experiments on the biological cochlea [16]–[25], [27], [28] have provided us with deeper understanding of the cochlea behavior which brings more inspiration to build filters that behave faithfully to biology.

In fact, analog VLSI models of the cochlea have been studied for over two decades and a number of systems have been implemented [29]–[42]. These systems generally consist of filter banks based on second-order sections (SOS) in different configurations including cascade [29]–[35], parallel [36]–[38] and 2-dimensional (2-D) topology [39]–[42]. The filter cascade structure models the wave propagation in the basilar membrane of cochlea using from 32 to 120 stages of SOS connected in series [29], [30], [32]–[34]. Gain and filter roll-off steepness are accumulated with the long cascade, which provides good similarity with biological frequency response. Nevertheless, the cascade structure suffers from the accumulation of both noise and delays, and also, failure of one stage in the cascade will affect all of its following stages. On the contrary, the parallel

Manuscript received January 29, 2014; revised April 23, 2014; accepted May 29, 2014. This work was supported by EPSRC, U.K., under Grants to the University of Edinburgh (EP/G063710/1), and to the Universityof Stirling (EP/G062609/1). The China Scholarship Council provided support for the first author. This paper was recommended by Associate Editor S.-C. Liu.

S. Wang, T. J. Koickal, A. Hamilton, and R. Cheung are with the Institute for Integrated Micro and Nano Systems, University of Edinburgh, EH9 3JL Edinburgh, U.K. (e-mail: shiwei.wang@ed.ac.uk).

L. S. Smith is with the Department of Computer Science and Mathematics, University of Stirling, FK9 4LA Stirling, U.K.

Color versions of one or more of the figures in this paper are available online at http://ieeexplore.ieee.org.

Digital Object Identifier 10.1109/TBCAS.2014.2328321

This article has been accepted for inclusion in a future issue of this journal. Content is final as presented, with the exception of pagination.



structure avoids these drawbacks by employing independent filter channels, and the number of SOS stages in each channel is limited to 1 or 2 [36]–[38]. However, as the filter complexity is significantly reduced in each channel, its frequency response is no longer comparable with that observed in the biological cochlea. The 2-D topology solves the problems in both noise and delay accumulation and bio-fidelity. It agrees with the parallel structure in the aspect that SOS stages are configured in a parallel manner, and only one SOS stage is used for each channel [39]–[42]. However, the channels are not independent of each other but are coupled through a resistive network which models the effects of cochlea fluid, and the coupling between the channels results in fairly faithful response compared with biology [40]–[42]. Nevertheless, while the usability of the 2-D topology designs has not been convincingly proven, the cascade and parallel structures have already been used in a variety of audio processing tasks [43]–[45] and particularly, the feasibility of the parallel structure in cochlea implant products has been sufficiently demonstrated [36], [37], [46].

In this work, we aim to improve the performance of the parallel structure in terms of bio-faithful frequency tuning and roll-off steepness. A filter channel which closely emulates the frequency response measured from biological cochlea is developed to replace the simple band-pass filters used in the existing parallel designs [36]–[38]. The filter is designed by directly following the implications from recent physiological experiments. Inspired by the fact that the biological cochlea has separate response features from low to high frequencies [1], the proposed design consists of three cascaded sub-filter stages, which respectively resemble the passive response in low frequencies, active response in mid-band frequencies and steep roll-off in transition frequencies. The use of specialized sub-filters increases overall efficiency, reducing filter tuning complexity and filter order required to achieve bio-faithful response. The sub-filters are built in balanced ladder topology using floating active inductors, which reduces the design complexity. The proposed cochlea filter is superior to the gammatone-based design [47] in terms of ease of analog VLSI implementation and bio-realism of frequency response. Besides, the filter can directly interface with microphone output, unlike the design reported in [48] which has to be operated with a floating current source as input.

The paper is organized as following. The system-level filter structure is introduced in Section II. The details of circuit implementation are discussed in Section III. The circuit non-idealities are analyzed in Section IV. The measured chip results are discussed in Section V, followed by a conclusion of the paper in Section VI.

## II. System Design

Physiological experiments [1], [16]–[18], [21] indicate that magnitude frequency response of the basilar membrane in biological cochlea has an asymmetric shape and highly active behavior. It has a gentle slope in the low-frequency band (in the region of 20 dB/dec [1], [17], [18]) and a highly steep roll-off at the stop-band (330 dB/dec or even higher [1], [16]–[18]). In the mid-band, the gain, selectivity and center frequency increases with decreasing input strength: the increase of gain can reach in the range of $20 \sim 40$ dB [16]–[18], [21], the maximum Q factor can reach as high as 10 [16]–[18], [21], and the center frequency increases by over $40\%$ [1], [16]–[18], [21]. Generally speaking, the response is gentle and passive in low frequencies, selective and active in mid-band frequencies and steep in the transition from pass-band to stop-band, which indicates the frequency response of cochlea can be divided into three stages from low to high frequencies as first suggested in [1]. Based on this observation, a filter architecture composed of three cascaded sub-filters, each of which represents one stage of the cochlea response, is proposed as shown in Fig. 2. A biquad band-pass filter (BPF) whose center frequency determines the passive center frequency of the entire cochlea filter presents the gentle and passive response, a biquad low-pass filter (LPF) with tunable gain, Q factor and center frequency presents the active and selective response, and an elliptic filter which has sharpest transition among all filter types presents the steep roll-off. To match the steepness of roll-off slope, the elliptic filter is designed as $5^{th}$-order and the entire cochlea filter is a $9^{th}$-order system.

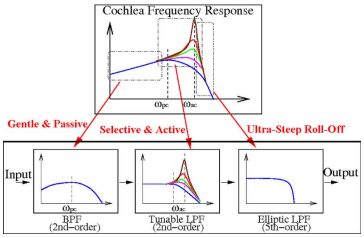


Fig. 2. System architecture. Each of the three sub-filters emulates one stage of the biological cochlea frequency behavior.

## III. Circuit Implementation

### A. Basic Cell: Floating Active Inductor (FAI)

Among the three filters proposed to build a cochlea filter, it is the high order elliptic filter that brings most design difficulty and challenge. For audio frequencies, implementation of passive LC-ladder topology in VLSI is unrealistic due to unfeasibly large size of passive inductors. Active RC [49] and switch-capacitor implementations [50] require the same number of op-amps with the filter order, and are thus constrained by power consumption. Reported log-domain implementations mostly use bipolar transistors targeting at high frequency applications [51], [52], while the CMOS implementations are either low-order [53], [54] or not proven with chip results [55]–[57].

Therefore, we developed a floating active inductor (FAI) as the basic cell to build active LC ladders, which is shown in Fig. 3. The FAI is inspired by several existing active inductor designs in [58], and has been modified so that it operates in floating mode as required by LC ladders. Also, the circuits are designed to operate in weak inversion so as to achieve the long time constant for audio frequencies. The FAI is based on gyrator-C topology. The transistor pair MN and MP respectively

This article has been accepted for inclusion in a future issue of this journal. Content is final as presented, with the exception of pagination.



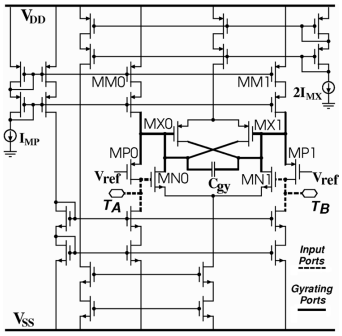


Fig. 3. Schematic of FAI. The basic cell for implementation of ladder filters. Three differential transistor pairs MP, MN and MX and a load capacitor $C_{gy}$ are configured in gyrator-C topology. The input ports and gyrating ports of the FAI are highlighted.

provide the forward and reverse transconductance to form a gyrator, and $C_{gy}$ is the capacitor loaded at the gyrating ports. The transistor pair MX functions as a compensation transconductor which reduces the resistive loading that the sources of the MP transistors add on the gyrating ports. The quality factor of the FAI is tunable by adjusting the transconductance difference between the MP pair and MX pair. More details about the FAI cell have been provided in [59]. The FAI-based active LC ladders are not only used to build the steep roll-off $5^{th}$ order elliptic filter, but also the BPF and LPF sub-filters shown in Fig. 2.

Deriving from [59], the equivalent impedance of the FAI is given by

$$Z(s) = \frac{4C_{gy} \cdot s}{g_{MP}g_{MN}} + \frac{2(g_{MP} - g_{MX})}{g_{MP}g_{MN}} \tag{1}$$

where $g_{MP}$, $g_{MN}$ and $g_{MX}$ are the transconductance of the transistor pairs. Substrates of MN, MP and MX pairs are all connected to power supplies, and as sources of MX0-MX1 and MN0-MN1 pairs are respectively tied together, the body effect does not have much influence on their differential transconductance. However, MP0 and MP1 have separate sources and thus the body effect transconductance $g_{mb}$ should be considered. The transistors operate in weak inversion and thus $g_{mb}$ approximately equals $n - 1/n \cdot I_D/U_T$ [60] where $n$ is slope factor, $I_D$ is biasing drain current and $U_T$ is thermal voltage. Besides, the currents in MN and MX are made equal as shown in Fig. 3. Thus, the equivalent inductance and resistance can be written as

$$L = \frac{4C_{gy}nU_T^2}{I_{MP}I_{MX}} \tag{2}$$

$$R = \frac{2U_T(nI_{MP} - I_{MX})}{I_{MP}I_{MX}}. \tag{3}$$

Equations (2) and (3) show that the FAI inductance and resistance can be tuned by adjusting $I_{MP}$ and $I_{MX}$.

The drain-source conductance ($g_{ds}$) due to channel length modulation is not considered. Because in weak inversion $g_{ds} = I_D/\lambda L$ will be at least one hundred times smaller than the transistor transconductance $g_m = I_D/nU_T$ according to the process parameters ($\lambda$ is channel length modulation parameter and L is transistor channel length).

### *B. Triple-Stage Cochlea Filter Design Based on FAI*

Based on the FAI cell, $2^{nd}$ order BPF, $2^{nd}$ order LPF, $5^{th}$ order elliptic filters and their cascaded cochlea filter channel are built as shown in Fig. 4. The BPF is built by loading a fully differential OTA (FDOTA: Fig. 5) with two FAIs and a capacitor, and the LPF is built upon FAI-C voltage divider with a fully differential difference amplifier (FDDA: Fig. 6) as input buffer, while the elliptic filter is built according to filter design handbook [61] with single-end OTAs (OTA: Fig. 7) providing equivalent source resistance. There are a total of eight FAIs in each channel, and their $I_{MP}$ currents are made equal through current mirrors, while $I_{MX}$ currents are set separately. We denote the $I_{MP}$ currents as $I_{STAT}$, and $I_{MX}$ as $I_{BPF}$, $I_{LPF}$ and $I_{ELLI}$ respectively. The FDOTA and the single-end OTA also operate in weak inversion and are biased with $2I_{STAT}$ currents. The FAIs in BPF and LPF are all loaded with equal capacitance of $C_0$, while $C_{BPF}$ is set as 1.2 $C_0$ and $C_{LPF}$ is set as $C_0$.

Thereby the transfer functions of BPF and LPF are derived as

$$H_{BPF}(s) = \frac{5I_{STAT}}{6nU_TC_0} \cdot \frac{s + \omega_{z,BPF}}{s^2 + \frac{\omega_{0,BPF}}{Q_{BPF}}s + \omega_{0,BPF}^2} \tag{4}$$

$$\begin{cases} \omega_{z,BPF} = \frac{nI_{STAT} - I_{BPF}}{2nU_TC_0} \\ \omega_{0,BPF} = \frac{1}{4nU_TC_0}\sqrt{\frac{5}{3}nI_{STAT}I_{BPF}} \\ Q_{BPF} = \frac{1}{2(nI_{STAT} - I_{BPF})}\sqrt{\frac{5}{3}nI_{STAT}I_{BPF}} \end{cases} \tag{5}$$

$$H_{LPF}(s) = \omega_{0,LPF}^2 \cdot \frac{1}{s^2 + \frac{\omega_{0,LPF}}{Q_{LPF}}s + \omega_{0,LPF}^2} \tag{6}$$

$$\begin{cases} \omega_{0,LPF} = \frac{1}{4nU_TC_0}\sqrt{2nI_{STAT}I_{LPF}} \\ Q_{LPF} = \frac{1}{2(nI_{STAT} - I_{LPF})}\sqrt{2nI_{STAT}I_{LPF}} \end{cases}. \tag{7}$$

The transfer function of the elliptic filter can be derived by obtaining poles and zeros from filter design tables [61]. In our design, the elliptic filter is $5^{th}$ order, with the reflection coefficient $\rho = 5\%$, the modular angle $\theta = 36°$ and power loss factor $K^2 = \infty$, which in theory can achieve pass-band ripple of 0.01 dB, steepness factor of 1.7013 and minimum stop-band attenuation of 40.81 dB (equivalent to cut-off slope of 176.8 dB/dec). The transfer function of the elliptic filter is given in (8) at the bottom of the next page, where $\omega_{-3\,\mathrm{dB}}$ is the $-3$ dB corner frequency.

We can also obtain the parameters of filter elements by referring to the filter design tables in [61]. By setting $\omega_{-3\,\mathrm{dB}}$ as $\sqrt{2}$

This article has been accepted for inclusion in a future issue of this journal. Content is final as presented, with the exception of pagination.



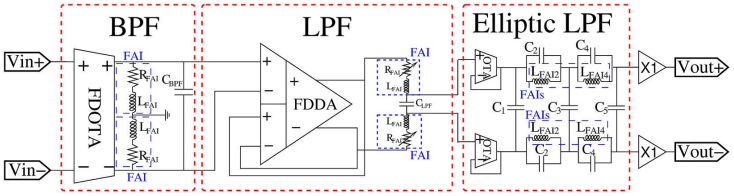


Fig. 4. Detailed structure of the cochlear filter channel consisting of three sub-filters. FAIs and capacitors are used to create the balanced ladder topologies.

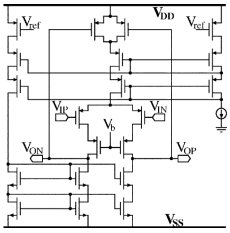


Fig. 5. Schematic of the fully differential operational transconductance amplifier (FDOTA).

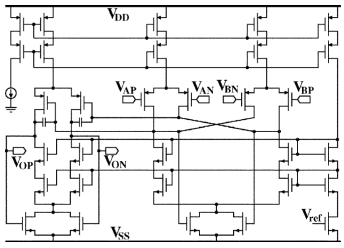


Fig. 6. Schematic of the fully differential difference amplifier (FDDA).

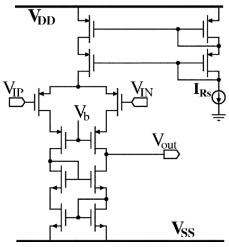


Fig. 7. Schematic of the single-end OTA. Its DC current $I_{Rs}$ sets the source resistance of the elliptic filter.

times of $\omega_{0,BPF}$ (center frequency of BPF), the values of required inductance and capacitance can be derived as following:

$$\begin{cases} L_{FAI2} = 0.8551(\frac{nU_T}{I_{STAT}})^2\sqrt{\frac{I_{STAT}}{nI_{BPF}}}C_0 \\ L_{FAI4} = 1.113(\frac{nU_T}{I_{STAT}})^2\sqrt{\frac{I_{STAT}}{nI_{BPF}}}C_0 \end{cases} \tag{9}$$

$$\begin{cases} C_1 = 0.5252\sqrt{\frac{I_{STAT}}{nI_{BPF}}}C_0 \\ C_2 = 0.7651\sqrt{\frac{I_{STAT}}{nI_{BPF}}}C_0 \\ C_3 = 2.296\sqrt{\frac{I_{STAT}}{nI_{BPF}}}C_0 \\ C_4 = 1.373\sqrt{\frac{I_{STAT}}{nI_{BPF}}}C_0 \\ C_5 = 2.293\sqrt{\frac{I_{STAT}}{nI_{BPF}}}C_0 \end{cases} . \tag{10}$$

Combining (2) and (9), the values of $C_{gy}$ in FAI2 and FAI4 can be derived

$$\begin{cases} C_{gy,FAI2} = 0.2138(\frac{I_{ELLI}}{I_{STAT}})\sqrt{\frac{nI_{STAT}}{I_{BPF}}}C_0 \\ C_{gy,FAI4} = 0.2783(\frac{I_{ELLI}}{I_{STAT}})\sqrt{\frac{nI_{STAT}}{I_{BPF}}}C_0 \end{cases} . \tag{11}$$

In the cochlea filter channel, only $I_{LPF}$ is actively tuned, while $I_{BPF}$ and $I_{ELLI}$ kept constant. Based on exhaustive simulations with extracted parameters in software, we choose to make $I_{BPF}$ equals $I_{STAT}$ so that the BPF has a relatively low Q factor and gentle response, and $I_{ELLI}$ equals $1.2I_{STAT}$ so that the FAIs in the elliptic filter are inductive enough to maintain the steep roll-off while enough margin is left to avoid negative-damping and instability. In addition, we use $x = I_{LPF}/I_{STAT}$ to denote the tuning factor of the LPF and also the entire cochlea filter, which can be dynamically controlled to mimic the active response of the biological cochlea. The transfer functions can be greatly simplified if we use $\omega_{pc}$ (the passive center frequency of the cochlea filter)

$$H_{ELLI}(s) = \frac{0.069851\omega_{-3\,\mathrm{dB}} \cdot (s^2 + 7.3381\omega_{-3\,\mathrm{dB}}^2)(s^2 + 3.1407\omega_{-3\,\mathrm{dB}}^2)}{(s + 0.96232\omega_{-3\,\mathrm{dB}})(s^2 + 1.2360\omega_{-3\,\mathrm{dB}}s + 1.1724\omega_{-3\,\mathrm{dB}}^2)(s^2 + 0.34350\omega_{-3\,\mathrm{dB}}s + 1.4269\omega_{-3d\,\mathrm{dB}}^2)} \tag{8}$$

This article has been accepted for inclusion in a future issue of this journal. Content is final as presented, with the exception of pagination.



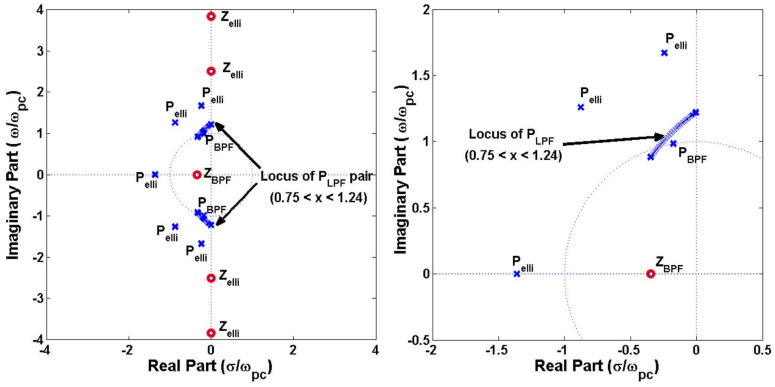


Fig. 8. (a) Normalized pole-zero plot of the proposed cochlea filter channel. (b) Pole-zero plot zoomed to left-up corner.

to replace $\omega_{0,BPF} = 1/4nU_TC_0\sqrt{5/3nI_{STAT}I_{BPF}}$. Combining (4), (6) and (8) with the above mentioned design settings ($\omega_{-3\,\mathrm{dB}} = \sqrt{2}\,\omega_{0,BPF}$, $I_{BPF} = I_{STAT}$, $x = I_{LPF}/I_{STAT}$, $I_{ELLI} = 1.2\ I_{STAT}$), the transfer function of the cascaded cochlea filter channel can be derived as (12) at the bottom of the page. As the slope factor $n$ in AMS 0.35 $\mu$m process is approximately 1.25, (12) can be further simplified into (13) at the bottom of the page. The proposed filter has nine poles and five zeros and its normalized zero-pole plot is shown in Fig. 8. As there are no zeros in the right half of the s-plane, the cochlea filter is a minimum-phase filter, as is the biological cochlea [63].

## IV. Analysis of Non-Idealities

### A. Mismatch

Naturally, the operation of the FAI is subject to transistor mismatches which cause circuit offsets. The mismatches can be classified into two categories: horizontal and vertical. The horizontal mismatch is the mismatch between transistors in differential pairs MP0-MP1, MN0-MN1 and MX0-MX1 which results in a DC current in the FAI running from port TA to TB. Taking the differential pair MN as an example, shown in Fig. 9(a), the mismatch between MN0 and MN1 will cause deviation in their transconductance, which results in a DC current running from

$$
\begin{aligned}
H_{tot}(s) = {} & (2.31\omega_{pc} \cdot \frac{s + 1.55\frac{n-1}{\sqrt{n}}\omega_{pc}}{s^2 + 1.55\frac{n-1}{\sqrt{n}}\omega_{pc}s + \omega_{pc}^2}) \\
& \cdot (\frac{1.2x\omega_{pc}^2}{s^2 + 1.55\frac{n-x}{\sqrt{n}}\omega_{pc}s + 1.2x\omega_{pc}^2}) \\
& \cdot [\frac{0.0988\omega_{pc} \cdot (s^2 + 14.7\omega_{pc}^2)(s^2 + 6.28\omega_{pc}^2)}{(s + 1.36\omega_{pc})(s^2 + 1.75\omega_{pc}s + 2.35\omega_{pc}^2)(s^2 + 0.486\omega_{pc}s + 2.85\omega_{pc}^2)}].
\end{aligned} \tag{12}
$$

$$
\begin{aligned}
& H_{tot}(s) \\
& = \frac{0.274x\omega_{pc}^4(s+0.347\omega_{pc})(s^2+14.7\omega_{pc}^2)(s^2+6.28\omega_{pc}^2)}{(s^2+0.347\omega_{pc}s+\omega_{pc}^2)[s^2+1.39(1.25-x)\omega_{pc}s+1.2x\omega_{pc}^2](s+1.36\omega_{pc})(s^2+1.75\omega_{pc}s+2.35\omega_{pc}^2)(s^2+0.486\omega_{pc}s+2.85\omega_{pc}^2)}.
\end{aligned} \tag{13}
$$

This article has been accepted for inclusion in a future issue of this journal. Content is final as presented, with the exception of pagination.



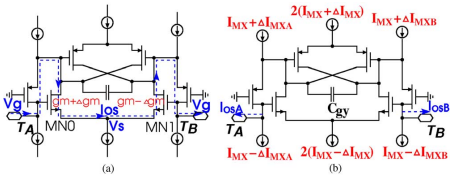


Fig. 9. Mismatch analysis of the FAI. (a) Offset current flowing between $T_A$ and $T_B$ results from horizontal mismatch between transistors in the differential pair. [Horizontal mismatch.] (b) Offset currents separately flowing at $T_A$ and $T_B$ result from vertical mismatch between the current sources. [Vertical mismatch.]

port TA to port TB even if TA and TB are tied to the same DC voltage $V_g$. The value and variance of the offset DC current can be derived as

$$I_{os} = \Delta gm(V_g - V_s) \approx \Delta gm U_T ln \frac{I_D}{I_0} \tag{14}$$

where $I_0$ is the transistor off current when $V_g = V_s = 0$ and is expressed as

$$I_0 = I_{spec} \cdot e^{-V_{th}/nU_T}. \tag{15}$$

$V_{th}$ is the transistor threshold voltage and $I_{spec}$ is the specific current defined as $2\beta n U_T^2$ where $\beta$ is the transconductance parameter. The ratio between $I_D$ and $I_{spec}$ is the inversion coefficient which is far less than unity in weak inversion [62].

The same analysis can be performed on transistor pair MP and MX, and the total offset currents resulting from horizontal mismatch can be expressed in the following as summation of three transistor pair mismatches:

$$I_{osH} = \Delta gm_{MN} U_T \ln \frac{I_{MX}}{I_{N0}} + \Delta gm_{MX} U_T \ln \frac{I_{MX}}{I_{P0}} + \Delta gm_{MP} U_T \ln \frac{I_{MP}}{I_{P0}}. \tag{16}$$

The vertical mismatch on the other hand refers to the mismatch between the current sources in the upper side and current sinks in the lower side. As shown in Fig. 9(b), the difference between the currents in the upper and lower side will flow out of the FAI through TA and TB. These two offset currents can be written as

$$I_{osVA(B)} = 2\Delta I_{MPA(B)} + 2\Delta I_{MX}. \tag{17}$$

### B. Noise

The noise model of the FAI is illustrated in Fig. 10, from which noise current density at the port TA and TB can be derived

$$\overline{i_n^2(\omega)} = g_{MP}^2[\overline{e_{nMP}^2} + \frac{g_{MX}^2 \overline{e_{nMX}^2} + g_{MN}^2 \overline{e_{nMN}^2}}{(g_{MX} - g_{MP})^2 + 4\omega^2 C_{gy}^2}]. \tag{18}$$

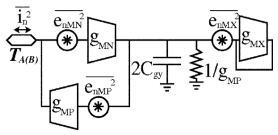


Fig. 10. Noise model of the FAI.

Note that the noise model in Fig. 10 does not include the source degeneration that $C_{gy}$ and MX have on the MP transistor. The actual noise tranconductance for $\overline{e_{nMP}^2}$ is smaller than $g_{MP}$ and thus (18) is in fact the worst-case noise estimation. According to the noise parameters given by the foundry, the transistor noise corner frequency is derived as $\omega_{corner} = 3\pi K_F I_D^{A_F - 1}/4qC_{ox}WL$ where $K_F$ and $A_F$ are flicker noise parameters, q is electron charge and $C_{ox}$ is gate oxide capacitance. For the cochlea filter, the biasing current $I_D$ is mapped with the passive center frequency $\omega_{pc}$, and thus we find the point where $\omega_{pc}$ equals $\omega_{corner}$ as follows:

$$\omega_{pc0} = [\frac{3\pi K_F (3.46 U_T C_0)^{A_F - 1}}{4qC_{ox}WL}]^{1/2 - A_F}. \tag{19}$$

Equation (19) is suitable for PMOS transistor, while for an NMOS transistor $WL$ should be replaced with $L^2$ according to the noise model provided by the foundry. Besides, parameter $A_F$ is between 1 and 2, and thus the $\omega_{pc}$ will be higher than $\omega_{corner}$ if it exceeds $\omega_{pc0}$. Therefore a set of values for $WL$ and $L^2$ which makes $\omega_{pc0}$ lower than 20 Hz can be derived so that the passive center frequency of the cochlea filter is always higher than the noise corner frequency and circuit noise is dominated by thermal noise. This setting not only simplifies the following noise calculation but also contributes to better noise performance as the cochlea filter has peak gain at a frequency equal or higher than $\omega_{pc}$. Calculation with the foundry parameters indicates the transistor dimension should meet the requirement that $WL$ is greater than $16 \sim 17\ \mu\text{m}^2$ for PMOS transistors and $L^2$ is greater than $9 \sim 10\ \mu\text{m}^2$ for NMOS transistors.

Considering only thermal noise, (18) is rewritten and simplified with the cochlear filter parameters as follows:

$$\overline{i_n^2(\omega)} = \frac{8kTI_{STAT}}{3U_T}[1 + \frac{2x}{(x - 1.25)^2 + 0.521(\frac{\omega}{\omega_{pc}})^2}]. \tag{20}$$

### C. Comprehensive Analysis

Based on the analysis above, a more complete FAI model with mismatch and noise considerations is derived and illustrated in Fig. 11. The DC offset currents affect the DC operation point of circuits and thus as shown in Fig. 4, at least one port of each FAIs is connected to low impedance source to release the offset currents. In the BPF and LPF, all FAIs have one port shorted to ground (BPF) or FDDA buffer output (LPF), releasing $I_{osH}$ and one branch of $I_{osV}$. The remaining branch of $I_{osV}$ flows through the FAI and causes a DC shift of $I_{osV} \cdot R_{FAI}$ which is in the worst case less than 1mV if the variances of parameters do not exceed 1%. FAIs in the elliptic filter should

This article has been accepted for inclusion in a future issue of this journal. Content is final as presented, with the exception of pagination.



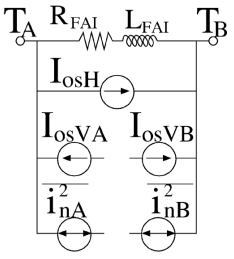


Fig. 11. FAI model with offsets and noise currents.

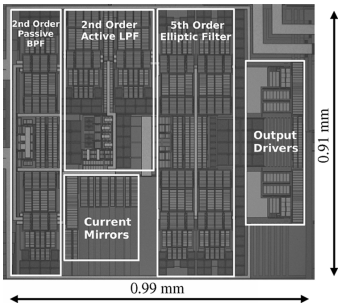


Fig. 12. Chip micrograph showing the cochlea filter channel.

be analyzed separately. The FAI2s have one port connected to the OTA followers while the FAI4s have one port connected to the other port of FAI2s. Thus $I_{osH}$ and $I_{osV}$ of both FAI2 and FAI4 flow through the OTA follower and cause DC shift of $(I_{osH}+2I_{osV})nU_T/I_{STAT}$ which is in the worst less than 40 mV if the variances of parameters do not exceed 1%. Besides, the offset currents in FAI4 flow through FAI2 in addition to one branch of $I_{osV}$ of FAI2 itself and cause DC shift of $(I_{osH}+3I_{osV})R_{FAI2}$ which is in the worst case less than 3 mV if the variances of parameters do not exceed 1%. In the end, one branch of $I_{osV}$ flows through FAI4 and causes DC shift of $I_{osV}R_{FAI4}$ which is less than 0.1 mV if the variances of parameters do not exceed 1%. Simulations prove the above-mentioned level of DC shift has insignificant effects on the circuit operation. Thus by referring to the parameter matching equations provided by the foundry, the width and length of the transistors in the FAIs are optimized so that the probability of the parameter variance being greater than 1% is limited to 1%.

Taking into consideration the parameter matching, the noise corner frequency setting explained in the previous section and also the weak inversion requirement, the dimensions of the transistor pairs in FAI are set to $W = 180\ \mu\mathrm{m}$ and $L = 3.5\ \mu\mathrm{m}$ for PMOS pairs MP and MX while $W = 100\ \mu\mathrm{m}$ and $L = 3.5\ \mu\mathrm{m}$ for NMOS pair MN.

For the noise analysis, the input referred noise of the BPF and LPF in the cochlea filter can be derived as following:

$$\overline{V_{niBPF}^2(\omega)} = 0.0651 \cdot \frac{\overline{i_{nBPF}^2(\omega)}}{\omega_{pc}^2 C_0^2} \tag{21}$$

$$\overline{V_{niLPF}^2(\omega)} = \frac{2\overline{i_{nLPF}^2(\omega)}}{x^2\omega_{pc}^2 C_0^2}[\frac{0.174\omega^2}{\omega_{pc}^2} + 0.333(1.25-x)^2]. \tag{22}$$

Noise calculation for the elliptic filter is far more complicated, but as the BPF and LPF provide all the gain for the cochlea filter, the noise from the elliptic filter is less significant compared with BPF and LPF when referred to the input. Therefore, neglecting the noise from elliptic filter, input referred noise density of the cochlea filter channel is the sum of BPF input referred noise and LPF input referred noise divided by gain of BPF and can be written as (23), at the bottom of the page, combining (4), (20), (21) and (22) and using $\xi$ to represent $\omega/\omega_{pc}$. As explained above, cochlea filter bandwidth has been set as $\sqrt{2}\omega_{pc}$, and thus integrated input referred noise of the cochlea filter is calculated as follows:

$$\begin{aligned} V_{inoise}^2 &= \int_0^{\sqrt{2}} \overline{V_{ni}^2(\xi)}d\xi \\ &= \frac{440kT}{\omega_{pc}C_0}[(\frac{1}{x}-\frac{1}{6})^2 + 0.65]. \end{aligned} \tag{24}$$

Equations (24) indicates that the filter input-referred noise decreases with increasing center frequency and tuning factor. A cochlea filter with passive center frequency of 100 Hz has 47 $\mu\mathrm{V_{rms}}$ input noise in the low Q mode ($x = 0.75$) and 27 $\mu\mathrm{V_{rms}}$ in the high Q mode ($x = 1.24$).

## V. Results

Based on the design explained above, a cochlea filter channel has been fabricated using AMS 0.35 $\mu$m 2-poly 4-metal process, as shown in Fig. 12. A prototype PCB and an NI PXI platform are built to characterize the filter, as illustrated in Fig. 13.

$$\begin{aligned} &\overline{V_{ni}^2(\xi)} \\ &= \frac{1.15kT}{\omega_{pc}C_0}\{\frac{[(1.25-x)^2+2x+0.521\xi^2](\xi^4-1.86\xi^2+1)}{x^2(\xi^2+0.14)} + 0.521 + \frac{2}{0.12+\xi}\} \end{aligned} \tag{23}$$

This article has been accepted for inclusion in a future issue of this journal. Content is final as presented, with the exception of pagination.



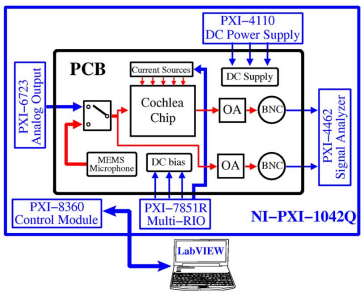


Fig. 13. Block diagram of the experimental setup. Input to the cochlea filter chip can be switched between the PXI-6723 analog output module and a MEMS microphone (ADMP401). Biasing currents that set the operating condition of the cochlea filters are controlled by the PXI-7851R multi-function reconfigurable IO module. The output of the cochlea filters are further amplified by an off-chip amplifier (OA) and interfaced with the PXI-4462 dynamic signal analyzer through BNC connectors.

The static current of the cochlea filter $I_{STAT}$ is set with different values from 37.14 pA to 9.915 nA so as to make the filter operate in nine frequency regions corresponding to the octave audio bands from 31 Hz to 8 kHz. The BPF current $I_{BPF}$ is set where $\omega_{pc}$ is approximately $10 \sim 20\%$ smaller than the corresponding octave frequency value. The LPF current $I_{LPF}$ is tuned in the region from where the LPF center frequency overlays with $\omega_{pc}$ (LQ mode), to where the LPF peak gain is maximized (HQ mode). The elliptic filter current $I_{ELLI}$ is set as $1.2I_{STAT}$ as explained in Section III.

### A. Frequency Response

*1) Magnitude Response:* Frequency responses of the nine filter bands in magnitude are measured and plotted in Fig. 14. Apart from the LQ and HQ modes mentioned above, responses of the cochlea filters in medium Q (MQ) mode are also measured, where $I_{LPF}$ is adjusted so that center frequency (CF) of the entire filter is located approximately at the corresponding octave frequency value. As shown in Fig. 14, the passive and gentle low-frequency band, active and selective mid-band and steep roll-off are achieved in all of the filters. Although a 40dB of peak gain variation range has been measured from chinchilla cochlea [16], [18], more physiological measurements in recent years report approximately $20 \sim 30$ dB of gain variation [17], [19]–[21], [23]. The high-frequency amplitude plateau in biological cochlea [28] is also found in the 31 Hz, 63 Hz, 125 Hz, 500 Hz, 1 kHz and 2 kHz bands. Besides, it is observed that CFs of LQ mode locate approximately $10 \sim 20\%$ leftwards from the CFs of MQ, while CFs of HQ mode locate $10 \sim 20\%$ rightwards. In other words, the CFs become higher together with increasing peak gain and selectivity, which agrees with biological cochlea behavior [16]–[21]. The detailed results are listed in Table I. Noticing that as parasitic resistance of wires exists in real VLSI implementation, the range of tuning factor $x$ in Table I is wider than the value used in previous section $(0.75 \sim 1.24)$. To improve the precision of current measurement, current mirrors with 1:100 ratio are used on chip. Therefore, the actually measured off-chip currents are 100 times as much as those values in Table I.

*2) Phase Response:* As both biological cochlea and the proposed filter have minimum-phase property, their phase responses should also be similar when the magnitude responses are matched. The phase responses of the 31 Hz and 8 kHz bands are illustrated in Fig. 15. As also observed in the physiological results, the filter phase lag increases with frequency in the pass-band [16]–[19], [21], [23]. The LQ phase lag at the passive centre frequency is slightly over half cycle [17], [18], [20], [21], while the HQ phase lag at the active centre frequency is approximately one cycle [17], [21]–[23]. The LQ response has more phase lag at frequencies lower than $\omega_{ac}$ (active center frequency) while the HQ response has more phase lag at frequencies higher than $\omega_{ac}$ [17]–[21].

*3) Group Delay:* Fig. 15 indicates that the group delay reaches maximum at $\omega_{ac}$ where the phase response curve has steepest slope. Fig. 16 shows the maximum group delay in unit of periods across different center frequencies. As expected, the group delay increases from LQ to HQ mode. The maximum group delays in LQ and MQ modes are approximately 5 periods while the maximum group delay in HQ mode is in the region of 10 periods. Fig. 17 shows the physiologically measured maximum group delay in human cochlea [64]. The measurement in [64] is based on the stimulus-frequency emission method which stimulates the cochlea with low-intensity input. Therefore the results in [64] correspond to the HQ response in this work. The comparison in Fig. 17 shows the cochlea filter has similar order of group delay with human cochlea.

### B. Time Domain Response

Impulse responses of the cochlea filter in 31 Hz and 8 kHz bands are given in Fig. 18, combined with response from BPF, LPF and elliptic filter separately. As the cochlea filter is a composite of three filters in cascade, its overall impulse response is the convolution of three individual responses. From Fig. 18, it is observed that for HQ mode, envelopes of response are not smooth and there is a trough near the third ringing crests, while for LQ mode, however, the envelopes are fairly smooth. The reason for this phenomenon is that, as shown in the decomposed response plots, BPF and elliptic filters settle much quicker than LPF in HQ mode, and thus although their responses are significant enough to affect the convolved overall response in the early stage, after 100 ms in Fig. 18(a) and 0.4 ms in Fig. 18(b), the overall responses are fully dominated by LPF. Therefore the impulse responses appear to have two stages of behavior, the convoluted response and the LPF-dominant response, separated by the settling of BPF and elliptic filter. As for the LQ mode, the LPF settles even faster than the BPF and elliptic filter, and thus the overall responses are smooth over time.

The post-dominance of LPF in HQ mode results in a shift of ringing frequency. As shown in Fig. 18, initial ringing periods in convolved responses $(t_{d1})$ are wider than ringing periods in the LPF-dominant responses $(t_{d2})$. This effect agrees with the frequency gliding phenomenon observed in physiological measurements, where instantaneous frequency of biological cochlea response to clicks is not constant but increases over time until

This article has been accepted for inclusion in a future issue of this journal. Content is final as presented, with the exception of pagination.



TABLE I
FREQUENCY RESPONSE SPECIFICATIONS OF COCHLEA FILTER IN DIFFERENT CONFIGURATIONS

| | | CF * | CF Variation | GD * | ERB * | $I_{STAT}$ | $x$ | PG * | PG Variation | Q factor | Roll-off Slope |
|---|---|---|---|---|---|---|---|---|---|---|---|
| Filter1 | LQ | 25Hz | -19.3% ∼+12.9% | 132ms | 14.3Hz | 37.14pA | 0.68 | 7.736dB | 18.8dB | 2.08 | 125.5dB/dec |
| | MQ | 31Hz | | 126ms | 14.8Hz | | 1.07 | 12.48dB | | 3.16 | 189.3dB/dec |
| | HQ | 35Hz | | 396ms | 3.97Hz | | 1.39 | 26.53dB | | 15.9 | 336.2dB/dec |
| Filter2 | LQ | 53Hz | -15.9% ∼+17.5% | 53.9ms | 32.5Hz | 78.41pA | 0.68 | 8.787dB | 20.4dB | 2.11 | 110.8dB/dec |
| | MQ | 63Hz | | 63.5ms | 27.5Hz | | 0.95 | 14.26dB | | 3.28 | 159.2dB/dec |
| | HQ | 74Hz | | 168ms | 7.87Hz | | 1.45 | 29.14dB | | 19.5 | 274.2dB/dec |
| Filter3 | LQ | 105Hz | -16% ∼+12% | 32.8ms | 54.3Hz | 143.7pA | 0.82 | 9.971dB | 21.5dB | 2.28 | 124.1dB/dec |
| | MQ | 125Hz | | 35.1ms | 41.8Hz | | 1.26 | 19.07dB | | 3.79 | 183.9dB/dec |
| | HQ | 140Hz | | 73.6ms | 11.0Hz | | 1.48 | 31.51dB | | 19.4 | 301.8dB/dec |
| Filter4 | LQ | 220Hz | -12% ∼+10% | 16.3ms | 106Hz | 279.1pA | 0.92 | 11.52dB | 20.6dB | 2.44 | 132.4dB/dec |
| | MQ | 250Hz | | 16.8ms | 88.1Hz | | 1.23 | 17.72dB | | 3.57 | 172.4dB/dec |
| | HQ | 275Hz | | 33.1ms | 24.6Hz | | 1.53 | 32.10dB | | 15.3 | 290.9dB/dec |
| Filter5 | LQ | 430Hz | -12.2% ∼+11.2% | 10.6ms | 203Hz | 554.0pA | 0.88 | 13.14dB | 20.5dB | 2.69 | 110.6dB/dec |
| | MQ | 490Hz | | 11.4ms | 162Hz | | 1.26 | 21.32dB | | 4.26 | 161.9dB/dec |
| | HQ | 545Hz | | 17.4ms | 53.4Hz | | 1.55 | 33.64dB | | 14.0 | 240.5dB/dec |
| Filter6 | LQ | 0.9kHz | -14.3% ∼+14.3% | 4.03ms | 484Hz | 1.189nA | 0.89 | 10.79dB | 21.3dB | 2.20 | 116.3dB/dec |
| | MQ | 1.05kHz | | 4.82ms | 386Hz | | 1.24 | 17.74dB | | 3.00 | 160.9dB/dec |
| | HQ | 1.2kHz | | 7.65ms | 101Hz | | 1.55 | 32.07dB | | 16.0 | 391.4dB/dec |
| Filter7 | LQ | 1.7kHz | -15% ∼+10.8% | 1.36ms | 0.864kHz | 2.156nA | 0.88 | 12.23dB | 20.0dB | 2.62 | 114.6dB/dec |
| | MQ | 2kHz | | 1.47ms | 0.629kHz | | 1.31 | 21.38dB | | 3.64 | 166.8dB/dec |
| | HQ | 2.2kHz | | 4.04ms | 0.238kHz | | 1.54 | 32.22dB | | 14.7 | 238.5dB/dec |
| Filter8 | LQ | 3.5kHz | -10.3% ∼+12.8% | 706$\mu$s | 1.69kHz | 4.291nA | 0.91 | 11.28dB | 20.0dB | 2.76 | 120.7dB/dec |
| | MQ | 3.9kHz | | 950$\mu$s | 1.33kHz | | 1.29 | 18.95dB | | 3.71 | 160.6dB/dec |
| | HQ | 4.4kHz | | 2.04ms | 0.375kHz | | 1.55 | 31.26dB | | 18.3 | 272.1dB/dec |
| Filter9 | LQ | 7.1kHz | -14.5% ∼+10.8% | 223$\mu$s | 4.01kHz | 9.915nA | 0.68 | 8.152dB | 21.1dB | 2.25 | 123.6dB/dec |
| | MQ | 8.3kHz | | 369$\mu$s | 2.94kHz | | 1.20 | 19.03dB | | 3.32 | 176.0dB/dec |
| | HQ | 9.2kHz | | 1.24ms | 1.28kHz | | 1.55 | 29.23dB | | 10.6 | 268.4dB/dec |

*CF = Center Frequency; GD = Group Delay; ERB = Equivalent Rectangular Bandwidth; PG = Peak Gain.

settled at steady state [24]–[27]. The gliding phenomenon is a standard for cochlea model evaluation suggested by the physiologists [24], [26]. Its origin has been proved to be independent of the nonlinear active process [24], [26]. Similarly, the frequency shift in this cochlea filter is not based any active control and thus provide a basis for future research on how the gliding effects influence signal processing in the cochlea.

### C. Noise Measurement

Output noise spectrum from the 31 Hz and 8 kHz bands, with comparison between LQ, MQ and HQ modes are illustrated in Fig. 19. The 50 Hz harmonics shown are due to the ripples of power supply. Besides, the noise spectrum of the HQ mode of 8 kHz band has prominent peaks at CF harmonics. This indicates that the 8 kHz band has more harmonic distortion than the 31 Hz band especially in the HQ mode. As shown in Table I, the DC current in FAI scales with CF. Therefore, the operation of transistors in the FAI moves from weak inversion towards moderate inversion when the center frequency increases. However, the DC operating points of the filter are designed based on the weak inversion assumption, and the circuit linearity will be affected by the DC variation. The CF harmonics should be theoretically well attenuated by the elliptic filter. However, the transistor in moderate inversion has lower $gm/I_D$ compared with weak inversion which makes the FAI inductance deviate from designed values and consequently degrade the elliptic filter performance. The harmonic distortion issue will be discussed further in Section V-D.

The input-referred noise density at the center frequency of the 9 filter bands in LQ, MQ and HQ modes are illustrated in Fig. 20. Compared with noise predication function of (24), the measured results in MQ and HQ modes agree in terms of the fact that input referred noise decreases for higher center frequencies. However, LQ mode shows noise does not vary much from low to high frequencies, because the filter selectivity is not high enough to overcome the added power supply harmonics from the increase of filter bandwidth. Besides, Fig. 20 also proves the increase of tuning factor $x$ results in lower input referred noise except the 31 Hz band where MQ has even wider equivalent rectangular bandwidth than LQ mode as shown in Table I.

### D. Distortion Measurement

*1) Total Harmonic Distortion (THD) and Signal-to-Noise-and Distortion Ratio(SINAD):* Fig. 21 shows the plots of THD and SINAD against input level based on the measured results from the 31 Hz and 8 kHz bands. The SINAD of both filters generally maintain above the 12 dB SINAD threshold for intelligent hearing before THD reaches the edge of 5% limit. The HQ mode has most significant harmonic distortion due to high LPF gain and thus high signal amplitude at the elliptic filter input. As predicted in the noise spectrum [Fig. 19(b)], the 8 kHz band has more harmonic distortion than the 31 Hz band. Based on the 5% THD limit, the maximum input level is plotted against filter center frequencies, so is the maximum SINAD. Fig. 22 shows the filter linearity tends to degrade with higher frequencies.

*2) Two-Tone Inter-Modulation Distortion:* Inter-modulation distortion test is performed and the results are shown in Fig. 23. The third-order inter-modulation product $2f_1 - f_2$ appears to be the most prominent distortion component because it is designed to coincide with the filter center frequency. The inter-modulation distortion is also found in the biological cochlea, which

This article has been accepted for inclusion in a future issue of this journal. Content is final as presented, with the exception of pagination.



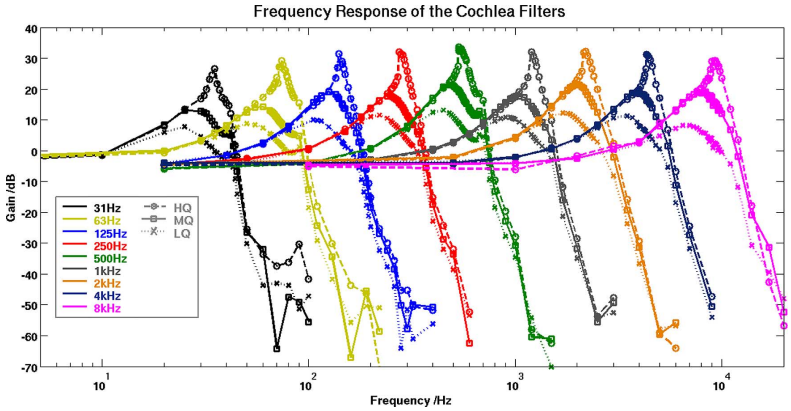


Fig. 14. Measured frequency responses of 9 cochlea filters covering octave audio bands from 31 Hz to 8 kHz. The LQ, MQ and HQ modes respectively correspond to the biological response with high, normal and low intensity sound stimulus. Tuning of the filter from LQ to HQ is achieved by adjusting only one circuit parameter ($I_{LPF}$).

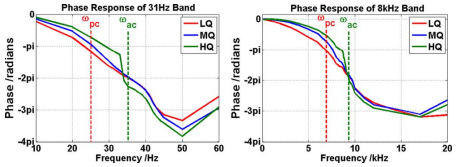


Fig. 15. Measured phase response of the 31 Hz band and 8 kHz band.

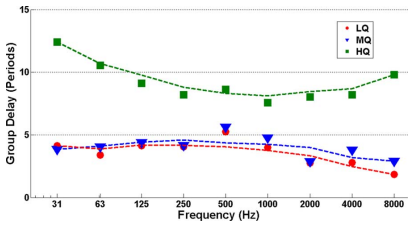


Fig. 16. Measured maximum group delay across different center frequencies.

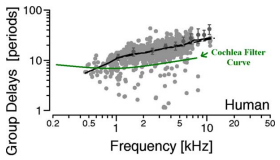


Fig. 17. The HQ maximum group delay curve in comparison with physiologically measured results from human cochlea. The figure is adapted from the Fig. 5 in [64].

proves that the biological hearing system can tolerate 17 $\sim$ 24 dB worst-case spurious free dynamic range (SFDR) [28]. Fig. 24 plots the filter maximum input range measured using the 17 dB SFDR limit. It shows in most frequency bands the maximum input range is further reduced compared with the results based on the 5% THD limit. Nevertheless, the input range of the 8 kHz band appears even higher than the results in Fig. 22 and there is no significant degradation compared with the other bands. The distortion products of interest in the inter-modulation measurement are in-band signals while the CF harmonics measured in the THD test are out-of-band signals. Therefore, the high harmonic distortion measured in the 8 kHz band is probably due to the degraded stop-band attenuation.

### *E. Critical Bandwidth*

An equivalent rectangular band-pass filter model is illustrated in Fig. 25, which helps us to understand the critical band and frequency discrimination feature of the designed cochlea filters. The calculated equivalent rectangular bandwidth (ERB) and measured $-3$ dB bandwidth of the cochlea filters are plotted versus corresponding CF in Fig. 26, together with the approximated bandwidth of human auditory filters derived from the formula given by Glasberg and Moore [65] for comparison. It shows that $-3$ dB bandwidth is generally narrower than the ERB, but their discrepancy is not significant. The exact bandwidth values are listed in Table I. We observe from Fig. 26 that the ERB curve given by Glasberg and Moore from psycho-acoustical research lies in-between the ERB curves of the MQ and HQ modes. However as the cochlea filter can be continuously tuned, it is possible to find a condition between the MQ and HQ modes where the ERB versus CF curve corresponds with better agreement to psycho-acoustical results [65].

### *F. Testing With Acoustic Signals*

A segment of acoustic signal (mixed sounds from musical instruments of the horn and bass drum) is applied to the cochlea

This article has been accepted for inclusion in a future issue of this journal. Content is final as presented, with the exception of pagination.



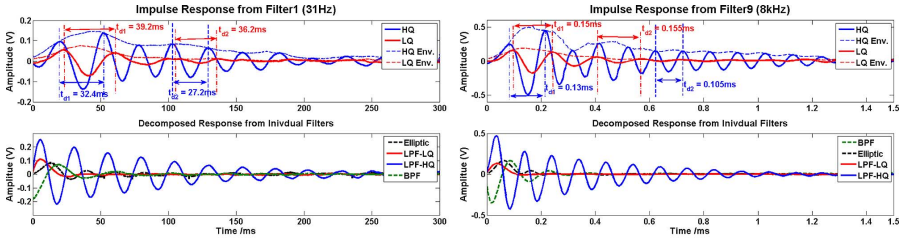


(a) (b)

Fig. 18. Measured impulse response from (a) 31 Hz and (b) 8 kHz band cochlea filters. The decrease of ringing period ($t_d$) with time agrees with the gliding phenomenon in biological cochlea.

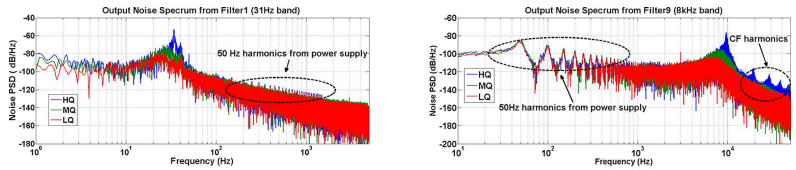


(a) (b)

Fig. 19. Measured output noise spectrum from (a) 31 Hz and (b) 8 kHz band filters. Like the frequency response shown in Fig. 14, the spectrum shape has stable low-frequency band (does not vary with tuning), tunable mid-frequency band and steep roll-off at stop-band.

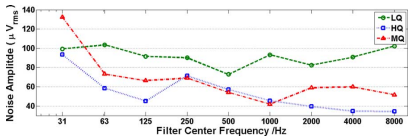


Fig. 20. Plot of measured integrated input-referred noise versus center frequency.

filter. As the frequencies around 63 Hz, 1 kHz and 2 kHz have highest intensity, the cochlea filter is tested in these three frequency bands accordingly and the results are shown in Fig. 27. It is notable that, the noise around center frequency is selectively amplified rather than the signal in the HQ output of the 1 kHz band, as the cochlea filter currently does not have the capability to distinguish between signal and noise. This problem can be potentially solved with the addition of an SNR estimation mechanism [66]. Also, the results show that the octave distribution of filter center frequencies is inadequate for high performance auditory processing task. The purpose of using octave distribution in this paper is only to prove the frequency range that the cochlea filter covers. As for future applications, more sophisticated distributions like one third octave or bark scale will be investigated.

### G. Summary

Table II summarizes the measured specifications of the cochlea filter chip. Note that the power dissipation of the FDDA and the output buffers does not scale with filter center

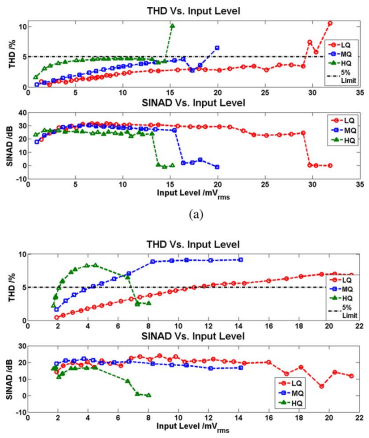


(a)




(b)

Fig. 21. Measured THD and SINAD plots versus input level from (a) 31 Hz and (b) 8 kHz band filters. The 5% THD limit is suggested for auditory circuits [48].

frequency. Consequently, the power dissipation of the 31 Hz filter is only one-third less than that of the 8 kHz filter. Table III gives scores in terms of auditory filter model following the criteria given by Lyon [67]. Noticing that the current cochlea filter has not been integrated with automatic-Q-control (AQC) mechanism, but as the measured results indicate the filter can

This article has been accepted for inclusion in a future issue of this journal. Content is final as presented, with the exception of pagination.



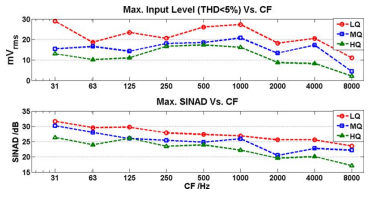


Fig. 22. Measured maximum input range and SINAD across different center frequencies.

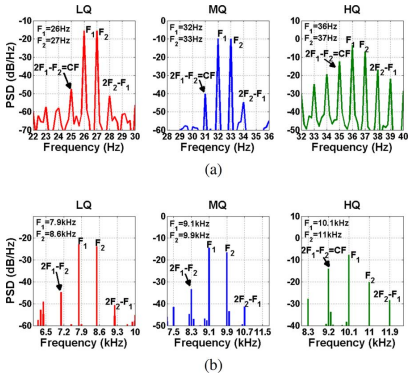


Fig. 23. Two-tone inter-modulation distortion measured from (a) 31 Hz and (b) 8 kHz band filters. Two signals in equal amplitude (10 mV) with primary frequencies $f_1$ and $f_2$ such that $2f_1 - f_2 = \mathrm{CF}$ are applied to the cochlea filter.

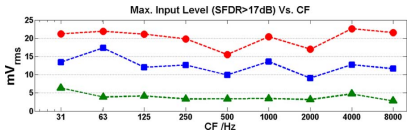


Fig. 24. Maximum input range measured across different center frequencies using the 17dB SFDR limit.

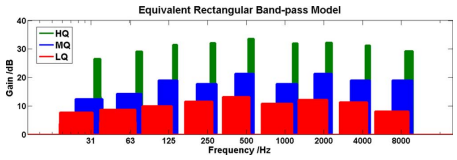


Fig. 25. Equivalent rectangular band-pass filter model of the cochlea filters. The rectangular filters pass the equal amount of energy with the corresponding cochlea filters in Fig. 14.

be actively tuned according to sound level, a potential '+' credit is given in the 'dynamic' criterion.

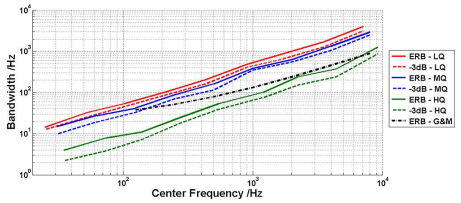


Fig. 26. ERB and −3 dB bandwidth of the cochlea filters in comparison with approximated ERB of human auditory filters [65].

## VI. Conclusion

Design and experimental results of a bio-realistic analog cochlea filter have been presented, the highlights of which can be summarized as following:

- The filter is highly faithful with measured response from physiological experiment on mammalian cochlea, with passive and gentle response in low-frequency band, active and selective response in mid-band and a sharp transition from pass-band into stop-band. Besides, similarity of the filter in phase response and impulse response has also been demonstrated.
- The filter can operate at center frequencies from as low as 31 Hz to 8 kHz. Experimental results show that the operation in deep low frequency is even more robust than in high frequencies.
- Filter efficiency has been improved by the specialized triple-stage design, to the extent that:
  - The active behavior observed in biology is emulated by tuning only one circuit parameter (tuning factor $x$), and positions of only one pair of poles (poles of LPF) are shifted in tuning. The reduced tuning complexity will prospectively increase the robustness and dynamic performance of the proposed cochlea system in Fig. 1.
  - In previous second-order section based filters, the bio-realistic 330 dB/dec roll-off requires the filter order to be at least 16 [68]. The same steepness is achieved in our $9^{th}$ order design by using a sharp cut-off elliptic filter. The lower filter order leads to less power consumption and smaller chip area for each channel, and thus a larger number of channels can be implemented in a parallel filter bank, which will prospectively increase the functionality of the cochlea system shown in Fig. 1.

On the other hand, additional improvement and future work are still necessary including:

- The filter dynamic range is constrained by the limited linear range of the tanh transconductance in FAIs. Linearisation techniques such as multi-tanh [69] may be investigated in the future.
- Filter array with center frequencies distributed in more applicable manner such as one-third octave or bark scale should be implemented so as to fulfill practical auditory processing tasks.
- Other mechanisms including local control (AQC) and signal-noise distinguishing will be integrated with the

This article has been accepted for inclusion in a future issue of this journal. Content is final as presented, with the exception of pagination.



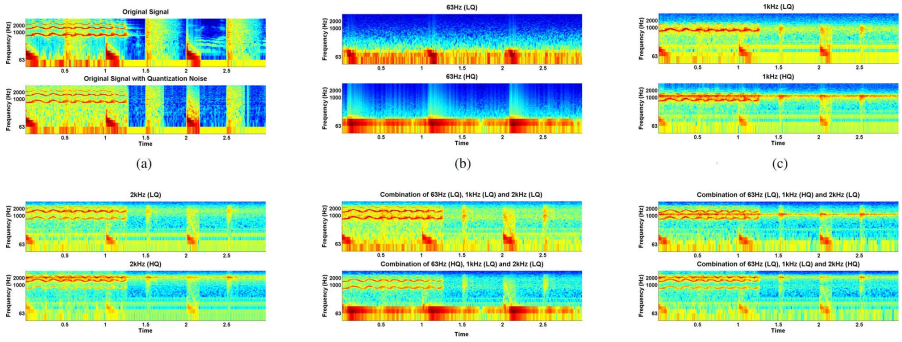


Fig. 27. Measured time-frequency spectrogram of outputs from cochlea filters in response to mixed signals of the horn and bass drum. The signal is applied together with quantization noise from the 13-bit DAC in NI-6732 analog output. Outputs from the three bands and their combinations prove the frequency selectivity of the cochlea filters. Also, the quantization noise has been attenuated, especially by the filter in HQ mode. (a) Input signals. (b) Output from 63Hz filter. (c) Output from 1 kHz filter. (d) Output from 2 kHz filter. (e) Combination of the three filter outputs. (f) Combination of the three filter outputs.

TABLE II
SUMMARY OF CHIP SPECIFICATIONS

| | |
|---|---|
| Fabrication process | AMS 0.35 $\mu$m 3.3V 2P4M |
| Channel area | $0.9mm^2$ (0.99mm X 0.91mm) |
| Center frequency | 31Hz∼8kHz |
| Power dissipation | 59.5$\mu$W @31Hz;<br>90.0$\mu$W @8kHz. |
| Peak gain variation | 18.8dB @31Hz;<br>21.1dB @8kHz. |
| Cut-off slope | 125.5dB/dec(LQ) ∼ 336.2dB/dec(HQ) @31Hz;<br>123.6dB/dec(LQ) ∼ 268.4dB/dec(HQ) @8kHz. |
| Phase delay @CF | 210.5degree(LQ) ∼ 373.1degree(HQ) @31Hz;<br>204.8degree(LQ) ∼ 347.4degree(HQ) @8kHz. |
| Min. input noise | 93.34$\mu V_{rms}$ @31Hz;<br>34.32$\mu V_{rms}$ @8kHZ. |
| Max. input swing<br>(THD< 5%) | 82.0 $mV_{p-p}$ @31Hz;<br>31.2 $mV_{p-p}$ @8kHz. |
| Max. input swing<br>(SFDR>17dB)) | 60 $mV_{p-p}$ @31Hz;<br>61 $mV_{p-p}$ @8kHz. |
| SINAD | 26.38dB (HQ) ∼ 31.67dB (LQ) @31Hz;<br>17.13dB (HQ) ∼ 23.56dB (LQ) @8kHz. |
| Expected dynamic<br>range with AQC * | 49.8dB @31Hz;<br>50.2dB @8kHz. |

*The lower bound is determined by the HQ input-referred noise and the upper bound is determined by the LQ linear range.

TABLE III
SCORES AS AUDITORY FILTER MODEL [67]

| | | | |
|---|---|---|---|
| 1. Simple | Laplace domain | 6. Stable tail | + |
| 2. BW control | + | 7. Runnable | + |
| 3. Peak/skirts | + | 8. Waves | - |
| 4. Asymmetry | + | 9. Impulse resp. | + |
| 5. Gain Variation | + | 10. Dynamic | + (potentially) |

filter and ultimately a system illustrated in Fig. 1 will be implemented.

## ACKNOWLEDGMENT

The authors would like thank Mr. T. Chen for his help in taking the chip micrograph.

## REFERENCES

[1] W. S. Rhode, "Some observations on cochlear mechanics," *J. Acoust. Soc. Amer.*, vol. 64, no. 1, pp. 158–176, Jul. 1978.
[2] B. S. Wilson and M. F. Dorman, "Interfacing sensors with the nervous system: lessons from the development and success of the cochlear implant," *IEEE Sensors J.*, vol. 8, no. 1, pp. 131–147, Jan. 2008.
[3] K. H. Kim, S. J. Choi, J. H. Kim, and D. H. Kim, "An improved speech processing strategy for cochlear implants based on an active nonlinear filterbank model of the biological cochlea," *IEEE Trans. Biomed. Circuits Syst.*, vol. 56, no. 3, pp. 828–836, Mar. 2009.
[4] T. Harczos, A. Chilian, and P. Husar, "Making use of auditory models for better mimicking of normal hearing processes with cochlear implants: the SAM coding strategy," *IEEE Trans. Biomed. Circuits Syst.*, vol. 7, no. 4, pp. 414–425, Aug. 2013.
[5] Z. Tuske, P. Golik, R. Schluter, and F. R. Drepper, "Non-stationary feature extraction for automatic speech recognition," in *Proc. Int. Conf. Acoustics, Speech and Signal Processing*, 2011, pp. 5204–5207.
[6] M. J. Newton and L. S. Smith, "A neurally inspired musical instrument classification system based upon the sound onset," *J. Acoust. Soc. Amer.*, vol. 131, no. 6, pp. 4785–4798, Jun. 2012.
[7] X. Valero and F. Alias, "Gammatone cepstral coefficients: biologically inspired features for non-speech audio classification," *IEEE Trans. Multimedia*, vol. 14, no. 6, pp. 1684–1689, Dec. 2012.
[8] X. Zhao, Y. Shao, and D. Wang, "CASA-based robust speaker identification," *IEEE Audio, Speech, Language Process.*, vol. 20, no. 5, pp. 1608–1616, Feb. 2012.
[9] B. Gao, W. L. Woo, and S. S. Dlay, "Unsupervised single-channel separation of nonstationary signals using gammatone filterbank and itakura-saito nonnegative matrix two-dimensional factorizations," *IEEE Trans. Circuits Syst. I, Reg. Papers*, vol. 60, no. 3, pp. 662–675, Mar. 2013.
[10] J. Qi, D. Wang, Y. Jiang, and R. Liu, "Auditory features based on gammatone filters for robust speech recognition," in *Proc. IEEE Int. Symp. Circuits and Syst.*, 2013, pp. 305–308.
[11] S. Mandal, S. M. Zhak, and R. Sarpeshkar, "A bio-inspired active radio-frequency silicon cochlea," *IEEE. J. Solid-State Circuits*, vol. 44, no. 6, pp. 1814–1828, Jun. 2009.
[12] C. J. Galbraith, R. D. White, L. Cheng, K. Grosh, and G. M. Rebeiz, "Cochlea-based RF channelizing filters," *IEEE Trans. Circuits Syst. I, Reg. Papers*, vol. 55, no. 4, pp. 969–979, May 2008.
[13] R. Sarpeshkar, *Ultra Low Power Bioelectronics: Fundamentals, Biomedical Applications, and Bio-Inspired Systems*. Cambridge, U.K.: Cambridge Univ. Press, 2011, pp. 9–14.
[14] L. Gouveia, T. J. Koickal, and A. Hamilton, "An asynchronous spike-event coding scheme for programmable analog array," *IEEE Trans. Circuits Syst. I, Reg. Papers*, vol. 58, no. 4, pp. 791–799, Apr. 2011.

[15] G. Sanchez, T. J. Koickal, A. Sripad, L. C. Gouveia, A. Hamilton, and J. Madrenas, "Spike-based analog-digital neuromorphic information processing system for sensor applications," in *Proc. IEEE Int. Symp. Circuits and Syst.*, 2013, pp. 1624–1627.

[16] M. A. Ruggero, S. S. Narayan, A. N. Temchin, and A. Recio, "Mechanical bases of frequency tuning and neural excitation at the base of the cochlea: Comparison of basilar-membrane vibrations and auditory-nerve-fiber responses in chinchilla," *Proc. Nat. Acad. Sci. USA*, vol. 97, no. 22, pp. 11744–11750, Oct. 2000.

[17] T. Ren and A. L. Nuttall, "Basilar membrane vibration in the basal turn of the sensitive gerbil," *Hear. Res.*, vol. 151, no. 1-2, pp. 48–60, Jan. 2001.

[18] W. S. Rhode, "Basilar membrane mechanics in the 6-9 kHz region of sensitive chinchilla cochleae," *J. Acoust. Soc. Amer.*, vol. 121, no. 5, pp. 2792–2804, May 2007.

[19] A. R. -Spinoso, S. S. Narayan, and M. A. Ruggero, "Basilar membrane responses to noise at a basal site of the chinchilla cochlea: quasi-linear filtering," *J. Assoc. Res. Otolaryngol*, vol. 10, no. 4, pp. 471–484, Dec. 2009.

[20] F. Chen, D. Zha, A. Fridberger, J. Zheng, N. Choudhurry, S. L. Jacques, R. K. Wang, X. Shi, and A. L. Nuttall, "A differentially amplified motion in the ear for near-threshold sound detection," *Nat. Neurosci.*, vol. 14, no. 6, pp. 770–774, Jun. 2011.

[21] C. P. Versteegh and M. v. d. Heijden, "Basilar membrane responses to tones and tone complexes: nonlinear effects of stimulus intensity," *J. Assoc. Res. Otolaryngol.*, vol. 13, no. 6, pp. 785–798, Dec. 2012.

[22] A. N. Temchin, A. R. -Spinoso, H. Cai, and M. A. Ruggero, "Traveling waves on the organ of Corti of the chinchilla cochlea: spatial trajectories of inner hair cell depolarization inferred from responses of auditory-nerve fibers," *J. Neurosci.*, vol. 32, no. 31, pp. 10522–10529, Aug. 2012.

[23] W. He and T. Ren, "Basilar membrane vibration is not involved in the reverse propagation of otoacoustic emissions," *Sci. Rep.*, vol. 3, doi: 10.1038/sre01874.

[24] E. d. Boer and A. L. Nuttal, "The mechanical waveform of the basilar membrane. I. frequency modulations (glides) in impulse responses and cross-correlation functions," *J. Acoust. Soc. Amer.*, vol. 101, no. 6, pp. 3583–3592, Jun. 1997.

[25] A. Recio and W. S. Rhode, "Basilar membrane responses to broadband stimuli," *J. Acoust. Soc. Amer.*, vol. 108, no. 5, pp. 2281–2298, Nov. 2000.

[26] C. A. Shera, "Frequency glides in click responses of the basilar membrane and auditory nerve: their scaling bahavior and origin in traveling-wave dispersion," *J. Acoust. Soc. Amer.*, vol. 109, no. 5, pp. 2023–2034, May 2001.

[27] A. N. Temchin and A. R. -Spinoso, "Timing of cochlear responses inferred from frequency-threshold tuning curves of auditory-nerve fibers," *Hear. Res.*, vol. 272, no. 1-2, pp. 178–186, Feb. 2011.

[28] L. Robles, M. A. Ruggero, and N. C. Rich, "Two-tone distortion in the basilar membrane of the cochlea," *Nature*, vol. 349, pp. 413–414, Jan. 1991.

[29] R. F. Lyon and C. Mead, "An analog electronic cochlea," *IEEE Trans. Acoust. Speech Signal Process.*, vol. 36, no. 7, pp. 1119–1134, Jul. 1988.

[30] L. Watts, A. Kerns, R. F. Lyon, and C. Mead, "Improved implementation of the silicon cochlea," *IEEE J. Solid-State Circuits*, vol. 27, no. 5, pp. 692–700, May 1992.

[31] E. Fragniere, A. v. Schaik, and E. A. Vittoz, "Design of an analogue VLSI model of an active cochlea," *Analog Integr. Circuits Signal Process.*, vol. 12, pp. 19–35, 1997.

[32] R. Sarpeshkar, R. F. Lyon, and C. Mead, "A low-power wide-dynamic-range analog VLSI cochlea," *Analog Integr. Circuits Signal Process.*, vol. 16, pp. 245–274, 1998.

[33] V. Chan, S.-C. Liu, and A. v. Schaik, "AEAR EAR: A matched silicon cochlea pair with address event representation interface," *IEEE Trans. Circuits Syst. I, Reg. Papers*, vol. 54, no. 1, pp. 48–59, Jan. 2007.

[34] S.-C. Liu, A. v. Schaik, B. A. Minch, and T. Delbruck, "Asynchronous binaural spatial sensor with 2 x 64 x 4 channel output, 10.1109/TBCAS. 2013.2281834," *IEEE Trans. Biomed. Circuits Syst.*, 2013.

[35] D. S. Freedman, H. I. Cohen, S. Deligeorges, C. Karl, and A. E. Hubbard, "An analog VLSI implementation of the inner hair cell and auditory nerve using a dual AGC model," *IEEE Trans. Biomed. Circuits Syst.*, vol. 8, no. 2, pp. 240–256, Apr. 2014.

[36] W. Germanovix and C. Toumazou, "Design of a micropower current-mode log-domain analog cochlear implant," *IEEE Trans. Circuits Syst. II, Analog Digit. Signal Process.*, vol. 47, no. 10, pp. 1023–1046, Oct. 2000.

[37] J. Georgiou and C. Toumazou, "A 126-$\mu$W cochlear chip for a totally implantable system," *IEEE J. Solid-State Circuits*, vol. 40, no. 2, pp. 430–443, Feb. 2005.

[38] R. Sarpeshkar, C. Salthouse, J.-J. Sit, M. W. Baker, S. M. Zhak, T. K.-T. Lu, L. Turicchia, and S. Balster, "An ultra-low-power programmable analog bionic ear processor," *IEEE Trans. Biomed. Eng.*, vol. 52, no. 4, pp. 711–727, Apr. 2005.

[39] A. v. Schaik and E. Fragniere, "Pseudo-voltage domain implementation of a 2-Dimensional silicon cochlea," in *Proc. IEEE Int. Symp. Circuits and Syst.*, 2001, vol. 2, pp. 185–188.

[40] E. Fragniere, "A 100-channel analog CMOS auditory filter bank for speech recognition," in *Proc. IEEE Int. Solid-State Circuits Conf., Dig. Tech. Papers*, 2005, pp. 140–141.

[41] T. J. Hamilton, C. Jin, A. v. Schaik, and J. Tapson, "An active 2-D silicon cochlea," *IEEE Trans. Biomed. Circuits Syst.*, vol. 2, no. 1, pp. 30–43, Mar. 2008.

[42] B. Wen and K. Boahen, "A silicon cochlea with active coupling," *IEEE Trans. Biomed. Circuits Syst.*, vol. 3, no. 6, pp. 444–455, Dec. 2009.

[43] H. Finger and S.-C. Liu, "Estimating the location of a sound source with a spike-timing localization algorithm," in *Proc. IEEE Int. Symp. Circuits and Systems*, 2011, pp. 2461–2464.

[44] C.-H Li, T. Delbruck, and S.-C. Liu, "Real-time speaker identification using the AEREAR2-event-based silicon cochlea," in *Proc. IEEE Int. Symp. Circuits and Systems*, 2012, pp. 1159–1162.

[45] K. H. Wee, L. Turicchia, and R. Sarpeshkar, "An articulatory silicon vocal tract for speech and hearing prostheses," *IEEE Trans. Biomed. Circuits Syst.*, vol. 5, no. 4, pp. 339–346, Aug. 2011.

[46] J.-J. Sit and R. Sarpeshkar, "A cochlear-implant processor for encoding music and lowering stimulation power," *IEEE Pervasive Comput.–Special Issue Implantable Electronics*, vol. 7, no. 1, pp. 40–48, 2008.

[47] W. Ngamkham, C. Sawigun, S. Hiseni, and W. A. Serdijn, "Analog complex gammatone filter for cochlear implant channels," in *Proc. IEEE Int. Symp. Circuits and Systems*, 2010, pp. 969–972.

[48] A. G. Katsiamis, E. M. Drakakis, and R. F. Lyon, "A biomimetic, 4.5 $\mu$W, 120+ dB, log-domain cochlea channel with AGC," *IEEE J. Solid-State Circuits*, vol. 44, no. 3, pp. 1006–1022, Mar. 2009.

[49] M. Banu and Y. Tsividis, "An elliptic continuous-time CMOS filter with on-chip automatic tuning," *IEEE J. Solid-State Circuits*, vol. 20, no. 6, pp. 1114–1121, Dec. 1985.

[50] J. Adut, J. Silva-Martinez, and M. Rocha-Perez, "A 10.7-MHz six-order SC ladder filter in 0.35 $\mu$m CMOS technology," *IEEE Trans. Circuits Syst. I, Reg. Papers*, vol. 53, no. 8, pp. 1625–1635, Aug. 2006.

[51] D. Perry and G. W. Roberts, "The design of log-domain filters based on the operational simulation of LC ladders," *IEEE Trans. Circuits Syst. II, Analog Digit. Signal Process.*, vol. 43, no. 11, pp. 763–774, Nov. 1996.

[52] G. D. Duerden, G. W. Roberts, and M. J. Deen, "A 10 MHz elliptic log-domain filter in a standard CMOS process," in *Proc. IEEE Symp. Circuits and Systems*, 2002, vol. 2, pp. II-5–II-8.

[53] C. Toumazou, J. Ngarmnil, and T. S. Lande, "Micropower log-domain filter for electronic cochlea," *Electron. Lett.*, vol. 30, no. 22, pp. 1839–1841, Oct. 1994.

[54] D. Python and C. C. Enz, "A micropower class-AB CMOS log-domain filter for DECT applications," *IEEE J. Solid-State Circuits*, vol. 36, no. 7, pp. 1067–1075, Jul. 2001.

[55] F. Yang, C. Enz, and G. v. Ruymbeke, "Design of low-power and low-voltage log-domain filters," in *Proc. IEEE Symp. Circuits and Systems*, 1996, vol. 1, pp. 117–120.

[56] C. Psychalinos and S. Vlassis, "On the exact realization of log-domain elliptic filters using the signal flow graph approach," *IEEE Trans. Circuits Syst. II, Analog Digit. Signal Process.*, vol. 49, no. 12, pp. 770–774, Dec. 2002.

[57] E. M. Drakakis, A. J. Payne, C. Toumazou, A. E. J. Ng, and J. I. Sewell, "High-order lowpass and bandpass elliptic log-domain ladder filters," in *Proc. IEEE Symp. Circuits and Systems*, 2001, vol. 1, pp. 141–144.

[58] F. Yuan, *CMOS Active Inductors and Transformers: Principle, Implementation, and Applications*. New York, NY, USA: Springer, 2008.

[59] S. Wang, T. J. Koickal, A. Hamilton, E. Mastropaolo, R. Cheung, and L. Smith, "A floating active inductor based CMOS cochlea filter with high tunability and sharp cut-off," in *Proc. IEEE Symp. Circuits and Systems*, 2013, pp. 193–196.

[60] Y. P. Tsividis, *Operation and Modeling of the MOS transistor*. New York, NY, USA: McGraw-Hill, 1987.

[61] A. B. Williams and F. J. Taylor, *Electronic Filter Design Handbook*. New York, NY, USA: McGraw-Hill, 1995.

[62] C. C. Enz and E. A. Vittoz, *Charge-Based MOS Transistor Modeling: The EKV Model for Low-Power and RFIC Design*. Hoboken, NJ, USA: Wiley, 2006.
[63] E. d. Boer, "Cochlear models and minimum phase," *J. Acoust. Soc. Amer.*, vol. 102, no. 6, pp. 3810–3813, Dec. 1997.
[64] C. A. Shera and J. J. Guinan, "Stimulus-frequency-emission group delay: A test of coherent reflection filtering and a window on cochlear tuning," *J. Acoust. Soc. Amer.*, vol. 113, no. 5, pp. 2762–2772, May 2003.
[65] B. R. Glasberg and B. C. J. Moore, "Derivation of auditory filter shapes from notched-noise data," *Hear. Res.*, vol. 47, no. 1-2, pp. 103–128, Aug. 1990.
[66] S. Ramakrishnan, A. Basu, L. K. Chiu, J. Hasler, D. Anderson, and S. Brink, "Speech processing on a reconfigurable analog platform," *IEEE Trans. Very Large Scale Integr. (VLSI) Syst.*, vol. 22, no. 2, pp. 430–433, Feb. 2014.
[67] R. F. Lyon, A. G. Katsiamis, and E. M. Drakakis, "History and future of auditory filter models," in *Proc. IEEE Int. Symp. Circuits and Systems*, 2010, pp. 3809–3812.
[68] A. G. Katsiamis, E. M. Drakakis, and R. F. Lyon, "Practical gammatone-like filters for auditory processing, doi:10.1155/2007/63685," *EURASIP J. Audio, Speech, Music Process.*, 2007.
[69] B. Gilbert, "The multi-tanh principle: a tutorial overview," *IEEE J. Solid-State Circuits*, vol. 33, no. 1, pp. 2–17, Jan. 1998.

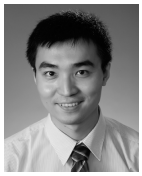

**Shiwei Wang** (S'13) was born in China in 1987. He received the B.S. degree in electrical engineering from Zhejiang University, Zhejiang, China, in 2010.

Currently, he is working toward the Ph.D degree at the Institute for Integrated Micro and Nano Systems, The University of Edinburgh, Edinburgh, U.K. His research interests include analog VLSI and bio-inspired circuits and systems.

**Thomas Jacob Koickal** received the Ph.D degree in electronics and electrical communication engineering from the Indian Institute of Technology, Kharagpur, India.

From 1998 to 2002, he was a Scientist at the Control and Guidance Design Group, Indian Space Research Organization, Trivandrum. From 2002 to 2014, he was with the Institute of Micro and Nano Systems, University of Edinburgh, U.K. Currently, he is with Beach Theory, a startup company which he cofounded. His research interests include predictive modeling, time event based computation, neuromorphic systems, and multisensory bio-inspired systems in analog VLSI.

**Alister Hamilton** is a Senior Lecturer in the discipline of electronics at the School of Engineering, University of Edinburgh, Edinburgh U.K., where he has worked since 1988.

His research interests are in the implementation of neural networks and neuromorphic systems in analog VLSI, and in novel design strategies for programmable analog arrays.

**Rebecca Cheung** (M'96–SM'02) received first-class honours and the Ph.D degree in electronics and electrical engineering from the University of Glasgow, Glasgow, U.K., in 1986 and 1990, respectively.

In 1986, she was awarded a Croucher Foundation scholarship to study towards a doctoral degree. During her doctoral work, she was a Visiting Researcher at IBM Thomas J. Watson Research Center, Yorktown Heights, NY, USA, where high density plasma etching techniques were developed to form nanostructured GaAs. From 1990 to 2000, she was a Visiting Scientist at the Delft Institute of Microelectronics and Submicron Technology, The Netherlands; the Laboratory for Electromagnetic Fields and Microwave Electronics at ETHZ, Switzerland; and the Nanoelectronics Research Center at the University of Glasgow, working on various topics related to semiconductor technology, process-induced materials damage, mesoscopic physics in SiGe heterostructures, and microwave circuits in InP for gigabit electronics. Additionally, she was a founding member of the Nanostructure Engineering Science and Technology (NEST) Group at the University of Canterbury, New Zealand, in 1998. Currently, she holds a Chair in Nanoelectronics in the School of Engineering at the University of Edinburgh. She has an international reputation for her contribution in the development and application of micro- and nano- fabrication. More recently, her research focuses on bio-inspired micro-electromechanical systems. She has authored over 140 scientific articles with more than 85 peer-reviewed journal papers, including 15 invited review papers, one patent, and one book.

Dr. Cheung serves on numerous scientific panels and committees, has been elected a Fellow of the Royal Society of Edinburgh, and is an Honorary Professor with the School of Engineering and Physical Sciences, Heriot-Watt University, Currie, U.K.

**Leslie S. Smith** (M'84–SM'04) received the B.Sc. degree in mathematics and the Ph.D. degree in computers from the University of Glasgow, Glagow, U.K., in 1973 and 1982, respectively.

Having worked on parallel systems, he moved on to working on neural networks, gradually exploring both real (biological) and artificial (neuromorphic) implementations. He became interested in the auditory area initially as a source of time-varying data, and remained interested after discovering the problems posed by this area. He was Head of Department at Stirling University, Stirling, U.K, and is currently researching cochlea-like transducers as well as neuroinformatics.

# A Power-Efficient Capacitive Read-Out Circuit with Parasitic-Cancellation for MEMS Cochlea Sensors

Shiwei Wang, *Student Member, IEEE,* Thomas Jacob Koickal, Alister Hamilton, Enrico Mastropaolo, Rebecca Cheung, *Senior Member, IEEE,* Andrew Abel, and Leslie S. Smith, *Senior Member, IEEE*

***Abstract*—This paper proposes a solution for signal read-out in the MEMS cochlea sensors that have very small sensing capacitance and do not have differential sensing structures. The key challenge in such sensors is the significant signal degradation caused by the parasitic capacitance at the MEMS-CMOS interface. Therefore, a novel capacitive read-out circuit with parasitic-cancellation mechanism is developed; the equivalent input capacitance of the circuit is negative and can be adjusted to cancel the parasitic capacitance. Chip results prove that the use of parasitic-cancellation is able to increase the sensor sensitivity by 35 dB without consuming any extra power. In general, the circuit follows a low-degradation low-amplification approach which is more power-efficient than the traditional high-degradation high-amplification approach; it employs parasitic-cancellation to reduce the signal degradation and therefore a lower gain is required in the amplification stage. Besides, the chopper-stabilization technique is employed to effectively reduce the low-frequency circuit noise and DC offsets. As a result of these design considerations, the prototype chip demonstrates the capability of converting a 7.5 fF capacitance change of a 1-Volt-biased 0.5 pF capacitive sensor pair into a 0.745 V signal-conditioned output at the cost of only 165.2 $\mu$W power consumption.**

***Index Terms*—MEMS cochlea, capacitive read-out, sensor interface, low capacitance measurement, parasitic-cancellation, negative-impedance, chopper-stabilization.**

## I. Introduction

THE development of cochlea-like sensors using MEMS technology has become an emerging research topic in recent years [1]–[5]. As an alternative to the traditional CMOS-based implementations [6]–[16], these MEMS cochlea sensors provide a new approach to build low-power, small-size and real-time silicon cochlea systems for hearing research and prosthetic applications. Like the biological cochlea, the MEMS cochlea sensors perform spectral decomposition mechanically; they are based on micromachined resonant structures such as the 'fishbone' [1], the cantilever [2], the tapered membrane [3], the beam-membrane [4] and the resonant gate transistors [5]. Among these structures, the resonant beams have been predominantly used as the sound sensing elements [1], [2], [4], [5]. Since the resonant frequency of a vibrating beam can be controlled by adjusting its length [17], an array of beams with appropriate lengths is usually employed to cover the audio frequency range as shown in Fig. 1.

This work was supported by EPSRC, UK, under Grants to the Univ. of Edinburgh (EP/G063710/1), and to the Univ. of Stirling (EP/G062609/1).

S. Wang, T. J. Koickal, A. Hamilton, E. Mastropaolo and R. Cheung are with the Institute for Integrated Micro & Nano Systems, University of Edinburgh, Edinburgh, UK(e-mail: shiwei.wang@ed.ac.uk).

A. Abel and L. S. Smith are with the Department of Computer Science and Mathematics, University of Stirling, Stirling, UK.

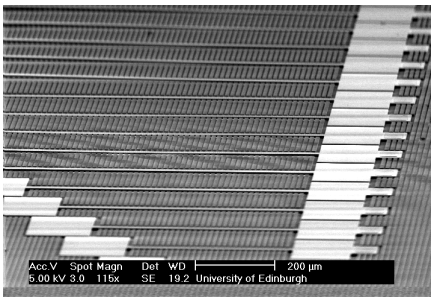


Fig. 1. The scanning electron micrograph (SEM) of a MEMS cochlea sensor based on the resonant beam array.

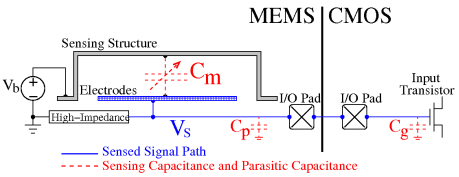


Fig. 2. Capacitive read-out approach: a sensing capacitor ($C_m$) is formed by the sensing structure and the bottom electrodes; the sensing structure is biased with a DC voltage ($V_b$) and the bottom electrodes are grounded through a high-impedance path; the charge stored on $C_m$ keeps approximately constant when the sensing capacitance varies and thus the capacitance variation is converted to the voltage output ($V_s$) which is fed to the CMOS transistors. $C_p$ represents the parasitic capacitance due to the I/O pads and wire connections and $C_g$ represents the input capacitance of the CMOS circuits. This read-out structure is based on the continuous-time voltage method which is most commonly used for capacitive sensors due to its low noise nature [24].

Compared with the CMOS counterparts, the major advantage of the MEMS cochlea is the reduced consumption of electrical power by virtue of the mechanical filtering. However, the instrumentation of these MEMS cochlea sensors requires additional signal read-out circuits; clearly, the power consumption of the signal read-out circuits has to be minimized to ensure the overall power efficiency of the MEMS-based cochlea systems. Due to the low-power and stability advantages, the capacitive read-out approach has been widely preferred for a variety of

MEMS sensors such as the microphones [21]–[23], pressure sensors [18]–[20] and accelerometers [24]–[27]. Nevertheless, it is a difficult challenge to design low-power capacitive read-out circuits for the MEMS cochlea sensors: as shown in Fig. 1, the resonant beams have much smaller effective plate area and thus much smaller sensing capacitance compared with those diaphragm structures in the microphones and pressure sensors [18]–[23]; also, since the open cavity is required for sound detection, the differential sensing structures like those in the accelerometers [24]–[27] are not applicable. The voltage output of the capacitive read-out structure depicted in Fig. 2 is given by

$$V_s = \frac{V_b \cdot \Delta C_m}{C_m + C_p + C_g}, \tag{1}$$

which indicates the output voltage will be significantly degraded by the parasitics if the sensing capacitance is small. In this case, a high gain amplifier is required to compensate the signal degradation, which increases power consumption of the read-out circuit. Besides, it is not applicable to build a balanced capacitive bridge without the differential sensing structure so that the common mode noise rejection becomes poor and also, it is difficult to implement the chopper-stabilization scheme like those used in the accelerometers to effectively eliminate the low-frequency noise in the CMOS circuits [24]–[27]. As a result, higher currents in the CMOS circuits are needed to improve the signal-to-noise ratio (SNR) which also increase the power consumption.

Thus far, research efforts have been made to reduce the parasitic capacitance $C_g$ in Eq. 1 [24], [26], [29], [30], while the signal degradation induced by $C_p$ has not been adequately addressed. Generally speaking, the existing capacitive read-out circuits follow a high-degradation high-amplification process which has low power-efficiency. To improve the SNR in non-differential sensors, the pseudo-differential structure based on a pair of identical sensors with reverse DC biasing has been introduced in [21]; also, a circuit architecture that uses the unity-gain buffer in between the sensor and the chopper-stabilized amplifier has been proposed to reduce the low-frequency noise in [29], [30].

In this paper a capacitative read-out circuit with low-degradation and low amplification is proposed. Its input stage is a parasitic-cancellation circuit (PCC) and its second-stage is a chopper-stabilized amplifier (CSA). The PCC is able to cancel the $C_p$ in Eq. 1 so that the signal degradation is further reduced and thus the gain requirement for the second-stage amplifier is much lower. The parasitic-cancellation mechanism does not require any extra power consumption and thus the system power efficiency is significantly improved. Besides, the PCC has similar function as the unity gain buffer used in [29], [30], but it has much better attenuation on the noise of the later stage circuits since its intrinsic gain is greater than unity. With thesis features, a low-power MEMS-based cochlea system can be built in the future based on the proposed power-efficient read-out circuit.

The paper is organized as follows: the circuit design is introduced in Section II, the experimental results from the prototype VLSI chip are discussed in Section III and the paper is summarized and concluded in Section IV.

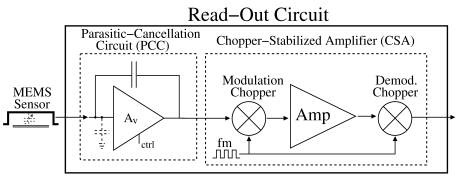


Fig. 3. System architecture of the proposed read-out circuit

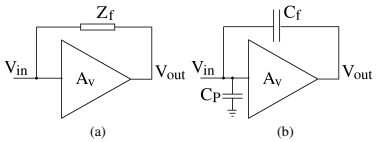


Fig. 4. Generation of equivalent negative input impedance based on positive feedback structures.

## II. Power-Efficient Capacitive read-out circuits with Parasitic-Cancellation and Chopper-stabilization

### A. System Architecture

Figure. 3 illustrates the architecture of the proposed read-out circuit which consists of the PCC and the CSA. Apart from cancelling the parasitic capacitance, the PCC also protects the sensor from the spurious effects such as the charge injections and clock feed-through induced by the choppers. The CSA provides gain to the sensed signal. The two choppers are controlled by the same clock signal and operate respectively as the modulator and the demodulator.

### B. Parasitic-Cancellation Circuit (PCC)

*1) Principle of parasitic-cancellation using negative impedance:* The proposed PCC cancels the parasitic capacitance using negative input impedance method. According to Miller theorem, the negative impedance can be obtained using the positive feedback structure shown in Fig. 4a. The output of the gain stage is positively fed-back to its input through an impedance element $Z_f$. The equivalent input impedance of the circuit is thus given by

$$Z_i = \frac{Z_f}{1 - A_v}. \tag{2}$$

Therefore the input impedance becomes negative when the gain exceeds unity. This principle can be applied for parasitic capacitance cancellation. As shown in Fig. 4b, $C_p$ represents the parasitic capacitance at the input of the gain stage and $C_f$ represents the feedback capacitance. Based on Miller theorem, the equivalent input impedance of the circuit is given by

$$\begin{aligned} Z_i(s) &= \frac{1}{sC_p - sC_f \cdot (A_v - 1)} \\ &= \frac{1}{s[C_p - (A_v - 1)C_f]}. \end{aligned} \tag{3}$$

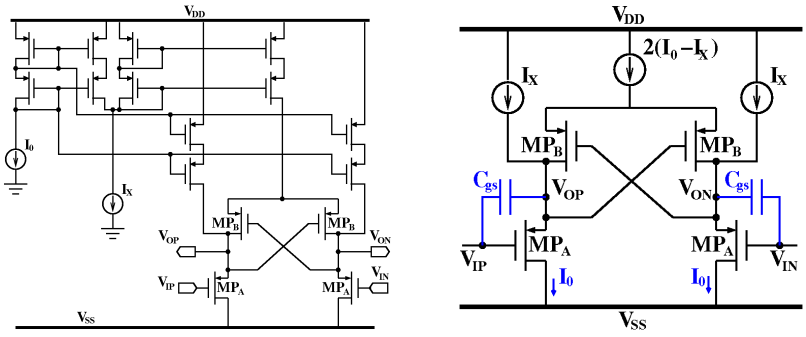


(a) Full Schematics (b) Simplified Representation

Fig. 5. Schematic of the PCC.

Thus the parasitic capacitance is reduced by $(A_v - 1)C_f$. For stability issue, Eq. 3 should always be positive and therefore $(A_v - 1)C_f$ should always be smaller than $C_p$.

*2) PCC design:* The schematic of the PCC is shown in Fig. 5a. All transistors operate in saturation region. The core components of the circuit are two pairs of PMOS transistors, $MP_A$ and $MP_B$. The other transistors in Fig. 5a are all components of the current mirrors. The simplified representation of the circuit is shown in Fig. 5b. The $MP_A$ transistors are input transistor pair based on the common-drain configuration. The cross-connected $MP_B$ transistors function as the active loads. The two pair of transistors are configured on a fully differential cross-connected source-follower topology. The PMOS transistors are used due to their lower flicker noise compared with the NMOS counterparts. Also, since the PMOS transistors are fabricated in the N-Well, the separate bulk connections are possible; the bulks of the transistors $MP_A$ and $MP_B$ are respectively connected to their sources so that the body effect is negligible.

The DC gain of the circuit is given by

$$A_v = \frac{V_{OP} - V_{ON}}{V_{IP} - V_{IN}} = \frac{gm_A}{gm_A - gm_B}, \tag{4}$$

where $gm_A$ and $gm_B$ respectively represent the transconductance of $MP_A$ and $MP_B$. As shown in Fig. 5, the bias current for $MP_A$ is $I_0$ and the bias current for $MP_B$ is $I_0 - I_X$. The dimensions of $MP_A$ and $MP_B$ are made identical for ease of analysis. Since low output impedance is required for the circuit, the $MP_A$ transistors are designed to operate in strong inversion. The current $I_X$ is designed to be tunable from 0 to $I_0$ and thus the operation of transistors $MP_B$ spans from strong to weak inversion. Therefore, the EKV model [31] which has uniform expression for different inversion regions is selected to perform the following circuit analysis,

In EKV model, the transconductance of transistors in saturation region is given by

$$gm = 2n\mu\frac{W}{L}U_T q_s, \tag{5}$$

where $q_s$ is the normalized charge at the source. $q_s$ is determined by the transistor current:

$$q_s = \frac{\sqrt{4i_f + 1} - 1}{2}, \tag{6}$$

where $i_f$ represents the normalized transistor forward current defined by [31]

$$i_f = \frac{I_D}{2n\mu C_{ox}\frac{W}{L}U_T^2}. \tag{7}$$

$i_f$ is far greater than unity when transistors operate in strong inversion and is far smaller than unity when transistors operate in weak inversion. Based on Eq. 5, Eq. 6 and Eq. 7, the gain of the PCC can be represented using currents:

$$A_v = \frac{2i_0 - \sqrt{i_0} + \sqrt{i_0 - i_x + \frac{1}{4}} - 2\sqrt{i_0(i_0 - i_x + \frac{1}{4})}}{2i_x}, \tag{8}$$

where $i_0$ and $i_x$ are respectively the normalized forms of $I_0$ and $I_X$. When $MP_B$ transistors operate in weak inversion, $i_0 - i_x$ is far less than unity and thus

$$A_v \approx \frac{2i_0 - 2\sqrt{i_0} + \frac{1}{2}}{2i_x} \approx \frac{i_0}{i_x} = \frac{I_0}{I_X}. \tag{9}$$

When $MP_A$ transistors operate in strong inversion, $i_0 - i_x$ is far greater than unity and thus

$$\begin{aligned} A_v &\approx \frac{2i_0 - \sqrt{i_0} + \sqrt{i_0 - i_x} - 2\sqrt{i_0}\sqrt{i_0 - i_x}}{2i_x} \\ &\approx \frac{i_0}{i_x}(1 - \sqrt{1 - \sqrt{i_x}i_0}) \\ &= \frac{I_0}{I_X}(1 - \sqrt{1 - \frac{I_X}{I_0}}). \end{aligned} \tag{10}$$

Therefore, the derivative of $A_v$ against $\frac{I_0}{I_X}$ decreases when $MP_B$ shifts from weak to strong inversion.

The transistors have intrinsic capacitance $C_{gs}$ between the gate and the source [31], [32]. As shown in Fig. 5b, $C_{gs}$ forms a positive feedback loop from the output to the input of the

PCC. According to Eq. 2, the equivalent input capacitance of the PCC is given by

$$C_g = -C_{gs} \cdot (A_v - 1). \tag{11}$$

According to Eq. 1, the sensed output voltage is derived as

$$V_s = \frac{V_b \cdot \Delta C_m}{C_m + C_p + C_g} = \frac{V_b \cdot \Delta C_m}{C_m + [C_p - (A_v - 1)C_{gs}]}. \tag{12}$$

Thus the output from the PCC is given by

$$V_o = V_s \cdot A_v = \frac{A_v V_b \cdot \Delta C_m}{C_m + [C_p - (A_v - 1)C_{gs}]}. \tag{13}$$

The output reaches maximum when $A_v$ equals $\frac{C_p}{C_{gs}} + 1$ so that $C_p$ is fully canceled. The output in this case is given by

$$V_{o,MAX} = \frac{V_b \cdot \Delta C_m (\frac{C_p}{C_{gs}} + 1)}{C_m}. \tag{14}$$

$A_v$ is designed to be variable by tuning the current $I_X$ so that the negative capacitance can be adjusted to match the parasitic capacitance. There are two advantages resulting from this design option. Firstly, both the DC operating points and the output resistance of the PCC are determined by the transconductance of $MP_A$. As the current in $MP_A$ keeps constant, neither the DC operating point nor the driving ability of the circuit is affected when $I_X$ varies. Therefore, the designed tuning mechanism has high flexibility. Secondly, the power consumption of the circuit is dependent on $I_0$ rather than $I_X$. Therefore the increase of sensed signal and gain does not result in any extra power consumption, which to a large extent benefits the power efficiency of the entire read-out circuit. This issue will be further discussed in Section. II-E1.

The transistor dimensions in Fig. 5b are determined based on two factors, the noise and the capacitance. As shown in Fig. 3, the PCC is the first stage of the read-out circuit and moreover, its low-frequency noise cannot be eliminated by the chopper-stabilization. Consequently, the noise of the PCC is critical for the overall noise performance of the read-out circuit. As analyzed in [30], the circuit noise can be optimized by choosing appropriate transistor dimensions. Based on the EKV model [31], the transistor thermal noise and flicker noise are respectively given by

$$\frac{\overline{V_{ntherm}^2}}{\Delta f}(f) = 4kT\frac{{G_{nD}}^2}{gm}, \tag{15}$$

$$\frac{\overline{V_{n1/f}^2}}{\Delta f}(f) = \frac{K_F}{C_{ox}^2 WLf}, \tag{16}$$

where $G_{nD}$ is transistor thermal noise conductance, $K_F$ is the flicker noise coefficient and $f$ is frequency. $G_{nD}$ is determined by

$$G_{nD} = \frac{n\beta U_T}{3} \cdot \frac{4q_s^2 + 3q_s}{q_s + 1}. \tag{17}$$

According to Eq. 6 and Eq. 7, Eq. 15 can be rewritten as

$$\frac{\overline{V_{ntherm}^2}}{\Delta f}(f) = \frac{2n^2 kT}{3I_D}\left(2\sqrt{\frac{2I_D L}{n\mu C_{ox} W} + U_T^2} + U_T\right). \tag{18}$$

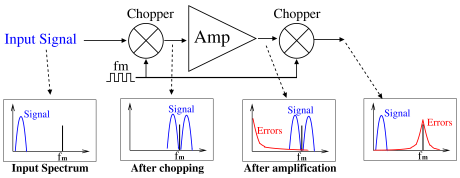


Fig. 6. Principle of chopper-stabilization technique for low-frequency error elimination

According to Eq. 18, low thermal noise results from the wide transistor width and short length, while according to Eq. 16, low flicker noise results from the wide transistor width and long length.

Besides, to increase the maximum output of the PCC, the capacitance $C_{gs}$ should be decreased according to Eq. 14. $C_{gs}$ is related with the transistor dimension in the following equation [31]

$$\begin{aligned} C_{gs} &= WLC_{ox} \cdot \frac{q_s}{3} \cdot \frac{2q_s + 3}{(q_s + 1)^2} \\ &= \frac{WLC_{ox}}{3}[2 - \frac{1}{q_s + 1} - \frac{1}{(q_s + 1)^2}]. \end{aligned} \tag{19}$$

Based on Eq. 6 and Eq. 7, the equation is rewritten using $i_f$ as

$$C_{gs} = \frac{2n\mu U_T^2 W^2 \cdot i_f}{3I_D}[2 - \frac{2}{\sqrt{4i_f + 1} + 1} - \frac{1}{(\sqrt{4i_f + 1} + 1)^2}]. \tag{20}$$

Thus small $C_{gs}$ results from the narrow transistor width and the low $i_f$ which prefers the short transistor length as Eq. 7 indicates.

TABLE I
OPTIMIZATION OF TRANSISTOR DIMENSIONS FOR NOISE AND CAPACITANCE.

| | W | L |
|---|---|---|
| Low flicker noise | ↑ | ↑ |
| Low thermal noise | ↑ | ↓ |
| Small $C_{gs}$ | ↓ | ↓ |

Above analysis is summarized in Table. I. To make compromise between thermal noise, flicker noise and capacitance, the combination of wide width and short length is selected since both of them are preferred for 2 out of the 3 criteria. In practice, the transistor width is set as 280 $\mu$m and the transistor length is set as 0.35 $\mu$m.

### C. Chopper-Stabilized Amplifier (CSA)

Chopper-stabilization technique is commonly used to reduce flicker noise and circuit offsets [33]. Both the flicker noise and circuit offsets are low-frequency circuit errors, and thus their negative effects are especially significant on low frequency audio circuits. The principle of chopper-stabilization is to remove low-frequency circuit errors from signals using

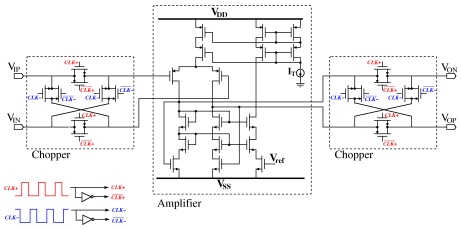


Fig. 7. Schematic of the CSA.

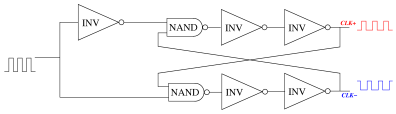


Fig. 8. Non-overlapping clock generator based on NAND gate and inverter.

a pair of chopper modulators. As shown in Figure. 6, the signal spectrum is shifted to the modulation frequency before amplification and is thus refrained from the low frequency errors of the amplifier; after the second modulation, the signal is recovered while the low frequency errors are shifted to the modulation frequency. As a result, the signal and the errors are separated.

The schematic of the CSA is shown in Fig. 7. As high gain is not required, a single-stage amplifier is used. The choppers are built using complementary MOS switches where a PMOS transistor and a NMOS transistor are connected in parallel. The PMOS and NMOS transistors have opposite charge injections which cancel with each other so that the charge injection effect of the switch is significantly reduced [32]. Each chopper consists of two pairs of switches, a forward pair and a cross pair. The forward pair is controlled by clock signal $CLK+$ and the cross pair is controlled by $CLK-$. $CLK+$ and $CLK-$ are required to be non-overlapping to avoid metastability. The circuit shown in Fig. 8 is used to generate the non-overlapping clock signals.

### *D. Other Circuits*

A sensor bias circuit is required to provide the high-impedance ground path shown in Fig. 2. To ensure that the

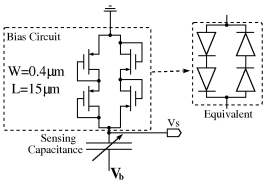


Fig. 9. Sensor bias circuit.

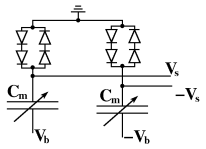

Fig. 10. Pseudo-differential capacitive sensing method.

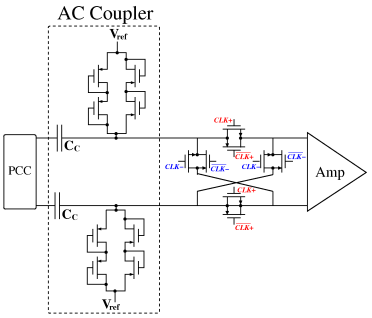


Fig. 11. The AC coupler circuit between the PCC and the CSA.

charge keeps approximately constant when sensing capacitance varies, the time constant of the RC circuit formed by the sensing capacitance and the AC resistance of the bias circuit has to be longer than the sensor vibration period. The sensing capacitance of the MEMS resonator is expected to be less than 1 pF and thus the biasing resistance has to be higher than 10 GΩ. As shown in Fig. 9, the diode-connected transistors are used to build such sensor bias circuit. The circuit operates equivalently as a cross-coupled double diode pair. The cross-coupled structure ensures that the DC voltage is passed through to the sensing capacitance while the AC signal is blocked when the sensed voltage is much lower than the diode threshold. To increase resistance, the transistors are optimized into narrow width and long length shape. Besides, double transistors are serially connected to further increase the resistance. The simulation in Cadence Spectre shows that such bias circuit has an AC resistance of roughly 500 GΩ, which sufficiently meets the requirement. To implement the pseudo-differential structure proposed in [21], a pair of the bias circuits is used as shown in Fig. 10.

As shown in Fig. 11, the same diode-connected transistors are used to build an AC coupler circuit between the PCC and the CSA. $C_c$ is the AC coupling capacitor and the diode-connected transistors provide DC bias for the CSA. The purpose of the AC coupler is to block the DC offset from the PCC which otherwise will cause errors and instabilities in later-stage circuits. To avoid loading effects from the input capacitance of the CSA, $C_c$ is set with high capacitance (80 pF).

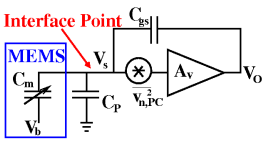


Fig. 12. Simplified circuit model at the MEMS interface end. $\overline{v_{n,PC}^2}$ represents the input-referred noise of the PCC.

### E. System-Level Analysis

Compared with typical designs [24]–[26], [28]–[30], the major improvement in the proposed read-out circuit is the employment of the parasitic-cancellation mechanism. This section is going to analyze how the PCC improves the system-level performance of the read-out circuit regarding power efficiency and noise performance.

*1) Power efficiency:* As stated above, the PCC significantly increases the sensitivity of capacitive sensors. In the typical designs based on the unity-gain buffers, the voltage output from the buffer is given by Eq. 1. In comparison, the output level is increased by at lease a factor of $\frac{A_v\cdot(C_m+C_p)}{C_m+C_p-(A_v-1)C_{gs}}$ in this design as suggested by Eq. 13. Under the extreme circumstance that the parasitic capacitance is fully canceled, the output level is increased by a factor of $(\frac{C_p}{C_{gs}}+1)\cdot\frac{C_m+C_p}{C_m}$ as suggested by Eq. 14. The $C_{gs}$ reaches maximum value of $\frac{2C_{ox}WL}{3}$ when transistor operates in deep strong inversion where $i_f$ in Eq. 20 is far less than unity [31]. According to the selected transistor dimensions and the process parameters, the maximum $C_{gs}$ is in the region of 0.3 pF. Based on the assumption that the sensing capacitance of the MEMS resonator is 0.5 pF and the parasitic capacitance $C_p$ is 5 pF, the proposed PCC increases the output level by at least 45 dB. As a result, the gain requirement for the CSA is reduced by 45 dB, so is the gain-bandwidth product (GBW) requirement. The relationship between amplifier GBW and power consumption is approximated by

$$P = K\cdot GBW^2C_L^2/(W/L) \tag{21}$$

where $K$ is a lumped amplifier constant and $C_L$ is the load capacitor [26]. According to Eq. 21, the amplifier is required to consume 38000 times more power to achieve 45 dB extra gain. Even if using cascaded-amplifier approach, more power consumption is still required since extra amplifier needs to be added. Notably, the PCC does not consume any extra power to increase the signal level as explained above. Therefore, the PCC significantly improves the overall power efficiency of the read-out circuits.

*2) Noise performance:* Fig. 12 shows the circuit model at the MEMS interface end. The AC output $v_o$ is derived based on Fig. 12:

$$\begin{aligned} v_o &= \frac{A_v(C_m+C_p+C_{gs})}{C_m+C_p+C_{gs}(1-A_v)} \\ &\quad\cdot(V_b\cdot\frac{\Delta C_m}{C_m+C_p+C_{gs}}\mp\sqrt{\overline{v_{n,PC}^2}}). \end{aligned} \tag{22}$$

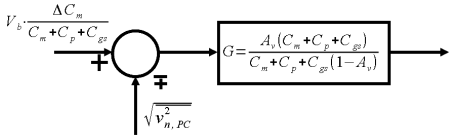


(a) Equivalent Signal-Flow Graph of the PCC with Noise

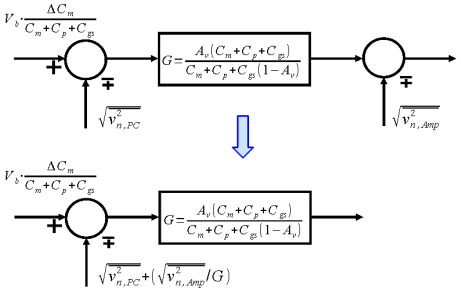


(b) Equivalent Signal-Flow Graph Considering Noise from the Amplifier

Fig. 13. Signal-flow graph representation of the PCC. $\overline{v_{n,Amp}^2}$ represents the noise from the amplifier.

The equivalent signal-flow graph is illustrated in Fig. 13a; the SNR of the PCC output is given by

$$SNR = \frac{(V_b\cdot\frac{\Delta C_m}{C_m+C_p+C_{gs}})^2}{\overline{v_{n,PC}^2}}. \tag{23}$$

The PCC is in the source-follower configuration and thus its input-referred noise is given by

$$\overline{v_{n,PC}^2} = \overline{v_{nA}^2} + \frac{\overline{i_{nB}^2}}{gm_A^2}, \tag{24}$$

where $\overline{v_{nA}^2}$ represents the noise voltage power of the input transistor $MP_A$ and $\overline{i_{nB}^2}$ represents the noise current power of the load transistor $MP_B$ [32]. If the PCC has unity gain and no parasitic-cancellation is performed, the current in $MP_B$ is close to zero and its noise contribution is negligible compared with $MP_A$ and thus $\overline{v_{n,PC}^2}$ roughly equals $\overline{v_{nA}^2}$. Under the circumstance that the parasitic capacitance is fully canceled, the current in $MP_B$ is close to the current in $MP_A$. Since $MP_A$ and $MP_B$ have identical dimension, their noise contribution are roughly the same and thus $\overline{v_{n,PC}^2}$ equals $2\overline{v_{nA}^2}$. Therefore, the SNR of the PCC is degraded by half when the parasitic capacitance is fully canceled. Nevertheless, the gain of the PCC results in attenuation of the noise from the CSA, as shown in Fig. 13b. When PCC has no parasitic-cancellation, the overall SNR is roughly given by

$$SNR = \frac{(V_b\cdot\frac{\Delta C_m}{C_m+C_p+C_{gs}})^2}{\overline{v_{nA}^2}+\overline{v_{n,Amp}^2}}. \tag{25}$$

When the parasitic capacitance is fully canceled, the noise

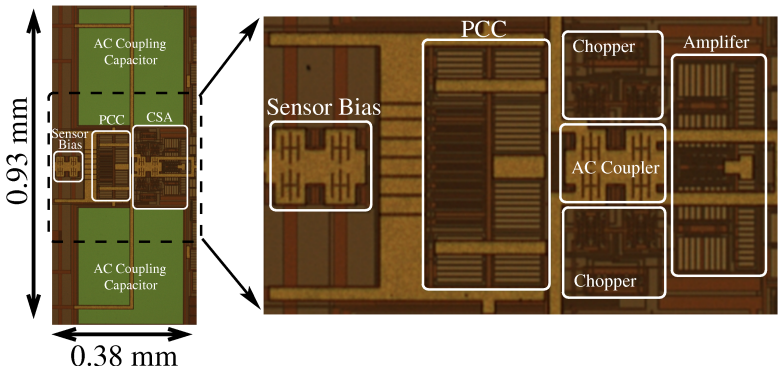


Fig. 14. Chip micrograph of the read-out circuit

from the amplifier is negligible and the overall SNR is roughly given by

$$SNR = \frac{(V_b \cdot \frac{\Delta C_m}{C_m+C_p+C_{gs}})^2}{2v_{nA}^2}. \quad (26)$$

Consequently, the parasitic-cancellation has approximately no effect on system SNR when the input-referred noise of the PCC and the CSA are equal. However, the SNR is maximally reduced by 3 dB if the noise of the CSA is much less than that of the PCC. The principle of this design is to use parasitic-cancellation to reduce signal degradation and thus reduce the gain and power of the CSA. The reduction of power in the CSA increases its noise. According to Eq. 25 and Eq. 26, the parasitic-cancellation improves the system SNR when the CSA becomes more noisy than the PCC. Therefore, the improvement of noise performance from the parasitic-cancellation is concurrent with the improvement of power efficiency.

## III. VLSI Chip Results

### A. VLSI Chip and Experimental Setup

As shown in Fig. 14, the proposed read-out circuit is implemented in an analog VLSI chip which is fabricated using AMS 0.35 $\mu$m standard CMOS process. The chip is tested electronically since the capacitive sensor has equivalent circuit model shown in Fig. 15 where the sensing capacitance is represented by a constant capacitor and the capacitance variation is represented by an AC voltage source with amplitude of $v_{ac} = \frac{V_b \Delta C_m}{C_m}$.

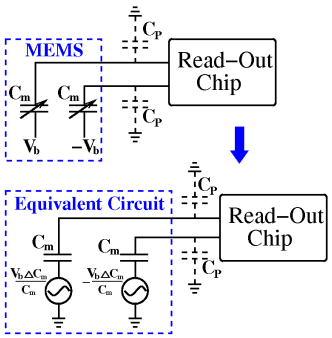


Fig. 15. Equivalent circuit model for the MEMS capacitive sensor.

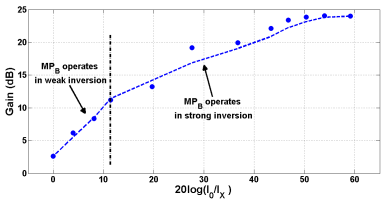


Fig. 16. Measured gain of the PCC versus $\frac{I_0}{I_X}$.

### B. Experimental Results

*1) Gain variation of the PCC:* The PCC is tested with the 500 Hz, 3 mV amplitude sinusoidal input signal. $I_0$ is set constantly as 5 $\mu$A and $I_X$ is adjusted from 7 nA to 5 $\mu$A. Figure. 16 illustrates the log-log plot of the measured gain of the PCC against $\frac{I_0}{I_X}$. The transistor $MP_B$ operates in weak inversion when $\frac{I_0}{I_X}$ is small and shifts to strong inversion when $\frac{I_0}{I_X}$ grows large. The results in Fig. 16 agree with Eq. 9 and Eq. 10: the gain of the PCC linearly increases with $\frac{I_0}{I_X}$ when $MP_B$ operates in weak inversion and the slope of gain growth becomes compressed when $MP_B$ shifts into strong inversion.

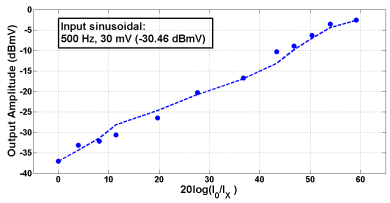


(a) Measured Growth of Output Amplitude with $\frac{I_0}{I_X}$

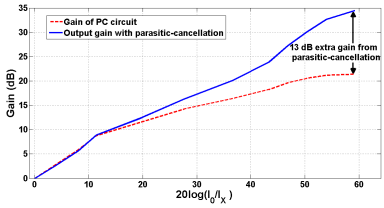


(b) Comparison with the Curve in Fig. 16

Fig. 17. Measured output amplitude from the capacitive read-out experiment.

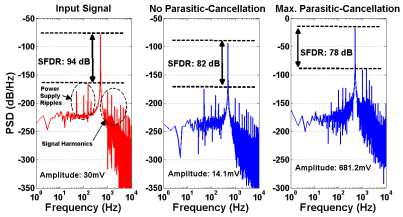


Fig. 18. Measured input and output spectrum from the capacitive read-out experiments.

*2) Effects of parasitic-cancellation:* The circuit model shown in Fig. 15 is used to test the capacitive read-out function of the chip. A pair of 0.5 pF capacitance is used to model the sensing capacitance and a differential sinusoidal voltage signal with 500 Hz frequency and 30 mV amplitude is applied as $v_{ac}$. This input setting is equivalent to a 7.5 fF maximum capacitance variation from a pair of $\pm 1V$-biased MEMS sensors with 0.5 pF sensing capacitance. Same current settings are applied as that in Section. III-B1. The output amplitude of the read-out chip is plotted against $\frac{I_0}{I_X}$ as shown in Fig. 17a. The PCC provides about 35 dB higher gain compared with the unity-gain buffer ($\frac{I_0}{I_X}$=1). As shown in Fig. 17b, the output amplitude is normalized by the minimum output and compared with the curve in Fig. 16 within the same coordinate. The comparison shows that the parasitic-cancellation mechanism contributes to an extra 13 dB gain. The 35 dB gain is less than the expected (45 dB) probably because the actual parasitic capacitance $C_p$ is smaller then the assumed 5 pF value.

Fig. 18 illustrates the spectrum of the input signal and the read-out chip output under the two extreme circumstances: the minimum and maximum $\frac{I_0}{I_X}$. As shown in Fig. 17b, there is no parasitic-cancellation under the minimum $\frac{I_0}{I_X}$ condition and there is maximum parasitic-cancellation under the maximum $\frac{I_0}{I_X}$ condition. The spectrum in Fig. 18 shows that the spurious-free dynamic range (SFDR) is slightly reduced by maximum parasitic-cancellation. Notably, in the input signal and the output signal when no parasitic-cancellation is applied, the most prominent spurious component results from the power supply ripples; by contrast, the most prominent spurious component in the maximum parasitic-cancellation output results from the signal harmonics. This shows that the parasitic-cancellation improves the spurious attenuation in low frequencies but also results in more circuit non-linearity due to the increase of signal amplitude.

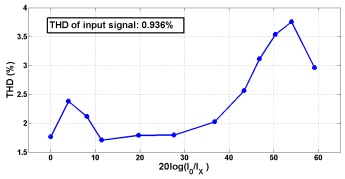


(a) Growth of THD with $\frac{I_0}{I_X}$

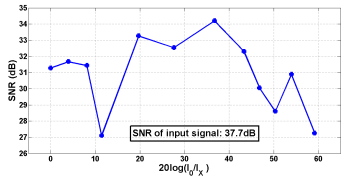


(b) Growth of SNR with $\frac{I_0}{I_X}$

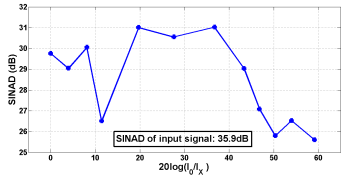


(c) Growth of SINAD with $\frac{I_0}{I_X}$

Fig. 19. Measured THD, SNR and SINAD from the capacitive interfacing experiment.

The total harmonic distortion (THD), SNR and signal-to-noise and distortion ratio (SINAD) of the outputs are respec-

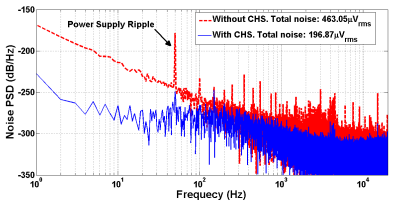


Fig. 20. Comparison of the measured output noise spectrum with and without chopper-stabilization.

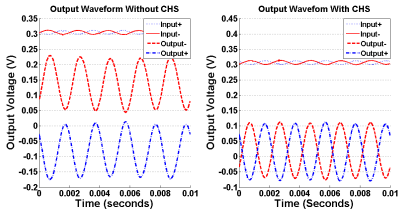


Fig. 21. Comparison of the measured output waveforms in response to sinusoidal input with and without chopper-stabilization.

tively plotted against $\frac{I_0}{I_X}$ in Fig. 19. As predicted by Fig. 18, the THD generally becomes higher when $\frac{I_0}{I_X}$ increases. The SNR is reduced by about 3∼4 dB when $\frac{I_0}{I_X}$ reaches maximum. As analyzed in Section. II-E2, this shows that the input-referred noise of the CSA is much less than that of the PCC, which probably results from the effective flicker noise removal by the chopper-stabilization. The SNR peaks with moderate $\frac{I_0}{I_X}$ where the noise attenuation on the CSA dominates the noise increase of the PCC. Compared with the input SNR, the noise figure of the read-out circuit is in the region of 3.5∼10.5 dB. The SINAD follows similar trend with SNR curve, but the degradation in high $\frac{I_0}{I_X}$ region appears to be slightly more significant since the harmonic distortion effect is included.

*3) Examination of the chopper-stabilization effects:* Two experiments are performed to examine the effectiveness of the chopper-stabilization (CHS) scheme: the output noise spectrum of the read-out chip with and without CHS are measured and compared in Fig. 20; the output waveforms in response to 500 Hz, 20 mV sinusoidal input are compared in Fig. 21 to show the offset elimination effect. The output noise is measured by grounding the input of the read-out chip and analyzing the output waveform. The total noise is calculated by performing mean-square-root operation on the output waveform. The result without CHS is obtained by connecting the chopper control signal to $VDD$ so that the forward choppers are always on while the cross choppers are always off. The comparison in Fig. 20 shows that the low frequency noise is significantly reduced. Also, the ripples from power supply are attenuated because the reduced offset from the CHS improves the common-error cancellation in the fully differential circuits. The effectiveness of offset elimination is proven in Fig. 21.

*4) Power consumption:* The power consumption of the read-out chip is summarized in Table. II. As shown in Fig. 17a, the PCC contributes to 35 dB extra gain compared with the typical unity-gain buffer. Therefore, if without the parasitic-cancellation, an extra amplifier with 35 dB gain is required. In fact, the measured gain of the CSA in this design is 29.6 dB which consumes 92.06 $\mu$W power. Therefore, the parasitic-cancellation scheme saves at least 92.06 $\mu$W power consumption.

TABLE II
SUMMARY OF POWER CONSUMPTION

| | |
|---|---|
| Total Power | 165.2 $\mu$W |
| PCC | 35.45 $\mu$W |
| CSA | 92.06 $\mu$W |
| Clock Generator & Others | 37.67 $\mu$W |

## IV. CONCLUSION

In this paper, a power-efficient MEMS capacitive read-out circuit with parasitic-cancellation and chopper-stabilization is introduced. The circuit addresses the signal degradation issue in sensors which have small sensing capacitance. By effectively cancelling the parasitic capacitance at the MEMS-CMOS interface, the read-out circuit follows a low-degradation low-amplification process which has better power-efficiency compared with the high-degradation high-amplification process in typical designs. Besides, the chopper-stabilization technique effectively reduces the low-frequency noise and circuit offsets which improves the precision and stability of the read-out circuit. The function of the read-out circuit is proven in the experimental results of the prototype VLSI chip. The chip specifications of the read-out circuit are summarized in Table. III.

The presented read-out circuit is especially suitable for the

TABLE III
SPECIFICATIONS SUMMARY OF THE READ-OUT CHIP

| | |
|---|---|
| Fabrication process | AMS 0.35 $\mu$m 3.3V 2P4M |
| Occupation Area | 0.35 $mm^2$ |
| Equivalent capacitive sensor specifications | |
| Sensing capacitance | 2 × 0.5 pF |
| Bias Voltage | ±1 V |
| Maximum Capacitance Variation | 7.5 fF |
| Output Amplitude | 745 mV (max. parasitic-cancellation); 14.1 mV (without parasitic-cancellation). |
| THD | 2.96% (max. parasitic-cancellation); 1.77% (without parasitic-cancellation). |
| SNR | 27.26 dB (max. parasitic-cancellation); 31.28 dB (without parasitic-cancellation). |
| Noise Figure | 10.4 dB (max. parasitic-cancellation); 6.4 dB (without parasitic-cancellation). |
| SINAD | 25.61 dB (max. parasitic-cancellation); 29.76 dB (without parasitic-cancellation). |
| SFDR | 78 dB (max. parasitic-cancellation); 82 dB (without parasitic-cancellation). |
| Power Consumption | 165.2 $\mu$W |

MEMS cochlea sensors due to its parasitic-cancellation feature and the fact that its chopper-stabilization scheme does not rely on the differential sensing structures. A MEMS cochlea sensor similar as the one shown in Fig. 1 has been fabricated and will be tested together with the proposed read-out circuit for the next step. Eventually, a MEMS-based cochlea system will be built for hearing-related research and development of future cochlea prosthetic devices.

## REFERENCES


[1] K. Tanaka, M. Abe and S. Ando, "A novel mechanical cochlea "fishbone" with dual sensor/actor characteristics", *IEEE/ASME Trans. Mechatronics*, vol. 3, no. 2, pp. 98-105, Jun. 1998.

[2] T. Xu, M. Bachman, F.-G. Zeng and G.-P. Li, "Polymeric micro-cantilever array for auditory front-end processing," *Sensor Actuat. A-phys.*, vol. 114, pp. 176-182, Feb. 2004.

[3] R. D. White and K. Grosh, "Microengineered hydromechanical cochlear model," *Proc. Natl. Acad. Sci. U. S. A.*, vol. 102, no. 5, pp. 12961301, Feb. 2005.

[4] F. Chen, H. I. Cohen, T. G. Bifano, J. Castle, J. Fortin, C. Kapusta, D. Mountain, A. Zosuls and A. E. Hubbard, "A hydromechanical biomimetic cochlea: Experiments and models," *J. Acoust. Soc. Am.*, vol. 119, no. 1, pp. 176-182, Jan. 2006.

[5] R. Latif, E. Mastropaolo, A. Bunting, R. Cheung, T. Koickal, A. Hamilton, M. Newton and L. Smith, "Low frequency tantalum electromechanical systems for biomimetical applications," *J. Vac. Sci. Technol. B*, vol. 29, no. 6, pp. 06FE05, 2011.

[6] R. F. Lyon and C. Mead, "An analog electronic cochlea," *IEEE Trans. Acoust. Speech Signal Process.*, vol. 36, no. 7, pp. 1119-1134, Jul. 1988.

[7] R. Sarpeshkar, R. F. Lyon and C. Mead, "A low-power wide-dynamic-range analog VLSI cochlea," *Analog Integrated Circuits and Signal Processing*, vol. 16, pp. 245-274, 1998.

[8] E. Fragniere, "A 100-channel analog CMOS auditory filter bank for speech recognition," *Proc. IEEE Int. Solid-State Circuits Conf. Dig. Tech. Papers*, 2005, pp. 140-141.

[9] J. Georgiou and C. Toumazou, "A 126-$\mu$W cochlear chip for a totally implantable system," *IEEE J. Solid-State Circuits*, vol. 40, no. 2, pp. 430-443, Feb. 2005.

[10] R. Sarpeshkar, C. Salthouse, J.-J. Sit, M. W. Baker, S. M. Zhak, T.K.-T. Lu, L. Turicchia and S. Balster, "An ultra-low-power programmable analog bionic ear processor," *IEEE Trans. Biomed. Eng.*, vol. 52, no. 4, pp. 711-727, Apr. 2005.

[11] T. J. Hamilton, C. Jin, A. van Schaik and J. Tapson, "An active 2-D silicon cochlea," *IEEE Trans. Biomed. Circuits Syst.*, vol. 2, no. 1, pp. 30-43, Mar. 2008.

[12] B. Wen and K. Boahen, "A silicon cochlea with active coupling," *IEEE Trans. Biomed. Circuits Syst.*, vol. 3, no. 6, pp. 444-455, Dec. 2009.

[13] S. Mandal, S. M. Zhak and R. Sarpeshkar, "A bio-inspired active radio-frequency silicon cochlea," *IEEE. J. Solid-State Circuits*, vol. 44, no. 6, pp. 1814-1828, Jun. 2009.

[14] A. G. Katsiamis, E. M. Drakakis and R. F. Lyon, "A biomimetic, 4.5 $\mu$W, 120+ dB, log-domain cochlea channel with AGC," *IEEE J. Solid-State Circuits*, vol. 44, no. 3, pp. 1006-1022, Mar. 2009.

[15] S.-C. Liu, A. van Schaik, B. A. Minch and T. Delbruck, "Asynchronous binaural spatial audition sensor with $2 \times 64 \times 4$ channel output," *IEEE Trans. Biomed. Circuits Syst.*, 2013. doi: 10.1109/TBCAS.2013.2281834.

[16] S. Wang, T. J. Koickal, A. Hamilton R. Cheung and L. S. Smith, "A bio-realistic analog CMOS cochlea filter with high tunability and ultra-steep roll-off," *IEEE Trans. Biomed. Circuits Syst.*, 2014. doi: 10.1109/TBCAS.2014.2328321.

[17] S. M. Han, H. Benaroya and T. Wei, "Dynamics of transversely vibrating beams using four engineering theories," *Journal of Sound and Vibration*, vol. 225, no. 5, pp. 935-988, 1999.

[18] J.-C. Liu, Y.-S. Hsiung and M.S.-C, Lu, "A CMOS micromachined capacitive sensor array for fingerprint detection," *IEEE Sensors J.*, vol. 12, no. 5, pp. 1004-1010, 2012.

[19] J. Han and M. A. Shanon, "Smooth contact capacitive pressure sensors in touch- and peeling-mode operation," *IEEE Sensor J.*, vol. 9, no, 3, pp. 199-206 , 2009

[20] X. Hao, S. Tanaka, A. Masuda, J. Nakamura, K. Sudoh, K. Maenaka, H. Takao and K. Higuchi, "Application of silicon on nothing structure for developing a novel capacitive absolute pressure sensor," *IEEE Sensor J.*, vol. 14, no, 3, pp. 808-815 , 2014

[21] J. Citakovic, P. F. Hovesten, G. Rocca, A van Halteren, P. Rombach, L. J. Stenberg, P. Andreani and E. Bruun, "A compact CMOS MEMS microphone with 66dB SNR," *Dig. Tech. Papers, IEEE Int. Solid-State Circuits Conf.*, pp 350-451, 2009

[22] S. Hur, Y. Jung, Y. H. Lee and J.-H. Kwak, "Two-chip MEMS capacitive microphone with CMOS analog amplifier ," *IEEE Sensor Conf.*, pp. 1-4 , 2012.

[23] C. H. Je, J. Lee, W. S. Yang and J.-k. Kwon, "A surface micromachined MEMS capacitive microphone with back-plate supporting pillars," *IEEE Sensor Conf.*, pp. 1-4 , 2013.

[24] J. Wu, K. Fedder and L. R. Carley, "A low noise low-offset capacitive sensing amplifier for a 50-$\mu g/\sqrt{Hz}$ monolithic CMOS MEMS accelerometer," *IEEE J. Solid-State Circuits*, vol. 39, no. 5, pp. 722-730, May 2004.

[25] S.-S. Tan, C.-Y. Liu,L.-K. Yeh, Y.-H. Chiu, M. S.-C. Liu and K. Y. J. Hsu, "An integrated low-noise sensing circuit with efficient bias stabilization for CMOS MEMS capacitive accelerometers," *IEEE Trans. Circuits Syst. I, Reg. Papers*, vol. 58, no, 5, pp. 2661-2672, Nov. 2011.

[26] Hongzhi Sun, D. Fang, K. Jia, F. Maarouf and H. Qu and H. Xie, "A low-power low-noise dual-chopper amplifier for capacitive CMOS-MEMS accelerometers," *IEEE Sensors J.*, vol. 11, no. 4, pp. 925-933, Apr. 2011.

[27] Y.-D. Lin, J.-Y. Lin, C.-K. Wang, L.-S. Fan and K.-A. Wen, "A monolithic CMOS MEMS accelerometer with low noise gain tunable interface in 0.18 $\mu$m CMOS MEMS technology," *Proc. IEEE Sensors Conf.*, pp. 1-4, 2012.

[28] M. Tavakoli and R. Sarpeshkar, "An offset-canceling low-noise lock-in architecture for capacitive sensing," *IEEE J. Solid-State Circuits*, vol. 38, no. 2, pp. 244-253, Feb. 2003.

[29] S. A. Jawed, J. H. Nielsen, M. Gottardi, Baschirotto and E. Bruun, "A multifunction low-power preamplifier for MEMS capacitive microphones," *Proc. Solid-State Circuits Conference, 2009. ESSCIRC 2009. 35th European*, pp. 292-295, 2009.

[30] S. Wang, T. J. Koickal, A. Hamilton, E. Mastropaolo, R. Latif, R. Cheung, M. Newton and L. Smith, "A low-noise interface circuit for MEMS cochlea-mimicking acoustic sensors," *Proc. IEEE Int. Symp. on Circuits and Systems*, pp. 1151-1154, 2012.

[31] C. C. Enz and E. A. Vittoz, *Charge-based MOS transistor Modeling: the EKV model for low-power and RFIC design*, John Wiley & Sons Inc., 2006.

[32] B. Razavi, *Design of Analog CMOS Integrated Circuits*, McGraw-Hill, 2001.

[33] P. E Allen and D. R. Holberg, *CMOS Analog Circuit Design*, Oxford University Press, 2002.

# A Floating Active Inductor Based CMOS Cochlea Filter with High Tunability and Sharp Cut-off

Shiwei Wang*, Thomas Jacob Koickal*, A. Hamilton*,
E. Mastropaolo*, R. Cheung*, and L. Smith†
*Inst. for Integrated Micro and Nano Systems, University of Edinburgh, Email: shiwei.wang@ed.ac.uk
†Dept. of Computer Sc. & Mathematics, University of Stirling, Email: l.s.smith@cs.stir.ac.uk

***Abstract*—This paper presents the design of a CMOS cochlea filter channel which achieves high tunability, sharp stopband cut-off and low power consumption with the use of floating active inductor (FAI) as the basic building block. Simulation results show that over 40dB of gain enhancement together with 20% frequency tuning can be achieved at the same time by adjusting only one circuit parameter. A fifth-order elliptic filter providing a stop-band slope of 65.4 $\sim$ 139.8 dB/octave is used as the last stage of the cochlea filter. The power consumption of the cochlea filter channel is 86$\mu$W.**

## I. Introduction

Recent years have seen many progressive studies on the implementation of silicon cochlea in analog VLSI [1]–[6], which are mostly driven by the increasing demand for high performance and power efficient auditory processing chips in biomedical applications (hearing aids and cochlea implants) as well as portable consumer electronics (eg. speech recognition front-end of cellphones). An essential building block of a silicon cochlea is the filters, as input signal needs to be separated into multiple frequency channels. Besides, the frequency response of the filters must be highly adjustable so as to achieve the active gain adaption and sharp tuning observed in biological cochlea [9].

The signal separation is achieved through cascade filtering structure in [3], which succeeds the first silicon cochlea model proposed by Lyon and Mead [7] two decades ago. However, more works adopt the parallel filterbank structure [1], [2], [6] to avoid issues like noise accumulation and linear range limitation in the cascade structure. Nevertheless, parallel structure has its own drawback. In [1], [2], each channel contains only one band-pass filter, which struggles to achieve the similar level of tunability as well as stopband cut-off steepness compared with the cascade structure and also the biological cochlea. Therefore, a one-zero gammatone filter (OZGF) is implemented in [6] for each channel of the parallel structure, which consists of four sections of biquads cascaded together to achieve reasonable biological fidelity. On the other hand, 2-Dimension topology is proposed and implemented in [4] and [5], which adopts a more bio-inspired approach with addition of coupling effects between frequency channels so as to seek better system performance.

In this paper, we carry forward the work on improving filter performance in parallel filterbank silicon cochlea topology. In particular, a floating active inductor (FAI) cell taking advantage of CMOS transistors in weak inversion is introduced and implemented. Based on the FAI cell, three classes of filters are established, each of which mimics one of three prominent signal processing features of the biological cochlea. With the three classes of filters cascaded together, a biomimetic cochlea filter channel is built. The performance of the cochlea filter is verified with simulation results.

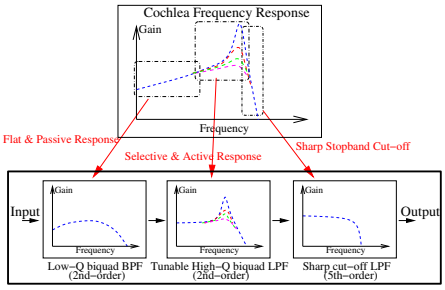


Fig. 1. System Architecture: each of the cascaded filters achieves one frequency behavior of biological cochlea

## II. Cochlea Filter Design

### A. System Architecture

Fig. 1 shows the system architecture of the proposed cochlea filter. Three classes of filters are cascaded together in the system: A low-Q biquad band-pass filter mimics the flat and passive response of the biological cochlea at low frequency range, a tunable high-Q biquad low-pass filter mimics the selective and active behavior at the center frequency band, and a $5^{th}$-order low-pass filter provides the required sharp cut-off in the stop-band. With the three filters cascaded together, the cochlea filter as a whole is able to behave similarly to a biological cochlea [9]. The cochlea filter in total is a $9^{th}$-order system.

### B. Floating Active Inductor (FAI)

Floating active inductors have been studied and designed for high-speed applications [10]. We propose an improved FAI cell based on classical gyrator-C topology as shown in Fig. 2. The transistors operate in weak inverstion, as

978-1-4673-5762-3/13/$31.00 ©2013 IEEE 

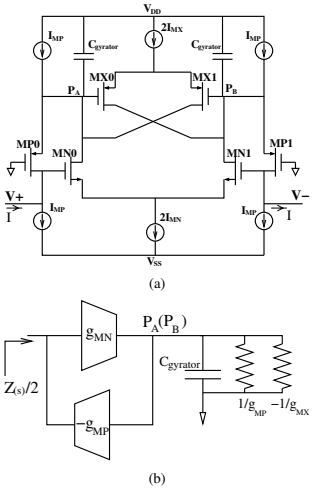


Fig. 2. FAI cell: (a)schematic. (b)simplified model.

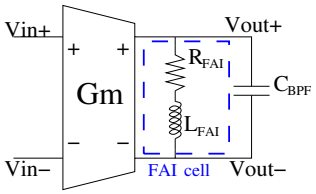


Fig. 3. Schematic of a low-Q biquad BPF based on FAI

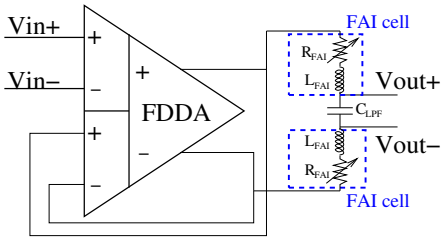


Fig. 4. Schematic of a tunable high-Q biquad LPF based on FAI

the requirement of low transconductance in audio-frequency applications leads the circuits to be extremely low-current biased. The NMOS transistor pair MN provides the positive transconductance, while the PMOS transistor pair MP provides the negative transconductance. The gyrating ports $P_A$ and $P_B$ are terminated with capacitive load $C_{gyrator}$. However $P_A$ ($P_B$) is connected at the source of transistor MP, which is a low impedance end, therefore an equivalent resistance of $1/g_{MP}$ exists in parallel with $C_{gyrator}$. On the other hand, another PMOS transistor pair MX provides a negative resistance of $-1/g_{MX}$ at $P_A$ ($P_B$). The simplified model of the FAI is shown in Fig. 2(b). The impedance of the FAI is thus given by

$$Z(s) = \frac{2C_{gyrator} \cdot s}{g_{MP}g_{MN}} + \frac{2(g_{MP} - g_{MX})}{g_{MP}g_{MN}}. \quad (1)$$

Therefore, the FAI cell can be modeled as an inductor in series with a resistor. For transistors in weak inversion, we can rewrite Eq. 1 and derive the equivalent inductance and resistance of the FAI and have

$$L = \frac{2C_{gyrator}(nU_T)^2}{I_{MP}I_{MN}} \quad (2)$$

$$R = \frac{2nU_T(I_{MP} - I_{MX})}{I_{MP}I_{MN}} \quad (3)$$

where $I_{MP}$, $I_{MN}$ and $I_{MX}$ are static currents running in transistor MP, MN and MX separately. Eq. 2 and Eq. 3 show that the inductance and resistance of the FAI can be directly tuned by adjusting the static currents in the transistors, and obviously, the Q factor of the FAI reaches maximum when $I_{MP}$ equals $I_{MX}$.

### C. Implementation of Filters based on FAI

*1) Low-Q Biquad Band-pass Filter:* As shown in Fig. 3, the low-Q biquad band-pass filter is implemented by loading a fully differential OTA with the FAI cell and a capacitor in parallel. The transfer function is given by

$$H(s) = \frac{G_m}{C_{BPF}} \cdot \frac{s + \omega_z}{s^2 + \frac{\omega_0}{Q}s + \omega_0^2} \quad (4)$$

$$\begin{cases} \omega_z = \frac{R_{FAI}}{L_{FAI}} = \frac{I_{MP}-I_{MX}}{nU_TC_{gyrator}} \\ \omega_0 = \sqrt{\frac{1}{C_{BPF}L_{FAI}}} = \frac{1}{nU_T}\sqrt{\frac{I_{MP}I_{MN}}{2C_{BPF}C_{gyrator}}} \\ Q = \frac{1}{R_{FAI}}\sqrt{\frac{L_{FAI}}{C_{BPF}}} = \frac{\sqrt{I_{MP}I_{MN}}}{I_{MP}-I_{MX}}\sqrt{\frac{C_{gyrator}}{2C_{BPF}}} \end{cases} \quad (5)$$

*2) Tunable High-Q Biquad Low-pass Filter:* The tunable high-Q biquad low-pass filter is implemented as a fully differential difference amplifier (FDDA) based buffer followed by an LC voltage divider, as shown in Fig. 4. A pair of FAI cells instead of a single one is used to build the LC voltage divider for three reasons. First, it keeps the circuits in fully differential configuration so as to minimize common-mode errors. Second, it allows the DC voltage across $C_{LPF}$ to approximate zero, so that the output offset is minimized. Third, as the transistors in FAI cell are operating in weak inversion, the signal linear range across the FAI cell is approximately 60mV, and by using a pair of FAI cells, the linear range of the filter is widened to 120mV.

The transfer function of the filter is given by

$$H(s) = \frac{1}{2C_{LPF}L_{FAI}} \cdot \frac{1}{s^2 + \frac{\omega_0}{Q}s + \omega_0^2} \quad (6)$$

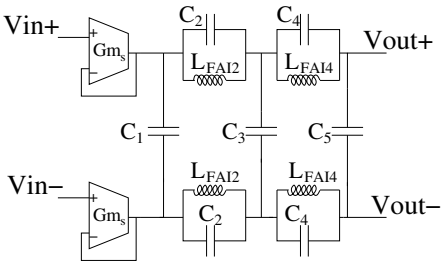


Fig. 5. Schematic of a $5^{th}$-order elliptic filter based on FAI. The FAI cells are represented by pure inductors as they are tuned into minimum-resistance mode ($I_{MX}$=$I_{MP}$).

$$\begin{cases} \omega_0 = \sqrt{\frac{1}{2C_{LPF}L_{FAI}}} = \frac{1}{2nU_T}\sqrt{\frac{I_{MP}I_{MN}}{C_{LPF}C_{gyrator}}} \\ Q = \frac{1}{R_{FAI}}\sqrt{\frac{L_{FAI}}{2C_{LPF}}} = \frac{\sqrt{I_{MP}I_{MN}}}{2(I_{MP}-I_{MX})}\sqrt{\frac{C_{gyrator}}{C_{LPF}}} \end{cases} \quad (7)$$

*3) Sharp Cut-off Low-pass Filter:* As shown in Fig. 5, a $5^{th}$-order elliptic filter is built to achieve sharp cut-off low-pass function. The pair of OTAs at the input works equivalently as source resistors. The value of the inductance and capacitance in Fig. 5 is given by:

$$L_{FAI,i} = \frac{2C_{gyrator,i}(nU_T)^2}{I_{MP}I_{MN}} = \frac{L_{norm,i}}{Gm_s \cdot \omega_{-3dB}} \quad (8)$$

$$C_i = \frac{Gm_s C_{norm,i}}{\omega_{-3dB}} \quad (9)$$

where $\omega_{-3dB}$ is the -3dB frequency of the low-pass filter, and $L_{norm,i}$ and $C_{norm,i}$ are normalized inductance and capacitance value which can be obtained from the filter design tables [8].

## III. Simulation Results

To verify the design proposed above, we simulated the circuits in Cadence SPECTRE with the process parameters of AMS 0.35$\mu$m 2-poly 4-metal CMOS technology. Fig. 6 shows separately the frequency response of the low-Q biquad band-pass, tunable high-Q biquad low-pass, and the sharp cut-off $5^{th}$ order elliptic low-pass filter. Fig. 6(a) shows that the low-Q biquad band-pass filter provides good similarity with the passive behavior of biological cochlea. In Fig. 6(b), by simply tuning the current $I_{MX}(I_{MN})$, a gain variation of over 40dB is obtained while the center frequency moves rightwards by roughly 80%. The elliptic filter is configured as $5^{th}$ order, $K^2 = \infty$, $\rho = 5\%$ and $\theta = 36°$. The results in Fig. 6(c) shows that although the passband ripple $R_{dB}$ is larger than the value in theory (0.01%) due to circuit non-idealities, the steepness factor $f_s/f_c = 5.06kHz/3.08kHz = 1.64$ reasonably agrees with expect value (1.70), while the minimum stopband attenuation $A_{min}$ is even superior than expected value (40.8dB), which makes the elliptic filter a sufficiently excellent option to provide the sharp stopband cut-off required in cochlea filter. Fig. 7 illustrates the frequency response of the entire cochlea

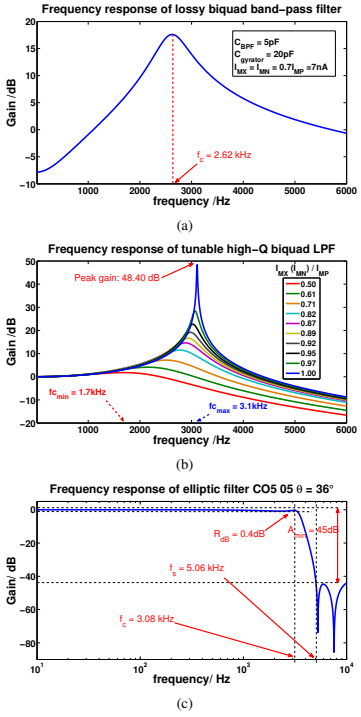


Fig. 6. Frequency response of:(a) Low-Q biquad BPF (tuned with $I_{MX} = I_{MN} = 0.7I_{MP} = 7nA$) , (b) High-Q tunable biquad LPF (tuned from $I_{MX} = I_{MN} = 0.5I_{MP} = 5nA$ to $I_{MX} = I_{MN} = I_{MP} = 10nA$), (c) Elliptic filter (tuned with $I_{MX} = I_{MN} = I_{MP} = 10nA$).

TABLE I
Summary of Specifications

| | |
|---|---|
| Supply voltage | 3.3 V |
| Power dissipation | 86 $\mu$W |
| Peak gain tuning range | 44.62 dB |
| Center frequency | 2.62 kHz $\sim$ 3.11 kHz |
| Cut-off slope | 65.4 $\sim$ 139.8 dB/octave |
| Input noise floor | 29 $\mu V_{rms}$(minimum gain), 0.82 $\mu V_{rms}$(maximum gain) |
| Maximum input swing with $\leq 5\%$ THD | 23 $mV_{p-p}$ |
| Total on-chip capacitance | 170 pF |

filter channel with these three filters cascaded together, which incorporates the passive, active and sharp stopband cut-off signal processing feature of biological cochlea. Due to the different pole position of the low-Q BPF and high-Q LPF, center frequency is shifted rightwards by roughly 20% instead of 80%, while the gain tuning is maintained as over 40dB of variation and the cut-off slope is as steep as 65.4 $\sim$ 139.8 dB/octave.

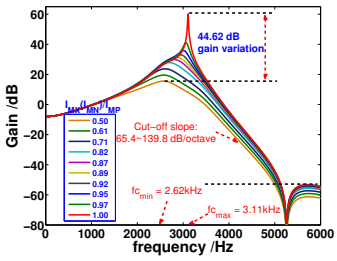


(a)

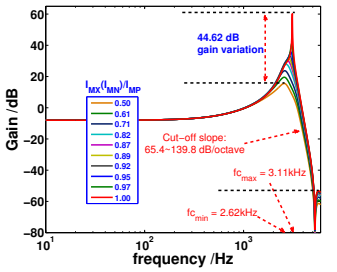


(b)

Fig. 7. Frequency response of the entire cochlear filter: (a)linear frequency scale. (b)logarithmic frequency scale.

## IV. Conclusions and Future Work

In this paper, we proposed the design of a CMOS cochlea filter based on floating active inductors. The advantages and highlight features of our design include the following points:

- Q factor and center frequency tuning of the filter is much easier and less likely to cause errors and stability problems. In the silicon cochlea design where biomimetic frequency response is achieved by using cascaded second order sections (SOS) [3], [6], [7], filter tunability is limited by the fact that the parameters of all sections need to be perfectly adjusted altogether so as to guarantee reasonable tuning accuracy and stability In our design, tuning is done by adjusting circuit parameter of only one second order section, which highly improves accuracy and stability, while at the same time maintains a wide tuning range as shown in the simulation results.
- Sharp stopband cut-off is achieved by an elliptic filter, which is a competent option to mimic this specific feature of biological cochlea, since elliptic filter has the steepest transition from passband to stopband with equal filter order. The reduction in filter order results in less circuit complexity. And also, while passband response can be severely affected by the variation of pole position in each sections of the cascaded SOS, the elliptic filter is less sensitive to component variations [11].
- Implementation of the cochlea filter is based on a basic circuit element, the FAI cell. As the FAI cell can be simply modeled as an inductor, the creation of the cochlea filter is highly straightforward. Besides, the compact and floating features make it flexible for building a variety of ladder LC topologies. The tunability of the FAI cell, as shown in the simulation results, also provides a fascinating feature which is essentially required in adaptive filters. Therefore, the FAI cell is a promising option as basic building block for high order intelligent filters.

For future work, we will fabricate the chip for prototype. Then we will add the automatic Q-control mechanism to make the cochlea filter self-adaptive, and also implement multiple channels with center frequency distributed throughout audio range. Finally we will interface the cochlea filters with the MEMS audio front-end we have proposed [12], and integrate with a spike-event coder that we have developed [13], so as to build an end-to-end silicon cochlea system [14].

## Acknowledgment

The authors would like to thank the EPSRC, UK, for supporting this project under Grants to the Univ. of Edinburgh (EP/G063710/1), and to the Univ. of Stirling (EP/G062609/1).

## References

[1] J. Georgiou and C. Toumazou, "A 126-$\mu$W cochlear chip for a totally implantable system," *IEEE J. Solid-State Circuits*, vol. 40, no. 2, pp. 430-443, Feb. 2005.
[2] R. Sarpeshkar, et al., "An ultra-low-power programmable analog bionic ear processor," *IEEE Trans. Biomed. Eng.*, vol. 52, no. 4, pp. 711-727, Apr. 2005.
[3] V. Chan, et al., "AER EAR: A matched silicon cochlea pair with address event representation interface," *IEEE Trans. Circuits Syst. I, Reg. Papers*, vol. 54, no. 1, pp. 48-59, Jan. 2007.
[4] T. J. Hamilton, et al., "An active 2-D silicon cochlea," *IEEE Trans. Biomed. Circuits Syst.*, vol. 2, no. 1, pp. 30-43, Mar. 2008.
[5] B. Wen and K. Boahen, "A silicon cochlea with active coupling," *IEEE Trans. Biomed. Circuits Syst.*, vol. 3, no. 6, pp. 444-455, Dec. 2009.
[6] A. G. Katsiamis, et al., "A biomimetic, 4.5 $\mu$W, 120+ dB, Log-Domain Cochlea Channel with AGC," *IEEE J. Solid-State Circuits*, vol. 44, no. 3, pp. 1006-1022, Mar. 2009.
[7] R. F. Lyon and C. Mead, "An analog electronic cochlea," *IEEE Trans. Acoust. Speech Signal Process.*, vol. 36, no. 7, pp. 1119-1134, Jul. 1988.
[8] A. B. Williams and F. J. Taylor, *Electronic Filter Design Handbook*, New York: McGraw-Hill, 1995.
[9] M. A. Ruggero, et al., "Mechanical bases of frequency tuning and neural excitation at the base of the cochlea: Comparison of basilar-membrane vibrations and auditory-nerve-fiber responses in chinchilla," *PNAS*, vol. 97, no. 22, pp.11744-11750, Oct. 2000.
[10] F. Yuan, *CMOS active inductors and transformers: principle, implementation, and applications*, Springer, 2008.
[11] G. C. Temes and H. J. Orchard, "First order sensitivity and worst-case analysis of doubly terminated reactance two-ports," *IEEE Trans. Circuit Theory.*, 20(5), pp. 567-571, 1973.
[12] S. Wang, et al., "A low-noise interface circuit for MEMS cochlea-mimicking acoustic sensors," *Proc. IEEE Int. Symp. on Circuits and Systems*, Seoul, pp. 1151-1154, 2012.
[13] L. Gouveia, et al., "An asynchronous spike-event coding scheme for programmable analog array," *IEEE Trans. Circuits Syst. I, Reg. Papers*, vol. 58, no. 4, pp. 791-799, Apr. 2011.
[14] T. Koickal, et al., "Design of a spike event coded RGT microphone for neuromorphic auditory systems," *Proc. IEEE Int. Symp. on Circuits and Systems*, Rio de Janeiro, pp. 2465-2468, 2011.

# A Low-Noise Interface Circuit for MEMS Cochlea-Mimicking Acoustic Sensors

Shiwei Wang*, Thomas Jacob Koickal*, A. Hamilton*,
E. Mastropaolo*, R. Latif*, R. Cheung*, M. Newton† and L. Smith†
*Inst. for Integrated Micro and Nano Systems, University of Edinburgh, Email: shiwei.wang@ed.ac.uk
†Dept. of Computer Sc. & Mathematics, University of Stirling, Email: l.s.smith@cs.stir.ac.uk

***Abstract*—This paper proposes a low-noise MEMS interface circuit which has very small parasitic capacitance at the input node. The circuit presented is suitable for the MEMS cochlea-mimicking acoustic sensors which are highly parasitic-sensitive due to their low intrinsic sensing capacitance. In order to reduce the electronic noise of the interface circuit, chopper stabilization technique is implemented, and an effective method to optimize the critical transistor size for best noise performance is derived. Simulation results show that, for a MEMS sensing structure with 200 fF static capacitance, the interface circuit achieves a 0.72 aF equivalent capacitance noise floor over 100 Hz to 20 kHz audio bandwidth.**

## I. Introduction

Over the past decade, a variety of frequency selective MEMS structures that mimic the signal processing features of mammalian cochlea have been reported [1]–[4]. These structures provide an alternative approach to build cochlea auditory systems, other than those implementations based upon cascaded band-pass filters [5], [6]. The MEMS based cochlea systems achieve higher stability and accuracy, since the functionality relies less on the behaviour of circuits, and a compact system can be built without using complex cascaded filters.

An interface circuit is needed to convert the movements of the MEMS structure into well-conditioned electrical signals for further processing. Capacitive approach is one of the most widely used sensing method in acoustic sensors, with the advantage of high resolution, low power consumption, low temperature sensitivity and high stability. To interface with the cochlea-mimicking MEMS structures with capacitive approach is a challenge, as those structures are typically optimized into beam shape, which forms a very low sensing capacitance. Besides, the electronic noise from the interface circuit needs to be attenuated to achieve a high detectable signal level.

Switch-capacitor (SC) architecture with correlated double sampling (CDS) has been used to build interface circuit with reduced low-frequency noise [7]. However, the noise folding problem in SC circuits has not been well solved thus far. Capacitive feedback charge amplifier based on floating-gate technique has been proposed to achieve a high signal-to-noise ratio with very low power consumption [8], but a feedback capacitance much smaller than the sensor capacitance is required to achieve sufficient gain, which is not applicable for low sensing capacitance sensors. Chopper stabilization (CHS) technique has been widely used to effectively remove low-frequency noise in inertial sensory systems [9]–[11], where differential sensing capacitor structure is available. Although it is difficult to fabricate acoustic sensors with differential structure, the principle of shifting the frequency band of signal and noise separately through modulation and demodulation can be adopted in building acoustic sensor interface circuit.

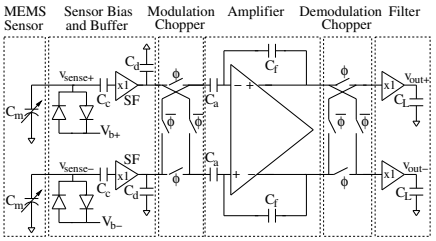


Fig. 1. Architecture of the interface circuit.

In this paper, we propose a low-noise solution for interfacing the highly parasitic-sensitive MEMS cochlea-mimicking acoustic sensors. Chopper stabilization technique is adopted to reduce transistor flicker noise which dominates in audio frequency band, and the critical transistor size is optimized to achieve best overall noise performance. Besides, the circuit feature of low parasitic capacitance is also derived.

## II. Interface Circuit Design

### A. Circuit Architecture

Chopper stabilization scheme is implemented as shown in Fig. 1. As the absence of differential capacitors in MEMS acoustic sensors makes it difficult to implement the bridge configuration in [9]–[11], two identical sensing capacitors biased with opposite DC voltages are adopted to obtain a pair of differential signals to achieve higher signal sensitivity. As shown in Fig. 1, $C_m$ represents the sensing capacitor formed by either the cantilever [1] or beam [2]–[4] structure in the MEMS sensor. The diode pairs provide high impedance DC path between the biasing voltage and the sensing capacitor. The charge stored on the sensing capacitor remains static when the beam vibrates within audio frequency band, and

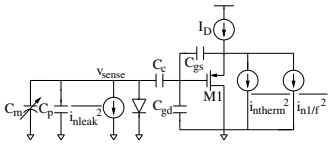


Fig. 2. Noise sources and parasitic components at the sensing node. M1 is the input transistor of the source follower buffer

therefore the capacitance variation due to beam vibration can be converted into voltage signal. A source follower (SF) buffer is added before the chopper amplifier to protect the sensing capacitor from the charge injection effect brought by MOSFET chopper switches. The parasitic capacitance of the source follower, which is shown in the following section, can be minimized without compromising noise performance. The amplifier is configured with capacitive feedback to achieve accurate gain. A simple first-order filter is used to filter out the harmonics after the demodulation stage. The entire interface circuit consists of an array of the circuit shown in Fig. 1. The transistor size of the source follower buffer at the sensing node is optimized separately for noise performance according to the respective sensing capacitance, which is discussed in detail in the following section.

### *B. Noise Optimization*

The source follower buffer at the sensing node is the most significant noise source in the circuit shown in Fig. 1, as the low frequency noise (flicker noise) of the amplifier is largely attenuated with the chopper stabilization technique, while its thermal noise is negligible if the transconductance of the amplifier input transistors are designed to be much larger than that of the source follower. The main noise sources and parasitic components at the sensing node are shown in Fig. 2. The sensed signal, taking the parasitic capacitance into account, is given by

$$V_{sense} = \frac{\Delta C_m V_b}{C_m + C_p + \frac{C_c C_g}{C_c + C_g}} \tag{1}$$

where $C_p$ is the interconnect parasitic capacitance, $C_c$ is the couple capacitance between the sense node and the source follower, $C_g$ is the equivalent parasitic capacitance at the gate of the input transistor M1, and $V_b$ is the biasing voltage. The gate-to-source capacitance $C_{gs}$ of the input transistor is canceled with Miller effect, as the gain of the source follower is unity. Therefore the gate parasitic capacitance $C_g$ is less more than $C_{gd}$, which is merely the gate-drain overlap capacitance if the transistor works in saturation region. As $C_g$ is typically much smaller than $C_c$ and $C_m$, we can simplify Eq. 1 and have

$$V_{sense} = \frac{\Delta C_m V_b}{C_m + C_p}. \tag{2}$$

Eq. 2 shows that the parasitic capacitances from the input transistors have little effect on the sensed signal level, which is fairly conducive to the optimization of circuit noise performance, as the size of the input transistors is far less constrained. The total noise power spectral density (PSD) referred at the sense node is given by

$$\begin{aligned}\frac{\overline{v_{nieq}^2}}{\Delta f}(f) &= \left[\frac{\overline{v_{ntherm}^2}}{\Delta f}(f) + \frac{\overline{v_{n1/f}^2}}{\Delta f}(f)\right]\left(\frac{C_c + C_g}{C_c}\right)^2 \\ &\quad + \frac{\overline{i_{nleak}^2}}{\Delta f}(f) \cdot \frac{1}{\left(C_m + C_p + \frac{C_c C_g}{C_c + C_g}\right)^2 f^2}\end{aligned} \tag{3}$$

where $v_{ntherm}$, $v_{n1/f}$, and $i_{nleak}$ are thermal noise, flicker noise of the input transistor M1, and shot noise due to the leakage current of the biasing diodes, and $f$ is the frequency that circuit is operating on. As $C_g$ is negligible compared with $C_c$ and $C_m$, we can simplify Eq. 3 and have

$$\begin{aligned}\frac{\overline{v_{nieq}^2}}{\Delta f}(f) &= \frac{\overline{v_{ntherm}^2}}{\Delta f}(f) + \frac{\overline{v_{n1/f}^2}}{\Delta f}(f) \\ &\quad + \frac{\overline{i_{nleak}^2}}{\Delta f}(f) \cdot \frac{1}{(C_m + C_p)^2 f^2}.\end{aligned} \tag{4}$$

The shot noise $i_{nleak}$ is proportional with the scale of leakage current, which can be reduced by minimizing the size of $pn$ junction of the biasing diodes. Thermal noise $v_{ntherm}$ and flicker noise $v_{n1/f}$ are both related to transistor size. Intuitively speaking, transistors with large width and small length are preferred, achieving objective of both high transconductance and large transistor size, which are respectively optimal for thermal noise and flicker noise reduction. However the maximization of width-to-length ratio will possibly push the transistor into moderate and even weak inversion. Therefore, we adopt the EKV model [12], in which the behavior modelling of transistors is not constrained by inversion regions, to investigate the optimal transistor size for noise performance. The thermal noise and flicker noise PSD referred at the transistor gate is respectively given by [12]

$$\frac{\overline{V_{ntherm}^2}}{\Delta f}(f) = 4kT\frac{G_{nD}}{G_m^2} \tag{5}$$

$$\frac{\overline{V_{n1/f}^2}}{\Delta f}(f) = \frac{K_f}{C_{ox}^2 WLf} \tag{6}$$

where $k$ is the Boltzmann constant, $T$ is the absolute temperature, $G_{nD}$ is transistor thermal noise conductance, $G_m$ is transistor transconductance, $K_f$ is the flicker noise coefficient, $C_{ox}$ is the gate oxide capacitance per unit area, $W$ is transistor width and $L$ is transistor length. $G_{nD}$ and $G_m$ are respectively defined by the following equations [12]:

$$G_{nD} = 2n\beta U_T\left(\frac{1}{6}\cdot\frac{4q_s^2 + 3q_s + 4q_s q_d + 3q_d + 4q_d^2}{q_s + q_d + 1}\right) \tag{7}$$

$$G_m = 2\beta U_T(q_s - q_d) \tag{8}$$

where $n$ is the slope factor, $\beta$ is the transconductance parameter which is defined as $\mu C_{ox}\frac{W}{L}$, $U_T$ is the thermal voltage $\frac{kT}{q}$, and $q_s$ and $q_d$ are respectively normalized charge at source

and drain of the transistor. $q_d$ is negligible compared with $q_s$ if the transistor works in saturation region, and therefore we can simplify Eq. 7 and Eq. 8 and have

$$G_{nD} = \frac{n\beta U_T}{3} \cdot \frac{4q_s^2 + 3q_s}{q_s + 1} \quad (9)$$

$$G_m = 2\beta U_T q_s. \quad (10)$$

$q_s$ is given by the following equation [12]:

$$q_s = \frac{\sqrt{4i_f + 1} - 1}{2} \quad (11)$$

where $i_f$ is the normalized transistor forward current which is defined as $\frac{I_D}{2n\beta U_T^2}$. Therefore we can rewrite Eq. 5 and get

$$\frac{\overline{V_{ntherm}^2}}{\Delta f}(f) = \frac{2n^2kT}{3I_D}\left(2\sqrt{\frac{2I_DL}{n\mu C_{ox}W} + U_T^2} + U_T\right). \quad (12)$$

With Eq. 6 and 12, the total integrated input referred noise can be calculated as

$$\begin{aligned} V_{nieq} &= \frac{2n^2kT}{3I_D}\left(2\sqrt{\frac{2I_DL}{n\mu C_{ox}W} + U_T^2} + U_T\right) \cdot \\ &\quad (f_{max} - f_{min}) + ln\frac{f_{max}}{f_{min}}\frac{K_f}{C_{ox}^2WL} \\ &\quad + V_{nleak} \end{aligned} \quad (13)$$

where $f_{max}$ and $f_{min}$ are maximum and minimum frequency in the relevant frequency band, and $V_{nleak}$ is the integrate shot noise from the diodes.

Eq. 13 shows that the total integrated noise is inversely proportional with the transistor width. However the transistor width is constrained by the assumption that the gate-to-drain capacitance $C_{gd}$ is negligible compared with sensing capacitance $C_m$. The relationship between integrate noise and transistor length is not monotonic, and an optimal length can be found to achieve minimum noise. The optimal transistor width and length are governed by the following equations:

$$C_{ov}W_{opt} = \frac{1}{10}C_m \quad (14)$$

$$A^2L_{opt}^4 - 4B^2L_{opt} - 4B^2C = 0 \quad (15)$$

where $C_{ov}$ is the gate-drain overlap capacitance per unit width, and parameter $A = \frac{4(f_{max}-f_{min})n^2kT}{3I_D}\sqrt{\frac{2I_D}{n\mu C_{ox}W}}$, $B = \frac{nU_T^2\mu C_{ox}W}{2I_D}$, and $C = ln\frac{f_{max}}{f_{min}} \cdot \frac{K_f}{C_{ox}^2W}$. With Eq. 14 and 15, the optimal size can be defined for the input transistors of the source follower buffer for each channel.

### C. Interfacing Low Sensing Capacitance

Typically, the sensing node is directly interfaced with an amplifier [9]–[11], the input transistor of which is common-source connected. The gate-to-source capacitance of the input transistors is proportional with transistor size, and therefore capacitive matching is extremely difficult if the sensing capacitance is very small. In our configuration, the sensing node is interfaced with a buffer, the input transistor of which is common-drain connected. We have shown that transistor parasitic capacitance is negligible as long as the transistor width does not exceed a corresponding extreme value. Besides, the interconnect parasitic capacitance $C_p$ in Eq. 2 can be further reduced with the integration of the MEMS sensor and CMOS interface circuit on the same chip.

Another challenge associated with low sensing capacitance is that, the impedance of the biasing path has to be accordingly high enough to achieve a sufficient RC time constant to keep the charge stored on the sensing node static. Therefore, the size of the reverse-biased diodes in Fig. 1 is minimized to reduce leakage current, which is in line with the requirement for noise optimization as well.

### D. Considerations for Device Mismatch

Apart from noise and parasitic components, device mismatch is another major imperfectness that can cause the circuit performance deviate from expected values. Although the DC offset due to device mismatch in the amplifier can be canceled with the chopper stabilization scheme, the offsets in the source follower and the modulation chopper which are indistinguishable from the useful signal are still present and will cause significant circuit degradation. To remove these undesired offsets, signal path is always connected through AC coupling, as shown in Fig. 1. Besides, the mismatch between the MOS switches in the chopper will preserve the differential structure from fully canceling the charge injection and clock feed-through effects. Therefore, an on-chip decoupling capacitor $C_d$ is added to remove the uncanceled distorted signals, as shown in Fig. 1.

## III. Simulation Results

A MEMS structure composed of an array of resonant beams has been fabricated using imec CMORE SiGeMEMS process for testing. Twin-beam structure is implemented for each channel in the MEMS chip to provide the identical sensing capacitor pair required for the interface circuit shown in Fig. 1. The interface circuit presented above is being implemented with TSMC 0.18-$\mu$m technology, which is highly compatible with the MEMS process we used.

Noise simulation is carried out using the Cadence Spectre noise analysis tools. Fig. 3 shows the comparison between the simulated output noise power of a source follower buffer, and the results calculated with Eq. 13. The input transistor is biased with 5 $\mu$A current, and the noise frequency range taken into account is from 100 Hz to 20 kHz. Fig. 3 shows that Eq. 13 provides a good estimation of the the relationship between transistor size and noise performance.

Fig. 4 compares the output referred noise density with and without chopper stabilization scheme. The result is obtained with periodic noise analysis (pnoise) in Spectre. The modulation frequency applied is 20 kHz. As shown in Fig. 4, the low frequency noise is largely attenuated.

Table. I shows the simulation results from the Cadence Spectre simulator for one channel of the interface circuit, the beam resonant frequency and sensing capacitance of which are

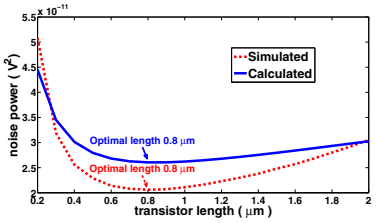


(a)

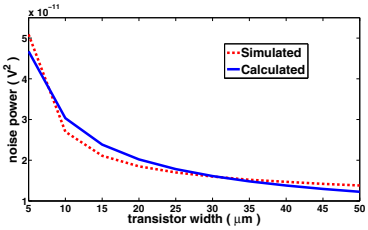


(b)

Fig. 3. Comparison between calculated and simulated noise values. (a) The integrate noise power versus transistor length, with constant transistor width of 15 $\mu$m. The optimal length predicted is consistent with simulated value. (b) The integrate noise power versus transistor width, with constant transistor length of 1 $\mu$m. Both calculated and simulated result show a monotonic relationship.

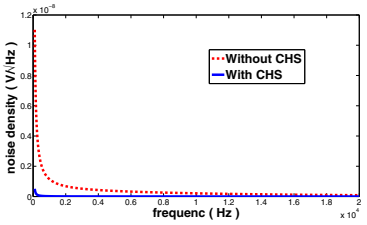


Fig. 4. Comparison of noise density with and without chopper stabilization.

respectively 8 kHz and 200 fF. The supply voltage is 1.8V, the sensor biasing voltage is $\pm$1V, and the modulation frequency is 200 kHz. The input noise floor is calculated taking into account the noise in audio frequency band from 100Hz to 20kHz, and the output linear range refers to the maximum range of output signals with less than 1% total harmonic distortion.

TABLE I
SUMMARY OF SPECIFICATIONS

| | |
|---|---|
| Supply voltage | 1.8 V |
| Power dissipation | 450 $\mu$W |
| Sensing capacitance | 200 fF |
| Resonant frequency | 8 kHz |
| Total Harmonic Distortion(THD) | $\leq$ 1% |
| Maximum linear output range | $\pm$ 0.7 V |
| Input noise floor | 3.6 $\mu V_{rms}$ |
| Equivalent capacitance noise floor | 0.72 aF |
| Dynamic range | 63 $dB$ |

## IV. Conclusions and Future Work

The design of a low-noise, low-parasitic interface circuit for beam-based MEMS cochlea-mimicking acoustic sensors is presented. Chopper stabilization technique is implemented to reduce low-frequency noise of the main amplifier, and intensive analysis is made on transistor sizing for optimal noise performance. The effectiveness of noise reduction is validated with simulation results. With a buffer added between the sensing node and chopper amplifier, the impact of circuit parasitic capacitance on the signal sensitivity is largely attenuated. Besides, the absence of high biasing voltage in the system makes it fairly suitable for building portable biomedical devices. A beam-based MEMS structure has already been fabricated for testing, and in the future we will integrate the CMOS interface circuit to build a monolithic MEMS-CMOS frequency selective microphone, which can be used as the sensing front end for a cochlea auditory system illustrated in [4].

## Acknowledgment

The authors would like to thank the EPSRC, UK, for supporting this project under Grants to the Univ. of Edinburgh (EP/G063710/1), and to the Univ. of Stirling (EP/G062609/1).

## References

[1] T. Xu, et al, "Polymeric micro-cantilever array for auditory front-end processing," *Sens. Actuators A Phys.* 114(2-3), pp. 176-182, 2004.
[2] R. D. White and k. Grosh, "Microengineered hydromechanical cochlear model," *Proc. Natl. Acad. Sci. U.S.A.* 102(5), pp. 1296-1301, 2005.
[3] F. Chen, et al., "A hydromechanical biomimetic cochlea: experiments and models," *J. Acoustic. Soc. Am.* 119(1), pp. 394-405, 2006.
[4] T. Koickal, et al., "Design of a spike event coded RGT microphone for neuromorphic auditory systems," *Proc. IEEE Int. Symp. on Circuits and Systems*, Rio de Janeiro, pp. 2465-2468, 2011.
[5] B. Wen and K. Boahen, "A silicon cochlea with active coupling," *IEEE Trans. Biomed. Circuits Syst.*, vol. 3, no. 6, pp. 444-455, Dec. 2009.
[6] S-C. Liu, A. V. Schaik, B. A. Minch, and T. Delbruck, "Event-based 64-channel binaural silicon cochlea with Q enhancement mechanisms," *Proc. IEEE Int. Symp. on Circuits and Systems*, Paris, pp. 2027-2030, 2010.
[7] W. Bracke, P. Merken, R. Puers, and C. V. Hoof, "Ultra-low-power interface chip for autonomous capacitive sensor systems," *IEEE. Trans. Circuits Syst. I, Reg. Papers*, vol. 54, no. 1, pp. 130-140, Jan. 2007.
[8] S-Y. Peng, M. S. Qureshi, P. E. Hasler, A. Basu, F. and L. Degertekin, "A charge-based low-power high-SNR capacitive sensing interface circuit," *IEEE Trans. Circuits Syst. I, Reg. Papers*, vol. 55, no. 7, Aug. 2008.
[9] J. Wu, G. K. Fedder, and L. R. Carley, "A low-noise low-offset capacitive sensing amplifier for a 50-$\mu g/\sqrt{Hz}$ monolithic CMOS MEMS Accelerometer," *IEEE J. Solid-State Circuits*, vol. 39, no. 5, May 2004.
[10] H. Sun, D. Fang, K. Jia, F. Maarouf, H. Qu, and H. Xie, "A low-power low-noise dual-chopper amplifier for capacitive CMOS-MEMS accelerometers," *IEEE Sensors J.*, vol.11, no.4, Apr. 2011.
[11] C-K. Wang, C-S. Chen, and K-A. Wen, "A monolithic CMOS MEMS accelerometer with chopper correlated double sampling readout circuit," *Proc. IEEE Int. Symp. on Circuits and Systems*, Rio de Janeiro, pp. 2023-2026, 2011.
[12] C. C. Enz and E. A. Vittoz, *Charge-Based MOS Transistor Modeling - The EKV model for low power and RF IC design*, Chichester, UK: Wiley, 2006.

# Design of a Spike Event Coded RGT Microphone for Neuromorphic Auditory Systems

Thomas Jacob Koickal, Rhonira Latif, L. Gouveia,
E. Mastropaolo, S. Wang, A. Hamilton and R. Cheung
Inst. for Integrated Micro and Nano Systems
University of Edinburgh, EH9 3JL, U.K
Email: thomas.koickal@ee.ed.ac.uk

M. Newton and L. Smith
Dept. of Computer Sc. & Mathematics
University of Stirling, FK9 4LA, U.K
Email: l.s.smith@cs.stir.ac.uk

***Abstract*—This paper presents the design of a spike event coded resonant gate transistor microphone system for neuromorphic auditory applications. The microphone system employs an array of resonant gate transistors (RGT) to transduce acoustic input directly into bandpass filtered analog outputs. The bandpass filtered analog outputs are encoded as spike time events by a spike event coder and are then transmitted asynchronously by using the Address Event Representation (AER) protocol. The microphone system is designed to receive external inputs in the spike time domain to actively control the RGT response, a feature not present in other MEMS microphone systems implemented so far. System level simulations showing the response of the RGT sensor model and its spike event coded response are presented.**

## I. Introduction

Microphones are used as the first stage in silicon cochlea for primary transduction of sound signals. The primary sound transduction organ in a biological cochlea is the organ of Corti. It is an active system which produces a large number of bandpassed outputs, dynamically altering the response of the filters depending on the signal characteristics. The parallel output of the organ of Corti and neurons of the spiral ganglion code the movement of the basilar membrane inside the cochlea. Silicon cochlea have been constructed for over two decades and recently several CMOS neuromorphic implementations have been reported [1]–[4].

MEMS provides several advantages over conventional ways of building microphones. MEMS microphones are small in size and can be directly integrated into CMOS chips. MEMS based microphones are now available commercially. However, thus far, their suitability to implement a neuromorphic active cochlea is limited: as the MEMS microphones do not demonstrate the adaptive output capability for the wide range of audio frequencies [5], [6].

In this paper, we present a neuromorphic auditory front end using an array of spike event coded RGT microphones having the following characteristics. First, it directly separates the acoustic input into many channels of bandpass filtered electrical outputs by employing an array of resonating gate transistors. Second, it encodes the bandpassed outputs from the RGTs into asynchronous spike time events and communicates to an external cochlea processor through an AER interface [7]. Third, the microphone receives feedback control signals in the spike time domain to dynamically control the RGT response characteristics, an important feature in active neuromorphic cochlea models.

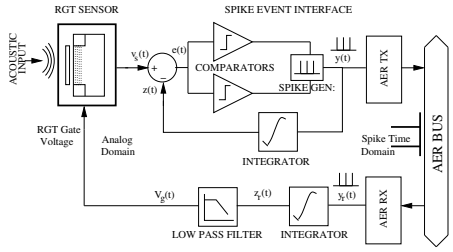


Fig. 1. Simplified block diagram of the spike event coded RGT Microphone.

## II. Block Diagram Description

The block diagram of the spike event coded microphone is shown in Fig. 1. The RGTs are used to transduce the acoustic input to electrical current. The acoustic signals are sensed by the mechanical bridges of the RGTs and are transformed into electrical signals by the modulated conductance between the source and drain. Each RGT is designed to function as a bandpass filter with a characteristic resonant frequency to separate the acoustic input into several channels. The signal conditioned RGT outputs (signal conditioner not shown) forms the input to a spike interface circuit [8]. The comparators in the feed forward loop of the spike interface circuit encodes the RGT output into spike time events. The microphone device communicates data in the spike time domain to external processors using the AER protocol. The asynchronous nature of the AER protocol preserves the information conveyed in the time difference between events. The device receives feedback control signals in the form of spike inputs which are then converted to analog form by the spike event decoder consisting of an integrator and a low pass filter. The feedback control signal is applied to the gate of the RGT to actively alter the dynamic response of the RGT.

978-1-4244-9474-3/11/$26.00 ©2011 IEEE 

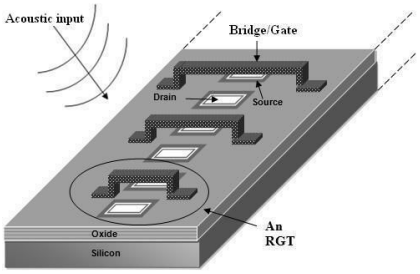


Fig. 2. The schematic of an RGT microphone.

## III. Resonant Gate Transistor

The schematic of the RGT sensor is shown in Fig. 2. It consists of a deflecting gate over the channel of a MOSFET. A sound wave incident on the gate causes it to vibrate. The vibrating gate modulates the MOSFET drain current [9]. The dynamics of the vibrating gate is modeled as:

$$\frac{X(s)}{F(s)} = \frac{1}{ms^2 + bs + k} = \frac{1}{k\left(1 + \left(\frac{s}{\omega_r}\right)^2 + \frac{s}{Q\omega_r}\right)} \quad (1)$$

where $F$ is the force on the deflecting gate, $x$ is the instantaneous displacement measured relative to the resting position, $m$ is the mass, $b$ is the damping coefficient and $k$ is the spring coefficient. The Eq. 1 is a simple approximation and does not take into account nonuniform deformation of the membrane such as spring hardening effects.

To model an auditory filter, the RGT has to approximate the function of a bandpass filter. The damping factor $b$ of the RGT should be small compared to $k$ and $m$ so that the poles are at $\pm j\sqrt{\frac{k}{m}}$. The natural frequency $\omega_r$ is $\sqrt{\frac{k}{m}}$ and the quality factor $Q$ is $\frac{\sqrt{mk}}{b}$.

The resonant frequency $\omega_r$ of the gate is given by,

$$\omega_r = \frac{6.46\ t}{l^2}\sqrt{\frac{E}{\rho}} \quad (2)$$

where E is the Young's modulus, $\rho$ is the density, $l$ is the length and $t$ is the thickness of the gate.

The resonant frequency is dependent on the properties of the gate material and on the gate dimensions (see Eq. 2). The gate material chosen to implement the resonating gate should have a relatively low $E/\rho$ ratio for it to resonate at audio frequencies. The gate material should be electrically conductive and should also be compatible with the MEMS-CMOS fabrication process. In our first batch of RGT prototypes we have chosen aluminum as the gate material which satisfies the above criteria. The dimensions of the gate, the length $l$ and the thickness $t$, are designed using Eq. 2.

Movement of the resonating gate at a constant voltage $V_g$ exerts a variable electric field perpendicular to the channel region of MOSFET, thus modulating the conductance of the channel. In the strong inversion region, the drain current $I_d(t)$ of the transistor is given by,

$$I_d(t) = \frac{\mu C_g(t) W_c}{2L_c}\left(V_g - V_{th}\right)^2 \quad (3)$$

where the total gate capacitance $C_g(t)$ between the beam and the substrate is the series capacitance between the air and oxide, $V_{th}$ is the threshold voltage and $\mu$ is the effective carrier mobility of the channel.

The transconductance of the RGT is given by $g_m = I_d(t)/V_g(t)$. The resonating beam is anchored above the channel of the MOSFET. The length $l$ of the beam corresponds to the channel width $W_c$ of the MOSFET and width of the beam corresponds to the channel length $L_c$. The sensed output voltage $v_s(t)$ is given by,

$$v_s(t) = g_m R_{out}\frac{x(t)}{d}V_g \quad (4)$$

where $R_{out}$ is the total output resistance and $d$ is the distance between the beam and the gate oxide at equilibrium. The voltage $V_g$ applied at the gate of the RGT effectively modifies the beam spring constant $k$ to

$$k_1 = k - \frac{\epsilon_0 A V_g^2}{d^3} \quad (5)$$

The resonant frequency of the gate is shifted from

$$\omega_r = \sqrt{\frac{k}{m}} \quad (6)$$

to

$$\omega_{r1} = \sqrt{\frac{k_1}{m}} \quad (7)$$

The applied gate voltage $V_g$ should be such that the total effects of the electrostatic and acoustical force does not exceed the pull-in voltage limit $V_{PI}$ of the gate. The pull-in voltage is expressed as $V_{PI} = \sqrt{\frac{8kd_o^2}{27\epsilon_0 A}}$, where $\epsilon_0$ is the permittivity of air, $A$ is the gate area, $d_o$ is the distance between the beam and the oxide when $V_g = 0$. If the gate voltage is increased beyond the pull-in voltage $V_{PI}$ of the device, the resulting electric force will cause the deflecting gate to collapse on to the oxide layer. In addition the gate voltage should be greater than the threshold voltage $V_{th}$ to turn on the device.

$$V_{th} < V_g < V_{PI} \quad (8)$$

Eq. 8 defines the limits of the feedback control voltage that is fed back to the RGT.

## IV. Spike Event Interface

The block diagram schematic of the spike event interface is shown in Fig. 1. This asynchronous interface works on the principle of irregular sampling and dissipates power based on the input signal activity (see [10] for a review). We had previously implemented this coder and decoder array along

with an AER interface for application in programmable analog arrays and the chip results were reported in [8]. In this section our emphasis is on the application of this implementation in the context of auditory filter encoding. Specifically we study the relation between the spike event response and the sensor analog response that will be used to derive the control law for active feedback tuning of the RGT.

The spike event coder operates by generating a feedback signal $z(t)$ that tracks the sensor signal $v_s(t)$ by bounding the error $e(t)$ between them:

$$e(t) = v_s(t) - z(t) = v_s(t) - k_c \int y(t)dt \tag{9}$$

where $y(t)$ is the coder output and $k_c$ is the integrator gain. The output is represented either by positive or negative pulses with a short and fixed duration (spikes). These spikes are produced by the Spike Generator and are transmitted externally by an AER transmitter. These spikes are internally fed back through an integrator.

On the receiver side, the decoded gate control output $V_g(t)$ is given by:

$$V_g(t) = LPF\left(z_r(t)\right) \approx \overline{z_r(t)} = k_d \overline{\int y_r(t)dt} \tag{10}$$

with the decoder Low Pass Filter (LPF) removing high frequency harmonics and averaging the signal $z_r(t)$, which is the result of integrating the incoming spikes $y_r(t)$. $k_d$ is the decoder integrator gain.

The spike interval $T_{spike}$ of the coder output is a function of the magnitude of its input derivative:

$$T_{spike} = \frac{\delta}{|\dot{v_s}(t)|} \tag{11}$$

where $\delta$ is the resolution to the coder. The minimum spike time interval $T_{spike(min)}$ at the AER output is defined by the maximum derivative of the input signal. For instance, if the RGT output is a bandpass filtered sine wave $v_s(t) = A\ \sin(\omega_r t)$, then

$$T_{spike(min)} = \frac{\delta}{\omega_r A} \tag{12}$$

Eq. 11 defines the RGT response in the spike domain and is used to control the gain and resonant frequency of the RGT.

## V. Results

The challenge in fabricating an RGT for the audio frequency range is in the development of a clean, reliable and damage-free process for release of long bridges. An etch release process capable of releasing long resonant gate transistor bridges from a sacrificial layer has been developed [11]. The developed etch release process involves the use of a gentle etch tool that is capable of a clean and damage free etch release. An array of aluminium bridges of length $0.28$ mm - $1.618$ mm which cover the frequencies from 1 kHz to 30 kHz have been released from a sacrificial layer. The resonating beams were then individually characterized. A set of 10 RGTs were then fabricated using this technique and the photograph

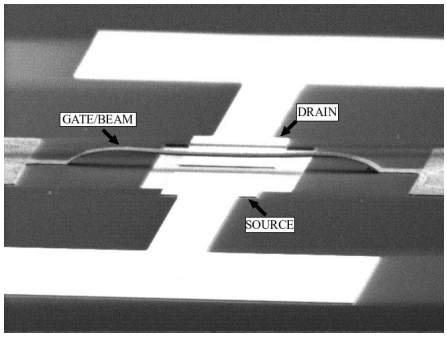


Fig. 3. SEM photograph of a prototype RGT with gate length of 280 $\mu$m and a resonant frequency of 30 kHz.

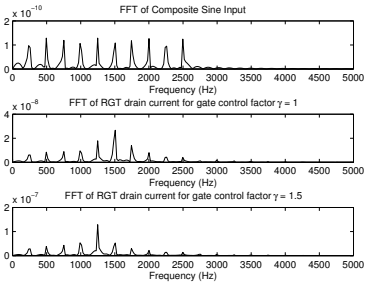


Fig. 4. The FFT of the simulated RGT output for varying gate control voltage. The input to the RGT model is a composite sinusoidal input signal with fundamental frequencies in multiples of 250 Hz. The RGT is designed for a resonant frequency of 1.5 kHz for $\gamma = 1$. When $\gamma$ is increased to 1.5 the resonant frequency decreases and the spectral component at 1.25 kHz becomes the dominant frequency.

of one such fabricated RGT for a resonant frequency of 30 kHz is shown in Fig. 3. Separately, we fabricated and tested a prototype event coder and decoder chip with an AER interface and the results were reported [8]. In this section we show the simulation results from the RGT sensor model and the measured results from the prototype spike encoder chip in the context of auditory signal encoding.

The frequency response of the RGT to varying gate voltage is studied by applying a composite sinusoidal input signal with fundamental frequencies in multiples of 250 Hz. The device dimensions for this RGT are designed for a resonant frequency of 1.5 kHz. The spectral response of the RGT for varying gate voltage is shown in Fig. 4. A gate control factor $\gamma = V_{gnew}/V_g$ is used to represent the change in gate voltage, where $V_{gnew}$ is the new gate voltage that changes the resonant frequency to $\omega_{rnew}$. When $\gamma$ is increased to 1.5, we see that

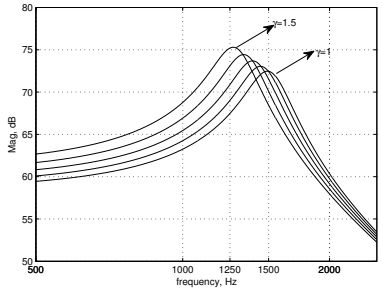


Fig. 5. The simulated frequency response of the RGT for varying gate control voltage. The resonant frequency decreases as the gate control voltage is increased.

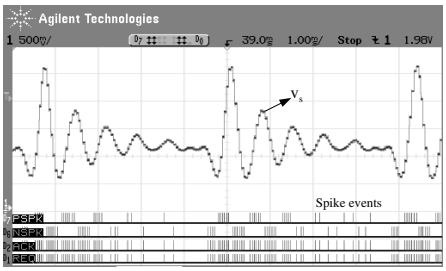


Fig. 6. Measured spike event response. The input to the coder chip is the simulated RGT sensor response $v_s$ for a composite acoustic sine wave input. The RGT resonant frequency is 1.5 kHz. The spike event output y(t) of the coder chip are shown as two separate signals: PSPK represents the positive spike events ($v_s$ going up) and NSPK represents the negative spike events ($v_s$ going down). REQ and ACK are the request and acknowledge signals from the AER. The events are generated asynchronously based on the input signal activity. The spike interval $T_{spike}$ decreases when the rate of change of RGT output increases as in Eq.11.

the resonant frequency decreases and the spectral component at 1.25 kHz becomes the dominant one while the spectral component at 1.5 kHz is significantly reduced (see Fig. 4). The corresponding frequency response of this RGT for varying gate voltage is shown in Fig. 5.

The RGT model output $v_s$ for the composite sine wave input is fed to the input of the coder chip and the chip results are shown in Fig. 6. The spikes are generated asynchronously depending on the activity of the RGT output $v_s$. The spike interval $T_{spike}$ decreases when the RGT output $v_s$ changes rapidly and no spikes are generated when $v_s$ is a constant or its amplitude changes are below a threshold range as shown in Fig. 6. Hence the power dissipation of the spike interface circuit is dependent upon the acoustic input signal activity.

## VI. Conclusions and Future Work

In this paper we presented a spike event coded RGT microphone model for neuromorphic auditory systems. Our microphone system directly converts acoustic signal into bandpassed filtered outputs and encode them as asynchronous spike time events. The microphone system alters its dynamic response by receiving inputs in the spike domain which are then decoded to vary the gate voltage of the RGT. We presented the simulation study of the RGT sensor model and also showed the measurement results from the spike encoder chip for a simulated RGT response. We have fabricated a set of 10 RGT sensors using an etch release process capable of releasing long resonant gate transistor bridges from the sacrificial layer. Our next step is to build a signal conditioning circuit and to interface the spike event coder with the RGT sensor array.

## Acknowledgment

The authors would like to thank the EPSRC, UK, for supporting this work under Grants to the Univ. of Edinburgh (EP/G063710/1), and to the Univ. of Stirling (EP/G062609/1).

## References

[1] B. Wen and K. Boahen, "A silicon cochlea with active coupling," *IEEE Trans. Biomedical Circuits and Systems.*, vol. 3, no. 6, pp. 444-455, 2009.
[2] T. J. Hamilton, C. Jin, A. van Schaik, and J. Tapson, "An active 2-D Silicon Cochlea," *IEEE Trans. Biomedical Circuits and Systems.*, vol. 2, no. 1, pp. 30-43, 2008.
[3] S-C Liu, A. van Schaik, B. A. Minch, T. Delbruck, "Event-based 64-channel binaural silicon cochlea with Q enhancement mechanisms," in *Proc. IEEE Int. Symp. on Circuits and Systems.*, Paris, pp. 2027-2030, 2010.
[4] R. Sarpeshkar, C. Salthouse, J-J. Sit, M. W. Baker, S. M. Zhak, T. K.-T. Lu, L. Turricchia, and S. Balster, "An ultra-low-power programmable analog bionic ear processor" *IEEE Trans. Biomedical Eng.* vol. 52, no. 4, pp. 711-727, 2005.
[5] J. J. Neumann Jr. and K. J. Garbirel, "A fully-integrated CMOS-MEMS audio microphone," in *Int. Conf. Solid State Actuators and Microsystems*, Boston, pp. 230-233, 2003.
[6] J. Citakovic, P. F. Hovesten, G. Rocca, A. van Halteren, P. Rombach, L. J. Stenberg, P. Andreani, and E. Bruun, "A compact CMOS MEMS microphone with 66dB SNR," in *Proc. IEEE Solid State Circuits Conf.*, San Francisco, pp. 350-351, 2009.
[7] K. Boahen, "Point-to-point connectivity between neuromorphic chips using address events," *IEEE Trans. Circuits and Syst. II, Analog and Digit. Signal Process.*, vol. 47, no. 5, pp. 416-434, 2000.
[8] L. Gouveia, T. J. Koickal and A. Hamilton, "Computation in Communication: Spike event coding for programmable analog arrays," in *Proc. IEEE Int. Symp. on Circuits and Systems.*, Paris, pp. 857-860, 2010.
[9] H. C. Nathanson, W. E. Newel, R. A. Wickstrom and J .R. Davis, Jr., "Resonant Gate Transistor," *IEEE Trans. Electron Devices*, vol. 14 no. 3, pp. 117-133, 1967.
[10] Y.P. Tsividis, "Event-Driven, Continuous-time ADCs and DSPs for Adapting Power Dissipation to Signal Activity," in *Proc. IEEE Int. Symp. on Circuits and Systems.*, Paris, pp. 3581-3584, 2010.
[11] R. Latif, E. Mastropaolo, A. Bunting, T. J. Koickal, M. Newton, A. Hamilton, L. Smith, and R. Cheung, "Microelectromechanical systems (MEMS) for biomimetical applications," *54th Int. Conf. Electron, Ion and Photon Beam Technology and Nanofabrication.*, Anchorage, 2010.

# References


[1] M. A. Ruggero, S. S. Narayan, A. N. Temchin, and A. Recio, "Mechanical bases of frequency tuning and neural excitation at the base of the cochlea: Comparison of basilar-membrane vibrations and auditory-nerve-fiber responses in chinchilla," *Proc. Natl. Acad. Sci. U. S. A.*, vol. 97, pp. 11744–11750, October 2000.

[2] D. Purves, G. J. Augustine, D. Fitzpatrick, W. C. Hall, A.-S. LaMantia, J. O. McNamara, and L. E. White, eds., *Neuroscience*. Sinauer Associates, Inc., fourth ed., 2008.

[3] J. O. Pickles, *An introduction to the physiology of hearing*. Emerald Group, fourth ed., 2012.

[4] A. F. Jahn and J. Santos-Sacchi, eds., *Physiology of the ear*. Singular-Thomson Learning, second ed., 2001.

[5] B. C. J. Moore, R. D. Patterson, I. M. Winter, R. P. Carlyon, and H. E. Gocket, eds., *Basic aspect of hearing: physiology and perception*. Springer, 2013.

[6] H. Fletcher, "Auditory patterns," *Rev. Mod. Phys.*, vol. 12, pp. 47–65, 1940.

[7] W. S. Rhode, "Some observation on cochlear mechanics," *J. Acoust. Soc. Am.*, vol. 64, pp. 158–176, July 1978.

[8] M. A. Ruggero, N. C. Rich, A. Recio, S. S. Narayan, and L. Robles, "Basilar-membrane responses to tones at the base of the chinchilla cochlea," *J. Acoust. Soc. Am.*, vol. 101, no. 4, pp. 2151–2163, 1997.

[9] W. S. Rhode, "Basilar membrane mechanics in the 6-9khz region of sensitive chinchilla cochleae," *J. Acoust. Soc. Am.*, vol. 121, pp. 2792–2804, May 2007.

[10] T. Ren and A. L. Nuttall, "Basilar membrane vibration in the basal turn of the sensitive gerbil," *Hear. Res.*, vol. 151, pp. 48–60, January 2001.

[11] C. P. Versteegh and M. van der Heijden, "Basilar membrane responses to tones and tone complexes: nonlinear effects of stimulus intensity," *J. Assoc. Res. Otolaryngol*, vol. 13, pp. 785–798, December 2012.

[12] M.-H. Giard, A. Fort, Y. Mouchetant-Rostaing, and J. Pernier, "Neurophysiological mechanisms of auditory selective attention in humans," *Front Biosci.*, vol. 5, pp. 84–94, January 2000.

[13] B. S. Wilson and M. F. Dorman, "Interfacing sensors with the nervous system: lessons from the development and success of the cochlear implant," *IEEE Sensors J.*, vol. 8, pp. 131–147, January 2008.

[14] F.-G. Zeng, S. Rebscher, W. Harrison, X. Sun, and H. Feng, "Cochlear implants: System design, integration, and evaluation," *IEEE Rev. Biomed. Eng.*, vol. 1, pp. 115–142, February 2008.

[15] D. Wang and G. J. Brown, eds., *Computational auditory scene analysis: principles, algorithms, and applications*. Wiley, 2006.

[16] R. F. Lyon and C. Mead, "An analog electronic cochlea," *IEEE Trans. Acoust. Speech Signal Process.*, vol. 36, pp. 1119–1134, July 1988.

[17] R. Sarpeshkar, R. F. Lyon, and C. Mead, "A low-power wide-dynamic-range analog VLSI cochlea," *Analog Integrated Circuits and Signal Processing*, vol. 16, pp. 245–274, 1998.

[18] T. J. Hamilton, C. Jin, A. van Schaik, and J. Tapson, "An active 2-D silicon cochlea," *IEEE Trans. Biomed. Circuits Syst.*, vol. 2, pp. 30–43, March 2008.

[19] B. Wen and K. Boahen, "A silicon cochlea with active coupling," *IEEE Trans. Biomed. Circuits Syst.*, vol. 3, pp. 444–455, December 2009.

[20] S.-C. Liu, A. van Schaik, B. A. Minch, and T. Delbruck, "Asynchronous binaural audition sensor with $2 \times 64 \times 4$ channel output," *IEEE Trans. Biomed. Circuits Syst.*, 2014. To be published. doi:10.1109/TBCAS.2013.2281834.

[21] B. S. Wilson, R. Schatzer, E. A. Lopez-Poveda, X. Sun, D. T. Lawson, and R. D. Wolford, "Two new directions in speech processor design for cochlear implants," *Ear Hearing*, vol. 26, no. 4, pp. 73S–81S, 2005.

[22] R. Patterson, I. Nimmo-Smith, J. Holdsworth, and P. Rice, "An efficient auditory filterbank based on the gammatone function," annex b of the svos final report, MRC Applied Psychology Unit, 1987.

[23] R. Sarpeshkar, ed., *Ultra Low Power Bioelectronics: fundamentals, biomedical applications, and bio-inspired systems*. Cambridge University Press, 2010.

[24] E. A. Vittoz, "Future of analog in the VLSI environment," in *Proc. IEEE Int. Symp. on Circuits and Systems*, vol. 2, pp. 1372 – 1375, 1990.

[25] W. Germanovix and C. Toumazou, "Design of a micropower current-mode log-domain analog cochlear implant," *IEEE Trans. Circuits Syst. II, Analog Digit. Signal Process.*, vol. 47, pp. 1023–1046, October 2000.

[26] J. Georgiou and C. Toumazou, "A 126-$\mu$w cochlear chip for a totally implantable system," *IEEE J. Solid-State Circuits*, vol. 40, pp. 430–443, February 2005.

[27] R. Sarpeshkar, C. Salthouse, J.-J. Sit, M. W. Baker, S. M. Zhak, T.-T. Lu, L. Turicchia, and S. Balster, "An ultra-low-power programmable analog bionic ear processor," *IEEE Trans. Biomed. Eng.*, vol. 52, pp. 711–727, April 2005.

[28] N. Kumar, W. Himmelbauer, G. Cauwenberghs, and A. G. Andreou, "An analog VLSI chip with asynchronous interface for auditory feature extraction," *IEEE Trans. Circuits Syst. II, Analog Digit. Signal Process.*, vol. 45, pp. 600–606, May 1998.

[29] E. Fragnière, "A 100-channel analog CMOS auditory filter bank for speech recognition," in *Proc. IEEE Int. Solid-State Circuits Conf. Dig. Tech. Papers*, pp. 140–141, 2005.

[30] S. Ramakrishnan, A. Basu, L. K. Chiu, J. Hasler, D. Anderson, and S. Brink, "Speech processing on a reconfigurable analog platform," *IEEE Trans. Very Large Scale Integr. (VLSI) Syst.*, vol. 22, no. 2, pp. 430–433, 2014.

[31] L. Gouveia, T. J. Koickal, and A. Hamilton, "An asynchronous spike-event coding scheme for programmable analog array," *IEEE Trans. Circuits Syst. I, Reg. Papers*, vol. 58, pp. 791–799, April 2011.

[32] G. Sanchez, T. J. Koickal, A. Sripad, L. C. Gouveia, A. Hamilton, and J. Madrenas, "Spike-based analog-digital neuromorphic information processing system for sensor applications," in *Proc. IEEE Int. Symp. on Circuits and Systems*, pp. 1624–1627, 2013.

[33] E. de Boer, "Cochlear models and minimum phase," *J. Acoust. Soc. Am.*, vol. 102, pp. 3810–3813, December 1997.

[34] D. J. Aidley, *The physiology of excitable cells*. Cambridge University Press, fourth ed., 1998.

[35] D. O. Kim, "Functional roles of the inner- and outer-hair-cell subsystems in the cochlea and brainstem," in *Hearing Science: Recent Advances* (C. I. Berlin, ed.), pp. 241–261, College-Hill Press, 1984.

[36] G. von Békésy, *Experiments in hearing*. McGraw-Hill, 1960.

[37] A. J. King and I. Nelken, "Unravelling the principles of auditory cortical processing: can we learn from the visual system?," *Nat. Neurosci.*, vol. 12, pp. 698–701, June 2009.

[38] M. Moerel, F. D. Martino, and E. Formisano, "Processing of natural sounds in human auditory cortex: Tonotopy, spectral tuning, and relation to voice sensitivity," *J. Neurosci.*, vol. 32, pp. 14205–14216, October 2012.

[39] D. T. Kemp, "Stimulated acoustic emissions from within the human auditory system," *J. Acoust. Soc. Am.*, vol. 64, no. 5, pp. 1386–1391, 1978.

[40] P. M. Zurek, "Spontaneous narrowband acoustic signals emitted by human ears," *J. Acoust. Soc. Am.*, vol. 69, no. 2, pp. 514–523, 1981.

[41] W. E. Brownell, C. R. Bader, D. Bertrand, and Y. de Ribaupierre, "Evoked mechanical responses of isolated cochlear outer hair cells," *Science*, vol. 227, pp. 194–196, January 1985.

[42] S. T. Neely and D. O. Kim, "An active cochlear model showing sharp tuning and high sensitivity," *Hear. Res.*, vol. 9, pp. 123–130, February 1983.

[43] T. S. Sridhar, M. C. Liberman, M. C. Brown, and W. F. Sewell, "A novel cholinergic "slow effect" of efferent stimulation on cochlear potentials in the guinea pig," *J. Neurosci.*, vol. 15, pp. 3667–3678, May 1995.

[44] E. R. Reiter and M. C. Liberman, "Efferent-mediated protection from acoustic overexposure: relation to slow effects of olivocochlear stimulation," *J. Neurophysiol.*, vol. 73, pp. 506–514, February 1995.

[45] W. B. Warr and J. J. Guinan, "Efferent innervation of the organ of corti: two separate systems," *Brain Res.*, vol. 173, pp. 152–155, 1979.

[46] J. H. Siegel and D. O. Kim, "Efferent neural control of cochlear mechanics? olivocochlear bundle stimulation affects cochlear biomechanical nonlinearity," *Hear. Res.*, vol. 6, pp. 171–182, 1982.

[47] M.-H. Girad, L. Collect, P. Bouchet, and J. Pernier, "Auditory selective attention in the human cochlea," *Brain Res.*, vol. 633, pp. 353–356, 1994.

[48] A. N. Temchin, A. R. Spinoso, H. Cai, and M. A. Ruggero, "Travelling waves on the organ of corti of the chinchilla cochlea: spatial trajectories of inner hair cell depolarization inferred from responses of auditory-nerve fibers," *J. Neurosci.*, vol. 32(31), pp. 10522–10529, August 2012.

[49] E. S. Olson, H. Duifhuis, and C. R. Steele, "Von Békésy and cochlear mechanics," *Hear. Res.*, vol. 293, pp. 31–43, November 2012.

[50] H. Duifhuis, *Cochlear mechanics: introduction to a time domain analysis*. Springer, 2012.

[51] J. J. Zwislocki, "Theory of the acoustical action of the cochlea," *J. Acoust. Soc. Am.*, vol. 22, pp. 778–784, November 1950.

[52] L. C. Peterson and B. P. Bogert, "A dynamical theory of the cochlea," *J. Acoust. Soc. Am.*, vol. 22, pp. 369–380, May 1950.

[53] G. Zweig, R. Lipes, and J. R. Pierce, "The cochlear compromise," *J. Acoust. Soc. Am.*, vol. 59, pp. 975–982, April 1976.

[54] G. Zweig, "Finding the impedance of the organ of corti," *J. Acoust. Soc. Am.*, vol. 89, pp. 1229–1254, March 1991.

[55] W. S. Rhode, "Observations of the vibration of the basilar membrane in squirrel monkeys using the Mössbauer technique," *J. Acoust. Soc. Am.*, vol. 49, no. 4B, pp. 1218–1231, 1971.

[56] K. Tanaka, M. Abe, and S. Ando, "A novel mechanical cochlea "fishbone" with dual sensor/actor characteristics," *IEEE/ASME Trans. Mechatronics*, vol. 3, pp. 98–105, June 1998.

[57] J.-C. Bor and C.-Y. Wu, "Analog electronic cochlea design using multiplexing switched-capacitor circuits," *IEEE Trans. Neural Netw.*, vol. 7, pp. 155–166, January 1996.

[58] S. Mandal, S. M. Zhak, and R. Sarpeshkar, "A bio-inspired active radio-frequency silicon cochlea," *IEEE J. Solid-State Circuits*, vol. 44, pp. 1814–1828, June 2009.

[59] R. F. Lyon, "A computational model of filtering, detection and compression in the cochlea," in *Proc. IEEE Intl. Conf. on Acoustics, Speech and Signal Processing*, pp. 1282–1285, 1984.

[60] R. F. Lyon and C. Mead, "Cochlear hydrodynamics demystified," Caltech Computer Science Technical Report Caltech-CS-TR-88-4, Caltech, 1989.

[61] R. F. Lyon, "Filter cascades as analogs of the cochlea," in *Neuromorphic Systems Engineering* (T. Lande, ed.), vol. 447 of *The Springer International Series in Engineering and Computer Science*, pp. 3–18, Springer US, 1998.

[62] O. F. Ranke, "Theory of operation of the cochlea: a contribution to the hydrodynamics of the cocchlea," *J. Acoust. Soc. Am.*, vol. 22, pp. 772–777, November 1950.

[63] W. M. Siebert, "Ranke revisited – a simple short-wave cochlear model," *J. Acoust. Soc. Am.*, vol. 56, pp. 594–600, August 1974.

[64] M. B. Lesser and D. A. Berkley, "Fluid mechanics of the cochlea. part 1," *J. Acoust. Soc. Am.*, vol. 51, no. 3, pp. 497–512, 1972.

[65] C. R. Steele and L. A. Taber, "Comparison of wkb and finite difference calculations for a two-dimensional cochlear model," *J. Acoust. Soc. Am.*, vol. 65, pp. 1001–1006, April 1979.

[66] C. Mead, *Analog VLSI and neural systems*. Addison-Wesley, 1989.

[67] L. Watts, A. Kerns, R. F. Lyon, and C. Mead, "Improved implementation of the silicon cochlea," *IEEE J. Solid-State Circucits*, vol. 27, pp. 692–700, May 1992.

[68] J. Lazzaro and C. Mead, "Circuit models of sensory transduction in the cochlea," in *Analog VLSI Implementation of Neural Systems* (C. Mead and M. Ismail, eds.), vol. 80 of *The Kluwer International Series in Engineering and Computer Science*, pp. 85–101, Springer, 1989.

[69] W. Liu, A. G. Andreou, and M. H. Goldstein, "Voiced-speech representation by an analog silicon model of the auditory periphery," *IEEE Trans. Neural Netw.*, vol. 3, pp. 477–487, May 1992.

[70] C. Toumazou, J. Ngarmnil, and T. S. Lande, "Micropower log-domain filter for electronic cochlea," *Electron. Lett.*, vol. 30, pp. 1839–1841, October 1994.

[71] P. M. Furth and A. G. Andreou, "Cochlear models implemented with linearized transconductors," in *Proc. IEEE Int. Symp. on Circuits and Systems*, pp. 491–494, 1996.

[72] A. van Schaik, E. Fragnire, and E. Vittoz, "Improved silicon cochlea using compatible lateral bipolar transistors," in *Advances in Neural Information Processing Systems* (D. S. Touretzky *et al.*, eds.), vol. 8, pp. 671–677, MIT Press, 1996.

[73] E. Fragniere, A. van Schaik, and E. A. Vittoz, "Design of an analogue VLSI model of an active cochlea," *Analog Integrated Circuits and Signal Processing*, vol. 12, pp. 19–35, 1997.

[74] Ø. Næss and E. A. Olsen and Y. Berg and T. S. Lande, "A low voltage second order biquad using pseudo floating-gate transistors," in *Proc. IEEE Int. Symp. on Circuits and Systems*, pp. I125–I128, 2003.

[75] V. Chan, S.-C. Liu, and A. van Schaik, "AER EAR: A matched silicon cochlea pair with address event representation interface," *IEEE Trans. Circuits Syst. I, Reg. Papers*, vol. 54, pp. 48–59, January 2007.

[76] J. Lazzaro and C. Mead, "Silicon modeling of pitch perception," *Proc. Natl. Acad. Sci. U. S. A.*, vol. 86, pp. 9597–9601, December 1989.

[77] T. Yu, A. Schwartz, J. Harris, M. Slaney, and S.-C. Liu, "Periodicity detection and localization using spike timing form the aer ear," in *Proc. IEEE Int. Symp. on Circuits and Systems*, pp. 109–112, 2009.

[78] A. van Schaik, V. Chan, and C. Jin, "Sound localisation iwth a silicon cochlea pair," in *Proc. IEEE Intl. Conf. on Acoustics, Speech and Signal Processing*, pp. 2197–2200, 2010.

[79] M. Abdollahi and S.-C. Liu, "Speaker-independent isolated digit recognition using an aer silicon cochlea," in *Proc. IEEE Biomedical Circuits and Systems Conf.*, pp. 269–272, 2011.

[80] H. Finger and S.-C. Liu, "Estimating the location of a sound source with as spike-timing localization algorithm," in *Proc. IEEE Int. Symp. on Circuits and Systems*, pp. 2561–2464, 2011.

[81] C.-H. Li, T. Delbruck, and S.-C. Liu, "Real-time speaker identification using the aerear2-event-based silicon cochlea," in *Proc. IEEE Int. Symp. on Circuits and Systems*, pp. 1159–1162, 2012.

[82] E. Fragnière, *Analogue VLSI emulation of the cochlea.* PhD thesis, Swiss Federal Institute of Technology, Lausanne, 1998.

[83] L. Watts, *Cochlear mechanics: analysis and analog VLSI.* PhD thesis, California Institute of Technology, 1993.

[84] A. van Schaik and E. Fragniere, "Pseudo-voltage domain implementation of a 2-dimensional silicon cochlea," in *Proc. IEEE Int. Symp. on Circuits and Systems*, vol. 2, pp. 185–188, 2001.

[85] H. L. F. Helmholtz, *On the sensations of the tone as a physiological basis for the theory of music*. Longmans, Green Co., 1895.

[86] R. D. Patterson, "Auditory filter shapes derived with noise stimuli," *J. Acoust. Soc. Am.*, vol. 59, pp. 640–654, March 1976.

[87] B. R. Glasberg and B. C. Moore, "Derivation of auditory filter shapes from notched-noise data," *Hear. Res.*, vol. 47, pp. 103–128, August 1990.

[88] B. C. J. Moore, R. W. Peters, and B. R. Glasberg, "Auditory filter shapes at low center frequencies," *J. Acoust. Soc. Am.*, vol. 88, pp. 132–140, July 1990.

[89] R. D. Patterson, "The sound of a sinusoid: spectral models," *J. Acoust. Soc. Am.*, vol. 96, pp. 1409–1418, September 1994.

[90] J. Holdsworth, I. Nimmo-Smith, R. Patterson, and P. Rice, "Implementing a gammatone filter bank," annex c of the svos final report, Cambridge Electronic Design, 1988.

[91] M. Cooke, *Modelling Auditory Processing and Organisation*. Cambridge University Press, 1993.

[92] M. Slaney, "An efficient implementation of the patterson-holdsworth auditory filter bank," apple computer technical report 35, Apple Computer, Inc., 1993.

[93] R. F. Lyon, "All-pole models of auditory filtering," in *Diversity in auditory mechanics* (Lewis and et al., eds.), pp. 205–211, World Scientific Publishing, Singapore, 1997.

[94] A. G. Katsiamis, M. D. E, and R. F. Lyon, "Practical gammatone-like filters for auditory processing," *EURASIP Journal on Audio, Speech, and Music Processing*, vol. 2007, 2007.

[95] A. G. Katsiamis, E. M. Drakakis, and R. F. Lyon, "A biomimetic, 4.5 $\mu$w, 120+ dB, log-domain cochlea channel with AGC," *IEEE J. Solid-State Circuits*, vol. 44, pp. 1006–1022, March 2009.

[96] K. H. Kim, S. J. Choi, J. H. Kim, and D. H. Kim, "An improved speech processing strategy for cochlear implants based on an active nonlinear filterbank model of the biological cochlea," *IEEE Trans. Biomed. Circuits Syst.*, vol. 56, pp. 828–836, March 2009.

[97] T. Harczos, A. Chilian, and P. Husar, "Making use of auditory models for better mimicking of normal hearing processes with cochlear implants: the SAM coding strategy," *IEEE Trans. Biomed. Circuits Syst.*, vol. 7, pp. 414–425, August 2013.

[98] A. B. Williams and F. J. Taylor, *Electronic filter design handbook*. McGraw-Hill, 1995.

[99] A. Recio-Spinoso, S. S. Narayan, and M. A. Ruggero, "Basilar membrane responses to noise at a basal site of the chinchilla cochlea: quasi-linear filtering," *J. Assoc. Res. Otolaryngol*, vol. 10, pp. 471–484, December 2009.

[100] F. Chen, A. F. D. Zha, J. Zheng, N. Choudhurry, S. L. Jacques, R. K. Wang, X. Shi, and A. L. Nuttall, "A differentially amplified motion in the ear for near-threshold sound detection," *Nat. Neurosci.*, vol. 14, pp. 770–774, June 2011.

[101] W. He and T. Ren, "Basilar membrane vibration is not involved in the reverse propagation of otoacoustic emissions," *Sci. Rep.*, vol. 3:1874, May 2013.

[102] C. A. Shera and J. J. Guinan, "Stimulus-frequency-emission group delay: a test of coherent reflection filtering and a window on cochlear tuning," *J. Acoust. Soc. Am.*, vol. 113, no. 5, pp. 2762–2772, 2003.

[103] L. E. Dreisbach, J. H. Siegel, and W. Chen, "Stimulus-frequency otoacoustic emission measured at low and high frequencies in untrained human subjects," *Assoc. Res. Otolaryngol. Abs.*, vol. 21, p. 349, 1998.

[104] E. de Boer and H. R. de Jongh, "On cochlear encoding: potentialities and limitations of the reverse-correlation technique," *J. Acoust. Soc. Am.*, vol. 63, pp. 115–135, January 1978.

[105] C. A. Shera, "Frequency glides in click responses of the basilar membrane and auditory nerve: their scaling behaviour and origin in traveling-wave dispersion," *J. Acoust. Soc. Am.*, vol. 109, pp. 2023–2034, May 2001.

[106] A. Recio and W. S. Rhode, "Basilar membrane responses to broadband stimuli," *J. Acoust. Soc. Am.*, vol. 108, pp. 2281–2298, November 2000.

[107] E. de Boer and A. L. Nuttal, "The mechanical waveform of the basilar membrane. i. frequency modulations ("glides") in impulse responses and cross-correlation functions," *J. Acoust. Soc. Am.*, vol. 101, pp. 3583–3592, June 1997.

[108] W. E. Brownell, "Outer hair cell electromotility and otoacoustic emissions," *Ear Hear.*, vol. 11, no. 2, pp. 82–92, 1990.

[109] D. A. Johns and K. Martin, *Analog Integrated Circuit Design*. John Wiley & Sons, Inc., 1997.

[110] F. Yuan, *CMOS active inductors and transformers: principle, implementation, and applications*. Springer, 2001.

[111] Y. P. Tsividis, *Operation and modelling of the MOS transistor*. McGraw-Hill, 1988.

[112] C. C. Enz and E. A. Vittoz, *Charge-based MOS transistor Modeling: the EKV model for low-power and RFIC design*. John Wiley & Sons Inc., 2006.

[113] P. E. Allen and D. R. Holberg, *CMOS Analog Circuit Design*. Oxford University Press, second ed., 2002.

[114] P. R. Gray, P. J. Hurst, S. H. Lewis, and R. G. Meyer, *Analysis and design of analog integrated circuits*. John Wiley & Sons Inc., fourth ed., 2001.

[115] B. Razavi, *Design of Analog CMOS Integrated Circuits*. McGraw-Hill, 2001.

[116] L. Robles, M. A. Ruggero, and N. C. Rich, "Two-tone distortion in the basilar membrane of the cochlea," *Nature*, vol. 349, pp. 413 – 414, January 1991.

[117] R. F. Lyon, A. G. Katsiamis, and E. M. Drakakis, "History and future of auditory filter models," in *Proc. IEEE Int. Symp. on Circuits and Systems*, pp. 3809–3812, 2010.

[118] B. Gilbert, "The multi-tanh principle: a tutorial overview," *IEEE J. Solid-State Circuits*, vol. 33, pp. 2–17, January 1998.

[119] T. Xu, M. Bachman, F.-G. Zeng, and G.-P. Li, "Polymeric micro-cantilever array for auditory front-end processing," *Sensor Actuat. A-phys.*, vol. 114, pp. 176–182, February 2004.

[120] F. Chen, H. I. Cohen, T. G. Bifano, J. Castle, J. Fortin, C. Kapusta, D. Mountain, A. Zosuls, and A. E. Hubbard, "A hydromechanical biomimetic cochlea: Experiments and models," *J. Acoust. Soc. Am.*, vol. 119, pp. 176–182, January 2006.

[121] R. Latif, E. Mastropaolo, A. Bunting, R. Cheung, T. Koickal, A. Hamilton, M. Newton, and L. Smith, "Low frequency tantalum electromechanical systems for biomimetical applications," *J. Vac. Sci. Technol. B*, vol. 29, p. 06FE05, Nov./Dec. 2011.

[122] M. Tavakoli and R. Sarpeshkar, "An offset-canceling low-noise lock-in architecture for capacitive sensing," *IEEE J. Solid-State Circuits*, vol. 38, pp. 244–253, February 2003.

[123] J. Wu, K. Fedder, and L. R. Carley, "A low noise low-offset capacitive sensing amplifier for a 50-$\mu g/\sqrt{Hz}$ monolithic CMOS MEMS accelerometer," *IEEE J. Solid-State Circuits*, vol. 39, pp. 722–730, May 2004.

[124] S.-S. Tan, C.-Y. Liu, L.-K. Yeh, Y.-H. Chiu, M. S.-C. Liu, and K. Y. J. Hsu, "An integrated low-noise sensing circuit with efficient bias stabilization fro CMOS MEMS capacitive accelerometers," *IEEE Trans. Circuits Syst. I, Reg. Papers*, vol. 58, pp. 2661–2672, November 2011.

[125] H. Sun, D. Fang, K. Jia, F. Maarouf, H. Qu, and H. Xie, "A low-power low-noise dual-chopper amplifier for capacitive CMOS-MEMS accelerometers," *IEEE Sensors J.*, vol. 11, pp. 925–933, April 2011.

[126] S. A. Jawed, J. H. Nielsen, M. Gottardi, A. Baschirotto, and E. Bruun, "A multifunction low-power preamplifier for MEMS capacitive microphones," in *Proc. Solid-State Circuits Conference, 2009. ESSCIRC 2009. 35th European*, pp. 292–295, 2009.

[127] Shiwei Wang and T. J. Koickal and A. Hamilton and E. Mastropaolo and R. Latif and R. Cheung and M. Newton and L. Smith, "A low-noise interface circuit for MEMS cochlea-mimicking acoustic sensors," in *Proc. IEEE Int. Symp. on Circuits and Systems*, pp. 1151–1154, 2012.

[128] J. Citakovic and P. F. Hovesten and G. Rocca and A van Halteren and P. Rombach and L. J. Stenberg and P. Andreani and E. Bruun, "A compact cmos mems microphone with 66db snr," in *Dig. Tech. Papers, IEEE Int. Solid-State Circuits Conf.*, pp. 350–351, 2009.